Measuring and Utilising Visible Light Scattering Functions for the Lunar Regolith using the Visible Oxford Space Environment Goniometer

Rowan James Curtis

Trinity College

University of Oxford

A thesis submitted for the degree of

Doctor of Philosophy

Hilary Term 2022

Abstract

An accurate description of how visible light scatters from the lunar surface enables 1) constraints to be placed on the physical and compositional properties of the surface, using a photometric model such as the Hapke BRDF model, which has nine free parameters related to compositional and physical properties, and 2) more realistic scattering function inputs to be set within thermal models. Until a recent study by Foote *et al*. in 2010, lunar visible light scattering functions had been theoretically derived using limited laboratory measurements. Within thermal models, unrealistic scattering functions may be partly responsible for modelled temperature discrepancies of up to ~15-50 K (dependent on location)—when compared to remote sensing data from Diviner, onboard the Lunar Reconnaissance Orbiter—in regions such as polar craters, where light scattering due to surface topography dominates heat transfer.

In this project, a laboratory goniometer setup was developed, which was used to measure a suite of visible light scattering functions for Apollo 11 (10084) and Apollo 16 (68810) lunar regolith samples across a wider range of viewing angles than has previously been measured. These samples were characterized in terms of their surface roughness and porosity profiles, and this enabled two of the free parameters within the Hapke BRDF model to be constrained. By fitting the model to the dataset, Hapke parameters could be deduced for the two representative (mare and highlands) regolith samples, and further constraints could be placed on the 'practical' size-scale of the model's slope angle parameter. Thus, the dataset enabled Diviner's visible-wavelength off-nadir data to be interpreted in a novel way, due to the reduction of free terms within the model. This led to surface roughness and compositional deductions (via the Hapke parameters h_s, b and $\bar{\theta}$) for seven Diviner targets. Finally, the dataset was used to set more realistic scattering functions within the Oxford 3D Thermal Model, and it was demonstrated that this 1) could affect modelled high-latitude lunar surface temperature profiles by up to ~30 K—as compared to using previously assumed scattering functions—and 2) could increase the minimum depth at which water ice is predicted to be stable in the lunar subsurface by up to ~0.8 m. Hence, this dataset may help to constrain the possible distribution of water ice on the lunar surface, and this may be crucial for future lunar exploration missions such as Luna-27 and Artemis.

Rowan Curtis Hilary Term 2022

Acknowledgements

Firstly, I would like to wholeheartedly thank my supervisor, **Professor Neil Bowles**, for his academic support and guidance, his exemplary running of our group, his unique sense of humour (which grows even stronger before major deadlines), and for being a joy to work with, despite his rants and rambling meetings—which, as I'm all too aware, my presence only encourages. Most of all, I would like to thank him for allowing me the opportunity to carry out this project, the undertaking of which has been one of the greatest privileges of my life. I would like to thank **Dr. Tristram Warren** for being a constant source of help and guidance, and for all the time and effort he has invested in this project, which has helped me immeasurably to grow as a scientist. I would like to thank **Arjuna James**, **Burtie 'The Muscle' Spry** and **Ashwin Braude** for keeping me company in the office, and for many productive and enjoyable conversations. I would like to thank **Jon Temple**, **Andy Clack**, **Rory Evans**, **Jordan Hoe**, **Jack Mellors**, **Dr. Henrique Laitenberger**, **Dr. Kalin Dragnevski**, **Dr. Marzena Tkaczyk**, **Professor Michael Shepard, Professor Radan Slavik** and **Professor Kerri Donaldson Hanna** for their help at various stages of this project. I am also grateful to **Professor David Paige** for lending us the Apollo samples, without which this work would not have been possible. I would like to thank my examiners, **Professor Simon Calcutt**, **Professor Raymond Pierrehumbert**, **Professor Carly Howett** and **Professor Benjamin Greenhagen**. I would like to thank **Mum**, **Dad**, **Papa**, **Gus**, and **Sam** for all their love and support over the course of this project. Finally, I would like to express my sincere and loving gratitude to **Dr. Bethany White** for all her support, companionship, and academic help over the past three and a half extraordinary years. You are a shining light in my life and I could not have done it without you.

When I heard the learn’d astronomer,
When the proofs, the figures, were ranged in columns before me,
When I was shown the charts and diagrams, to add, divide, and measure them,
When I sitting heard the astronomer where he lectured with much applause in the lecture-room,
How soon unaccountable I became tired and sick,
Till rising and gliding out I wander’d off by myself,
In the mystical moist night-air, and from time to time,
Look’d up in perfect silence at the stars.

When I Heard the Learn’d Astronomer—Walt Whitman

For my Dad,

beside whom I first wondered at the stars.

Table of Contents

Scientific Aims and Goals

Table 1 outlines the three overarching science questions and the scientific aims (A#) and goals (G#) of the project. In general, each aim maps to the corresponding goal, as in A2 to G2 and A4 to G4, but importantly, every one of the goals also depends on A1.

<table>
<tr><th colspan="3">Science Questions</th></tr>
<tr><td>1. What is the form and distribution of ice volatiles, such as water ice, on the Moon?</td><td colspan="2">2. What compositional and physical property variations across the lunar surface can be deduced from remote sensing photometry datasets?</td><td>3. How does the lunar regolith scatter light across a range of viewing angles depending on composition, porosity and surface roughness?</td></tr>
<tr><th colspan="2">Aims</th><th>Goals</th></tr>
<tr><td colspan="2">A1—Develop a visible-wavelength goniometer system which can measure BRDFs for the White Spectralon® reflectance standard material that agree with other goniometer systems for a wide range of viewing angles.</td><td>G0—Provide the planetary science community with a well-characterized goniometer system, for use in current and future studies of returned and simulant samples.</td></tr>
<tr><td colspan="2" rowspan="2">A2—Measure a comprehensive suite of BRDFs for mare and highlands Apollo regolith samples with measured—and various—porosity (i.e. filling factor) and RMS slope angle values, across a range of size-scales.</td><td>G1—Provide the lunar science community with a comprehensive suite of laboratory measured BRDFs for two representative—mare and highlands—and well-characterised Apollo regolith samples.</td></tr>
<tr><td>G2—Test the Hapke BRDF model by determining the size-scale of the Hapke slope angle parameter (to within 1-2 orders of magnitude) and hence, by evaluating the physicality of the terms within the model.</td></tr>
<tr><td colspan="2">A3—Compare the laboratory measured BRDFs (from A2-BRDF) to visible-wavelength Diviner off-nadir data, for various representative (mare and highlands) regions of the lunar surface.</td><td>G3—Provide a novel interpretation of the visible-wavelength Diviner off-nadir data, by comparing it to the laboratory measured suite of BRDFs with known porosity and RMS slope angle values.</td></tr>
<tr><td colspan="2">A4—Utilize the laboratory measured suite of BRDFs as scattering function inputs for the Oxford 3D Thermal Model.</td><td>G4—Reduce the temperature discrepancies between remote sensing (e.g. Diviner) data and thermal model predictions, for high-latitude permanently shadowed regions. This is in preparation for future robotic and/or crewed missions to the lunar surface.</td></tr>
</table>

Table 1: Outlining the three overarching science questions and the scientific aims (A#) and goals (G#) of this research project.

1. Introduction and Motivation

1.1 The Lunar Surface

Until the Lunar Ranger (1959-1965), Surveyor (1966-1968), Apollo (1969-1972) and Luna (1959-1976) missions visited the Moon, little was known about the lunar surface (Turkevich, Franzgrote and Patterson, 1967; Scherer, 1971; Zelenyi, Zakharov and Zakutnyaya, 2011; Burke, 2014; Lund, 2018) beyond what could be deduced from telescope studies; that the surface is heavily cratered and that there are two main distinct regions: the generally higher albedo 'highlands', and the generally darker 'mare' regions (Gold, 1955). To describe the features of the lunar surface, many hypotheses have been proposed since antiquity about the nature and evolution of the Moon, but it is only since the mid twentieth century that any of these have been able to be disproved or confirmed. Thomas Gold's photometric studies in the 1950s suggested that the Moon is predominantly covered in fine-grained material (Gold, 1955), and this was proved by the robotic and crewed lunar landings of the 1960s. The lunar samples returned by the Apollo and Luna landings were some of the first 'ground truth' samples (from a known location) for any planetary body other than Earth, and the study detailed in this thesis is an example of how we still scientifically benefit from them today (Morris, 1983). Because of those missions, we now have better-constrained theories about the nature and evolution of the Moon (Whipple, 1993; Dunkin and Heather, 1999; Bottke and Norman, 2017), and we know that on the lunar surface there are (at least) four distinct groups of materials (Hiesinger, 2006): 1) Pristine highlands rocks; 2) pristine basaltic volcanic rocks, which include lava flows and pyroclastic deposits; 3) polymict clastic breccias, which include impact melt rocks and thermally metamorphosed granulitic breccias and 4) regolith, which covers almost the entire lunar surface and so is the most important material to understand for remote sensing and thermal modelling studies of the Moon (Morris, 1983; Hapke, 1993; Sato *et al.*, 2014).

1.1.1 Lunar Regolith and the Lunar Thermal Environment

Regolith—which derives from the Greek for 'blanket rock'—is the term used to describe the finely powdered (mostly 10-100 μm), poorly conducting (~$1.5x10^{-3}$ W/mK), and highly porous unconsolidated material that almost entirely covers the surface of the Moon except from rare exposures of bedrock, mainly on the walls of steep craters (Birkebak, 1974; King *et al.*, 1977). The composition of lunar regolith varies with location on the Moon, from dominantly basaltic rock (for the mare), to dominantly anorthositic rock (for the highlands), but the structures formed by it are generally homogenous across the lunar surface. Regolith grain sizes vary between ~10 μm and ~1 cm, with an average (by mass) of ~60-80 μm and consist of five particle types: Mineral fragments, pristine crystalline rock fragments, breccia fragments, glasses, and agglutinates, which are aggregated particles welded together by glasses produced in micrometeorite impacts (McKay et al., 1991). **Figure 1** shows an example of an abnormally large agglutinate grain collected during the Luna 16 mission, from *Mare Fecunditatis* (Rode, 1979).

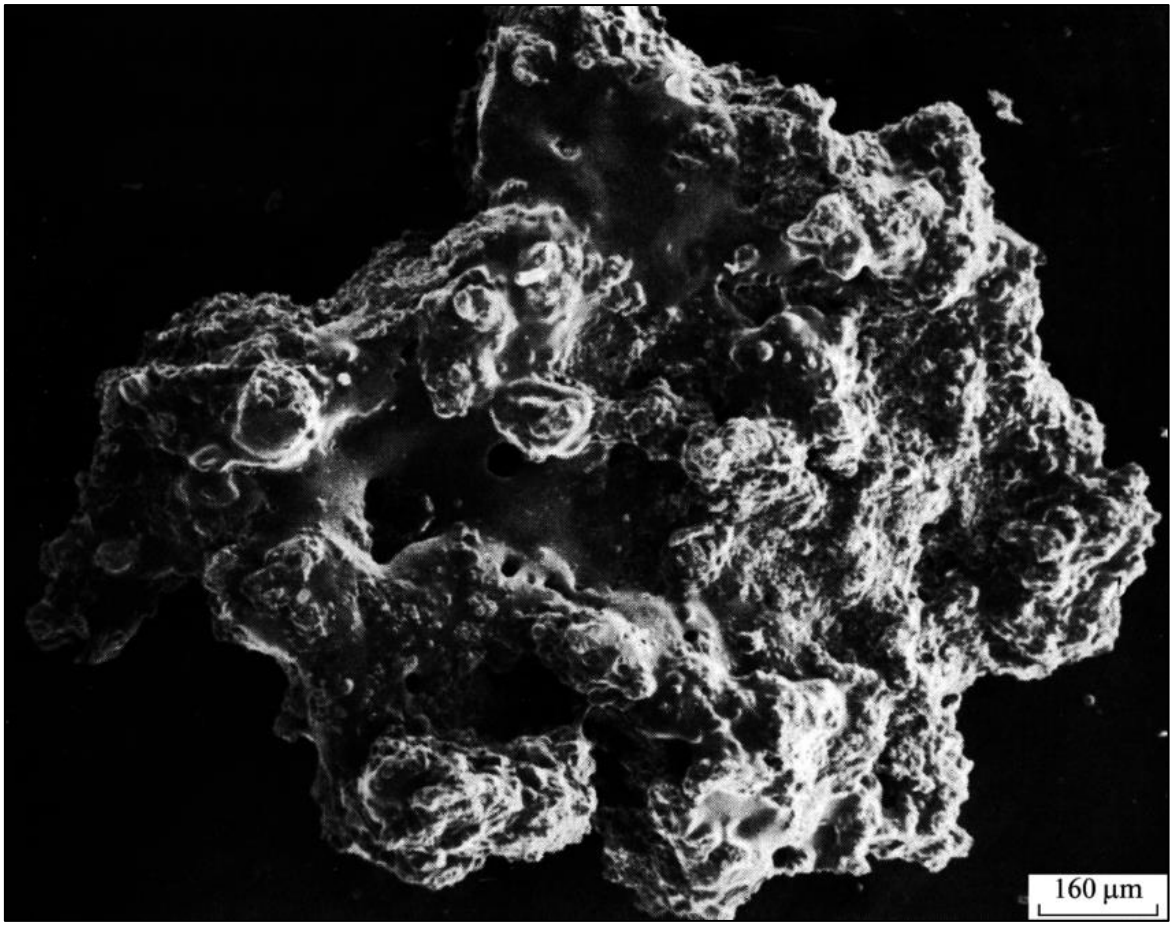

Figure 1: An abnormally large agglutinate particle of lunar regolith collected during the Luna 16 mission (Mare Fecunditatis). The nature of the shape and surface of the particle is caused by the melting and subsequent agglomeration of lytic fragments and mineral and glass grains into a single particle after a high velocity meteorite impact. Image from (Rode, 1979).

Regolith particles are generally irregular and 'spiky', as in **Figure 1**, so when they are layered on top of one another they create minimally conducting, highly porous structures known as 'fairy castles'. These structures are preserved on the lunar surface because there are no atmospheric erosion processes (e.g. winds) and because the surface gravity is ~1/6th that of Earth's (King *et al.*, 1977). **Figure 2** shows (left) an image from the surface of the Moon and (right) the sort of 'fairy castle' structures created by the lunar regolith (Salisbury and Wald, 1992).

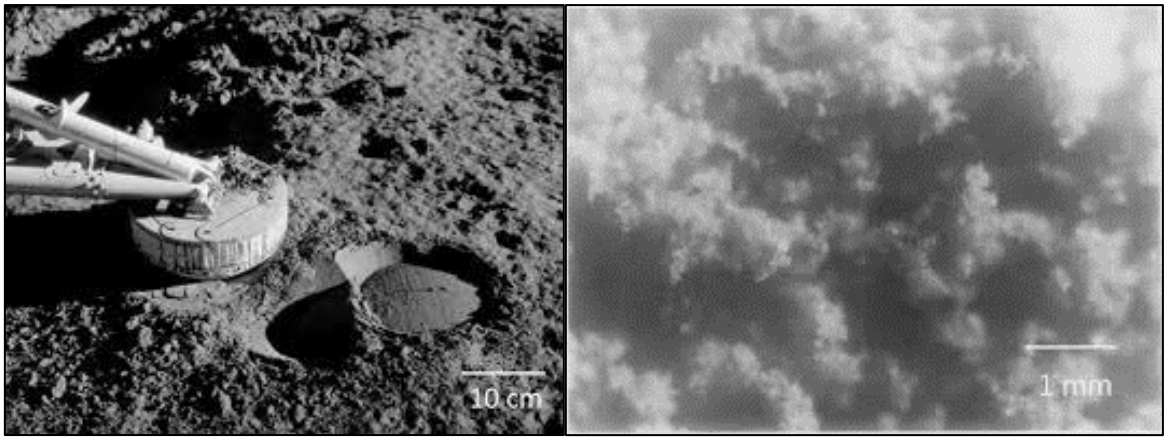

Figure 2: Left—a photograph from the surface of the predominantly basaltic Mare Cognitum region of the Moon taken by the Surveyor-3 mission, from the NASA Archives. Right—an example of a "fairy castle" structure, similar to those made by the regolith on the lunar surface (see also, Figure 21). Image from (Salisbury and Wald, 1992).

The minimally conducting nature of the lunar regolith, coupled with the lack of appreciable atmosphere over large time periods (>$1x10^6$ years) gives rise to a thermal environment on the lunar surface which is very different to that of Earth.

For a planetary body with an atmosphere, a significant amount of heat can be transferred across the surface via conduction, convection and radiation (Chandrasekhar, 1960). However, for the Moon, radiation dominates the thermal environment. Therefore, on the lunar surface, thermal gradients between shadowed and illuminated regions can be >100 K/m (Paige et al., 2010). Lunar daytime regions can reach ~400 K at the equator, and, as for nighttime regions, surface temperatures are dependent on latitude (Williams *et al.*, 2017a). The low conductivity of the lunar regolith, from minimal contact between regolith particles, leads to large temperature gradients between the surface and subsurface. Considering the daytime subsurface, at ~0.3-1 m, is modelled to be ~250 K for equatorial regions, the vertical temperature gradient is modelled to be up to ~170 K/m (Hayne *et al.*, 2017).

Additionally, due to the Moon's low ecliptic obliquity (the angle between the rotational and orbital axis of a planetary body with respect to the ecliptic plane), the thermal environment becomes most extreme in lunar polar cratered regions, where large shadows are cast (Ward,

1975). **Figure 3** shows the orbital details of the Earth-Moon system. Note that the ecliptic obliquity of the Earth is ~23.4° and hence it experiences more considerable seasonal variations than the Moon, which has an ecliptic obliquity of ~1.54°.

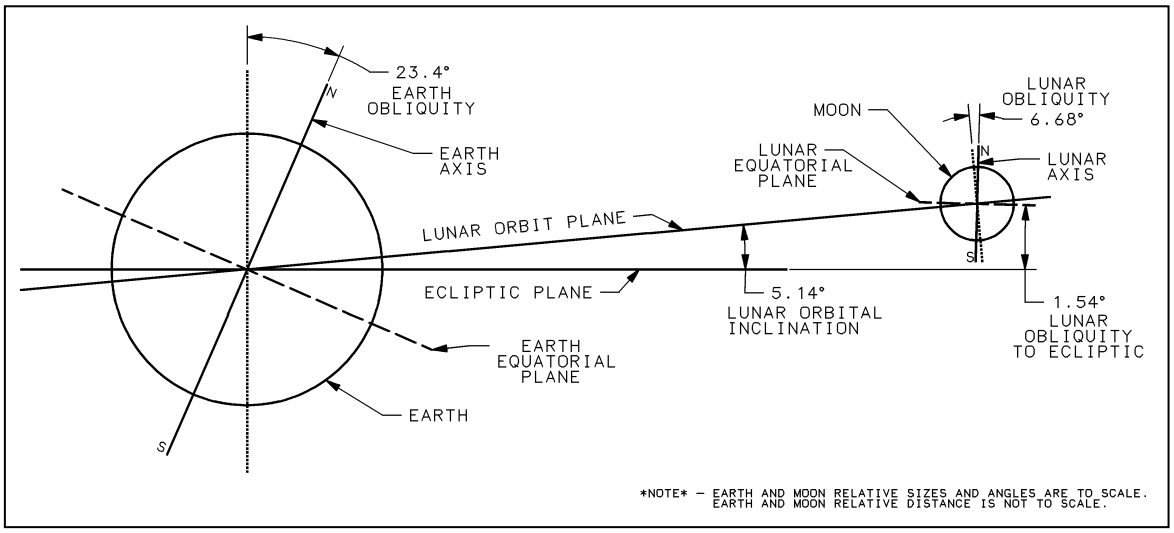

Figure 3: This figure shows the details of the Earth-Moon orbital system. Importantly, the Obliquity to the Ecliptic (which defines the extremity of the seasons) of the Moon is 1.54°. Image credit: Peter Sobchak, Wikicommons.

Figure 3 demonstrates how at the lunar poles (>60°), incoming rays of light can be permanently at low incidence angles (<10°), for some surface topographies. This leads to permanent shadows being cast within and around lunar polar craters (see Part 1.1.2) (Williams *et al.*, 2019). Temperatures within these permanently shadowed regions (PSRs) can be invariably <112 K (the maximum temperature for which water ice will not sublimate and escape the surface gravity of the Moon according to the Jeans escape formula), and in places <30 K (lower than the boiling points of Nitrogen and Carbon Monoxide) (Basilevsky, Abdrakhimov and Dorofeeva, 2012).

1.1.2 Permanently Shadowed Regions at the Lunar Poles

As described in Part 1.1.1, due to the Moon's heavily cratered surface and its low (~1.54°) ecliptic obliquity, the lunar poles contain PSRs, as observed on other airless bodies such as Mercury and Ceres (Rubanenko, Venkatraman and Paige, 2019). PSRs can trap ice volatiles

within them. Ice volatiles are chemical elements and compounds with low (but >100 K) sublimation points contained within a planetary bodies' crust or atmosphere (varying for each planet), and hence, they are targets of interest for various upcoming remote sensing, crewed and robotic missions such as Artemis and Luna-27 (for full descriptions of Artemis and Luna-27, see (Chavers *et al.*, 2019; Hambleton, 2020) and (Fisackerly *et al.*, 2015; Trautner *et al.*, 2018), respectively). **Figure 4** shows how an area of permanent shadow can be cast at the bottom of a hypothetical lunar PSR crater, due to the cratered topographies and low solar incidence angles cast within high-latitude regions of the lunar surface. From **Figure 4** an important point (which was mentioned above) emerges: that the dominant source of heat transferred into a PSR is from reradiation and visible light scattering from the surrounding surfaces (i.e., the crater walls).

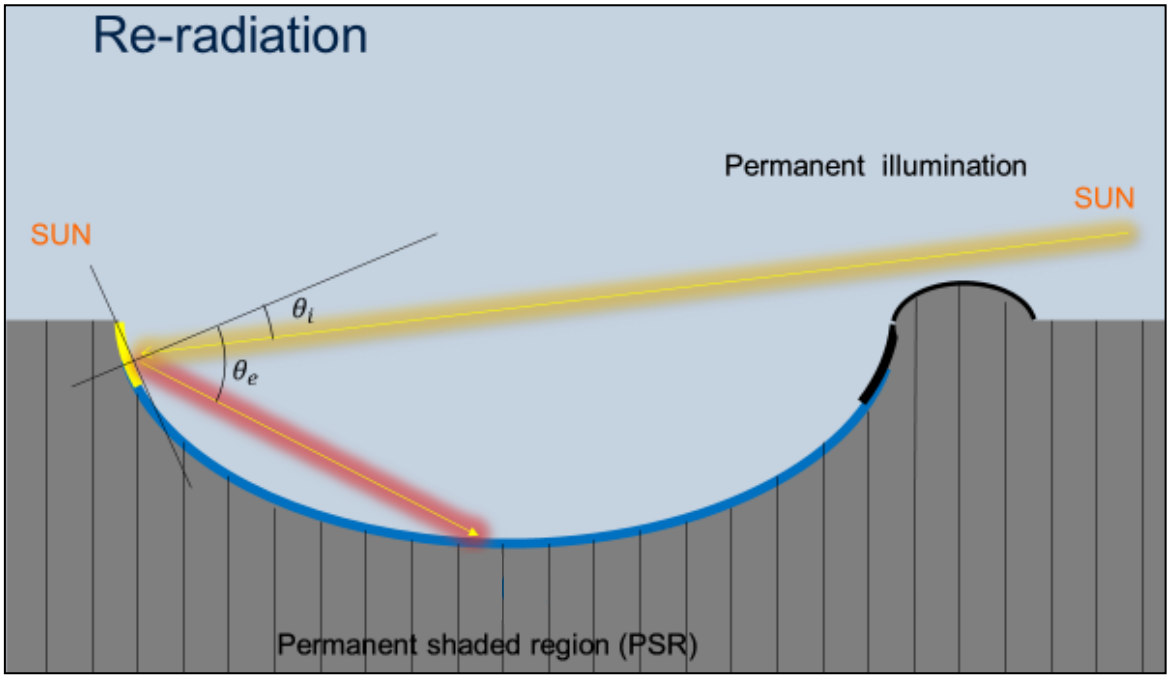

Figure 4: A simplified 2-Dimensional slice of a gridded cratered region of the Moon, showing how radiation is reradiated/scattered from illuminated regolith onto other areas of the crater; hence, influencing the crater's temperature profile. Image from (Warren, 2015).

Such PSRs within high-latitude regions of the lunar surface were first proposed as regions of interest in (Watson, B. Murray and Brown, 1961), but more recently, they have been imaged by remote sensing instruments, such as those onboard the Lunar Reconnaissance

Orbiter (LRO) (see Part 1.2) (Robinson *et al.*, 2010). Using remote sensing to determine the regions in which it is thermodynamically possible for water ice and other ice volatiles to be trapped is one of the crucial steps towards proving their existence, and defining their abundance, on the lunar surface. **Figure 5** shows surface and subsurface temperatures, and areas for which water ice may exist, at various locations and depths at the lunar South Pole, as estimated by the Paige 3D Thermal Model (see Part 1.3) and constrained by Diviner's surface bolometric temperature data (see Part 1.2.2) (Paige et al., 2010). For the study which produced **Figure 5**, a thermal model was used to interpret LRO's remote sensing data. A detailed description of lunar thermal models and their relevance to this project is given in Part 1.3.

According to basic Jeans atmospheric escape calculations, water ice delivered to, or created on, the lunar surface may be permanently trapped in PSRs if the temperature does not exceed 112 K (Arnold, 1979). For temperatures larger than 112 K, the thermal velocity of the water molecules would lead to their escape from the surface. As demonstrated in **Figure 4**, temperatures within PSRs are dependent on surface topography, regolith surface properties/composition and incident solar radiation, with a small additional flux from residual internal heat (predominantly from the radioactive decay of elements) (Arnold, 1979). Hence, to more accurately determine the possible distribution of ice volatiles on the Moon, it is vital to accurately describe how the lunar regolith surface scatters visible—and reradiates thermal infrared—radiation over a range of viewing angles. This information can then be used to set accurate visible scattering function inputs within thermal models (Hapke, 1981; Vasavada, Paige and Wood, 1999; Rozitis and Green, 2011; King *et al.*, 2019). However, before exploring lunar light scattering functions in Part 1.3.3, the importance of discovering ice volatiles, such as water ice, at the lunar poles will be considered.

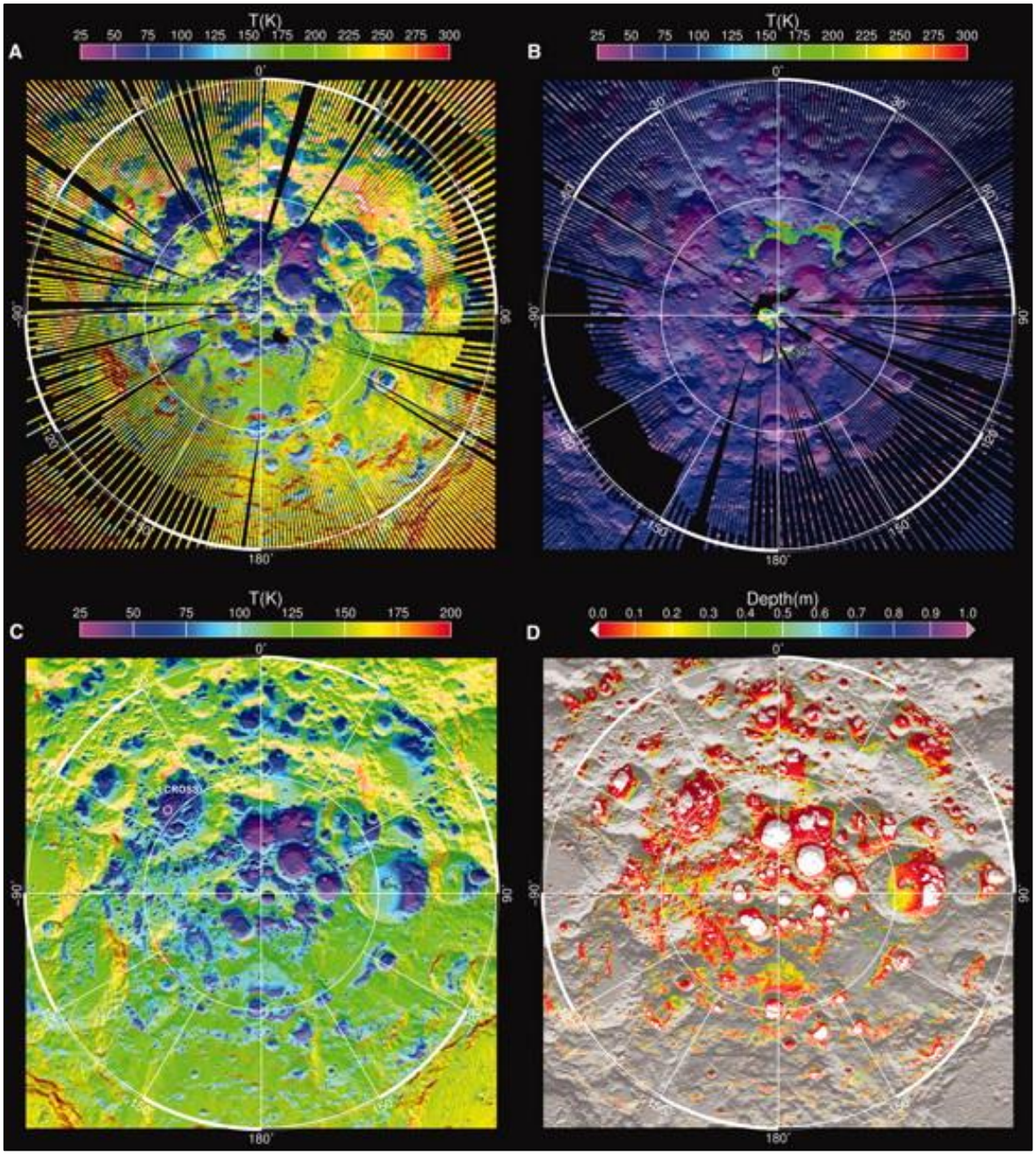

Figure 5: Maps of measured and modelled surface and subsurface temperatures in the lunar south pole. (A**) Diviner-measured daytime bolometric brightness temperatures. (**B**) Diviner-measured night-time bolometric brightness temperatures. (**C**) Model-calculated annual average near-surface temperatures and the location of the Lunar Crater Observation and Sensing Satellite (LCROSS) impact in Cabeus Crater. (**D**) Model-calculated depths at which water ice would be lost to sublimation at a rate of less than 1 kg/m^2 per billion years. The white regions define the locations where water ice may currently be cold trapped on the surface, the coloured regions define the upper surface of the lunar ice permafrost boundary, and the grey regions define locations where subsurface temperatures are too warm to permit the cold-trapping of water ice within 1 m of the surface. Image from (Paige et al., 2010).**

1.1.3 The Importance of Discovering Ice Volatiles at the Lunar Poles

It has been speculated since (Watson, B. Murray and Brown, 1961)—and for Mercury, since (Thomas, 1974)—that water ice and other ice volatiles may have been delivered to the lunar surface by comets, meteorites and outgassing. These can then migrate to the polar regions from lower latitude areas of the Moon by diffusion or ballistic migration (Watson, B. C. Murray and Brown, 1961; Butler, 1997; Dunkin and Heather, 1999; Arnold, 2008). Furthermore, water molecules may be created when protons from the solar wind are implanted in the lunar surface (e.g., via reduction of FeO) (King *et al.*, 1977). **Figure 6** shows a description of the lunar water/ice volatiles cycle (Lucey, 2009).

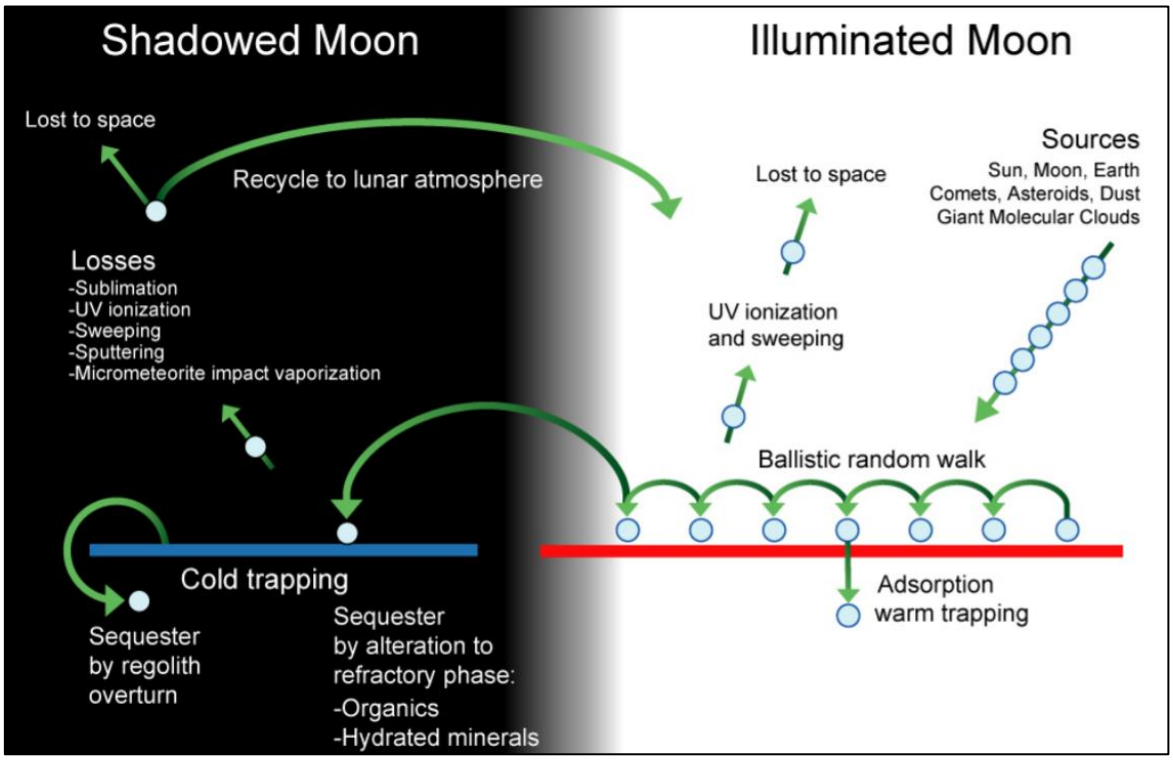

Figure 6: Showing the lunar water/ice volatiles cycle, for illuminated and shadowed regions. Ice volatiles may be delivered to the lunar surface primarily by comets, meteorites and outgassing; or they may be implanted via the solar wind (e.g., by reduction of FeO). Subsequently, lunar ice volatiles may ballistically migrate and become cold trapped in permanently shadowed regions on the Moon. Image from (Lucey, 2009).

There have been many potential but non-unique detections of water ice on the lunar surface, such as 1) the detection of large quantities of hydrogen in lunar PSRs by Lunar Prospector's

neutron detector (Binder, 1998); 2) the LCROSS mission's spectral identification of H_2O ice and vapour in Cabeus crater's ejecta plume (after smashing a hollow Centaur rocket booster into it) (see **Figure 7**) (Colaprete *et al.*, 2010). This was supported by UV and neutron spectroscopy of LRO's instruments LAMP and LEND, respectively; 3) LRO's Mini-RF and radar data, which also suggested that any water ice in the surface/subsurface is unlikely to be in contiguous blocks >10 cm (Spudis *et al.*, 2013); and 4) the (Rubanenko, Venkatraman and Paige, 2019) study, which showed that depth-diameter ratios for simple shallow craters at the lunar South Pole are consistent with ice deposits forming within them, as was observed at both of Mercury's poles. (Mercury has a similar thermal environment to the Moon, and studies akin to this one could be performed for Mercury, once the global TIR science campaign of BepiColombo begins in 2025 (Benkhoff *et al.*, 2010).)

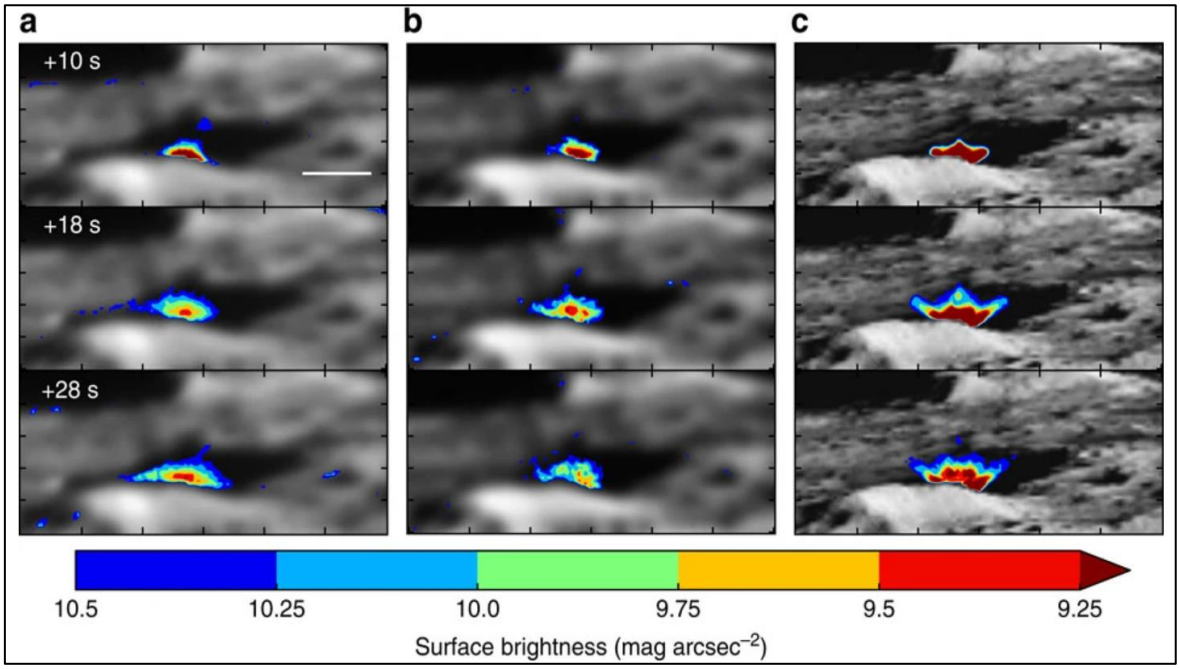

Figure 7: Brightness images of Cabeus crater during LCROSS impact in 2009. Image credit: NASA JPL.

It is only as recently as 2021, in the (Honniball *et al.*, 2021) study, that a unique detection of molecular water ice was made using the Stratospheric Observatory for Infrared Astronomy (SOFIA). This study not only detected the non-unique 3 µm absorption feature associated with potential water ice, but also detected the 6 µm spectral signature associated

with fundamental vibrations of water molecules, and which, importantly, is not shared by other hydroxyl compounds. In addition to this unique detection of molecular water, this study estimated a molecular water ice abundance of ~100-400 $\mu g g^{-1}$ for the ice-regolith mixtures observed in the given location—Clavius Crater—and suggested 1) that the majority of the water ice detected must have been hidden from the harsh lunar surface in voids between regolith grains or within glasses; and 2) that the lunar surface's water ice distribution is dependent on local geology and is not likely to be a global phenomenon.

In light of the above studies, it is strongly expected that water ice exists on the lunar surface/subsurface within—and potentially around—polar PSRs, however, absolute conformation of the nature and existence of lunar water ice awaits proof from 'ground truth' sampling.

From a scientific perspective, studying the quantity, form and location of ancient water ice which may have been trapped on the Moon for millions-to-billions of years may help to answer questions such as: What is the nature and timescale of the lunar late-heavy bombardment (Bottke and Norman, 2017)? What are the delivery, migration and loss mechanisms for water on the lunar surface (Hauri *et al.*, 2015)? And which of our theories for solar system evolution and the history of the Earth-Moon system are most accurate (i.e. grand-tack etc.) (Hiesinger, 2006)?

Furthermore, from a practical perspective, human exploration of the Moon and beyond could be facilitated by In-Situ Resource Utilization (ISRU) of water ice. This is because 1) finding H_2O may be more energy and time efficient than other lunar water production methods (i.e. hydrogen reduction of ilmenite ($FeTiO_3+H_2 \rightarrow Fe+TiO_2+H_2O$)), if sufficient ice deposits are discovered; and 2) lunar water ice deposits may increase the habitibility of the Moon by providing the necessary material for propulsion, cooling, and basic human survival (Steklov,

Vidmachenko and Minyaylo, 2019). If water ice is present on the lunar surface/subsurface, the lunar surface may provide the required environment not just for living on the Moon, but also for travelling to Mars and beyond (Chavers *et al.*, 2019; Hambleton, 2020).

The potential for answering the above science questions through the study of lunar water ice has led to PSRs being suggested as targets for current and future lunar exploration missions (Fisackerly *et al.*, 2015; Chavers *et al.*, 2019). Therefore, it is vital that the temperature profiles and topographies of PSRs are well-constrained and accurate. As demonstrated in **Figure 5**, remote sensing data and thermal models must be used in tandem to predict PSR surface/subsurface temperature profiles for all times of day across the Moon's seasonal variations (Hayne *et al.*, 2017; King *et al.*, 2019). Yet remote sensing studies are not only crucial to the search for lunar water ice because they provide temperature measurements, but also because they can detect potential direct signatures of water ice. This has been shown in various studies (such as (Colaprete *et al.*, 2010; Spudis *et al.*, 2013; Rubanenko, Venkatraman and Paige, 2019)), using the instruments onboard the LRO, which have measured the most comprehensive suite of lunar remote sensing measurements to date. The LRO and its instruments are therefore described in the following section.

1.2 The Lunar Reconnaissance Orbiter and its Relevant Instruments

1.2.1 The Lunar Reconnaissance Orbiter (LRO)

The LRO is currently the most comprehensive orbital remote sensing mission to observe the Moon, and since its launch in June 2009 its suite of instruments have imaged ~the entire lunar surface from altitudes ranging from ~20-170 km for almost all times of day (Robinson *et al.*, 2010). Studies using data from LRO have 1) produced temperature maps for the poles of the Moon which demonstrate the thermodynamic possibility of water ice being trapped there (Williams *et al.*, 2017b), 2) provided depth-diameter ratios for PSR craters which

highlight key differences between the North and South Poles of the Moon (Rubanenko, Venkatraman and Paige, 2019), and 3) measured potential signatures of water ice and other ice volatiles trapped on the lunar surface (Hayne *et al.*, 2010). These are just a few examples, and studies using the extensive datasets measured by LRO's instruments are still producing important results today, over a decade after its launch.

The LRO spacecraft carries six remote sensing instruments with varying (but often overlapping) science objectives: 1) The Cosmic Ray Telescope for the Effects of Radiation (CRaTER), 2) the Diviner Lunar Radiometer Experiment (DLRE), 3) the Lyman-alpha Mapping Project (LAMP), 4) the Lunar Exploration Neutron Detector (LEND), 5) the Lunar Orbiter Laser Altimeter (LOLA) and 6) the Lunar Reconnaissance Orbiter Camera (LROC) (Tooley *et al.*, 2010). **Table 2** details the instruments and their objectives.

LRO instrument	***Primary measurements***	***Key characteristics***
1) CRaTER—Cosmic Ray Telescope for the Effects of Radiation (Boston/MIT)	Lunar and Deep Space Radiation Environment.	- Nadir Field of view (FOV) 70˚ - Zenith FOV 35˚.
2) DLRE—Diviner Lunar Radiometer Experiment (UCLA/JPL)	- 300-500 m resolution maps of surface temperature profiles, including PSRs - Characterizes rock abundance and albedo.	- 40-400 K 9 channel radiometer - 21-pixel push-broom line detector; 3.15 km swath - Can measure off-nadir.
3) LAMP—Lyman-Alpha Mapping Project (Southwest Research Institute)	Maps ice and landforms in permanently shadowed regions using Lyman-alpha albedo.	- 465-1880 A passband - 0.3x6.1˚ slit - 1.8 A full slit spectral resolution.
4) LEND—Lunar Exploration Neutron Detector (Russian Space Agency)	Maps Hydrogen in upper 1 m of regolith at 10 km scale using neutron albedo.	- Collimated neutron telescope - Measures and differentiates thermal, epithermal and energetic neutrons.

5) LOLA—Lunar Orbiter Laser Altimeter (Goddard Space Flight Centre)	- Global topography with 10 cm vertical and 1 km (equator) to 25 m (poles) horizontal resolution.	- 1064 nm laser pulsed at 28 Hz - Can be used to characterize slopes, roughness and brightness.
6) LROC—Lunar Reconnaissance Orbiter Camera **NAC** (x2)—Narrow Angle Cameras **WAC**—Wide Angle Camera (ASU/MSSS)	- Target imagery at 0.5 m resolution at poles and selected sites - Global imagery in visible and UV at 100 m resolution - Maps ilmenite and other minerals.	<u>NACs:</u> - Focal length (FL) = 700 mm - FOV 2.86° per NAC <u>WAC:</u> - FL = 6 mm (vis)/4.7 mm (UV) - FOV = 90° (vis)/60° (UV) - Can measure off-nadir.
(Demo) Mini-RF—Technology Demo of Small Synthetic Aperture Radar (SAR) (DOD/NAWC)	- Radar imagery and interferometry - Can contribute to topography and resource identification.	- X & S band radar - 15-150 m resolution (mode dependent).

Table 2: Summary of instruments onboard the Lunar Reconnaissance Orbiter—from (Tooley *et al.*, 2010).

For this project, CRaTER, LAMP and LEND are not as relevant as the DLRE, LOLA and LROC, and so for further details about them, see (Tooley *et al.*, 2010). LOLA is of interest to this project because its topographical maps are used within thermal models. LROC is of interest to this project because a photometric study similar to the one detailed in Part 2.2 was performed using LROC data by (Sato *et al.*, 2014). Therefore, it is described in detail below.

LROC is a system of three cameras which can take high spatial resolution black-and-white images and moderate spatial resolution multi-spectral images of the lunar surface for narrow-band wavelengths. LROC consists of two monochrome Narrow Angle Cameras (NACs) which capture 0.5 m-scale panchromatic images (over a 5 km swath), and a Wide Angle Camera (WAC) which provides images at 100 m/pixel, at seven distinct wavelength bands (over a 60 km swath) (Robinson *et al.*, 2010). In (Sato *et al.*, 2014), WAC and NAC images were used to derive a range of parameters related to the compositional and physical

properties of the lunar surface. Later, these will be compared to the equivalent parameters measured in this study.

The most relevant instrument to this project, because data from its off-nadir measurement campaign is used in Part 5.3, is instrument 2, the DLRE (a.k.a. and hence referred to as Diviner). Details of this instrument are given in the following section.

1.2.2 The Diviner Lunar Radiometer Experiment

Diviner is a nine-channel 'push broom' mapping radiometer (solar and infrared), as shown in **Figure 8**. It is the first instrument to map the daytime and night-time temperatures of ~the entire lunar surface (Paige et al., 2010; Hayne et al., 2010). When used in conjunction with thermal models, data taken by Diviner has been used to derive surface/subsurface temperature profiles, to measure rock abundances and albedo variations and to identify possible cold traps in PSRs for almost all regions of the lunar surface (Paige *et al.*, 2010).

Diviner's primary mission goals have been 1) to characterize the Moon's surface thermal environments (i.e. in daytime, night-time and polar regions); 2) to map the properties of the lunar surface (i.e. bulk thermal properties, rock abundance and composition); and 3) to characterize polar cold traps (i.e. their locations, their temperatures and their thermophysical properties), thus assessing potential lunar volatile resources (Williams *et al.*, 2017b, 2019; Woods-Robinson, Siegler and Paige, 2019). The spectral range of Diviner is 0.35-400 μm across nine channels (see **Table 3**), and thus, the instrument can measure surface and subsurface temperatures with its four broadband channels; compositional (Christiansen Feature) variations with its three narrow-band channels; and visible-λ scattering functions with its two solar channels.

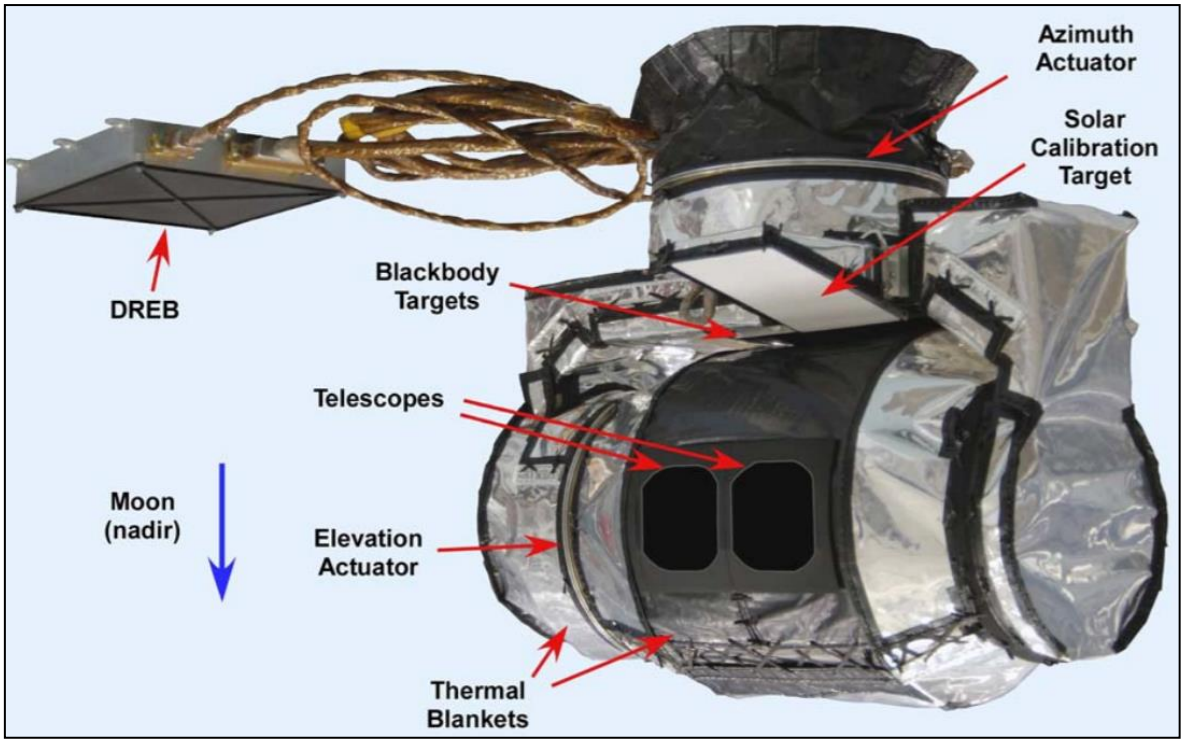

Figure 8: Diviner instrument with major parts labelled. Image from (Paige *et al.*, 2010).

Channel number	***Wavelength (μm)***	***Purpose***
1	0.35 - 2.80	High sensitivity solar
2	0.35 – 2.80	Mid sensitivity solar
3	7.55 – 8.05	Christiansen Feature
4	8.10 – 8.40	Christiansen Feature
5	8.38 – 8.68	Christiansen Feature
6	13 – 23	Thermal (most sensitive channel for >178 K)
7	25 – 41	Thermal (most sensitive channel for 69-178 K)
8	50 – 100	Thermal (most sensitive channel for 43-69 K)
9	100 - 400	Thermal (most sensitive channel for <43 K)

Table 3: Detailing the nine channels of Diviner and their purposes—from (Paige *et al.*, 2010a).

Using the thermal channels (6-9) of Diviner, various temperature maps have been created for global and specific regions of the lunar surface (Hayne *et al.*, 2017; Williams *et al.*, 2019). These provide remote sensing measurements across a wide range of locations and times of day (although, as mentioned previously, to gain a complete picture of the lunar

thermal environment over all times of day, a thermal model is required). Notably, (Williams *et al.*, 2017b) compiled data from Diviner's nadir observations (i.e. looking straight down, with emission angles < 10˚) from July 5, 2009 to April 1, 2015 (over 25,000 orbits) into bins of 0.5˚ latitude/longitude, and 0.25 hours of local time. This study produced global average temperature maps for the Moon at lunar noon and lunar midnight—as shown in **Figure 9**—in addition to producing maximum/minimum temperature maps for specific regions of interest such as Tycho Crater and Oceanus Procellarum.

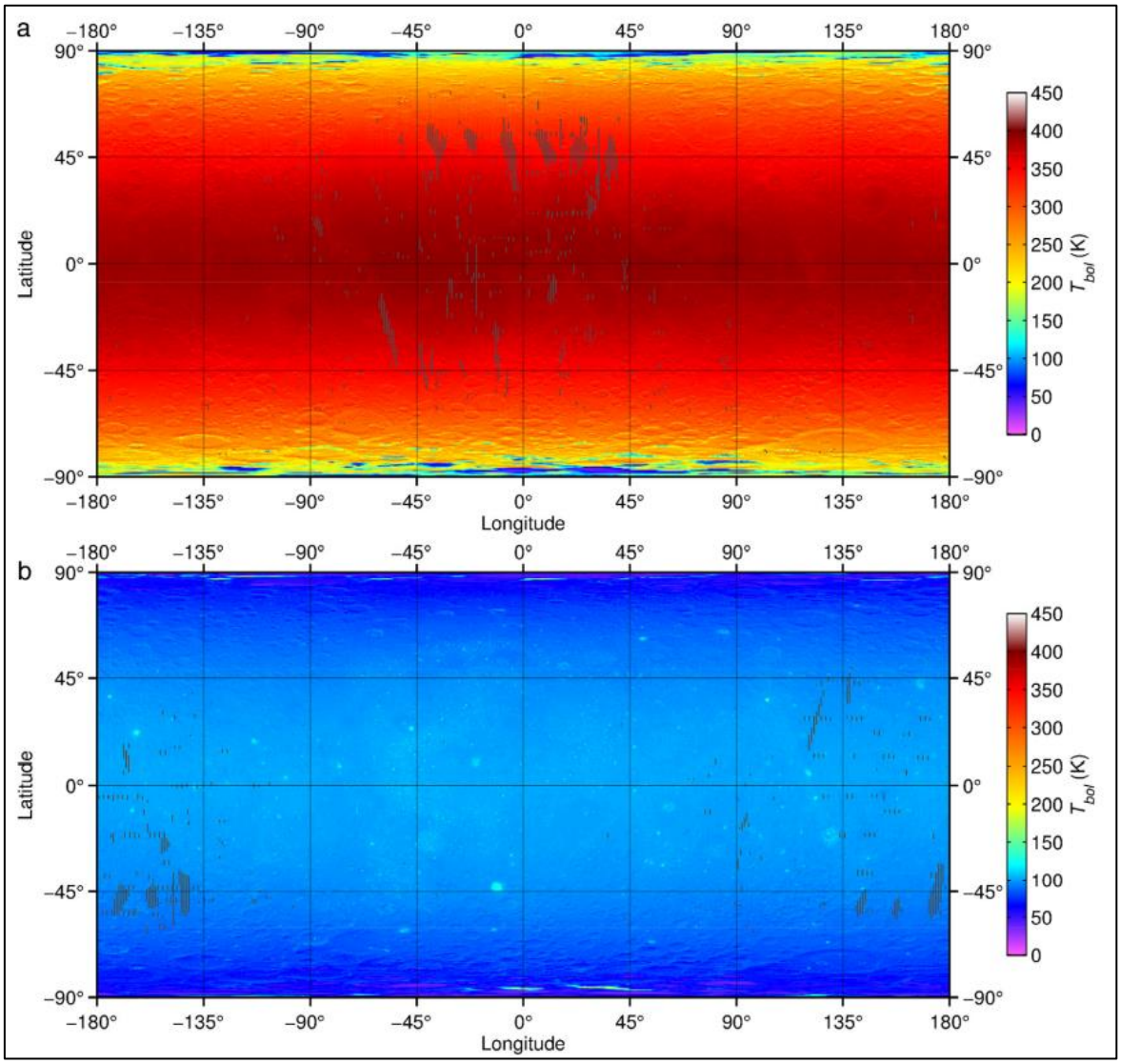

Figure 9: Mean global bolometric temperatures for one hour of local time centred on (a) noon and (b) midnight. Image from (Williams *et al.*, 2017b).

Figure 9 shows, again, that for latitudes <~60˚ N/S, lunar surface temperatures are dominantly dependent upon time of day. For high-latitude regions, temperature profiles are

dominantly influenced by topography, as well as by time of day (except for PSRs). Furthermore, although the ecliptic obliquity of the Moon is very low (~1.54°), it does still exhibit seasonal variations in temperature, and these should be considered when mapping the potential lunar PSRs in which ice volatiles could be trapped for long time periods. In the subsequent (Williams *et al.*, 2019) study, temperature maps were produced for PSR locations—in addition to semi-shaded regions, which may contain reservoirs of ice volatiles that are more accessible than those in PSRs—taking diurnal and seasonal variability into account.

For water ice and other ice volatiles to be trapped for long time periods (i.e. >millions of years), PSR temperatures must remain below the sublimation temperature of a given ice volatile throughout all diurnal and seasonal temperature variations. Temperature maps such as **Figure 5**—showing PSR regions which never exceed the sublimation temperatures of ice volatiles, including water ice—have therefore demonstrated the thermodynamic possibility of ice volatiles being trapped at the lunar poles, by measuring lunar surface temperatures over the full range of times of day and seasons.

Here it is important to consider the precision of Diviner-measured lunar surface temperatures. The radiometric accuracy of channels 3-9—and thus, the precision of measured temperatures—is dependent on both offset and gain. Offset uncertainty, which is the dominant source of uncertainty for viewing cold (<150 K) temperature targets, is due to both detector/electronics noise and to uncertainties in the interpolation of signals from space and 'blackbody looks' at 10-minute intervals. Gain uncertainty, which is dominant for hot temperatures (>250 K), is due to various reasons, such as ground radiometric calibration uncertainties, non-unity blackbody emissivity, detector noise and interpolation between points for different blackbody temperatures (Paige *et al.*, 2010a). The estimated overall

radiometric accuracy profiles for single measurements by these channels are shown in **Figure 10**.

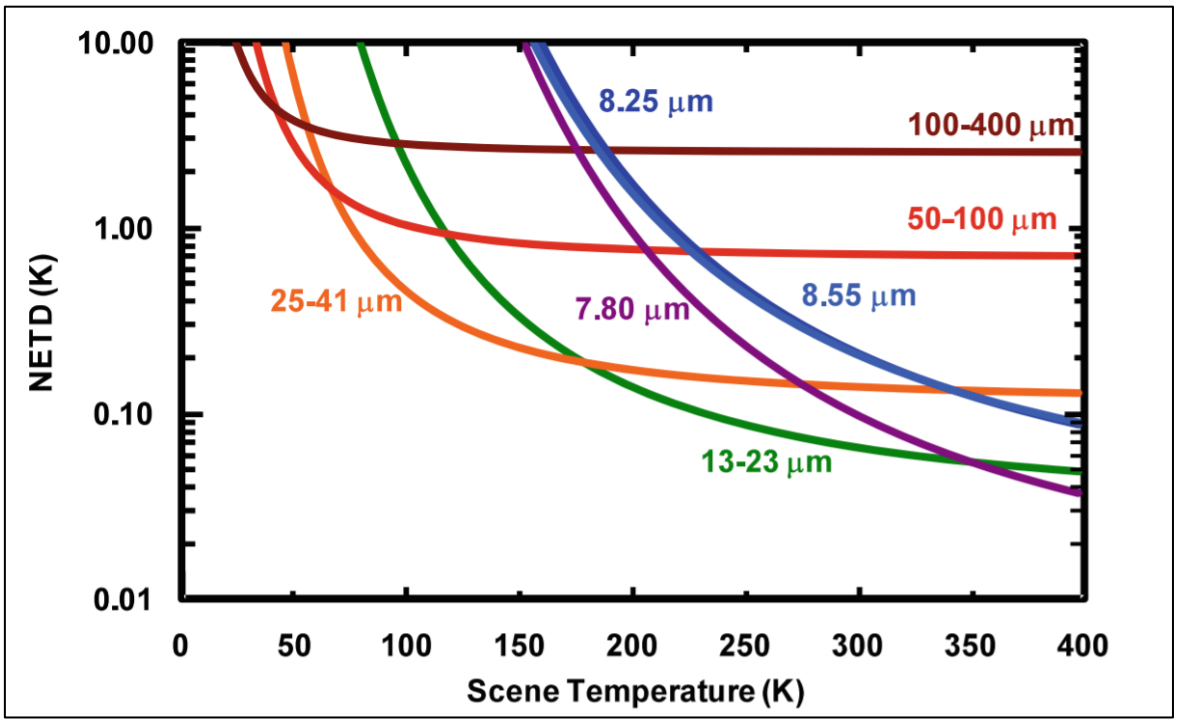

Figure 10: Noise equivalent temperature difference (NETD) radiometric accuracy profiles for each of the Christiansen Feature (3-5) and thermal channels (6-9) of the Diviner Lunar Radiometer Experiment. Image from (Paige *et al.*, 2010a).

Figure 10 shows that for temperatures >250 K the accuracy of a single measurement is <±1 K; however, for temperatures <~100 K, this accuracy varies, and for temperatures approaching 40 K (the lowest expected temperatures in some PSR cold traps), the accuracy of a single measurement is up to ±10 K. However, once many observations are made for a given location, the data can be averaged over multiple points, and so the precision of Diviner's temperature data is on the order of ~±1 K (Paige *et al.*, 2010a). This becomes important in Part 6 when comparing thermal modelling outputs to remote sensing data. One of this project's goals, G4, is to improve thermal models so that ice volatile locations in lunar PSRs can be more accurately modelled. The radiometric precision of Diviner demonstrates that thermal models should match Diviner's temperature measurements to within ~±1 K to be considered in agreement with the remote sensing results. Currently, thermal models disagree with Diviner by up to ~30 K in some lunar PSR locations, and, as

described in Part 1.3.3, this may be due to inaccurate visible scattering functions being set within them.

Attempting to reduce this temperature discrepancy is one of the major aims of this project, A4. Another major aim of this project, A3, is to compare laboratory measured visible scattering functions to those measured for the lunar surface. This can be done using emission phase function data taken during Diviner's targeted visible-λ off-nadir campaign, which is described in the following section (Bandfield et al., 2015; Greenhagen et al., 2017).

1.2.3 Diviner's Visible Off-nadir Campaign

In addition to its main measurement campaign—the goal of which has been nadir-viewing of ~the entire lunar surface for almost all local times of day—Diviner has completed various extended mission campaigns. The goal of one of these extended mission campaigns has been to take off-nadir (i.e. not only looking straight down) measurements at a wide range of viewing angles (~0-160° phase angles) for various selected regions of interest (Greenhagen *et al.*, 2017). These regions of the lunar surface—and the % hemispheric angular coverage measured for each of them by Diviner up until October 2021—are given in **Table 4**, and it is hoped that in future more regions will be imaged.

Region	***Latitude***	***Longitude***	***Hemispheric Angular Coverage***
High-latitude Mare	52.97°N	71.50°W	49%
High-latitude Highlands	49.55°N	109.55°W	39%
Equatorial Mare	1.96°S	0.60°W	15%
Equatorial Highlands	0.36°N	141.39°E	20%
Aristarchus Plateau	27.36°N	51.73°W	18%
Reiner Gamma (lunar swirl)	7.41°N	58.98°W	1%
Kepler Crater Ejecta	8.33°N	36.53°W	12%

King Crater Melt Pond	6.60°N	119.84°E	1%
Dufay Albedo Anomaly	7.65°N	170.43°E	25%
Equatorial Cold Spot	3.30°S	151.90°E	22%

Table 4: Showing the targets of the Diviner off-nadir campaign, with their coordinates and % hemispheric angular coverage up until October 2021 (Greenhagen *et al.*, 2017; Warren *et al.*, 2021).

Thermal-λ (channels 3-9) off-nadir observations can be used to characterize the radiative balance and emission phase functions of the lunar surface, in addition to providing information about thermal-scale surface roughness (Greenhagen *et al.*, 2017) (see **Figure 11** in Part 1.3). The visible-λ (channels 1-2) off-nadir observations shed light on lunar regolith scattering behavior at broadband wavelengths, and can be interpreted with a photometric model to deduce compositional and physical properties of the lunar regolith (Hapke, 1993).

In 2014, (Sato *et al.*, 2014) compared light scattering functions measured for the lunar surface by LROC's WAC to Hapke's photometric model (see Part 2) (Hapke, 2012). This study deduced Hapke parameter maps for 70°S to 70°N latitudes over seven wavelength bands—two UV bands, 321 and 360 nm, and five visible-wavelength bands, 415, 566, 604, 643 and 689 nm. This enabled compositional and regolith physical property variations to be deduced for various regions of the lunar surface.

In addition to remote sensing studies such as (Sato *et al.*, 2014), visible-λ off-nadir observations can be directly compared to light scattering functions measured in the laboratory. These light scattering functions can be measured for specific wavelength bands, using filters (or lasers) at the desired wavelengths, thus making them comparable to LROC's WAC and NAC data. Alternatively, a broadband light source equivalent to Diviner's spectral range (0.35-2.80 μm) can be used. Using a broadband light source enables Hapke parameter fits to be deduced with a similar method to the (Sato *et al.*, 2014) study, but—instead of LROC—using *Diviner*'s broadband off-nadir data for each of the various target locations

(as given in **Table 4**). To compare laboratory measured light scattering functions with Diviner's off-nadir data is one of major aims of this project, A3.

Until recently, only very limited analysis has been performed using Diviner's visible-λ off-nadir data, but projects such as this one are beginning to study this dataset with greater interest, as it provides a unique opportunity 1) to test and interpret photometric models such as the Hapke BRDF model (see Part 2), and 2) to more-accurately set visible-λ light scattering functions within thermal models (see Part 1.3.4) (Greenhagen *et al.*, 2017; Warren *et al.*, 2019). Now the relevant remote sensing instruments have been explained, the 1D and 3D thermal models relevant to this study will also be described.

1.3 Thermal Modelling for the Lunar Surface

Remote sensing measurements at Thermal Infrared (TIR) wavelengths provide useful information about lunar surface temperatures. However, to interpret such data and to extrapolate the results to all locations, depths, times of day and seasons thermal models are required, which accurately capture the physics of heat transfer on an airless body such as the Moon (Vasavada, Paige and Wood, 1999; Rozitis and Green, 2011; Hayne *et al.*, 2017; King *et al.*, 2019). Thermal models are not only used to extrapolate temperature profiles to a wider range of time points, but also to deduce physical properties (i.e., density and conductivity profiles) of the lunar regolith. This is done by inverting them and finding best fits between modelled and remotely-sensed temperatures (Hayne *et al.*, 2017; Woods-Robinson, Siegler and Paige, 2019). Furthermore, thermal models enable temperature profiles to be estimated for the lunar regolith subsurface at depths up to ~1-10 m, where diurnal and seasonal thermal signals dominate. This is particularly important because of the difficulty in determining lunar regolith sub-surface temperatures using a radiometer such as Diviner, and because subsurface regolith temperature profiles in PSRs must be accurate in order to constrain the

potential locations and abundances of water ice on/within the lunar surface/subsurface (Williams *et al.*, 2019).

Figure 11, from (Vasavada, Paige and Wood, 1999), shows an example of thermal model calculations for average lunar regolith surface/subsurface temperatures down to 0.6 m depths, over the course of a lunar day (diurnal wave).

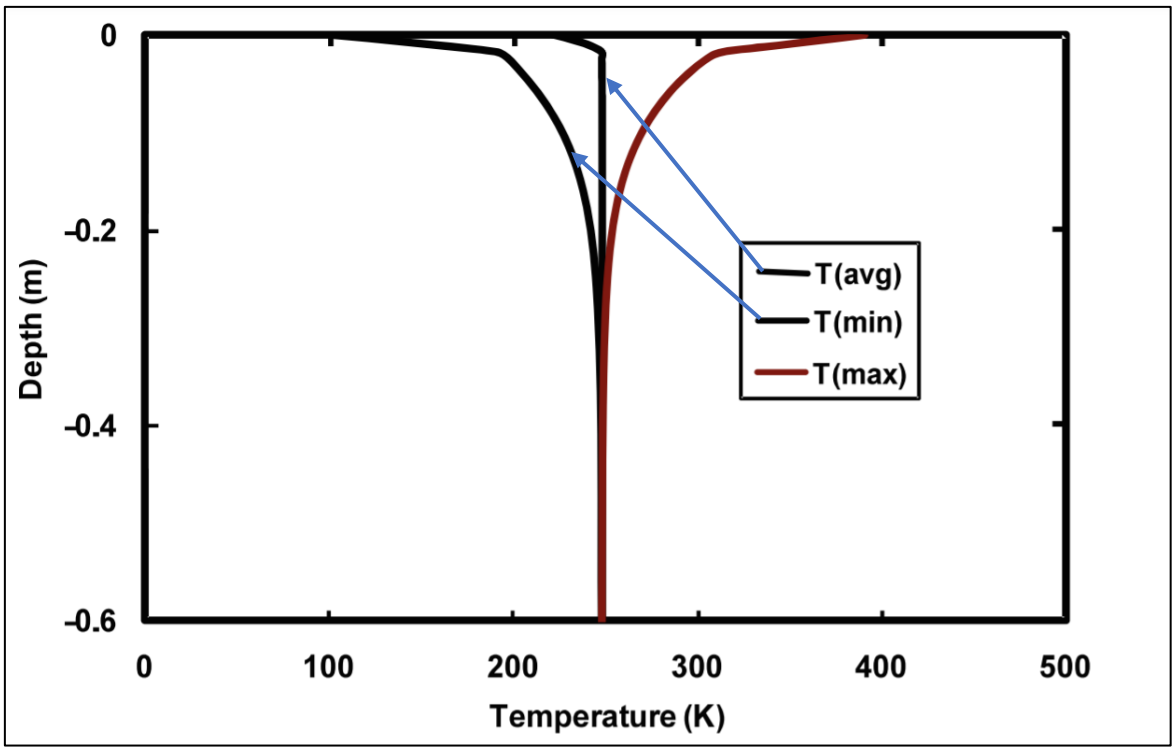

Figure 11: Model calculations of diurnal minimum, maximum and average temperatures at the lunar equator as a function of depth. Image from (Vasavada, Paige and Wood, 1999).

The term thermal model can refer to either a 1D thermal model (see Part 1.3.1), which solves the Heat Transfer Equation for a one-dimensional solid medium, or a 3D thermal model (see Part 1.3.2), which runs a 1D thermal model and incorporates ray tracing algorithms to deduce temperature profiles for 3D gridded areas. Because of their importance in lunar science, there are multiple 1D and 3D lunar thermal models. These include ((Keihm, 1984; Vasavada *et al.*, 2012; Hayne *et al.*, 2017)). Of the major lunar 1D thermal models, the Hayne model (see Part 1.3.1) is the most important for this project, as it forms the basis of the 3D model used in this study—the Oxford 3D Thermal Model (O3DTM) (see Part 1.3.2)

(Hayne *et al.*, 2017; King *et al.*, 2019). The underlying physics of the Hayne model—and how the model differs from other similar 1D thermal models—is explained in detail in Part 1.3.1.

1.3.1 The Hayne 1D Thermal Model

The Hayne 1D thermal model was developed in 2017 and is used to interpret lunar surface temperature data, specifically from Diviner (Hayne *et al.*, 2017). It is one of various 1D thermal models for the Moon, but it is used in this study as the standard in thermal modelling of the lunar surface/subsurface because 1) it is based on an extensively validated finite-difference approach; 2) it contains a sophisticated density parameterization by incorporating the H-parameter (Equation 1.2); and 3) results from the model have been validated using Diviner temperature measurements and various measurements of the Apollo samples (for density profiles, conductivity profiles etc., but *not* for visible albedo (see Part 1.3.3)) (Hayne *et al.*, 2017; Foote *et al.*, 2020).

Like the majority of 1D thermal models, it is based on the Heat Transfer Equation for a one-dimensional solid medium, given in Equation 1.1.

$$\rho c_p \frac{\partial T}{\partial t} = \frac{\partial}{\partial z}\left(K_T \frac{\partial T}{\partial z}\right) \quad [1.1]$$

Where ρ is density, c_p is specific heat capacity and K_T is the thermal conductivity of the material. The model separates the regolith subsurface into layers and runs the model for each layer, where z is the layer-depth from the surface, T is temperature and t is time (Hayne *et al.*, 2017). A standard finite-difference approximation for the derivatives of Equation 1.1 is then used, which has been validated using diurnal temperature measurements of the Moon by Diviner (Vasavada *et al.*, 2012; Kieffer, 2013; Hayne *et al.*, 2017).

The depth-dependent density used in the model is described by Equation 1.2.

$$\rho(z) = \rho_d - (\rho_d - \rho_s)e^{-\frac{z}{H}} \quad [1.2]$$

Where ρ_d and ρ_s are the depths at the boundary conditions: at depths >> H and at the surface, respectively. H is the scale height of the vertical profile, and it is this parameter which makes the Hayne model unique. As opposed to setting only two different density values for the regolith layers, such as within the (Vasavada, Paige and Wood, 1999) 'two-slab' model, the Hayne model sets a H-parameter, which describes how regolith density increases from the surface to a lowest boundary layer at ~1 m depth and thus simulates the density profiles created by the top few millimeters of the lunar regolith. Appropriate H-parameters can be deduced by running the model for gridded areas of the Moon in a Monte Carlo style until the minimum temperatures (for night-time and daytime) match the Diviner temperature data. Typical H values and how they describe the evolution of density with depth are shown in **Figure 12**. The density values for the H-parameter were set using data from the Apollo core samples and range between 1,100–1,800 kgm^{-3} (Carrier III, Olhoeft and Mendell, 1991; Hayne *et al.*, 2013).

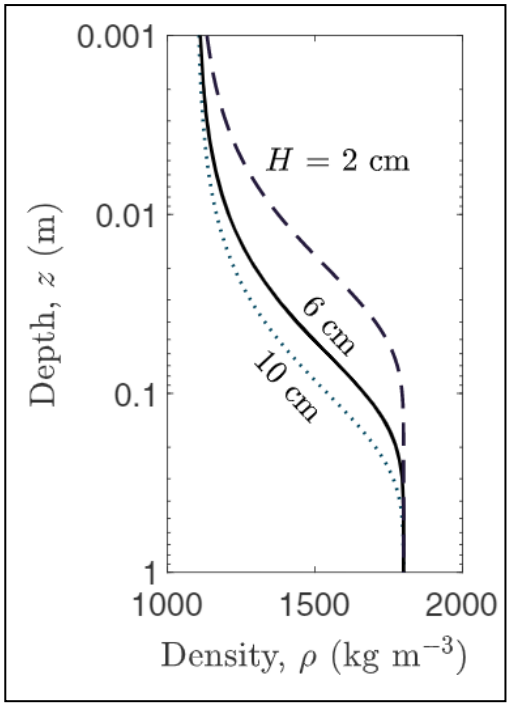

Figure 12: Showing the density parameterisation within the Hayne model—the H-parameter. Three different values of the H-parameter are indicated: 2 cm (dashed), 6 cm (solid) and 10 cm (dotted). Image from (Hayne *et al.*, 2017).

Setting an accurate density profile for the lunar regolith within a thermal model is crucial, as density affects various processes within the regolith such as visible light scattering and thermal conduction. In the Hayne model, as is standard, the thermal conductivity varies with composition, density and temperature and is described by Equation 1.3.

$$K_T(T, \rho) = K_c(\rho) + BT^3 \qquad [1.3]$$

Where K_c is the solid phonon conductivity and B, the radiative conductivity factor, is approximated by $B \sim \sigma \bar{\bar{\varepsilon}}_0 l$, where σ is the Stefan-Boltzmann constant, $\bar{\bar{\varepsilon}}_0$ is the bolometric infrared emissivity of an individual grain and l is the inter-grain spacing. $B = \frac{K_c \chi}{350^3}$ where χ is a dimensionless parameter and therefore it is possible to write the equation in the form of Equation 1.4.

$$K_T = K_c \left[1 + \chi \left(\frac{T}{350}\right)^3\right] \qquad [1.4]$$

The conductivity of the lunar surface is linearly proportional to density over the relevant temperature range and is described by Equation 1.5.

$$K_c = K_d - (K_d - K_s)\frac{\rho_d - \rho}{\rho_d - \rho_s} \quad [1.5]$$

Where K_c and K_d are the boundary contact conductivities for the surface and the lowest depth, respectively. Furthermore, the heat capacity is temperature dependent and is derived to follow a polynomial, as in Equation 1.6.

$$c_p(T) = c_0 + c_1 T + c_2 T^2 + \cdots + c_N T^N \quad [1.6]$$

With the values of c_i given in **Table 5**, alongside all other key parameter values. The polynomial fit is valid until $T < 1.3$ K, where it becomes negative. (Hayne *et al.*, 2017) concluded that additional experimental data was needed to constrain the heat capacity of lunar materials in extremely low temperature conditions, as potentially encountered in lunar polar regions, and this was investigated in (Woods-Robinson, Siegler and Paige, 2019).

Parameter	***Symbol***	***Value***
Solar constant	S	1361 Wm^{-2}
Lunar diurnal period (synodic month)	P	2.55024 x 10^6 s
Infrared emissivity	$\bar{\varepsilon}$	0.95
Bond albedo at normal solar incidence (lunar average)	A_0	0.12
Bond albedo at arbitrary solar incidence	A	$A = A_0 + a(\frac{\theta}{\pi/4})^3 + b(\frac{\theta}{\pi/4})^8$
Single scattering albedo function constant	a	0.06
Multiple scattering albedo function constant	b	0.25
Thermal conductivity	K_T	$K_c + BT^3$
Phonon conductivity	K_c	$K_d - (K_d - K_s)\frac{\rho_d - \rho}{\rho_d - \rho_s}$

Surface layer conductivity	K_s	7.4 x 10^{-4} $Wm^{-1}K^{-1}$
Deep layer conductivity	K_d	3.4 x 10^{-4} $Wm^{-1}K^{-1}$
Radiative conductivity factor	B	$K_{c\chi}/(350\ K)^3$
Radiative conductivity parameter	χ	2.7
Regolith density	ρ	$\rho_d - (\rho_d - \rho_s)e^{-z/H}$
Surface layer density	ρ_s	1,100 kgm^{-3}
Deep layer density	ρ_d	1,800 kgm^{-3}
H-parameter (scale factor)	H	0 to >0.20 m (average = 0.06 m)
Specific heat capacity	c_p	$c_0 + c_1T + c_2T^2 + c_3T^3 + c_4T^4$
Coefficients for specific heat capacity function	c_0	-3.613 $Jkg^{-1}K^{-1}$
	c_1	+2.743 $Jkg^{-1}K^{-2}$
	c_2	+2.362 x 10^{-3} $Jkg^{-1}K^{-3}$
	c_3	-1.234 x 10^{-5} $Jkg^{-1}K^{-4}$
	c_4	+8.909 x 10^{-9} $Jkg^{-1}K^{-5}$
Interior heat flow	Q	0.018 Wm^{-2}

Table 5: Table providing the parameters used in the Hayne thermal model—from (Hayne *et al.*, 2017).

Due to the dependence on temperature for the values of specific heat capacity and conductivity, it is necessary to use the finite-difference method to make an initial estimate of the temperature at the lunar surface at a particular point for the model to work. The numerical solution for the upper boundary condition is solved using Newton's root finding method which iteratively improves the estimate for the surface temperature, T_0. Equations 1.7, 1.8, 1.9, 2.0 and 2.1, define how the upper boundary condition is solved.

$$T_0{}' = T_0 + \delta T \quad [1.7]$$

$$\delta T = -\frac{f}{f'} \quad [1.8]$$

Where f is the function for which zeroes are found.

$$f \equiv \bar{\varepsilon}\sigma T^4 - K_T\frac{\partial T}{\partial z} - Q_s = 0 \quad [1.9]$$

Here, the spatial derivative can be approximated using a three-point numerical scheme, to give:

$$f \equiv \bar{\varepsilon}\sigma T^4 - Q_s - \left(K_{c,0} + B_0 {T_0}^3\right)\left[\frac{-3T_0 + 4T_1 - T_2}{2\Delta z_0}\right] \quad [1.10]$$

The first partial derivative with respect to temperature is, then:

$$f' \equiv 4\bar{\varepsilon}\sigma {T_0}^3 - 3B_0 {T_0}^2\left[\frac{4T_1 - 3T_0 - T_2}{2\Delta z_0}\right] + \frac{3}{2\Delta z_0}\left(K_{c,0} + B_0 {T_0}^3\right) \quad [1.11]$$

These two equations can be solved iteratively with Equation 1.8, until $\delta T \ll 1$ K. For the bottom boundary, N, the finite difference equation gives Equation 1.12.

$$T_N = T_{N-1} + \frac{Q}{K_{N-1}}\Delta z_{N-1} \quad [1.12]$$

The flux across each layer of the lunar regolith is then approximated by the forward difference formula, given in Equation 1.13.

$$F_i \approx K_i \frac{T_{i+1} - T_i}{\Delta z_i} \quad [1.13]$$

With $\Delta z_i = \Delta z_{i+1} - z_i$ and thermal conductivity taken to be that between layer i and $i + 1$. The flux gradient for Equation 1.1 can then be approximated as in Equation 1.14.

$$\frac{\partial}{\partial z}F_i \approx \frac{F_i - F_{i-1}}{\frac{1}{2}(\Delta z_i + \Delta z_{i-1})} \approx \frac{2}{\Delta^3 z_i}\{T_{i-1}K_{i-1}\Delta z_i - T_i(K_{i-1}\Delta z_i + K_i\Delta z_{i-1}) + T_{i+1}K_i\Delta z_{i-1}\} \quad [1.14]$$

Where $\Delta^3 z_i \equiv \Delta z_i \Delta z_{i-1}(\Delta z_i + \Delta z_{i-1})$. Equation 1.14 can then be simplified by defining $\alpha_{Hi} \equiv 2K_{i-1}\Delta z_i/\Delta^3 z_i$ and $\beta_{Hi} \equiv 2K_i\Delta z_{i-1}/\Delta^3 z_i$, thus, the temperature at each layer is updated over a time increment Δt, using Equation 1.15.

$${T_i}^{(n+1)} = {T_i}^{(n)} + \frac{\Delta t}{\left(\rho c_p\right)_i}\left\{\alpha_{Hi}{T_{i-1}}^{(n)} - (\alpha_{Hi} + \beta_{Hi}){T_i}^{(n)} + \beta_{Hi}{T_{i+1}}^{(n)}\right\} \quad [1.15]$$

Where n is the previous time step. In practice, the numerical grid remains fixed throughout each simulation, such that the factors in Equations 1.16 and 1.17, only need to be calculated once and the coefficients of Equation 1.15 are calculated at each time step. Even though density is typically constant in time, the heat capacity varies with temperature and so the prefactor $\Delta t/\rho c_p$ must be calculated at each time step.

$$p_i \equiv \frac{2\Delta z_i}{\Delta^3 z_i} \quad [1.16]$$

$$q_i \equiv \frac{2\Delta z_{i-1}}{\Delta^3 z_i} \quad [1.17]$$

For numerical stability the one-dimensional Fourier mesh must be <0.5, as given in Equation 1.18.

$$FoM = \frac{\Delta t}{\rho c_p}(\alpha_H + \beta_H) < 0.5 \quad [1.18]$$

And the maximum time step is therefore given by Equation 1.19.

$$\Delta t_{max} = \left[\frac{\rho c_p}{2(\alpha_H + \beta_H)}\right]_{min} \sim \Delta z^2 \quad [1.19]$$

Where subscript "min" refers to the minimum value among all the layers (Hayne *et al.*, 2017).

To summarize, the Hayne model uses a standard finite-difference approximation for the derivatives of the 1D Heat Transfer Equation (Equation 1.1) to estimate an initial surface temperature at a specific latitude and longitude. It outputs temperature profiles for a one-dimensional (1D) unit of the lunar surface, down to a depth, set by the user, for which the temperature is constant (sensitive to within <<1 K) (Hayne *et al.*, 2017).

1D data products produced by the Hayne model can be used to create thermal maps for the equatorial—and regions up to ~60° latitude—areas of the surface of the Moon over a

complete lunar diurnal period (Paige et al., 2010; Hayne et al., 2017). However, as is also the case for current 3DTMs, for higher-latitude areas (>60°), the model is inaccurate by up to ~15-30 K (dependent on location) when compared to Diviner data. This discrepancy is potentially due to it not including realistic light scattering functions for the lunar surface (see Part 1.3.3) (King *et al.*, 2019.

1.3.2 The Oxford 3D Thermal Model

Lunar 3DTMs run 1D surface/subsurface temperature calculations for gridded regions of the lunar surface, then apply ray tracing algorithms to calculate how each gridded region reradiates and scatters heat and light onto its neighboring surfaces (King *et al.*, 2019). When used in tandem with remotely sensed topography data from instruments such as LOLA (see Part 1.2.2), 3DTMs enable temperature profiles to be mapped for whole regions of the lunar surface (i.e. PSR craters).

Various 3DTMs exist for the lunar surface, and each aims to improve upon the agreement between modelled temperature profiles and remotely sensed temperature measurements. The **Paige 3D Thermal Model (2010)** is a three-dimensional model, in that it simulates temperature profiles for regions of the lunar surface and accounts for terrain blocking and scattering/reradiation between the model's gridded surface elements. However, it uses a 'two-slab' model similar to the one developed in (Mitchell and De Pater, 1994) and therefore it sets two discrete density layers within the regolith subsurface (using Apollo 12 core bulk density measurements): one of lower density, at the surface, and another of higher density, at depth (Paige et al., 2010). The **Vasavada 1D thermal model (1999, 2012)** built upon the underlying 'two-slab' density parameterization by also introducing a 'two-slab' conductivity profile. This improves the agreement between modelled temperature profiles and Diviner thermal data, in particular for sunrise and sunset times, when temperature profiles evolve rapidly. However, temperature discrepancies of up to ~15-30 K (dependent on location) still

exist (between the model and Diviner) in PSRs and other high-latitude regions (Vasavada *et al.*, 2012).

The **1D Hayne model (2017; see Part 1.3.1)** improves thermal models further still by incorporating the H-parameter density relation. This is an important step, as density parameterization affects various terms within the model such as conductivity and heat capacity. This model is particularly advantageous when modelling how fast the lunar surface cools at night and hence when calculating minimum surface temperatures (i.e. ice volatile stability) (Hayne *et al.*, 2017).

The **Oxford 3D Thermal Model (2019)** uses the 1D Hayne model as its basis, then splits each area of the modelled surface into gridded regions, as shown in **Figure 13**.

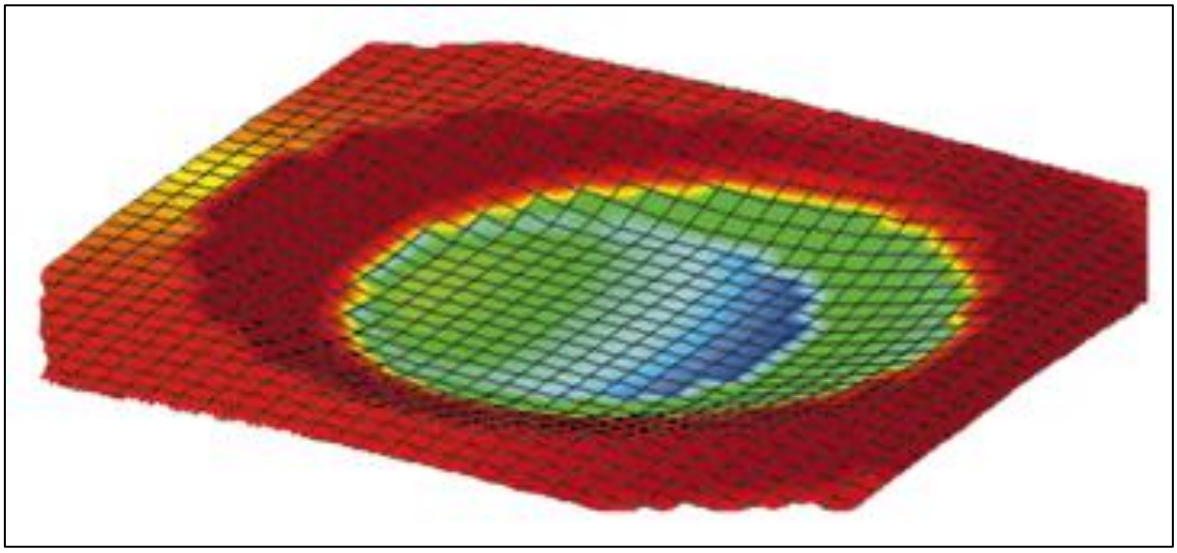

Figure 13: A lunar crater model, gridded so that 1-Dimensional thermal modelling can be done for each of the grids. Contributions for how light scatters from each of the gridded areas can then be incorporated into 3-Dimensional thermal modeling of the surface using ray tracing. Image from (Vasavada, Paige and Wood, 1999).

It then performs ray tracing and incorporates shadowing, scattering and reradiation between the gridded elements. Within (King *et al.*, 2019), the O3DTM was used to investigate water ice stability at the eight potential landing sites for a mission called the **P**ackage for **R**esource **O**bservation and in-**S**itu **P**rospecting for **E**xploration, **C**ommercial exploitation and **T**ransportation (PROSPECT), at ±5° longitude/±10° latitude for each site (Trautner *et al.*,

2018). The PROSPECT package—which hopes to launch onboard the Roscosmos 'Luna Resource', Luna-27 mission in the late-2020s—consists of a drill (ProSEED) that will collect samples from the regolith at up to ~1 m depths and transfer them to an in-situ miniaturized chemical laboratory (ProSPA). Once there, samples will be heated to 1000°C in the presence of different reagent gases to extract a range of different volatile species, including water. In addition to modelling the PROSPECT landing sites, the (King *et al.*, 2019) study 1) confirmed the result from (Paige et al., 2010; Siegler and Paige, 2019), that the minimum depth for which water ice could be stable in the lunar regolith subsurface is ~0.5 m and thus shallower than was once expected (Arnold, 1979); and 2) reduced the temperature discrepancies for some regions between modelled and Diviner temperature profiles from ~10 K to ~2 K. For high-latitude craters there are, however, still significant discrepancies (up to ~10 K) between modelled and remotely sensed temperature profiles.

It is clear that the accuracy and sophistication of 3DTMs has evolved considerably over the past decade. However, there are still improvements to be made concerning the underlying physics within the models. To consider where physical inaccuracies may still exist within the O3DTM, its simulation method and 3D radiative transfer regime will be explored.

1.3.2.1 The O3DTM Simulation Method

Firstly, the O3DTM loads regional topographies of the lunar surface as measured by LOLA (see Part 1.2.2)—similarly to the Paige and Vasavada 3D models—and splits them into gridded zones (see **Figure 13**).

For each gridded region, the O3DTM uses the 1D Hayne model to calculate surface and subsurface temperature profiles down to depth. Each individual grid typically represents a region hundreds of meters across due to LRO's 128 ppd topographical resolution (Paige *et al.*, 2010) (but this can be updated as higher spatial resolution datasets become available).

This is much larger than the temperature scale lengths within lunar regolith (<1 m), so horizontal subsurface heat transfer is neglected.

Once the surface temperature has initialized (which happens within the 1D model), the 1D model is run for ~5 simulation years. This allows temperatures to stabilize over several diurnal and seasonal cycles. Once stabilized, the model is run for a ~5-year period using Diviner data as a top-layer boundary condition, and this produces the surface temperature result.

Subsurface temperature initialization cannot be performed in the same way as for the surface, because this would involve running the model for ~50 lunar years. Therefore, the model is run for a shallow depth, and then model layers are added progressively to increase the simulation depth. This provides an accurate 'first guess' for the subsurface temperatures and leads to faster initialization. Once the temperatures of the top layers—down to depths of 2 diurnal thermal skin depths (~20 cm)—are initialized, the model is run for 1 year to allow the top-layer temperatures to stabilize over a seasonal cycle. Next, the model is run for 3 years, and deeper layers are progressively added at equal intervals, with a new layer added every three months. Next, the model is run for 5 years, which allows the temperature profiles at all layers to stabilize over multiple seasonal cycles. Finally, the model is run for a 5-year period and is overlapped onto the Diviner data to produce results. This method leads to subsurface temperature stabilization after ~9 years, as opposed to ~50 years. Within the (King *et al.*, 2019) study this streamlined method was shown to produce the same final output profiles—within uncertainty—for regions between ~50-350 K (i.e. for almost all regions of interest on the lunar surface).

Once surface and subsurface temperatures for each individual grid have been calculated, the model performs 3D radiative transfer between the gridded regions.

1.3.2.2 The O3DTM 3D Radiative Transfer Regime

The surface temperature for each element—i.e. the top-layer boundary condition—is set using Equation 1.20.

$$\bar{\varepsilon}\sigma T^4 = K_T \frac{dT}{dz}\Big|_{z=0} + Q_{abs} \quad [1.20]$$

With thermal emission from the surface ($\bar{\varepsilon}\sigma T^4$) balanced against heat flux from subsurface layers ($K_T \frac{dT}{dz}\Big|_{z=0}$) and absorbed flux incident on the surface (Q_{abs}). This absorbed flux includes 1) direct visible solar radiation, 2) visible radiation scattered onto the surface by the surrounding regions (single and multiple scattering) and 3) infrared radiation reemitted onto the surface by the surrounding regions.

Scattering is then performed as in Equation 1.21.

$$Q_j{}^{abs} = Q_{\odot j} + \sum_i \left(C_{ij}{}^{IR} Q_i{}^{IR} + C_{ij}{}^{vis} Q_i{}^{vis} \right) \quad [1.21]$$

For scattering matrices with flux coefficients $C_{ij}{}^{vis}$ and $C_{ij}{}^{IR}$. Elements of $C_{ij}{}^{vis}/C_{ij}{}^{IR}$ are the fractions of direct solar radiation/thermal radiation scattered/reemitted from surface element i onto surface element j. $Q_{\odot j}$ is the solar flux directly absorbed by surface element j. $Q_i{}^{IR} = \bar{\varepsilon}\sigma T^4$, as it represents the grey body thermal emission from surface element i and $Q_i{}^{vis}$ is the solar radiation directly scattered by surface element i.

The solar flux directly absorbed by a surface element is calculated using Equation 1.22.

$$Q_{\odot\, j} = F_{\odot}\big(1 - A(\theta)\big)\cos\theta \quad [1.22]$$

Where θ is the angle to the surface normal and $F_{\odot}$ is the solar flux (i.e. 1361 Wm^{-2}) when the sun is visible. Within the model, the albedo of the surface $A(\theta)$ depends purely on solar incidence angle and is parameterized using Equation 1.23.

$$A(\theta) = A_0 + a(\frac{\theta}{\frac{\pi}{4}})^3 + b(\frac{\theta}{\frac{\pi}{2}})^8 \quad [1.23]$$

Where A_0 is the albedo at normal solar incidence, derived from LOLA, θ is solar incidence angle (dependent on latitude and surface topography) and 'a' and 'b' are the single and multiple scattering function inputs, respectively—typically assumed to be a=0.06 and b=0.25 in the Hayne model (Hayne *et al.*, 2017)—but for the O3DTM, a and b can be set as in (Keihm, 1984), or by using laboratory measurements of Apollo samples, e.g., from (Foote *et al.*, 2020; Curtis, Warren and Bowles, 2021). C_{ij} coefficients are calculated by performing ray tracing between the centres of each pair of surface elements and incorporate the incidence angle dependence of visible scattering on albedo (as in Equation 1.23). The model can account for up to an infinite number of multiple scattering bounces (until the intensity becomes negligible), but it does not include any azimuthal variation within its albedo dependence. This is to reduce computation time and means the C_{ij} coefficients remain constant with time.

The (King *et al.*, 2019) study notes that, in reality, the intensity of scattered visible radiation *is* dependent upon azimuthal angle and therefore albedo variations would be more accurately modelled using Bidirectional Reflectance Distribution Functions (BRDFs) for the lunar regolith surface ((Foote *et al.*, 2010; King *et al.*, 2019). The study goes on to state that the inclusion of BRDFs within the model would improve its accuracy in modelling non-flat regions by more accurately simulating visible light scattering. The reason BRDFs were not included within the model for the (King *et al.*, 2019) study is that this would require ${C_{ij}}^{vis}$ to be calculated for each time step (due to the variations in sun position), and this would significantly increase the computational time.

Therefore, improving the physicality of the visible scattering parameterization within the O3DTM by including accurate BRDFs for the lunar regolith is one of the primary goals of this project, G4. This may lead to further improvements in lunar surface thermal modelling, and may reduce the temperature discrepancies between thermal models and Diviner for PSRs. The importance of including more accurate visible light scattering functions within thermal models such as the O3DTM is explored in Part 1.3.3.

1.3.3 Importance of Accurate Visible Light Scattering Functions within Thermal Models

The albedo parameterization used within previous thermal models (Equation 1.23), and how this may inaccurately represent light scattering from the lunar regolith, will now be explored.

Within Equation 1.23, the Bond albedo, A_0—which varies with lunar location (i.e. highlands ~0.13, mare ~0.08 and average for the Moon ~0.12)—is set using albedo data measured by LOLA (McEwen, 1996). The LOLA data is taken at zero phase angle, and so it eliminates topographical shadowing effects. However, it is measured at a narrow 1064 nm wavelength band which may lead to inaccuracies, as 1064 nm is not within the visible light regime and, furthermore, it is not representative of a broadband response (Chin *et al.*, 2007). Therefore, the albedo data is scaled to match broadband solar albedo measurements taken by Diviner's solar bolometric channel (Hayne *et al.*, 2017). Additionally, the 'a' and 'b' scattering terms, which define the shape of the curve, represent single ('a') and multiple scattering ('b') and are currently approximated by fitting thermal models to Diviner data, so that there is no variation in H-parameter with latitude (Paige et al., 2010). This is, in itself, potentially inaccurate as there are known physical processes which may potentially introduce latitudinal dependence on regolith porosity (Metzger, Anderson and Colaprete, 2018). But, importantly, the reason behind 1) setting A_0 using the unideal LOLA data, and 2) setting 'a' and 'b' using unideal Diviner data is due to a current lack of laboratory measured visible

scattering function data for the lunar regolith (Foote *et al.*, 2020). The only study which, prior to this project, has measured a suite of BRDFs for Apollo lunar regolith samples is the one detailed in (Foote *et al.*, 2010; Foote *et al.*, 2020), which is described in detail in Part 3.2. This study measured lunar regolith albedos across a range of viewing angles, and the extent to which these initial laboratory measurements disagree with the albedo parameterizations used in previous thermal models is demonstrated in **Figure 14**.

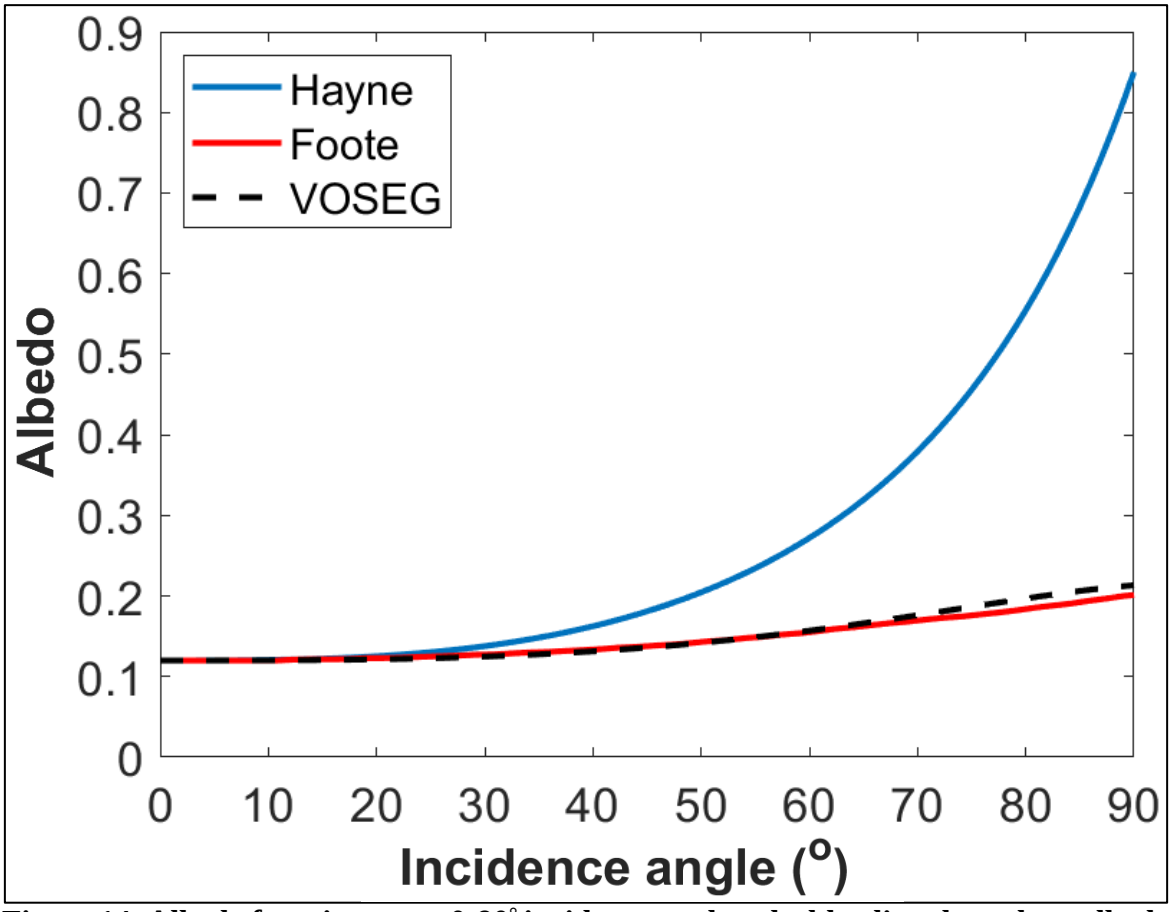

Figure 14: Albedo functions over 0-90° incidence angles: the blue line shows how albedo varies with incidence angle in the 1D Hayne model (which is set so that there is no variation in H-parameter with latitude). The red line shows (Foote *et al.*, 2020) measurements of Apollo regolith samples and the dashed black line shows measurements made during this project for Apollo 11 (10084) regolith (extrapolated beyond 70° using best fit polynomials). The input parameters used for the 1D Hayne model plot (blue line) were as follows: *a*=0.06 ; *b*=0.25; H-parameter=0.06; Bond albedo=0.12; Surface density=1100 kg/m^{-3}; Surface heat capacity=0.005 J/kgK (i.e. the standard inputs from (Hayne *et al.*, 2017)).

From **Figure 14**, it is clear the albedo function used within thermal models consistently and increasingly overestimates lunar regolith albedos for incidence angles >20°. It is useful to

consider how such variations in albedo relate to temperature outputs for 3D thermal modelling. **Figure 15** shows the difference in O3DTM modelled temperatures profiles for a hypothetical high-latitude (85°) lunar crater, when varying the albedo function between the one used in previous thermal models (Equation 1.23) and the one measured in the (Foote *et al.*, 2020) study.

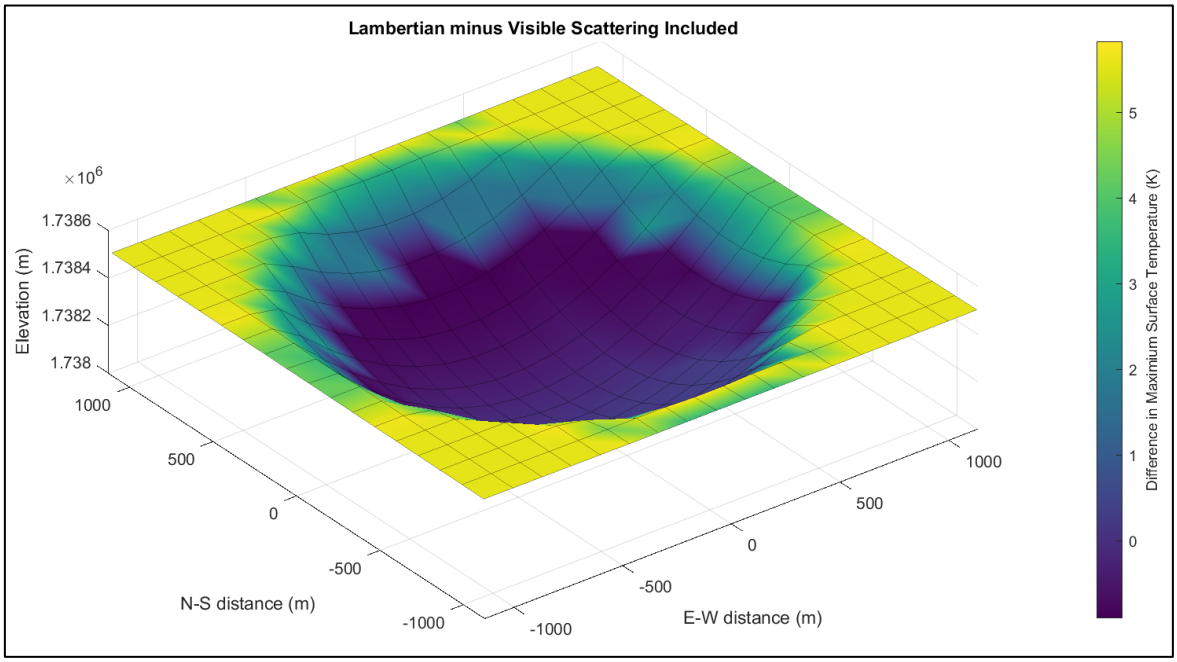

Figure 15: Modelled temperature differences between a Lambertian and a realistic visible scattering function model, for a hypothetical 500 m diameter crater at 85^{0}N latitude. No azimuthal variation, cos$^{-0.4}$ emission angle, *a*=0.0162, *b*=-0.03625 incidence angle. Image credit: Dr. Tristram Warren (private communication). Note: For all thermal modelling work presented in this thesis, the model run was designed by the author, and the model itself was written by the authors of (King *et al.*, 2019).

Figure 15 shows that modelled lunar surface temperatures can vary by up to ±5 K around PSR craters when including a laboratory measured scattering function, as opposed to the one set within previous thermal models. This result only accounts for albedo dependence on incidence angle and does not incorporate any azimuthal or reflectance angle variations. Therefore, by incorporating laboratory measured scattering functions within thermal models for a wide range of incidence, reflectance and azimuthal angles it may be possible to reduce the temperature discrepancies between thermal models and Diviner for high-latitude PSR craters. To measure a comprehensive suite of BRDFs which 1) describe how the lunar

surface scatters light over a wide range of viewing angles, and 2) can be used as accurate inputs within thermal models, is one of the aims of this project, A2. Hence, to deduce the requirements of this BRDF study, and to enable the interpretation and extrapolation of the measured dataset, a photometric model such as the Hapke BRDF model is required, which simulates how the lunar regolith scatters light over all viewing angles.

2. The Hapke Photometric Model

2.1 Introduction to the Hapke BRDF Model

The BRDF—which is related to Lambert Albedo, A_L by Equation 2.1—describes how visible and near-infrared light is scattered from a surface over all viewing angles (incidence, reflectance and azimuth/azimuthal) as defined in **Figure 16** (Hapke, 2011). The natural unit of the BRDF is Sr^{-1}, but standardly, it is described without it.

$$A_L(\theta_r, \theta_i, \theta_a) = \frac{\pi BRDF(\theta_r, \theta_i, \theta_a)}{\cos(\theta_i)} \quad [2.1]$$

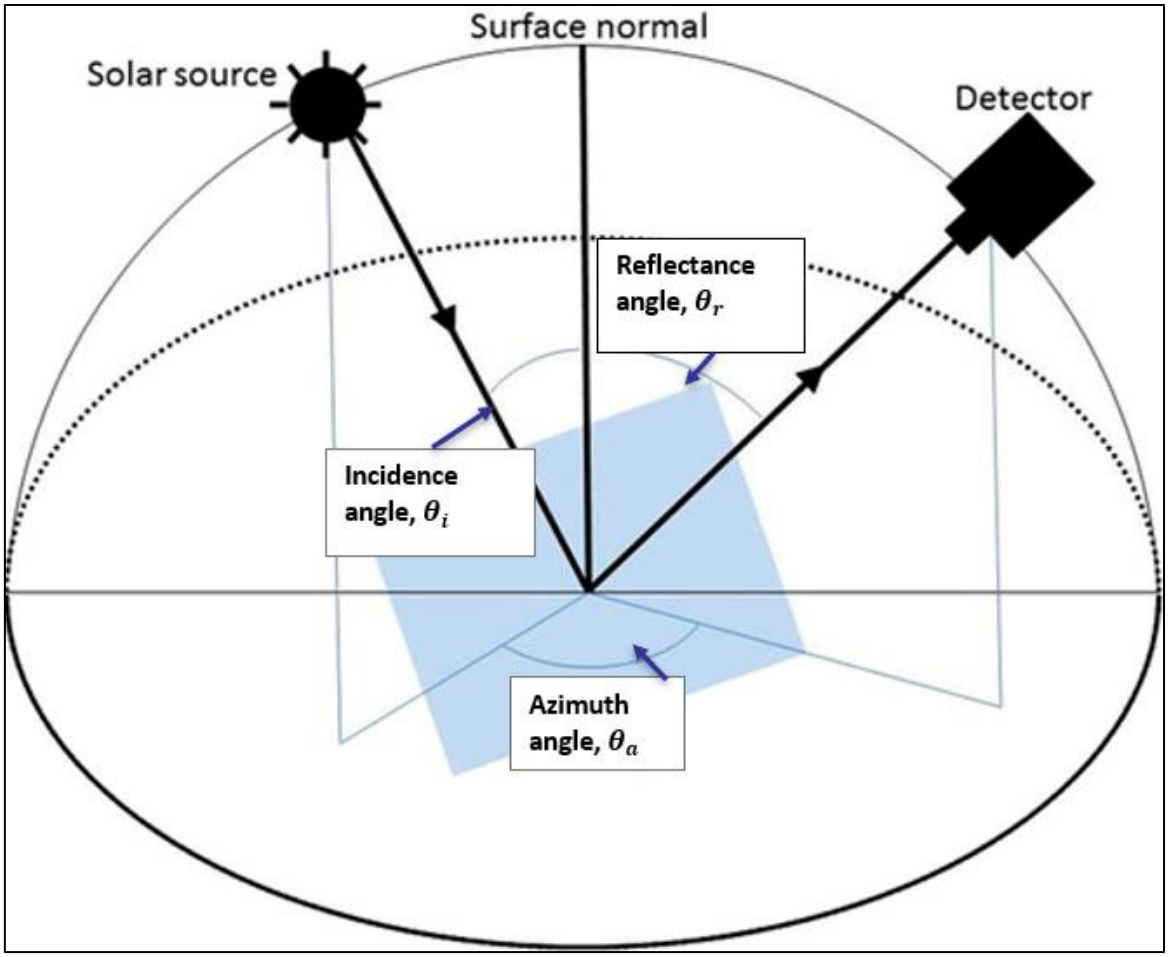

Figure 16: Definition of the angles (incidence, reflectance and azimuth/azimuthal) used in the Hapke BRDF model, remote sensing, and goniometry—from (Warren, 2015). The phase angle is the angle between the incidence and reflectance angles.

For a particulate surface such as the lunar regolith the BRDF varies with physical properties and compositional variations. Therefore, to interpret BRDFs measured for the lunar

surface—e.g. by Diviner—an accurate photometric model is required (Hapke, 2011). The most basic BRDF models such as (Nicodemus, 1976) are limited as they don't include free parameters which depend on the physical properties of the surface. The Hapke BRDF model, however, is the most commonly used BRDF model in planetary photometry (for particle sizes>'a few times' the wavelength of the incident light), as it is based upon radiative transfer equations and it defines nine free parameters which are related to surface properties, such as porosity and surface roughness (Nicodemus, 1976; Hapke, 2011). By including these nine free parameters, the model can be used to interpret remote sensing and goniometry data in terms of physical and compositional surface properties and to define experimental requirements for laboratory photometry studies of planetary regolith and regolith simulant samples. The Hapke BRDF model assumes the particle size of the medium is larger than the wavelength of the incoming and scattered radiation (Hapke, 2011). For lunar regolith, which typically has grain sizes of 10-100 μm, it is valid only in the visible and near-infrared regimes (Morris, 1983).

In light of various goniometry and remote sensing studies of planetary regolith and regolith simulant samples, many improvements have been made to the Hapke BRDF model since its conception in 1981 (Hapke, 1981, 1984, 1986, 1993, 2011). These improvements have included considerations for 1) empirical phase functions, such as the incorporation of the Henyey-Greenstein function which approximates Mie scattering (see Equation 2.8, below); 2) the volume average single scattering albedo, w, which is the ratio of scattering efficiency to total extinction efficiency and which depends on particle size and internal transmission (i.e. composition); 3) surface roughness, which can be parameterized using the slope angle of the surface, $\bar{\theta}$; and 4) the opposition effect, which is the non-linear surge in signal observed in the reflected brightness of a particulate medium around zero phase angle (~0-10°) (i.e. the brightening of a rough surface when the object is illuminated from directly

behind the observer). The term ‘opposition effect’ refers to an amalgamation of the Shadow-hiding Opposition Effect (SHOE) and the Coherent Backscattering Effect (CBOE) (Hapke, Nelson and Smythe, 1998). This effect was first observed in the autobiography of Benvenuto Cellini in the sixteenth century (Hendrix and Carman, 2010) and is evident in images taken during the Apollo 11 mission, with bright haloes appearing around the shadows cast by the astronauts’ heads (see **Figure 17**). It has also been observed in goniometry measurements of the Apollo regolith samples returned to Earth (Shepard and Helfenstein, 2007; Hapke, 2011; Foote *et al.*, 2020; Curtis, Warren and Bowles, 2021).

Figure 17: Demonstrating the opposition effect, as at close to zero phase angle a bright halo is observed around the shadow of an astronaut’s head. Image AS-11-40-5882 from the NASA Archives.

Here the mathematics of the Hapke BRDF model will be introduced. The model defines the reflectance, $r(\theta_r, \theta_i, \theta_a)$—given in Equation 2.2—as the ratio of scattered radiance at the detector to the collimated incident irradiance illuminating the surface (Hapke, 2011).

$$r(\theta_r, \theta_i, \theta_a) = \frac{E_r(\theta_r, \theta_a)}{L_i(\theta_i, \theta_a)} \quad [2.2]$$

Where θ_r, θ_i and θ_a are reflectance (a.k.a. emission, for TIR), incidence and azimuthal angles respectively (**Figure 16**). L_i is the irradiance incident on the surface at incidence angle θ_i and E_r is the radiance reflected from the surface at reflectance angle θ_r.

Hence, $E_r(\theta_r, \theta_a)$ and $L_i(\theta_i, \theta_a)$ can be expanded using their relations to the physical and compositional properties of the particulate surface. The (Hapke, 1981) equation for reflectance is given by Equation 2.3, which includes the CBOE and SHOE terms but does not yet include surface roughness (Hapke, 2011).

$$r(\theta_r, \theta_i, \theta_a) = K\frac{w}{4\pi}\frac{\mu_0}{\mu_0+1}p(\theta_p)\left\{\left[1 + B_{S0}B_S(\theta_p)\right] + \left[H\left(\frac{\mu_0}{K}\right)H\left(\frac{\mu_r}{K}\right) - 1\right]\right\}\left[1 + B_{C0}B_C(\theta_p)\right] \quad [2.3]$$

Where K is porosity coefficient, w is volume average single scattering albedo, $\frac{\mu_r}{\mu_0} = \cos(\theta_r) / \cos(\theta_i)$ and $p(\theta_p)$ is the volume average single-particle phase function, which describes the forward- and backscattering nature of the surface and depends on phase angle, θ_p and b and c, the forward- and backscattering coefficients, respectively. B_S and B_C are the SHOE and CBOE terms, respectively. B_{S0} is the amplitude of the SHOE effect, B_{C0} is the amplitude of the CBOE effect and $H(x)$ is the Ambartsumian-Chandrasekhar function, as described by Equation 2.4 (Hapke, 2011).

$$H(x) = \frac{1 + 2x}{1 + 2\gamma x} \quad [2.4]$$

Where x is the input of the Equation, either μ_0/K or μ/K. The albedo factor $\gamma = \sqrt{1 - w}$, can also be defined, for utility.

w—which quantifies the efficiency of an average regolith grain in scattering and absorbing light at a specific wavelength—is given by Equation 2.5.

$$w = \frac{\sigma_{sca}}{\sigma_{sca} + \sigma_{abs}} \quad [2.5]$$

Where σ_{sca} and σ_{abs} are the scattering and absorption coefficients, respectively. The possible range of w values is $0 \leq w \leq 1$, but typically for the lunar regolith, $0.2 \leq w \leq 0.6$ (Hapke, 2011).

K—which is a measure of how compaction or "porosity" affects transmission within a medium—is defined in its basic form by Equation 2.6.

$$K = \frac{-\ln(1 - EL)}{EL} \quad [2.6]$$

Where E (not to be confused with E_r) is the volume extinction coefficient of a particulate medium and L (not to be confused with L_i) is the length of the sample. For utility, K is related to the filling factor, φ (or ϕ), which varies between 0 and 1 (with 1 indicating a fully compacted sample), by Equation 2.7.

$$K = \frac{-\ln\left(1 - \left(1.209\phi^{\frac{2}{3}}\right)\right)}{\left(1.209\phi^{\frac{2}{3}}\right)} \quad [2.7]$$

Thus, if the range of the filling factors for lunar regolith from the Apollo cores is between $0.2 \leq \varphi \leq 0.6$, by Equation 2.7 the range of K for lunar regolith is $1.0583 \leq K \leq 1.4688$.

$p(\theta_p)$ is the volume average single-particle phase function which relates to the forward- and backscattering terms b and c and is modelled as a Henyey-Greenstein (HG) function of one, two or three terms. It can also be modelled as a Legendre polynomial, but the HG function is used here as it describes complex scattering derived from Mie theory with equal accuracy to the Legendre polynomial, but with fewer parameters. The three-term HG function is defined in Equation 2.8 (Hapke, 2011).

$$p(\theta_p) = (1-f)\frac{1-{g_1}^2}{\left(1-2g_1\cos(\theta_p)+{g_1}^2\right)^{1.5}} + f\frac{1-{g_2}^2}{\left(1+2g_2\cos(\theta_p)+{g_2}^2\right)^{1.5}} \quad [2.8]$$

Where $f = \frac{(1-c)}{2}$, $g_1 = b$ and $g_2 = -g_1$. g_1 and g_2 constrain the width of the forward- and backscattering lobes of a particle respectively and f is the relative partition coefficient, which can be $0.5 < f < 1$ for a dominantly backscattering particle and $0 < f < 0.5$ for a dominantly forward- scattering particle (Hapke, 2011). Additionally, *b* and *c* are related via a hockey-stick function, as given in Equation 2.9 and described in Part 2.2 (Sato *et al.*, 2014).

$$c = 3.29e^{-17.4b^2} - 0.908 \quad [2.9]$$

For a given particle, negative values of *c* indicate more forward-scattering ($-1 > c > 0$); positive values indicate more backscattering ($2.382 > c > 0$); and $c = 0$ indicates isotropic scattering. **Figure 18** shows how f varies with phase angle (for various *b* and *c* values).

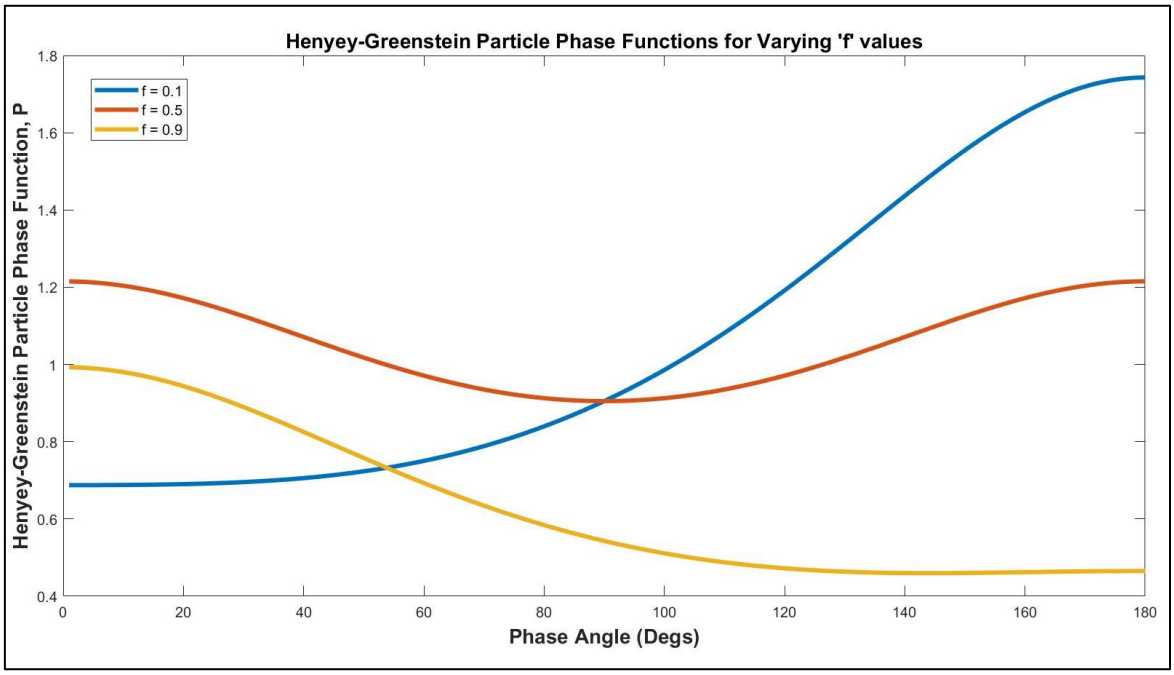

Figure 18: This shows the Henyey-Greenstein particle phase function for several values of the partition coefficient, *f*. For *f*=0.5 (i.e. *b*=0.2720 and *c*=0) (Red), the backward and forward-scattering lobes are equal. But for a value of *f*=0.9 (i.e. *b*=0.4431 and *c*=-0.8) there is more forward-scattering and for 0.1 (i.e. *b*=0.1941 and *c*=0.8) there is more backscattering.

The SHOE term, $B_S(\theta_p)$ is fully described in (Hapke, 2011), but can be accurately approximated using Equation 2.10.

$$B_S(\theta_p) \approx \left(1 + \frac{1}{h_s}\tan\left(\frac{\theta_p}{2}\right)\right)^{-1} \quad [2.10]$$

Where h_S is the SHOE width and is given by Equation 2.11.

$$h_S = \frac{KEa_E}{2} \quad [2.11]$$

a_E is the mean extinction radius and K and E are as given above. The magnitude of the SHOE, B_{S0} varies between 0 and 1 and can be approximated by its relation to w, as given in Equation 2.12.

$$B_{S0} \approx \frac{S(0)}{wp(0)} \quad [2.12]$$

Where $S(0)$ is the fraction of incident light scattered at (or close to) the illuminated particle's surface, and $wp(0)$ is the total amount of light scattered by the particle at zero phase. $S(0)$ is the specular component of the particle scattering function, which relates to the refractive indices n_r (real) and n_i (complex) by Equation 2.13.

$$S(0) = \frac{(n_r - 1)^2 + {n_i}^2}{(n_r + 1)^2 + {n_i}^2} \quad [2.13]$$

The CBOE term, $B_C(\theta_p)$ is fully described in (Hapke, 2011) and is accurately approximated using Equation 2.14.

$$B_C(\theta_p) \approx \left\{1 + [1.3 + K]\left[\left(\frac{1}{h_C}\tan\left(\frac{\theta_p}{2}\right)\right) + \left(\frac{1}{h_C}\tan\left(\frac{\theta_p}{2}\right)\right)^2\right]\right\}^{-1} \quad [2.14]$$

Where h_C is the width of the CBOE and is given by Equation 2.15.

$$h_C = \frac{\lambda}{4\pi\Lambda_T} \quad [2.15]$$

Where λ is the wavelength of the incident light and Λ_T is the transport mean free path (~1 μm for lunar regolith) (Hapke, 1981).

Conceptually, the SHOE contribution to the opposition effect is thought to be due to shadows within the medium being hidden when particles near the surface cast shadows over deeper grains. This occurs for samples with particles which are large compared to the wavelength of the light. These shadows contribute to the signal for phase angles >10° but at <10° they are hidden, so the signal increases (Hapke, 2011). The CBOE was included as another contributor to the opposition effect in 1998, to describe the intensity of the peak of the opposition effect for the Moon (Hapke, Nelson and Smythe, 1998). The CBOE describes the constructive interference of photons travelling in opposite directions, along multiply scattered paths. This effect peaks at phase angle, $\theta_p = 0$. CBOE dominates the signal at phase angles <5° and SHOE at phase angles >5°.

The surface roughness of a sample is another property which affects BRDF. This is due to various phenomena attributed to surface roughness such as shadowing, polarization effects and the ratio of multiple scatterers to single scatterers. Thus, Hapke incorporates surface roughness models such as (Helfenstein, 1988) into the BRDF model by multiplying $r(\theta_r, \theta_i, \theta_a)$ by a shadowing factor, $S(\theta_r, \theta_i, \theta_a)$, given by Equation 2.16, which is dependent on viewing angle, and $\bar{\theta}$:

$$S(\theta_r, \theta_i, \theta_a) = \frac{\mu_r}{\eta_r(\theta_r)} \frac{\mu_0}{\eta_{0r}(\theta_i)} \frac{\chi(\bar{\theta})}{1 - f(\theta_p) + f(\theta_p)\chi(\bar{\theta}) \left[\frac{\mu_0}{\eta_{0r}(\theta_i)}\right]} \quad [2.16]$$

Where $f(\theta_p) = \exp\left(-2\tan\left(\frac{\theta_p}{2}\right)\right)$, $\chi(\bar{\theta}) = \frac{1}{(1+\pi\tan^2(\bar{\theta}))^{1/2}}$ and $\eta_r(\theta_r)$ and $\eta_{0r}(\theta_i)$ are the effective cosines which appear within the shadowing factor—for reflectance and incidence angle, respectively—as defined in (Hapke, 2011). Conceptually, η_r is the coefficient for the amplitude of complex specular reflection at normal incidence angle (for η_{0r}), or at a specified incidence angle (for η_r); furthermore, $\chi(\bar{\theta})$ is the average cosine of the surface tilt angle.

The parametrization of $\bar{\theta}$ within the Hapke BRDF model will be discussed in detail in Parts 2.1.1, 4.5 and 5.2, but it should be noted that the slope angle value calculated for a given particulate surface is dependent on the size-scale, or 'resolution' defined for the rough surface (Helfenstein and Shepard, 1999).

Reflectance, with surface roughness considerations included within the model, is thus given by Equation 2.17.

$$r_R(\theta_r, \theta_i, \theta_a) = r(\theta_r, \theta_i, \theta_a) S(\theta_r, \theta_i, \theta_a) \quad [2.17]$$

And hence, this is then related to the BRDF by Equation 2.18.

$$BRDF(\theta_r, \theta_i, \theta_a) = \frac{r_R(\theta_r, \theta_i, \theta_a)}{\cos(\theta_i)} \quad [2.18]$$

To summarize, the BRDF—as modelled by the Hapke BRDF model—relates to nine free parameters which are dependent on the physical and compositional properties of the particulate surface in question. Descriptions of, and the associated correlations between these nine free parameters are given in **Table 6**.

Free parameter	***Description***	***Correlation to other parameters***
K	Porosity coefficient (related to the filling factor, φ)	Correlated with w and, for high phase angles, $\bar{\theta}$
$\bar{\theta}$	Slope angle (surface roughness)	For high phase angles, correlated to w and K
w	Volume average single scattering albedo	Correlated to K and, for high phase angles, $\bar{\theta}$
b	Amplitude of forward-scattering, within Henyey-Greenstein function.	Correlated to c via the 'Hockey-stick' relation (Equation 2.9)
c	Amplitude of backscattering, within Henyey-Greenstein function.	Correlated to b via the 'Hockey-stick' relation (Equation 2.9)

h_S	Width of the shadow-hiding opposition effect	Correlated to h_C and it is not currently possible to discriminate between their effects*
h_C	Width of the coherent backscattering opposition effect	Correlated to h_S and it is not currently possible to discriminate between their effects*
B_{C0}	Amplitude of the coherent backscattering opposition effect	Correlated to B_{S0} and it is not currently possible to discriminate between their effects*
B_{S0}	Amplitude of the shadow-hiding opposition effect	Correlated to B_{C0} and it is not currently possible to discriminate between their effects*

Table 6: Descriptions of the nine free parameters within the Hapke BRDF model and their functional correlations to one another shown using varying colours. K, w and $\bar{\theta}$ are correlated, b and c are correlated, B_{S0} and B_{C0} are correlated and h_C and h_S are correlated—from (Hapke, 2011). *Recent work has shown it may be possible to discriminate between the SHOE and CBOE contributions to the opposition effect, using linear and circular polarisers (Hapke, 2021).

2.1.1 Limitations of the Model

As described in **Table 6**, one clear limitation to interpreting remote sensing and goniometry data using the Hapke BRDF model is the correlated nature of some of the key parameters. Due to the correlation between K, w and $\bar{\theta}$ (see Equations 2.3 and 2.16), it is not possible, when interpreting measured BRDFs, to deduce the effect of one of these parameters in a non-degenerate way—i.e. if the values of the others are not known. There are similar correlations between b and c, within the Henyey-Greenstein function for $p(\theta_p)$, and for the opposition effect parameters, h_S, h_C—for the width of the opposition effect—and B_{C0} and B_{S0} for the amplitude of the opposition effect. **Figures 19** and **20** show graphically how BRDFs, for typical lunar regolith surfaces, vary as filling factor (related to porosity coefficient) and volume average single scattering albedo increases, respectively.

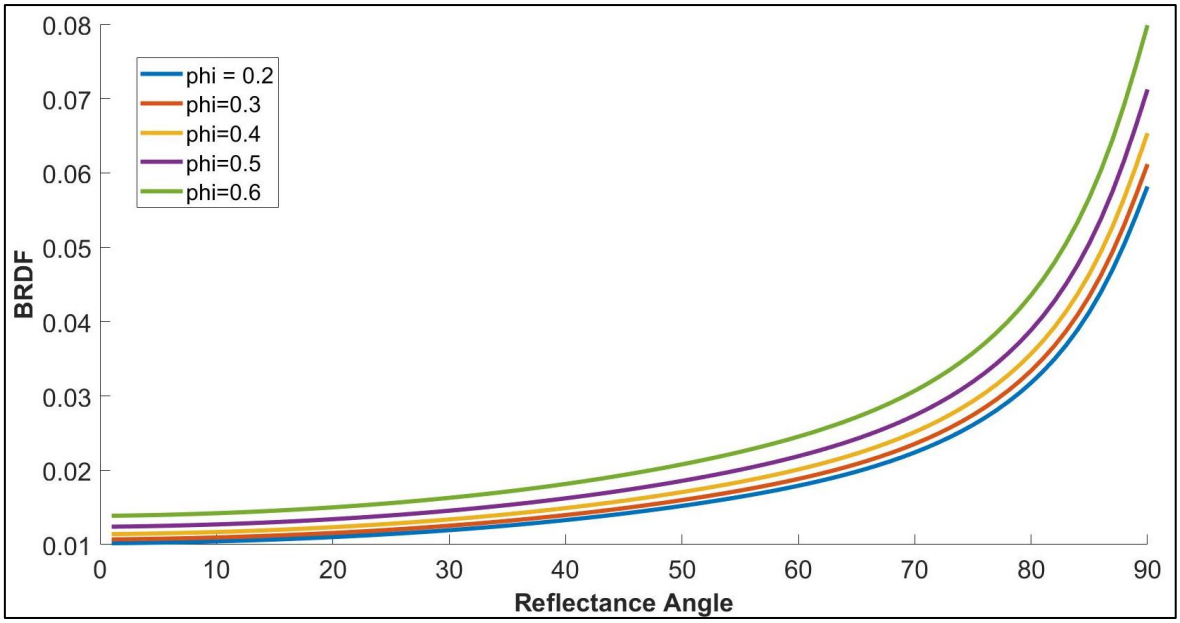

Figure 19: BRDF vs Reflectance angle, at 30˚ incidence angle, 180˚ azimuthal angle, for variations in filling factor, φ (and so, porosity coefficient, *K*) for a range of filling factors representative of lunar regolith structures, φ=0.2-0.6 (i.e. *K*=1.06-1.47), for *w*=0.29, *b*=0.20, *c*=0.73, $\bar{\theta}$=13˚.

For **Figure 19**, the filling factors are set to φ=0.2, 0.3, 0.4, 0.5 and 0.6, which result in *K*=1.06, 1.12, 1.19, 1.31 and 1.47, respectively. This range of phi values results in increases in BRDF of up to ~50% for all reflectance angles.

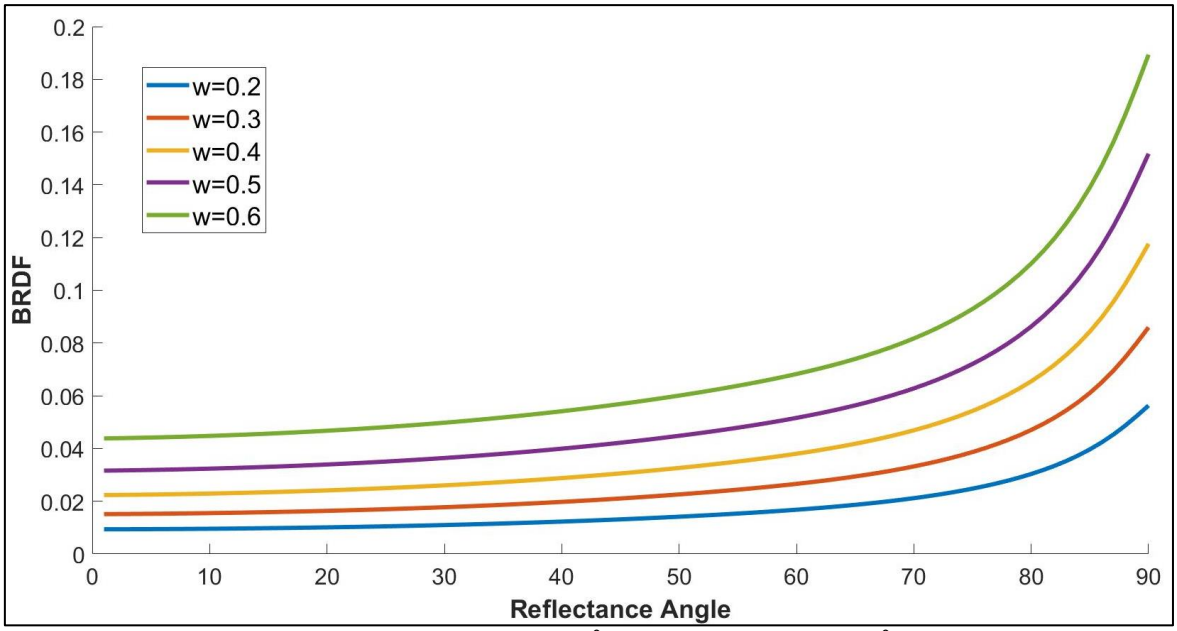

Figure 20: BRDF vs reflectance angle, at 30˚ incidence angle, 180˚ azimuthal angle, for variations in volume average single scattering albedo, *w*, for *w*=0.2, 0.3, 0.4, 0.5 and 0.6. For *b*=0.20, φ=0.6, *c*=0.73, $\bar{\theta}$=13˚.

For **Figure 20**, the w range is between 0.2 to 0.6, which is similar to the approximate range determined for the Apollo regolith samples (i.e. in (Foote *et al.*, 2020) w~0.324 for Apollo 11 (10084) and w~0.588 for Apollo 16 (68810)). For this range of w values, variations in w lead to significant (>10%) variations in the BRDF for each interval, for all reflectance angles. Varying between the minimum to maximum w values (i.e., 0.2-0.6) leads to increases in BRDF between ~250-400%, depending on reflectance angle.

Although the effect on BRDF of variations in w is generally more significant than for variations in K, it is clear from these figures how it would not be possible to deduce the effects of variations in either K or w separately, from the BRDFs alone. Therefore, to determine the value of one of these parameters from a measured BRDF, knowledge of the other value would be required. This principle is also true for the other correlated terms within the model.

Secondly, another significant limitation of the Hapke BRDF model, which was mentioned in Part 2.1, is the poorly constrained 'size-scale' of $\bar{\theta}$ (Helfenstein and Shepard, 1999). The size-scale refers to the 'resolution' used when calculating the slope angle value. For instance, a 0.085 mm size-scale implies that slope angles were calculated between points on the image which have a distance between them of 0.085 mm. Using a larger size-scale will naturally lead to lower values in $\bar{\theta}$, as smaller-scale topography variations will not be accounted for. Let us turn to the (Helfenstein and Shepard, 1999) stereophotogrammetry study—which analysed stereo images taken during the Apollo missions—to consider the importance of the $\bar{\theta}$ size-scale.

During the Apollo missions, astronauts took stereo images of the Moon's surface with the Apollo Lunar Surface Closeup Camera (ALSCC), which were later used to determine 'natural' surface roughness profiles for the lunar regolith. Each image provided stereoscopic

coverage of a 72.0x82.8 mm region of the lunar surface with a maximum resolution of 85 µm. In (J.K. Mitchell, L.G. Bromwell, W.D. Carrier III, N.C. Costes, 1971) the first study of these ALSCC images was performed, in which astronaut boot prints and tire tracks were used to investigate the mechanics of the lunar regolith, but in (Helfenstein and Shepard, 1999), these images were used to produce digital topographical relief maps of various imaged regions of the lunar surface. Using elevation histograms and fractal analysis, this study deduced surface roughness values for the lunar regolith surface over a range of size-scales. **Figure 21** shows two of ALSCC images which were analysed in the study; one for a mare region of the surface (Apollo 11) and another for the Fra Mauro (Mare Nubium) region (Apollo 14).

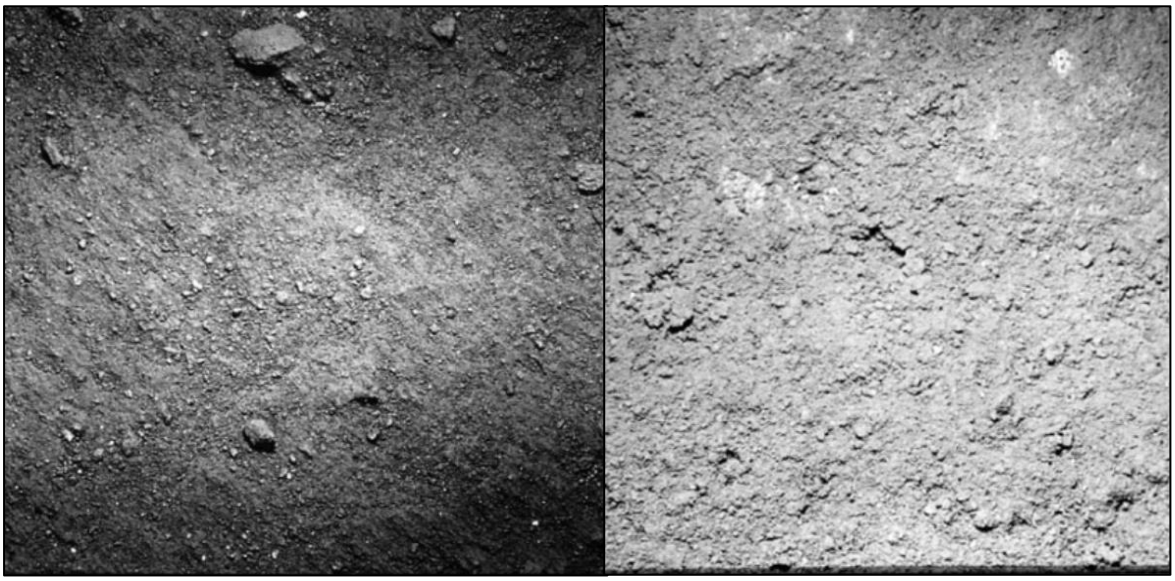

Figure 21: Apollo 11 (AS11-45-6701) (left) and Apollo 14 (AS14-77-10372) (right) surface images (72.0x82.8 mm). Image from (Helfenstein and Shepard, 1999).

Various images of the lunar surface were analyzed in the study from the Apollo 11, 12 and 14 missions and the images were named after their mission, i.e. AS11-XX-XXXXX for Apollo 11. 'Photometric surface roughness values'—which for the low albedo lunar surface are equivalent to RMS slope angles (see Part 2.2)—were then calculated in the study for each image across a range of size-scales, from 0.085 mm to 85 mm. **Table 7** shows this data.

Picture	Photometric roughness ($\bar{\theta}$)			
	0.085 mm	0.85 mm	8.5 mm	85 mm
AS11-45-6699[b]	$37 \pm 22^{\circ}$	$11.4 \pm 0.9^{\circ}$	$4.3 \pm 0.2^{\circ}$	$1.4 \pm 0.7^{\circ}$
AS11-45-6701[b]	$41 \pm 25^{\circ}$	$11.9 \pm 0.8^{\circ}$	$6.1 \pm 0.1^{\circ}$	$1.4 \pm 0.5^{\circ}$
AS11-45-6704	$44 \pm 28^{\circ}$	$14.0 \pm 0.6^{\circ}$	$7.7 \pm 0.2^{\circ}$	$1.2 \pm 0.5^{\circ}$
AS12-57-8449[b]	$36 \pm 21^{\circ}$	$11.8 \pm 1.0^{\circ}$	$5.2 \pm 0.2^{\circ}$	$1.01 \pm 0.2^{\circ}$
AS12-57-8452	$47 \pm 31^{\circ}$	$16 \pm 6^{\circ}$	$17 \pm {}^{23^{\circ}}_{17^{\circ}}$	$3.0 \pm 0.5^{\circ}$
AS12-57-8453[b]	$39 \pm 22^{\circ}$	$14.6 \pm 0.7^{\circ}$	$8.4 \pm 0.5^{\circ}$	$1.9 \pm 0.3^{\circ}$
AS12-57-8454	$46 \pm 15^{\circ}$	$21 \pm 9^{\circ}$	$13 \pm 3^{\circ}$	$2.0 \pm 0.4^{\circ}$
AS14-77-10368[b]	$41 \pm 23^{\circ}$	$17 \pm 3^{\circ}$	$13 \pm 2^{\circ}$	$3 \pm {}^{11^{\circ}}_{3^{\circ}}$
AS14-77-10370[b]	$42 \pm 23^{\circ}$	$17 \pm 4^{\circ}$	$8.3 \pm 0.4^{\circ}$	$1.5 \pm 0.5^{\circ}$
AS14-77-10371	$43 \pm 21^{\circ}$	$17 \pm 3^{\circ}$	$6.1 \pm 0.1^{\circ}$	$1.0 \pm 0.5^{\circ}$
AS14-77-10372	$45 \pm 16^{\circ}$	$17 \pm 5^{\circ}$	$8.2 \pm 0.3^{\circ}$	$1.3 \pm 0.4^{\circ}$

[b] Typical example of undisturbed lunar regolith.

Table 7: Photometric roughness values (RMS slope angles) of Apollo lunar regolith using stereophotogrammetry, for various size-scales. The ASXX denotes during which Apollo mission the image was taken, i.e. AS12-XX-XXXXX is an image from Apollo 12. From (Helfenstein and Shepard, 1999).

How photometric roughness (i.e. RMS slope angle) varies with size-scale can therefore be deduced, as is shown in **Figure 22**.

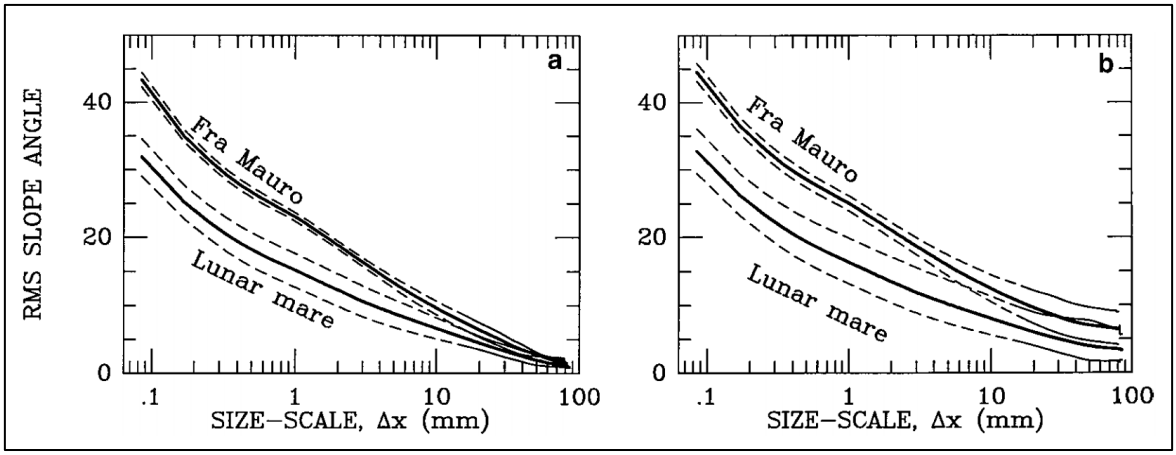

Figure 22: (a) Average RMS slope angles for undisturbed mare (Apollos 11 and 12) and Fra Mauro (Apollo 14) soils, respectively, measured as a function of size-scale from digital topography maps after subtracting regional tilt. Solid lines are measured values and dashed lines represent one standard deviation from the mean. (b) Data from (a) after statistical restoration of the decimetre-scale roughness contribution. Error envelopes (dashed lines) include the uncertainty in the large-scale roughness correction in addition to errors shown in (a)—from (Helfenstein and Shepard, 1999).

The constraint on the $\bar{\theta}$ size-scale given in Hapke is 100 µm to 1 km, due to the fact that $\bar{\theta}$ is expected to be affected by a convolution of all the scales within this range (e.g., by micro- and macro-scale roughness). For a given lunar regolith surface, $\bar{\theta}$ may be at least $\sim 5° < \bar{\theta} < \sim 45°$ across this range of size-scales. By showing how BRDF varies across this range of $\bar{\theta}$ values, **Figure 23** reiterates how further constraint is needed for the Hapke $\bar{\theta}$ size-scale.

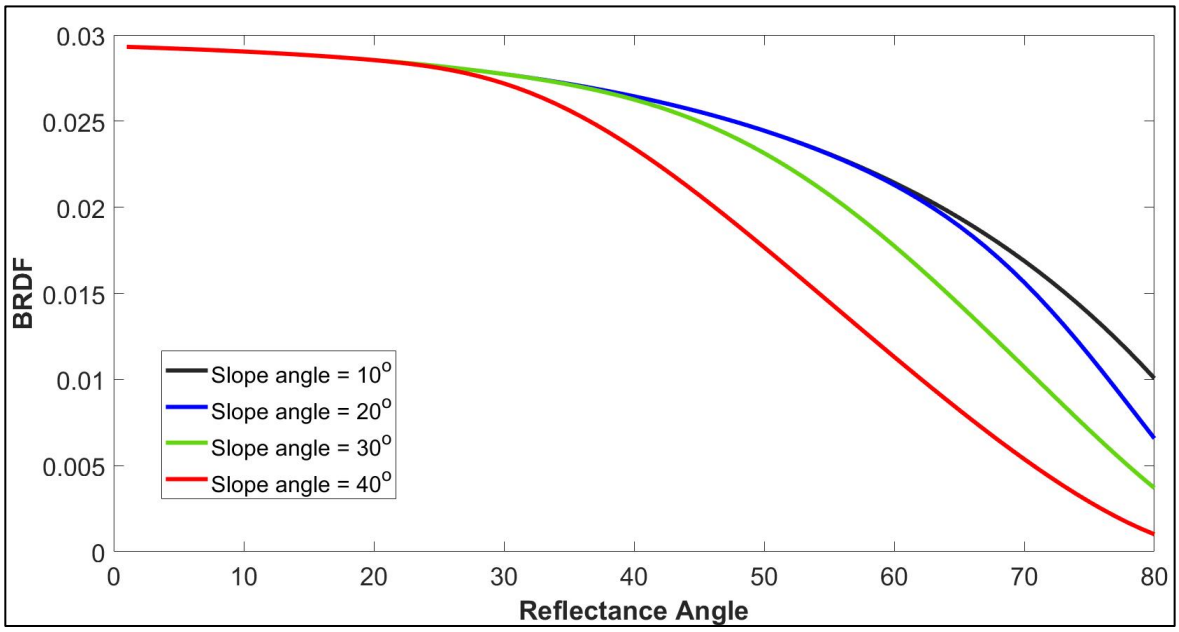

Figure 23: Showing how BRDF varies with reflectance angle for a lunar regolith-like sample over a range of slope angle values (10-40°). Modelled using the Hapke BRDF model at 60° incidence angle/180° azimuthal angle and with the following input parameters: *w*=0.48, *b*=0.2, *c*=0.7323, φ=0.5 (i.e. an Apollo 16-like sample, from (Foote *et al.*, 2020)).

As explained above and demonstrated in **Figure 22**, the upper and lower boundaries of the $\bar{\theta}$ size-scale must be well defined (within 1-2 orders of magnitude) for $\bar{\theta}$ to have any practical meaning. In (Hapke, 2011), the upper limit of $\bar{\theta}$ is described as the footprint of a standard remote sensing detector, which is typically meters to kilometers and the lower limit is given as several times the mean particle separation—i.e. typically on the order of 100-1000 µm for lunar regolith (Hapke, 2011). The Hapke slope angle therefore considers surface roughness contributions over a range of size-scales which spans 4-7 orders of magnitude, and this is too large a range for any practical relation to be made between slope angle values and a surface's physical state. Hence, to further constrain the practical size-scale of $\bar{\theta}$, to

within 1-2 orders of magnitude, is one of the major goals of this project, G2. As shown in multiple instances above, to deduce accurate physical parameters from remotely sensed, or laboratory measured, BRDFs using the Hapke BRDF model is only possible if the majority of the other parameters are well-defined, or, in the case of correlated parameters, if they are known. In (Sato *et al.*, 2014) it was demonstrated that once five or more of the Hapke parameters are defined, deductions can be made about the physical and compositional properties of the lunar surface. The methodology, results and limitations of this study are described in Part 2.2.

2.2 LROC WAC Hapke Parameter Map Study

In (Sato *et al.*, 2014) spatially resolved, near-global (70°S to 70°N latitude, 0° to 360° longitude) Hapke parameter maps of the Moon were derived, using LROC WAC reflectance observations, for seven wavelength bands—two UV bands, 321 and 360 nm, and five visible-wavelength bands, 415, 566, 604, 643 and 689 nm (Sato *et al.*, 2014). The study recognized the inability to accurately deduce any more than three free parameters from Least-Squares Levenberg-Marquardt fits, and therefore made the following assumptions: 1) set *K* to be 1 (filling factor, φ=0); 2) set effective photometric slope angle, $\bar{\theta}_p$ (described in Equation 2.19, where r_0 is diffuse reflectance and $\bar{\theta}$ is 'geometric' slope angle—or RMS slope angle), to be 23.4° (which is calculated within the study as the average 'best fit' value for the ±1° equatorial strip of the lunar surface); 3) set b and c via the 'Hockey-stick' relation, shown in **Figure 24**, and 4) incorporate the two causes (and hence two separate pairs of terms) of the opposition effect, under one pair of variables, B_{S0} and h_S (thus assuming B_{S0} and h_S describe the total opposition effect widths and amplitudes, which normally depend on contributions from B_{C0} and h_C, also).

$$\bar{\theta}_p = (1 - r_0)\bar{\theta} \qquad [2.19]$$

For a low albedo/reflectance case such as the lunar surface, $\bar{\theta}_p \approx \bar{\theta}$, as r_0 for the lunar regolith is typically 0.02-0.045, and so $(1 - r_0)$ will be ≥0.955. Therefore, for the purposes of this study 'geometric'/RMS slope angle can be equated to 'photometric roughness'.

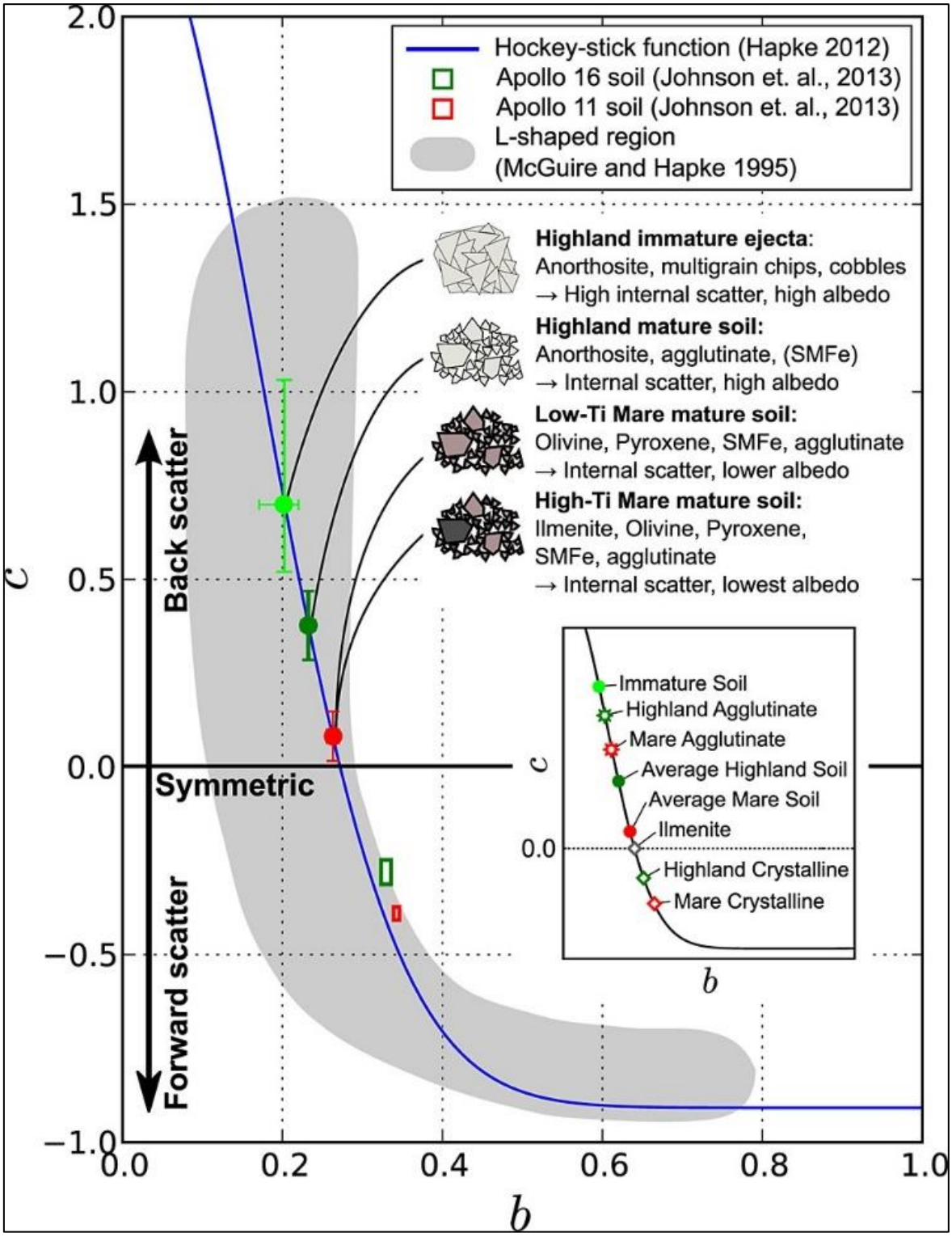

Figure 24: Showing the 'Hockey-stick' relation between *b* and *c*, and where the Apollo 11 and 16 regolith samples fit onto the curve. Image from (Sato *et al.*, 2014).

Finally, the data was binned in 1° latitude, 1° tiles, and each region was fitted, to produce near-global 'mosaic' maps such as those shown in **Figures 25**, **26** and **27**.

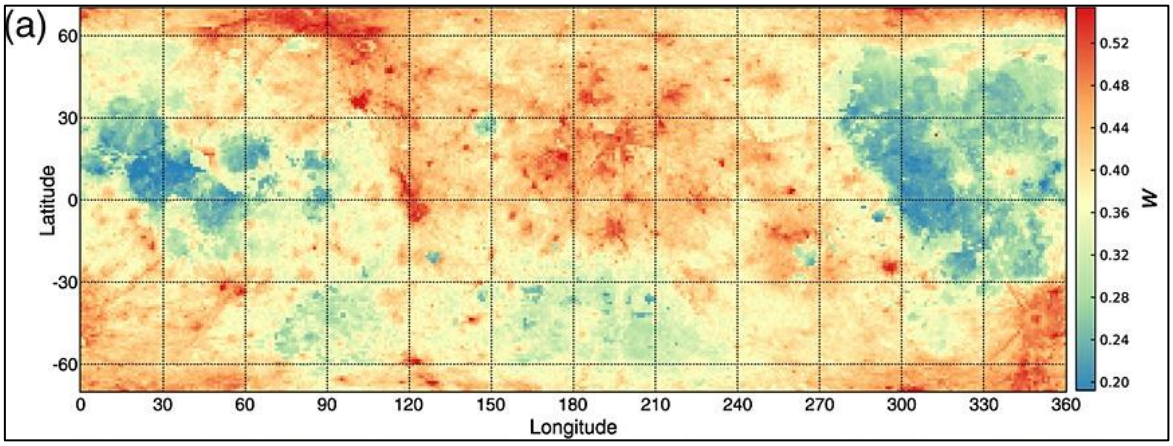

Figure 25: Showing the *w* Hapke parameter map (a) derived from the Lunar Reconnaissance Orbiter Camera (LROC) Wide Angle Camera (WAC) study. Image from (Sato *et al.*, 2014).

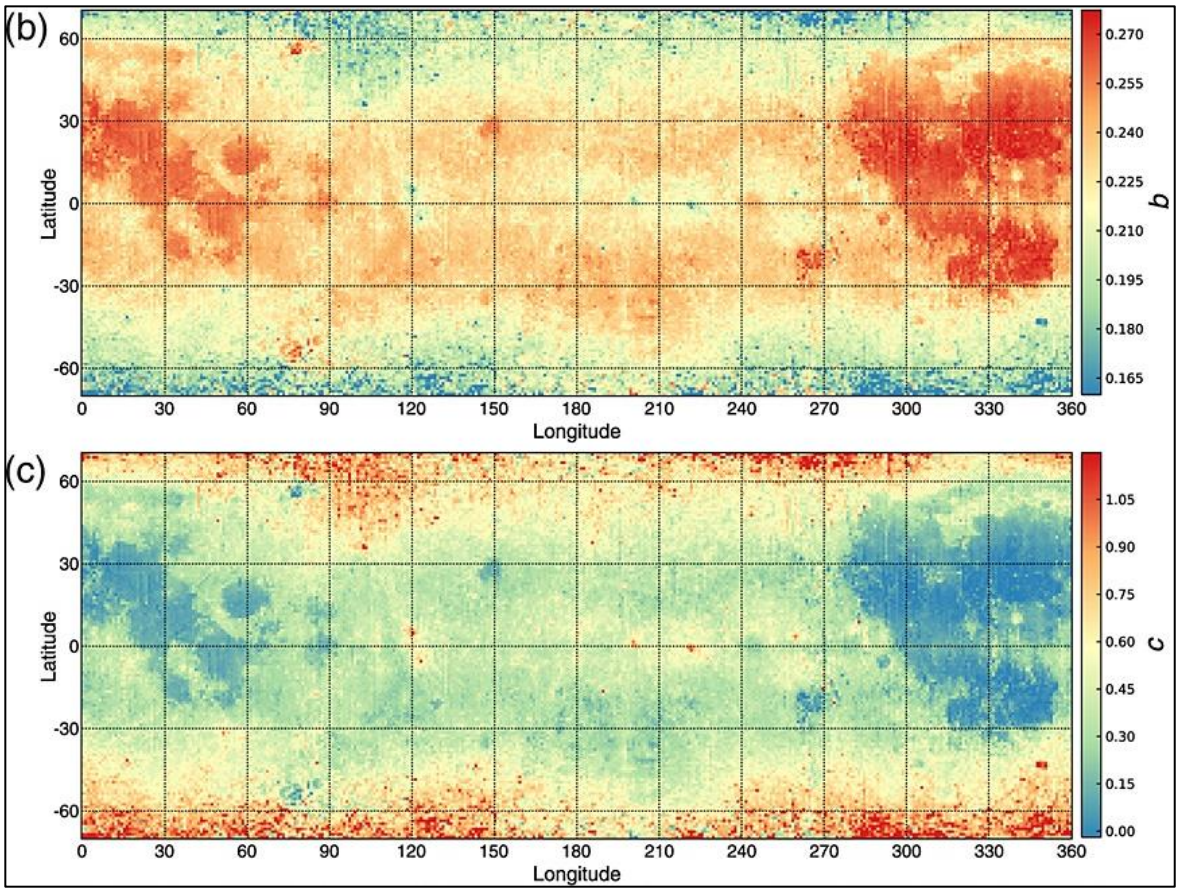

Figure 26: Showing the *b* and *c* Hapke parameter maps (*b* and *c*, respectively) derived from the Lunar Reconnaissance Orbiter Camera (LROC) Wide Angle Camera (WAC) study. Image from (Sato *et al.*, 2014).

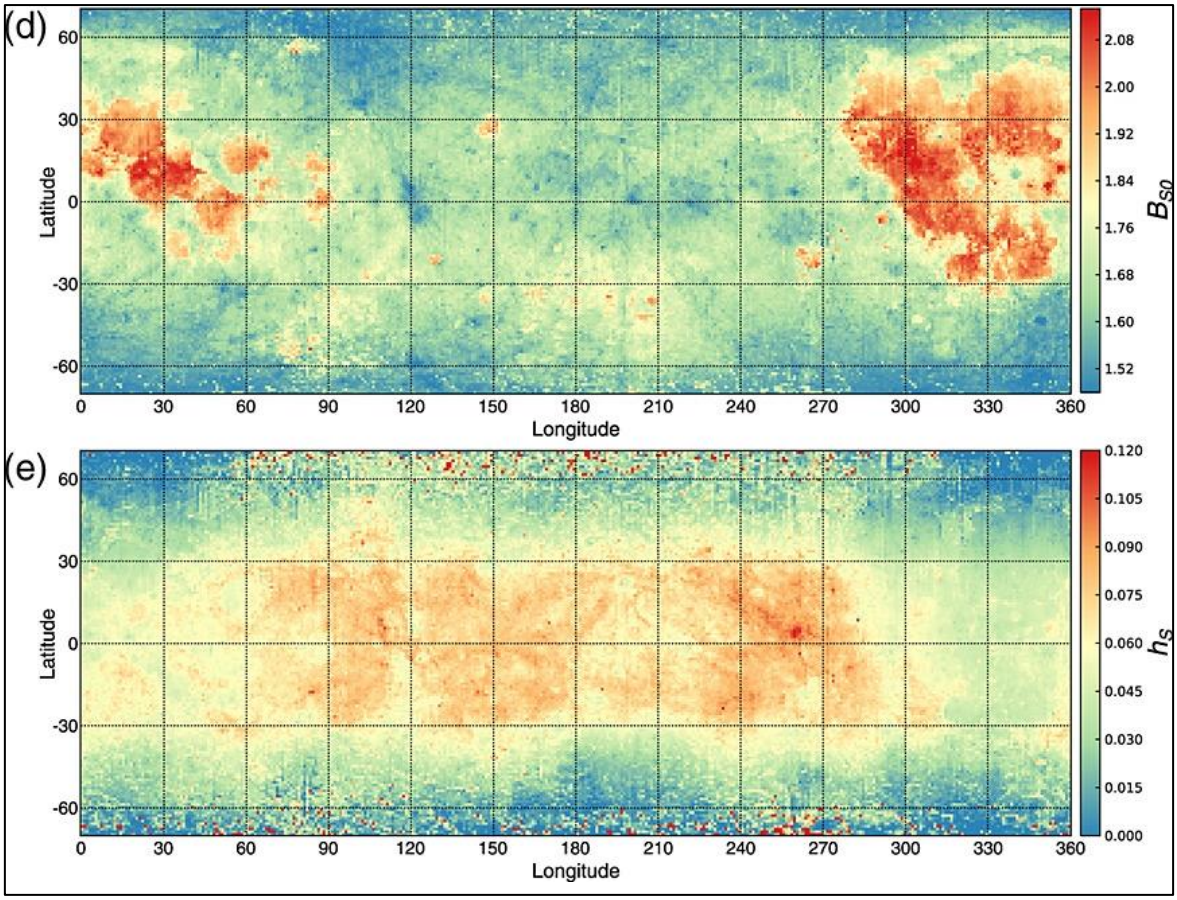

Figure 27: Showing the h_S and B_{S0} Hapke parameter maps (d and e, respectively) derived from the Lunar Reconnaissance Orbiter Camera (LROC) Wide Angle Camera (WAC) study. Image from (Sato *et al.*, 2014).

By assuming K=1 (φ=0), and ignoring the two coherent backscattering opposition effect terms (B_{C0} and h_C), the method used in the (Sato *et al.*, 2014) study may overestimate w, and the two opposition effect terms, B_{S0} and h_S. To break the degeneracy of the opposition effect terms would require a complex experimental study beyond the scope of this project in which BRDFs of lunar regolith samples are measured for various polarization ratios (Nelson *et al.*, 2000). However, to create more accurate Hapke parameter maps for w, b and c, laboratory BRDF measurements would be required for lunar regolith samples with known porosity and slope angle values, to help constrain the curve fits (Hapke, 2012).

The Hapke parameters derived in the (Sato *et al.*, 2014) study were used to photometrically normalize the observed reflectance of the LROC WAC data. However, deriving Hapke parameters for regions of the lunar surface is useful in its own right. The (Sato *et al.*, 2014)

study demonstrates how Hapke parameter maps allow inferences to be made about the likely compositional and physical properties for specific latitude/longitude regions of the lunar surface. For example, the b and c maps demonstrate decreased backscattering in the mare relative to the highlands (except for the 321 nm band). The study suggests this is likely due to higher contents of submicron iron (SMFe) and ilmenite in the interiors of backscattering agglutinates in the mare. Secondly, the h_S map (which standardly describes the angular width of the SHOE, but for this study describes width of the opposition effect as a whole) suggests relatively lower h_S values in the mare than the highlands and higher values for immature highland crater ejecta. This variation may be related to the grainsize distributions of the regolith (Sato *et al.*, 2014). Another interesting discovery is that of anonymously low b (~0.2) and high c (~0.7) values within relatively 'young', or 'fresh' craters. These b and c anomalies fade with distance from the crater rim and may result from fresh anorthosite chips and rocks—which are free from SMFe—being exposed during the crater-forming impact. Anorthosite chips are optically thick and generally have high albedo values—due to a high density of internal scatterers. Therefore, fresh anorthosite craters may be located by their strong backscattering properties (i.e. high c values) and their high w values.

It should be noted here that Hapke parameter maps could be made using LROC WAC multispectral (narrowband)—or Diviner's off-nadir visible-λ (broadband)—data, by fitting the remote sensing data to Hapke BRDFs set using BRDFs measured in the laboratory for lunar regolith samples with known φ and $\bar{\theta}$ values. Using this technique, it should be possible to break the K, w and $\bar{\theta}$ degeneracy within the model, and thus to make w maps which do not overestimate the derived values. Furthermore, by setting the w and $\bar{\theta}$ values using Apollo sample BRDFs it may be possible to map K values for the lunar surface for increasing latitudes, thus studying whether the porosity of the lunar regolith does increase with latitude, as was suggested in (Metzger, Anderson and Colaprete, 2018). The physical

mechanism behind this potential ‘fluffening’ has not been comprehensively studied, but, as mentioned in 1.3.3, it has been suggested to be due to an increased expansion and compaction of the regolith, and thus a reduction of the ‘fairy-castle’ state, for equatorial regions which experience higher amplitude temperature variations over the lunar diurnal wave.

Therefore, measuring a comprehensive laboratory BRDF dataset for samples with known porosities and surface roughnesses would allow remote sensing data taken by instruments such as LROC and Diviner to be analysed using the Hapke BRDF model—as was done in (Sato *et al.*, 2014)—but with further constraints placed on K and $\bar{\theta}$; thus, leading to more accurate derived values of w, b and c. To measure such a BRDF dataset is one of the major aims of this project, A2, and to do so requires the use of an instrument known as a goniometer which must be able to measure visible-wavelength BRDFs over a wide range of viewing angles. To derive the experimental requirements for a goniometer system which could be used to achieve the goals of our study, in accordance with aim A1, the predictions of Hapke BRDF model must be considered, in addition to relevant aspects of the off-nadir Diviner data and the O3DTM.

3. The Oxford Space Environment Goniometer and Derived Requirements

3.1 The Oxford Space Environment Goniometer

The Oxford Space Environment Goniometer (OSEG) is an automated three-axis goniometer which was originally designed to make automated emission phase function measurements at TIR wavelengths, to be used as ground support for Diviner (Warren, 2015). In (Warren, 2015), the TIR capabilities of OSEG were demonstrated, and its ability to measure emission phase functions using a source which heats the sample from below were shown. The OSEG setup allows variation of incidence, emission/reflectance and azimuthal angles and is located within a one-meter diameter vacuum chamber. This chamber is surrounded by a cold shield to enable TIR measurements to be taken under lunar environment conditions (i.e. in 10^{-6} mbar vacuum and surrounded by a 'cold', <150 K, space view). OSEG's basic parts can be split into mechanical parts, cold shield and vacuum chamber, radiometer carriage, light/heat source, chopper and SR830 analogue lock-in amplifier (which removes background light/noise by only detecting light chopped at a specific frequency) (**Figure 28**) (Warren, 2015).

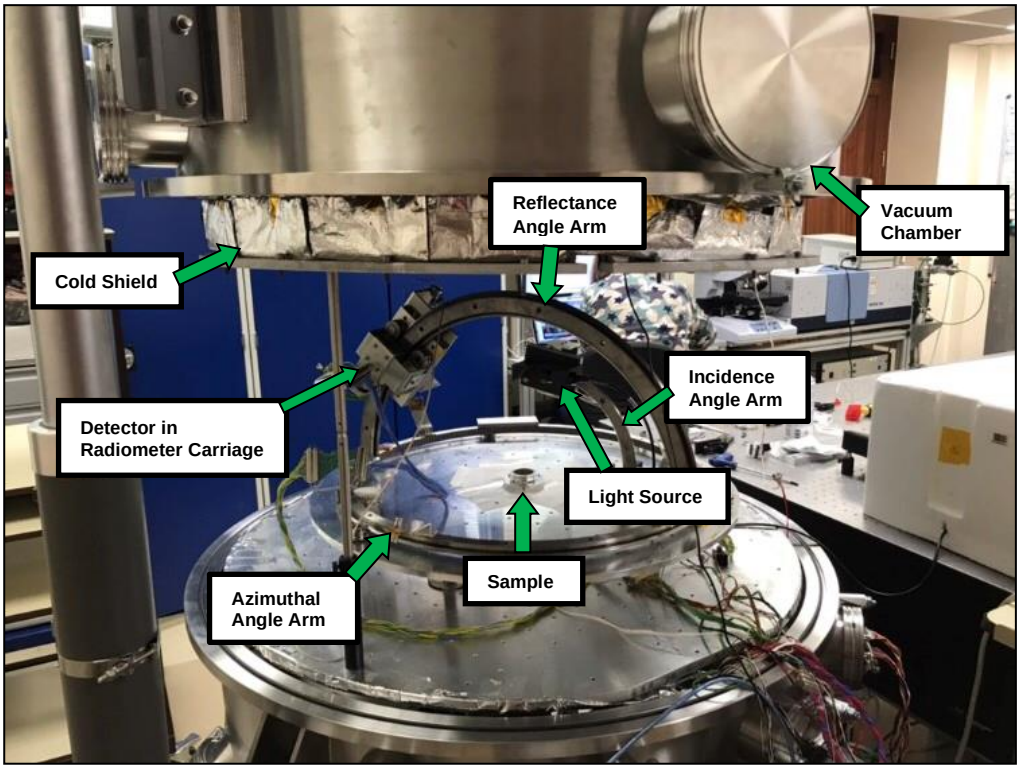

Figure 28: The original Oxford Space Environment Goniometer (OSEG) setup out of vacuum with major parts labelled.

Although OSEG was initially designed to measure emission phase functions at TIR wavelengths, it was shown in (Warren, 2015) that it should be possible to adapt its basic parts, so that BRDFs at visible wavelengths could be measured—as for our desired study of Apollo regolith samples with known physical properties. These BRDF measurements would not require vacuum conditions (although vacuum measurements would be possible), or to be made at lunar-like temperatures, and so could be taken in ambient conditions (if a lock-in amplifier were used, to remove the background signal), which would be more time efficient. However, various updates to OSEG are needed to ensure its visible-wavelength BRDF measurements are in agreement with those of similar goniometer instruments such as the Bloomsburg University Goniometer (BUG) (Johnson, 2008), the Physikalisches Institut Radiometer Experiments (PHIRE-1 and PHIRE-2) (Gunderson, Thomas and Whitby, 2006), the SHADOWS spectro-gonio radiometer (Potin *et al.*, 2018), and the Blacklab goniometer system (Biggar, Thome and Wisniewski, 2003). Developing a visible-λ goniometer using

the OSEG setup as a basis would be beneficial to using BUG, PHIRE-1, PHIRE-2, SHADOWS or the Blacklab goniometer due to 1) the automated nature of OSEG, enabling large datasets to be measured time-efficiently, and 2) OSEG's close proximity to surface profiling instruments.

Before making any updates to the current OSEG system, experimental requirements must be derived for the visible-wavelength adaptation of OSEG, which from here will be referred to as VOSEG (the Visible-OSEG). To do this, it is necessary to consider the previous reflectance/BRDF measurements of Apollo regolith and lunar regolith simulant samples (Part 3.2); and the Hapke BRDF model, with which 1) the range of viewing angles necessary for our experimental study, and 2) the parameter space for our BRDF study of how porosity and surface roughness affect BRDFs measured for Apollo regolith samples (Part 5.1) can be derived. Furthermore, the requirements which derive from the current available off-nadir Diviner dataset must be deduced, as well as the scattering function input parameterization within the O3DTM (Parts 1.2.3 and 1.3.3; then Parts 5.3 and 6, respectively).

3.2 Previous Visible-λ Reflectance Measurements of Apollo Regolith and Lunar Regolith Simulant Samples

After the return of the Apollo missions, hemispheric reflectance measurements of Apollo 11 lunar regolith samples were initially made using an integrating spectrophotometer, in the 1970s (Birkebak, 1974). These results were used as initial inputs for thermal models of the lunar surface (Keihm, 1984; Rozitis and Green, 2011; Vasavada *et al.*, 2012; Hayne *et al.*, 2017). However, hemispheric reflectance measurements only provide an average reflectance for a specific viewing angle (e.g. 45° incidence angle, 15° reflectance angle) and do not provide scattering information as a function of viewing angle, as the BRDF does. Furthermore, these earlier measurements of lunar mare samples are not representative of the

entire surface of the Moon (due to their composition). Hence, a more complete understanding of light scattering for the entire lunar surface was needed, i.e. BRDFs for a more extensive suite of lunar samples.

More recently in (Foote *et al.*, 2020), BRDF measurements of Apollo 11 (10084) and 16 (68810) lunar regolith samples were made. 10084 and 68810 are two representative regolith samples, originating from different areas of the Moon—10084 is from a mare region (*Statio tranquilatis*) and 68810 is from a highlands region (*Descartes Highlands*) (see (Shoemaker *et al.*, 1970; Muehlberger *et al.*, 1980; Morris, 1983; Korotev and Gillis, 2001; Hiesinger, 2006) for a full description of the Apollo samples). For the 10084 sample, the (Foote *et al.*, 2020) study details an agreement <10% for all viewing angles up to 70° reflectance angles, between remote sensing data and laboratory measured data for the albedo of the surface, which is inputted into the model to deduce bolometric surface temperatures. However, for the Apollo 16 sample, the laboratory measured albedos were ~33% brighter than those required to fit the Diviner data. The study attributed the observed discrepancy to the increased compaction and decreased maturity of the laboratory sample, as compared to the natural lunar surface, and in addition, to the fact that the local variability in the surface albedos of the Apollo 16 landing site is lower than the spatial resolution of Diviner (~300 m) (Foote *et al.*, 2020). Furthermore, for both samples the laboratory measured BRDFs began to diverge from the Hapke BRDF model for reflectance angles >60°. This could be due to inaccurately set $\bar{\theta}$ values within the model used in the study, or, more generally, to inaccuracies within the physics of the Hapke BRDF model, for extreme viewing angles.

Figures 29 and **30** show principal plane (0/180° azimuthal angle) Lambert Albedo plots produced by the study, for the 10084 and 68810 samples, respectively. The study illuminated the samples using a broadband light source, but various filters were added to measure BRDFs at a range of narrowband wavelengths (450, 550, 750 and 950 nm). These figures

show BRDF data for the 750 nm filter setup. The Lambert Albedo is the albedo of the surface relative to a Lambertian reflector, and is related to the BRDF as in Equation 2.1 (Foote *et al.*, 2020). Note, the BUG study reported no error bars.

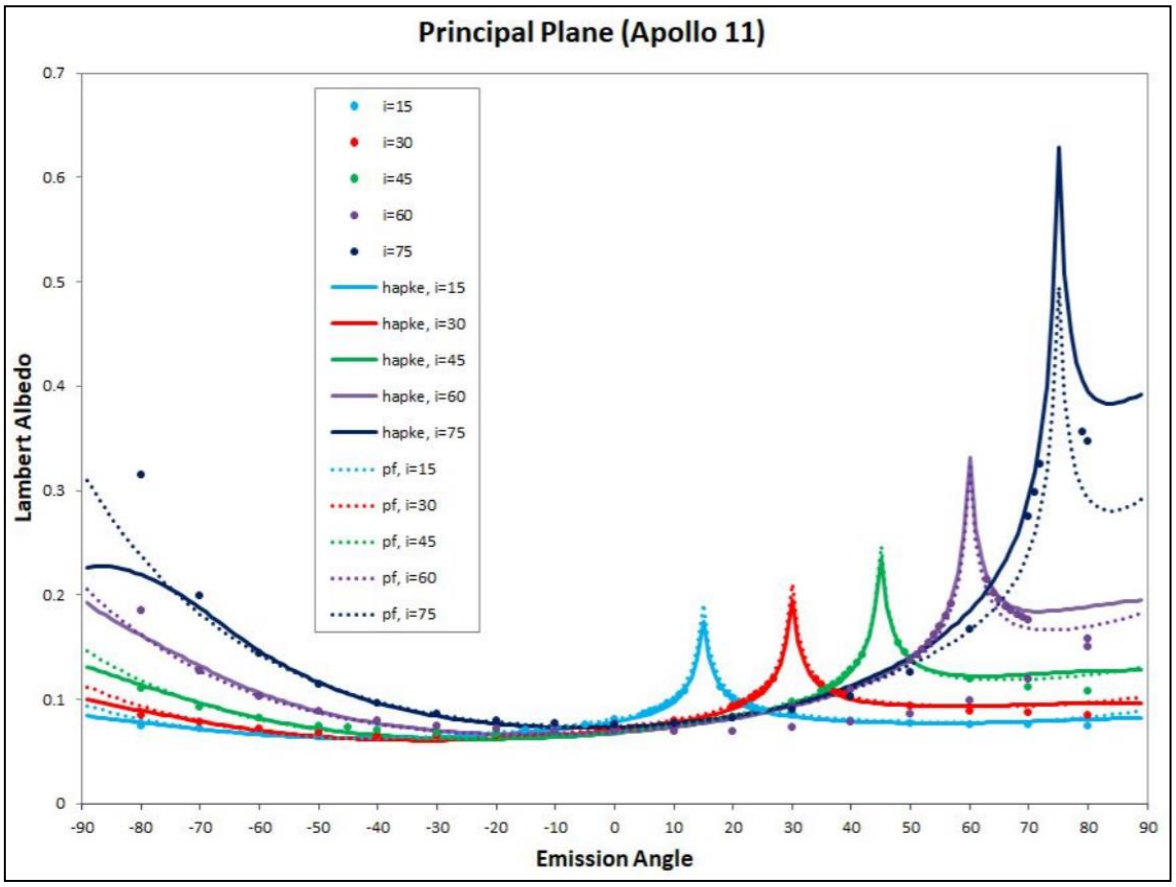

Figure 29: Lambert Albedo plots measured in the principal plane for Apollo 11 (10084) by BUG—from (Foote *et al.*, 2020). Dots are Apollo 11 BUG measured data, solid lines are Hapke modelled data and dashed lines are simplified functions made using best fit parameter values for 750 nm datasets (see text for details). Broadband light source used with 750 nm filter. Each colour represents a different incidence angle. For the Hapke BRDF model (run over all data simultaneously), w=0.347; b=0.292 and c=0.405; h=0.009; B_0=2.632; $\bar{\theta}$=10.25°. (For simplicity, h_S and h_C and incorporated under one parameter, h; and B_{S0} and B_{C0} are incorporated under one parameter, B_0.)

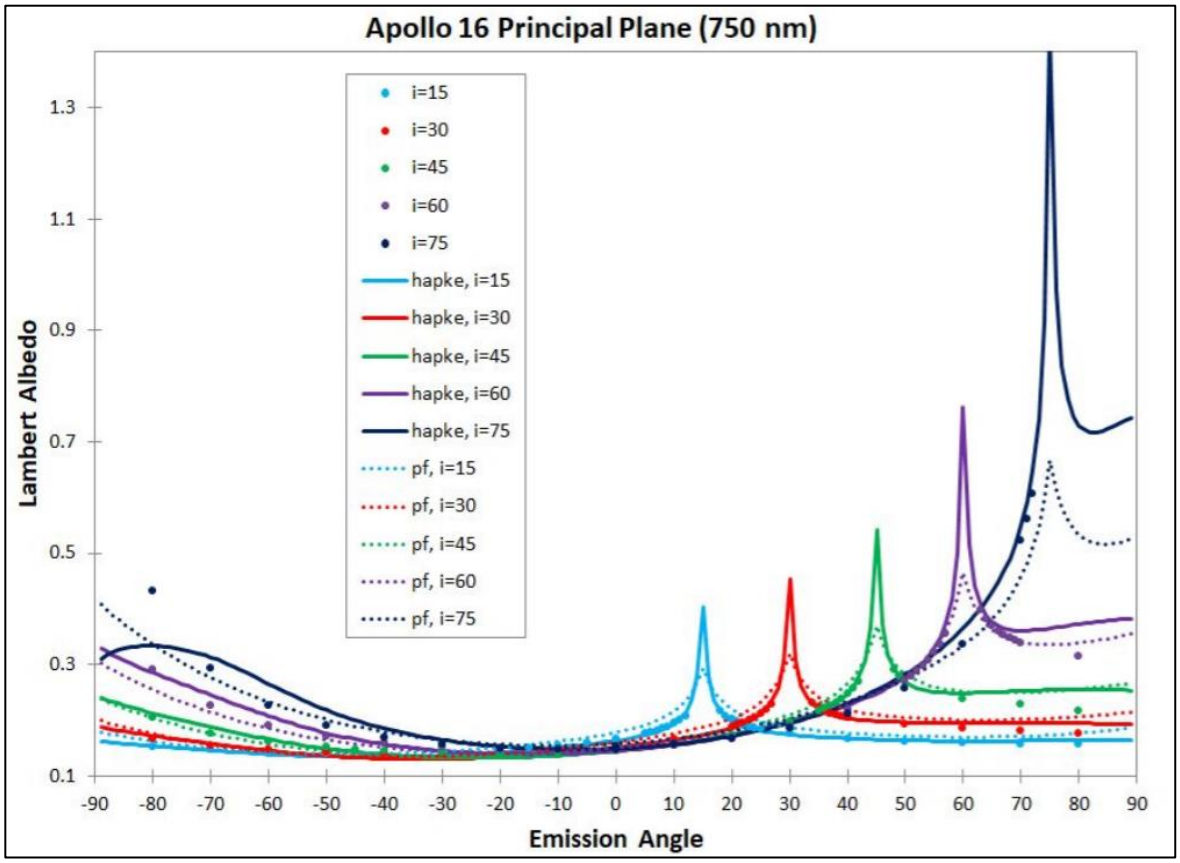

Figure 30: Lambert Albedo plots measured in the principal plane for Apollo 16 (68810) by BUG—from (Foote *et al.*, 2020). Dots are Apollo 16 BUG measured data, solid lines are Hapke modelled data and dashed lines are simplified functions made using best fit parameter values for 750 nm datasets (see text for details). Broadband light source used with 750 nm filter. Each colour represents a different incidence angle. For the Hapke BRDF model (run over all data simultaneously), single scattering albedo, w=0.566; Henyey-Greenstein coefficients, b=0.277 and c=0.474; h=0.011; B_0=2.265; $\bar{\theta}$=10.5°. (For simplicity, h_S and h_C and incorporated under one parameter, h; and B_{S0} and B_{C0} are incorporated under one parameter, B_0.)

The (Foote *et al.*, 2020) study measured BRDFs for the following range of viewing angles: 15-75° incidence; 0-80° reflectance; in the principal plane (0/180° azimuthal), and directly out of the principal plane (90/270° azimuthal). This angular range was determined to be sufficient to test the terms within the Hapke BRDF model. The study made measurements in steps of 10° reflectance angle, except when approaching <10° phase angle—i.e., the location of the opposition effect.

As in (Foote *et al.*, 2020), the Hapke BRDF model will also be used to derive the experimental requirements of our study, which aims 1) to measure a suite of BRDFs for

Apollo regolith samples with known porosity and slope angle values (A2), 2) to use this suite of BRDFs in the interpretation of Diviner visible-λ off-nadir data (A3), and 3) to input laboratory measured BRDFs into the O3DTM, in an attempt to reduce the temperature discrepancies observed between remote sensing and thermal models, for high-latitude PSRs (aim A4).

3.3 Deriving the Experimental Requirements for the Visible Oxford Space Environment Goniometer

Although ideally a BRDF study of Apollo samples would involve measuring at every theoretically possible angle within the scattering hemisphere, temporal and spatial constraints necessitate a reasonable parameter space to be derived, which will enable the study's scientific goals to be met within the available timeframe. Therefore, the minimum viewing angle range needed for our study will be deduced, bearing in mind our goals—to measure BRDFs for samples with known and varying porosity and slope angle values which 1) can be used to test the Hapke BRDF model and to constrain its slope angle parameterization, 2) can be compared to Diviner visible off-nadir data for the lunar surface (goal G3) and 3) can be used as scattering function inputs for thermal models; thus potentially improving agreements between thermal model predictions and Diviner's temperature measurements for PSRs (goal G4). Firstly, the minimum reflectance angle range will be considered.

3.3.1 Measuring at High (>50°) Reflectance Angles

As mentioned previously, the (Foote *et al.*, 2020) study concluded by attributing the discrepancies observed between laboratory measured and Hapke modelled BRDFs—in particular, at extreme (>50°) viewing angles—to sample porosity variations. However, discrepancies which increase with reflectance angle, and which are most prominent at >50° reflectance angle, may be more logically attributed to inaccuracies in slope angle.

The Hapke slope angle parameter, $\bar{\theta}$, captures the amplitude of a sample's surface roughness, e.g., the RMS slope angle. How this surface roughness affects a sample's BRDF through shadowing is then described by Equations 2.16, 2.17 and 2.18. By comparing Hapke modelled BRDFs for an Apollo-like sample with and without the inclusion of shadowing (for a maximum reasonable $\bar{\theta}$ value for the lunar surface (Helfenstein and Shepard, 1999))—as is done in **Figure 31**—it is possible to derive the minimum reflectance angle range requirement for the surface roughness study. The effect of porosity on BRDF does also vary with reflectance angle, but this effect is negligible (i.e., within the expected measured uncertainty) in comparison to the effect of slope angle variations (compare **Figures 19** and **31**), and so porosity is not considered when deriving the minimum reflectance angle range for the VOSEG setup.

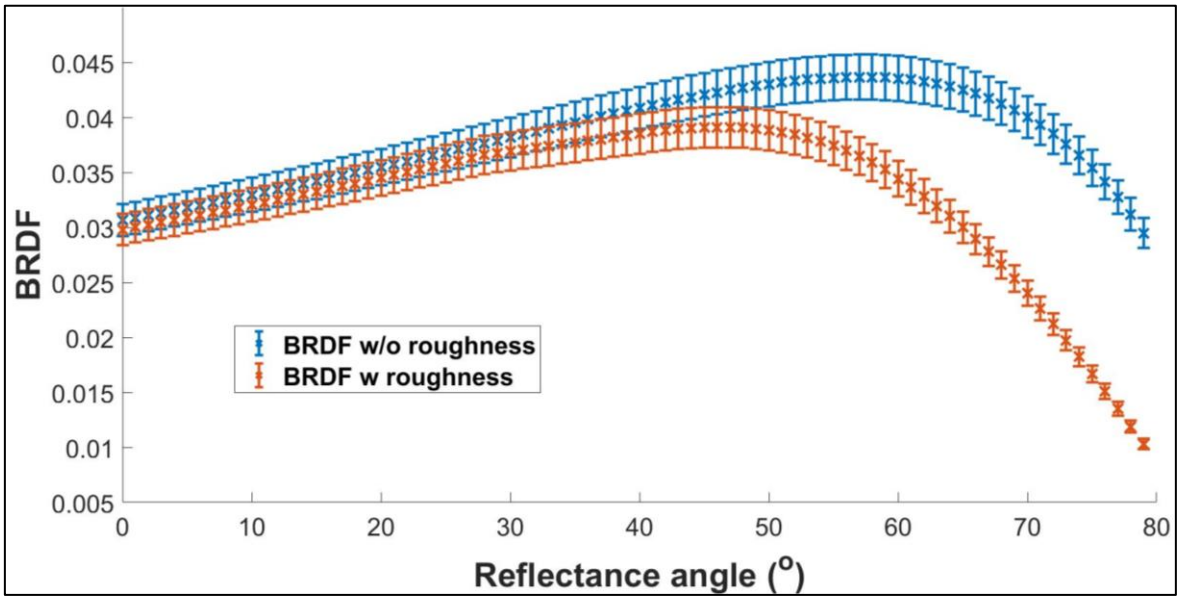

Figure 31: Hapke model BRDFs for an Apollo 11 regolith-like sample, with shadowing (orange crosses), and without shadowing (blue crosses), for 60° incidence and 180° azimuthal angles. $\bar{\theta}$=20°, average particle size=80 µm, φ=0.5, w=0.288, h_S=0.001, b=0.292 and c=0.405 (chosen in accordance with (Foote *et al.*, 2020)). Error bars represent VOSEG's 4.7% expected measurement uncertainty, as derived in Part 4.5.

It is clear from **Figure 31** that to measure the effect of surface roughness on BRDF, the VOSEG system must be able to measure reflectance angles >50°, as this is the region in which shadowing effects dominate. The minimum reflectance angle range for VOSEG must

be 0-65˚—given an experimental error of ~4.7%—as it is only once ~65˚ is reached that 1) the most considerable discrepancies—e.g., increases in signal of ~50% which are discriminant from porosity variations—can be observed between non-rough and rough surfaces (for $\bar{\theta}$=20˚, which is a reasonable value for the lunar surface (see (Sato *et al.*, 2014; Bandfield *et al.*, 2015)); and 2) the remaining part of the curve can be deduced using the Hapke BRDF model.

3.3.2 Measuring the Opposition Effect

It is possible to measure the opposition effect in the laboratory, as in (Nelson *et al.*, 2002; Gunderson and Thomas, 2008), but in order to do so a goniometer system must be able to measure phase angles <~10˚, as demonstrated in **Figure 32**, which shows how the SHOE variable B_S varies within the model, as it approaches $\theta_p = 0°$ (Shepard and Helfenstein, 2011).

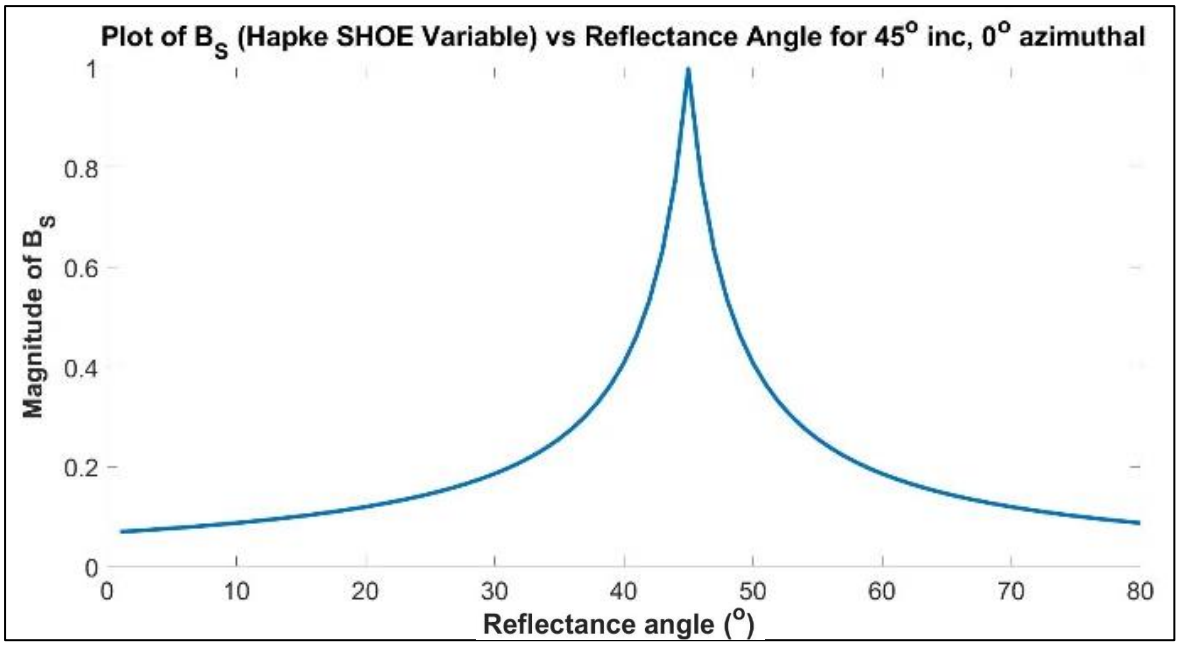

Figure 32: B_S, the Shadow-Hiding Opposition Effect variable within the Hapke BRDF model vs reflectance angle, for 45˚ incidence angle; 0˚ azimuthal angle; *w*=0.2883; Henyey-Greenstein coefficients, *b*=0.2917, *c*=0.4052 and h_S=0.03 as given for the Apollo 16 (68810) sample in the (Foote *et al.*, 2020) study.

Therefore, to test the opposition effect terms within the Hapke BRDF model, the first requirement for a goniometer system is to be able to measure phase angles as low as possible

(<10°), with a minimum phase angle of ~5° so that the shape of the steepest part of the curve can be captured. Following on from this, a goniometer system must be able to measure reflectance angles between at least 10-65°, and ideally, 5-70° so that the most significant part of the opposition effect (±10°) can be measured, for 15-60° incidence angles. **The minimum reflectance angle range requirement is, therefore, 0-65°.**

Now that our reflectance angle requirements have been determined using the Hapke BRDF model, it is important to also consider the incidence and azimuthal angular range requirements for the VOSEG setup. To do this, let us again turn to the Hapke BRDF model, in addition to considering our primary aims, A3 and A4: comparing VOSEG-measured BRDFs to Diviner's off-nadir data and using VOSEG-measured BRDFs as inputs for thermal models.

3.3.3 Measuring at a Range of Incidence and Azimuthal Angles

The incidence and azimuthal angular ranges selected for the (Foote *et al.*, 2020) study demonstrated the planes for which the Hapke BRDF model is most critically affected by variations in the Hapke parameters w, b, c and $\bar{\theta}$. This is why (Foote *et al.*, 2020) measured BRDFs for the Apollo samples in the principal (0/180°) and out-of-principal (90/270°) planes. By measuring BRDFs for these two planes over a range of incidence angles—i.e. 15/30/45/60/75°, as in the study—it is possible to test the parameterizations of the terms within the Hapke BRDF model. Varying w or $\bar{\theta}$ has equal effect on BRDF in all the measurement planes, but the effect of varying b and c, which describe forward-scattering and backscattering, respectively, is most prominent in the principal plane (0/180°). Therefore, from a perspective of fulfilling goals G1 and G2—i.e., measuring a suite of BRDFs and using them to further constrain the Hapke slope angle size-scale—the requirement can be placed on the VOSEG setup that it must be able to measure BRDFs in

the principal (0/180°), and out-of-principal (90/270°) planes, as in (Foote *et al.*, 2020). Furthermore, the VOSEG setup must be able to measure over a range of incidence angles, which covers those angles for which (Foote *et al.*, 2020) observes significant variations (≥10%) between laboratory measured and Hapke Modelled BRDFs. **Figure 30**, from (Foote *et al.*, 2020), demonstrates that this range must extend to 60° incidence angle, at least.

3.3.4 Requirements for Diviner Off-nadir Data Comparison

Aim A3 of this project is to compare the laboratory measured VOSEG data to Diviner off-nadir data for various regions of the lunar surface. To be able to do so, off-nadir reflectance/BRDF data from Diviner must be binned into angular bins of ±2.5°—given that the Hapke BRDF model predicts variations in BRDF <10% within this range, for the available range of viewing angles (e.g., less than the average measured uncertainty in the data) (see Part 5.3)—and plotted as a function of reflectance angle. Due to the discrepancies in measured BRDFs observed in (Foote *et al.*, 2020), it is crucial that BRDFs measured for the Apollo samples can be compared to Diviner data for at least mare and highlands regions of the lunar surface, in at least one measurement plane (i.e. for one azimuthal angle, one incidence angle and over a range of reflectance angles which encompass the opposition effect and values at both ends of the curve (i.e. at ~0-15° and ~50-70°)). Therefore, to deduce a minimum requirement for the incidence and azimuthal angular ranges of the VOSEG setup, the available off-nadir Diviner data will be explored. **Table 8** enables the available ranges of data points for the visible off-nadir Diviner data to be visualised, for each of the targeted regions of the lunar surface. Within the Table, regions/viewing angles which have sufficient data points for comparison to laboratory measured BRDFs—defined as having data for at least half the BRDF curve, from 0-70° reflectance angles—are coloured green; regions/viewing angles which potentially have enough data for some comparisons to be

drawn are coloured orange (i.e., data for ~10-35° reflectance angles); and regions which have insufficient data for comparison (<10° reflectance angles) are coloured red. King Crater, Equatorial Highlands and the Apollo landing sites are not included as there is currently insufficient data for these sites at all of the desired angular ranges. Note: All data mining and Diviner off-nadir analysis performed by the author.

Target location	***Incidence angle (±2.5°) (°)***	***Azimuthal angle (±2.5°) (°)***				
		0	**45**	**90**	**135**	**180**
Equatorial Mare	*15*					
	30					
	45					
	60					
High-latitude Mare	*15*					
	30					
	45					
	60					
High-latitude Highlands	*15*					
	30					
	45					
	60					
Aristarchus Plateau	*15*					
	30					
	45					
	60					
Equatorial Cold Spot	*15*					
	30					
	45					
	60					
Dufay Albedo Anomaly	*15*					
	30					
	45					

	60					
Kepler Crater Ejecta	*15*					
	30					
	45					
	60					
Reiner Gamma	15					
	30					
	45					
	60					

Table 8: Showing the available off-nadir Diviner data for the various regions of interest on the lunar surface. Green regions are those for which there is sufficient data to fit the Hapke BRDF Model (i.e., at least half the required BRDF curve from 0-70° reflectance angle); orange regions are those for which there is potentially enough data (i.e., data for ~10-35° reflectance angles); and red regions are those for which there is insufficient data (i.e., <10° reflectance angles).

Table 8 shows that for the Dufay Albedo Anomaly and the Equatorial Cold Spot, there is sufficient data in most measurement planes for comparisons to be made between Diviner off-nadir and laboratory BRDF data. However, for the High-latitude Highlands/Mare and Equatorial Mare regions, there is only sufficient comparable data at high incidence angles (45° and 60°). Considering the VOSEG study will be measuring Apollo samples from highlands and mare regions of the lunar surface, it is important that comparisons can be made between laboratory data and Diviner off-nadir data for both of these regions of the lunar surface. **Therefore, the requirement for VOSEG's minimum incidence angle range can be derived—i.e. it will be necessary to measure incidence angles up to at least 60°**, to allow mare and highlands regions to be compared to laboratory measured BRDFs, for various azimuthal angle planes. However, ultimately the incidence angle range is also bounded by the time limitations of the study, and the size of the spot on the Apollo sample (which increases with incidence angle).

In terms of deriving the required range of azimuthal angles to complete the goals of our study, it has already been deduced above that principal plane (0/180°) and out-of-principal

plane (90/270°) measurements must be made, in accordance with (Foote *et al.*, 2020). **Table 8** shows how the azimuthal angle requirement is not driven by the Diviner off-nadir data, as there are no locations for which data is only available for 45° or 135° regions—although for Reiner Gamma there is only comparable data for 0° azimuthal angle; but this plane is already included in our requirement as driven by the Hapke BRDF model. To further deduce the requirements for the reflectance, incidence and azimuthal angular ranges, let us turn to the O3DTM, into which our VOSEG-measured BRDFs will be inputted in accordance with aim A4 and goal G4.

3.3.5 Requirements from Thermal Models

Theoretically, considering a 3D thermal model must predict how regions of the lunar surface scatter light and reradiate heat onto all adjacent areas of regolith, ideally, scattering function inputs would be measured in the laboratory for all angles of the scattering hemisphere. However, due to temporal and spatial constraints (i.e., the goniometer sits within a vacuum chamber), this is not experimentally possible. Therefore, the angular requirements derived for VOSEG from thermal model scattering inputs must be driven by the question: What is the minimum angular range necessary, beyond which the rest of the curves can be extrapolated using polynomial functions or the Hapke BRDF model? For the reflectance angle range, to extrapolate a given BRDF curve reflectance angles of 0-65° must be measured (see **Figures 19**, **20** and **31**). For the incidence angle requirement, measuring as extreme angles as possible is particularly useful when attempting to model PSRs. This is, naturally, due to the extreme angles created between the topographies of the cratered lunar surface and the sun, for high-latitude (>60°) regions. Considering high-latitude regions are those >60°, the minimum requirement on the range of measurable incidence angles using VOSEG can be set as 0-60°. Beyond this region, as was done in (Foote *et al.*, 2020), BRDF curves can be extrapolated by 1) fitting the Hapke BRDF model to the measured data and

deducing best fit Hapke parameters, then 2) running the model for the higher angular regions, using the best fit parameters as inputs.

Aim A4 of this project is to input scattering functions within the O3DTM, which incorporates azimuthal variations into the modelling process. Therefore, if azimuthal angles are to be incorporated, it is necessary not only to measure BRDFs in the principal and out-of-principal planes, but also in the diagonal plane. If these planes are measured, the data can be trilinearly interpolated using the Hapke BRDF model to produce complete scattering hemisphere BRDFs. These BRDFs can be used as inputs for the O3DTM, and will have been derived from fitting Hapke BRDF model best fit curves to the laboratory data. Due to Helmholtz reciprocity/Kirchoff's Law, if one side of the out-of-principal or diagonal planes is measured, the other side can be deduced by mirroring the appropriate data (Greffet and Nieto-Vesperinas, 1998). Therefore, if a BRDF dataset is measured for 0/45/90/135^{o} and 180^{o} planes, it can be mapped out over a sample's complete scattering hemisphere; i.e. at 0, 45, 90, 135, 180, 225 and 270°. **This derives the azimuthal angle range for the VOSEG setup as 0-180° in steps of 45°, i.e. 0, 45, 90, 135 and 180°.**

To summarize: 1) to corroborate (Foote *et al.*, 2020)'s measured BRDFs (goal G1); 2) to test the Hapke BRDF model (with and without the surface roughness shadowing function) (goal G2); 3) to compare the laboratory measured BRDFs to Diviner off-nadir data (goal G3); and 4) to measure BRDFs which can be extrapolated, and then inputted into thermal models (goal G4), VOSEG requires the capability to measure low phase angles (<10°), high reflectance angles (up to at least 65°), incidence angles up to 60°, and azimuthal angles 0, 45, 90, 135 and 180° (at least).

One final requirement which must be mentioned is that of the experimental uncertainty/error within the BRDF data which derives from various factors, including chopper frequency drift

and light source instability. In Part 4.1.1 it is ascertained that for 1° viewing angle changes the Hapke BRDF model predicts BRDF variations of up to 3% and so the measured uncertainty/error must be less than this value. **Hence, our maximum light source stability uncertainty can be derived to be <3% of the measured BRDF data.** Furthermore, Hapke BRDF model predicts changes in BRDF ≤3% for viewing angle changes <1°, without this study's parameter space. To ensure that uncertainties in viewing angles do not lead to greater errors than those deriving from light source and chopper instabilities, the reflectance, incidence and azimuthal angle uncertainty requirements will be set as ≤0.33°, each. The above is summarized in the requirement table, **Table 9**.

Requirement	***Value***
Reflectance angle range	At least 0-65°, in 5° steps
Uncertainty in reflectance angle	≤0.33°
Incidence angle range	At least 0-60°, in 15° steps
Uncertainty in incidence angle	≤0.33°
Azimuthal angle range	0-180°, in 45° steps
Uncertainty in azimuthal angle	≤0.33°
Minimum phase angle	At least 5°
Light source stability and chopper frequency drift	<3%

Table 9: Requirement table for the Visible Oxford Space Environment Goniometer setup.

Now our experimental requirements are set out, the VOSEG instrument which was developed for this study can be described. Furthermore, the experimental tests which were carried out in order to validate VOSEG's BRDF measurements can be detailed, and finally the methodologies used to measure the porosity values and surface roughness profiles of the Apollo regolith samples used in this study can be outlined.

4 Updates to the Oxford Space Environment Goniometer and Preparation for the Visible-λ BRDF Study

This chapter details the various modifications made to the OSEG instrument in order to develop the visible-wavelength goniometer, VOSEG, in accordance with aim A1 and goal G0. It then details the experimental tests performed using the newly developed instrument, which demonstrate its utility as a goniometer, and goes on to present the instrument's experimental capabilities, in Part 4.5. Furthermore, in Parts 4.3 and 4.4, it defines how the porosity and surface roughness measurements of the Apollo samples were taken. These measurements, alongside the automated BRDF goniometry measurements, form the basis of the measured dataset and are performed using novel techniques, so their methodologies must be detailed.

4.1 Development of the Visible Oxford Space Environment Goniometer

VOSEG was developed by modifying the existing OSEG system, documented in (Warren *et al.*, 2017). The original OSEG setup, as shown in **Figure 28**, already had the capability of measuring reflectance angles between 0-70° and azimuthal angles between 0-360°, although no 'out-of-principal plane' measurements had been taken with the instrument, and so the capability to measure at and define such angles must be added, in line with our requirements (**Table 9**). Furthermore, OSEG's existing incident light source setup could only measure down to 6° phase angles, and up to 45° incidence angles, which are insufficient ranges for our requirements. Furthermore, OSEG's original optical setup led to measured BRDFs which were not in agreement with other goniometer systems (within experimental error). Therefore, the first modifications made to the OSEG system aimed to 1) devise a simple, time-efficient method for varying and defining VOSEG's azimuthal angle, for the

out-of-principal/diagonal planes; and 2) develop an optical setup (i.e. light source/detector/chopper/baffle etc.) which meets the requirements set out in Part 3.3.

4.1.1 Varying and Measuring Azimuthal Angles

To measure BRDFs at the azimuthal angles defined within our required experimental range, a method must be found for accurately calculating the angle between the radiometer carriage arm and the incident light source to within ±0.33°. This is because the Hapke BRDF model predicts <3% changes in BRDF across this change in angle for the combined viewing angles measured in our study, and 3% is the acceptable uncertainty in the measured data (see Part 4.5). Hence, to calculate VOSEG's θ_a, a USB camera which looks down at the goniometer system was attached to the roof of the cold shield. Then, as demonstrated in **Figure 33**, two coloured circles were printed on paper and were glued to the top of the radiometer carriage so that the line between their centres was parallel to the direction in which the radiometer carriage moves (i.e. the azimuthal angle).

Using this setup, VOSEG's θ_a can be determined by capturing an image and loading it into a code which calculates the angle between the light source's line of incidence and the radiometer carriage. The angle calculated by this method corresponds to θ_a. The angle can be varied using the motors on the azimuthal angle arm and can be calculated using a code, until the desired angle is achieved, to within ±0.1°. Using this method, it is possible to determine VOSEG's azimuthal angle across the full angular range (0-360°) to within an accuracy of ±0.1°, which derives from the error in making the lines exactly parallel to the reflectance and incidence angle arms of the goniometer.

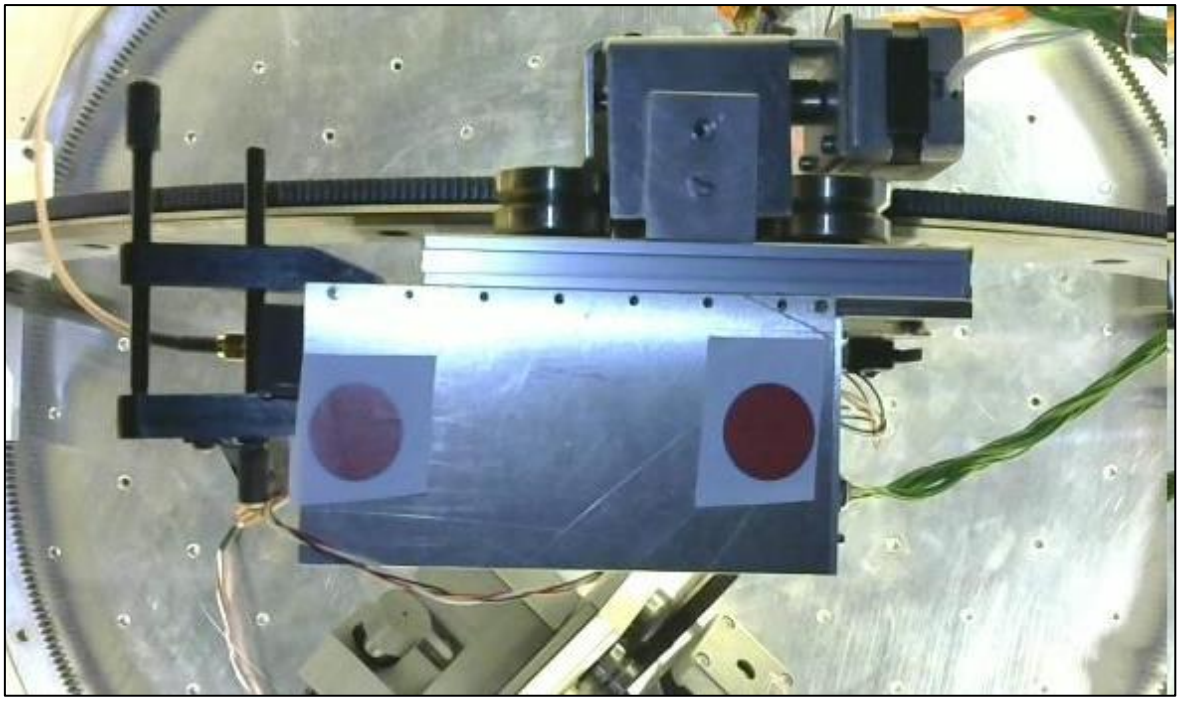

Figure 33: Demonstrating the printed coloured circles which are used to define the azimuthal angle of the Visible Oxford Space Environment Goniometer.

4.1.2 Modifying the Optical Setup of the Incident Light Source and the Detector

As explained in Part 4.1, the original OSEG TIR setup was adapted, and a new optical setup was developed which included an incident visible-λ light source and a photodiode detector. The angular requirements derived in Part 3.3 guided the development procedure, as did the necessity for VOSEG to be able to take BRDFs measurements which agreed with other similar visible-wavelength goniometer systems, such as BUG (Johnson, 2008).

OSEG's original radiometer carriage contained a right-angled mirror, which directed TIR radiation towards a detector. This detector was replaced with a visible-λ photodiode with a broadband wavelength range (RS Components—BPW21R), as shown in **Figure 34**.

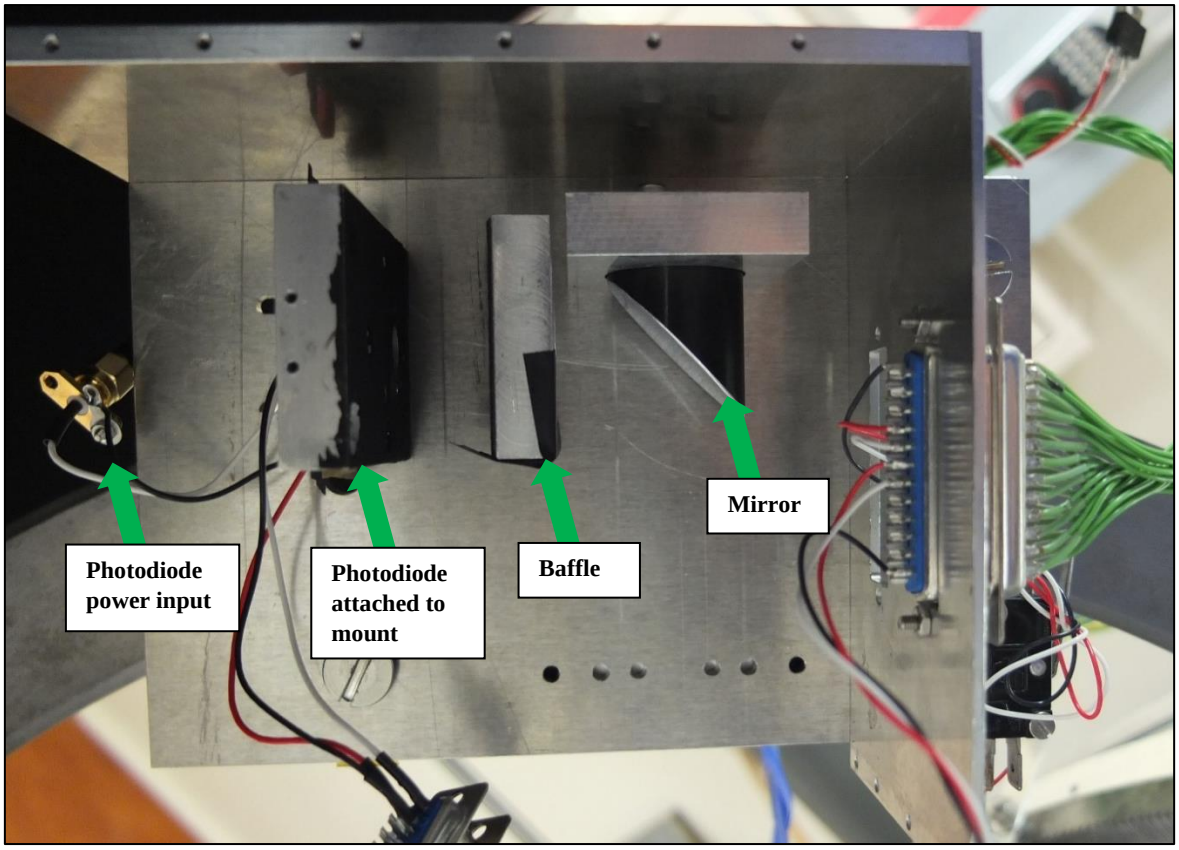

Figure 34: Showing the original Oxford Space Environment Goniometer's radiometer carriage setup, which contained a mirror, a baffle (to constrict the field of view), and which was uncovered. The photodiode was added for VOSEG.

Using this setup led to aberrations in measured BRDFs, due to a gaussian FOV being created by the mirror. Therefore, for the new VOSEG setup the mirror has been removed, and the photodiode has been mounted so that it looks straight down at the sample. Furthermore, a Nextel-painted 15x60x75 mm aluminum baffle plate has been mounted below the photodiode and the whole region which houses the photodiode is covered in black card, to reduce the signal from incident stray light to less than the uncertainty from the chopper frequency drift. These modifications are shown in **Figure 35**.

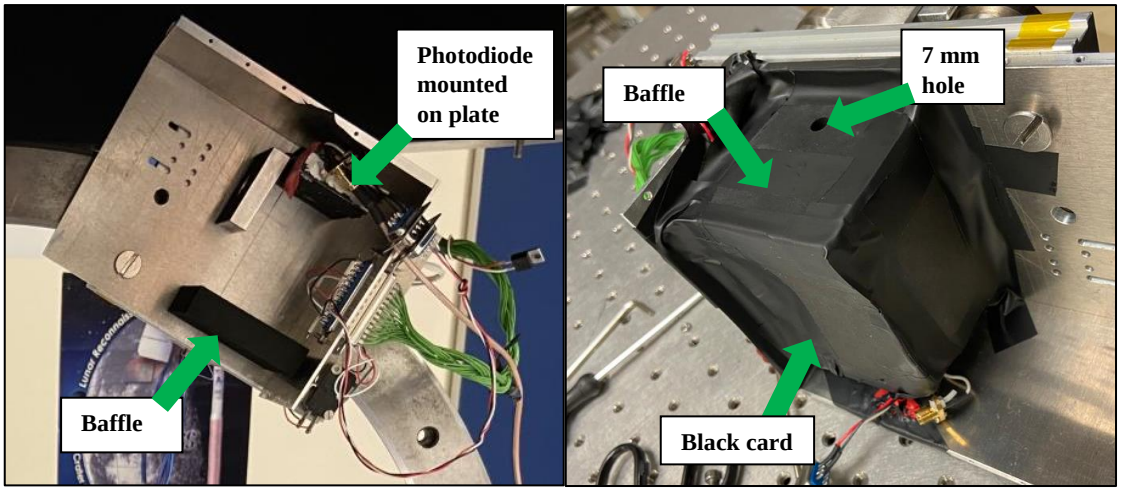

Figure 35: Left: showing the Visible Oxford Space Environment Goniometer's updated radiometer carriage, which has no mirror and within which the photodiode is mounted so that it is looking straight down at the sample. A Nextel-painted baffle, which has a 6.2 mm-diameter hole in it, is mounted at 65 mm below the photodiode, so that the field of view at the height of the target is a circle with a 20 mm diameter. Right: showing how the housing for the photodiode is covered using black card and tape, to reduce the amount of stray light incident on the photodiode.

The baffle plate is mounted so that the sample-side hole is at a distance of 65 mm from the photodiode, and it has a 6.2 mm-diameter hole in it, to constrain the photodiode's field of view (FOV) at the sample's surface to a 20 mm diameter circle (see Part 4.2.1). The distance between the target and the photodiode is ~310 mm. Considering the detector's FOV within the new setup is a 20 mm-diameter circle at the standard target height of 310 mm from the photodiode, let us now describe the development of VOSEG's incident light source setup—which produces a uniform illumination spot which does not exceed the FOV, at any angle of incidence. (The design choice of having a FOV which is larger than the illumination spot is due to the difficulty in producing a uniform spot of light.)

The modified incident light source setup was developed for VOSEG which enables low phase angles ($<5^{\circ}$) to be measured, and which produces a uniform illumination spot that does not exceed 20 mm at any angle of incidence, up to 60°. This updated incident light setup can be split into three parts: The fiber optic cable holder, the three-stage baffle, and the light source.

Firstly, a ‘slim-line’ (7 mm outer diameter) fiber optic cable holder was developed, which enabled the setup to measure phase angles down to 4°—and hence, to measure a more substantial part of the opposition effect. This new cable holder does not obscure the detector at any angles other than $\theta_p < 4^{\circ}$.

Secondly, a three-stage baffle was designed and built, which attached to the end of the fiber optic cable/to the cable holder, and at one end has a 1 mm-diameter hole in it; hence, the three-stage baffle restricts the spot size to a maximum of ~9 mm (effective outer diameter), when looking straight down (i.e. $\theta_i = 0^{\circ}$). 9 mm is the target spot size at $\theta_i = 0^{\circ}$, because when the VOSEG setup measures at 60° incidence angles, the illumination spot will become ellipsoidal and will increase its width to 18 mm (as, 9 mm x $\cos(60)$ = 18 mm). The FOV of the detector setup is ~20 mm and the spot must not exceed the FOV—hence, ~18 mm is a safe maximum spot size, which will illuminate as much of the sample as possible without exceeding the FOV (with a tolerance of ~10%). The baffle is made in two parts which are slotted into one another, as shown in the drawings in **Figure 36**.

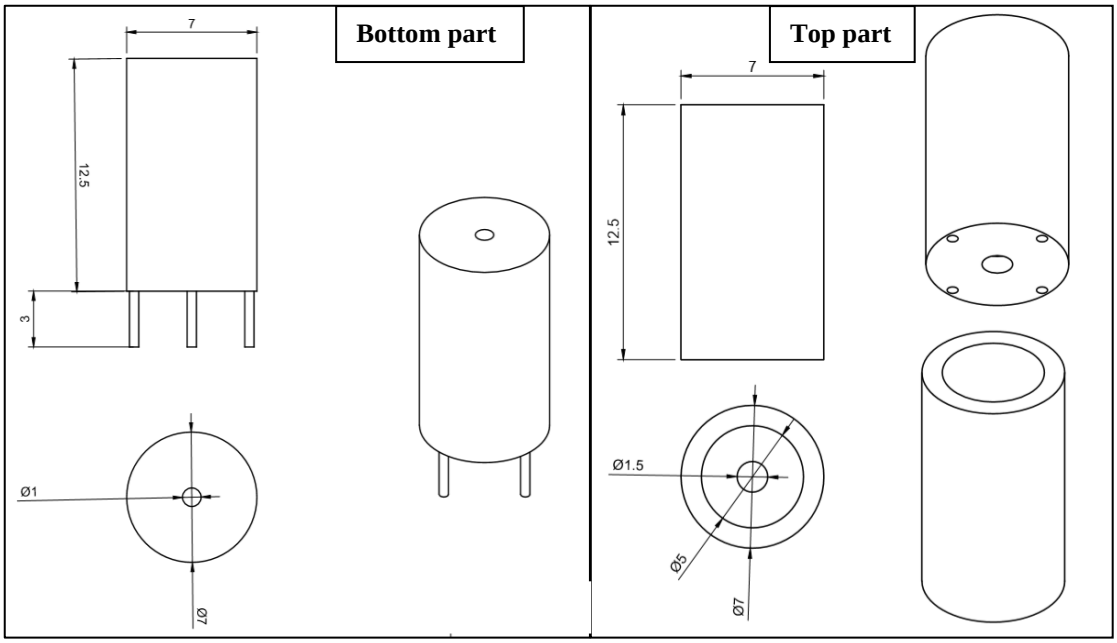

Figure 36: Left—bottom part of the light source baffle. Right—top part of the light source baffle. The 3 mm legs of the bottom part slide into the holes in the top part. Dimensions are given in mm.

The third part of VOSEG's updated incident light setup is the light source used itself. For the updated VOSEG setup, BRDF measurements can be made using any light source, provided it can be coupled to the optical fiber. In this project, BRDF measurements were either made by illuminating the surface of a sample with a beam of diode laser light, from a green laser such as the ThorLabs CPS532 (ThorLabs, 2013), which outputs light at 532 nm (near the peak wavelength of the Sun's power output maximum), or by illuminating the sample with light from a Quartz-Halogen broadband light source, such as a Bentham IL1 (350-4000 nm), which has a stabilised power output (Bentham, 2017). Having the capability to switch between either light source enables both narrow-band measurements to be taken—for studies such as the one mentioned in Part 2.2—and broadband (350-1250 nm) measurements to be taken (such as in (Foote *et al.*, 2020)), which can be compared to Diviner visible-λ off-nadir data (350-2800 nm) (see Part 1.2.3).

Beyond the modifications detailed above, the rest of the original OSEG setup remains unchanged. Thus, before propagating down the fiber optic cable, the beam of light is chopped. The chopped beam illuminates the target, which scatters light towards the photodiode housed in the radiometer carriage. Then, the voltage output of the photodiode passes into a lock-in amplifier (SR830–Stanford Research Systems), within which it is demodulated from the voltage output of the chopper reference signal. Chopping the light—typically at 130 Hz, away from the natural frequency of the lighting in the laboratory—and using the lock-in amplifier (referenced to 130 Hz) removes the signal due to background light. Finally, the output signal is recorded using a control code on a PC.

In summary, the updated VOSEG system shown in **Figure 37** is an automated three-axis goniometer, which allows variation of incidence, reflectance and azimuthal angles. MATLAB (Version 2020a) control codes (written by the author) are used to give the goniometer instructions on how to move, for each required viewing angle, using a computer

setup beside the goniometer. BRDF measurements over a range of scattering geometries are possible: up to 60^{o} incidence, up to 70^{o} reflectance and down to ~4° phase angles. The reflectance and incidence angles are determined using a Mitutoyo 950-317 digital protractor, which has an accuracy of $\pm 0.1^{\circ}$ Using either a broadband light source (i.e. a Bentham IL1), or a 532 nm laser (i.e. a Thorlabs CPS532), it is possible to measure BRDFs with VOSEG at broadband or narrowband wavelengths.

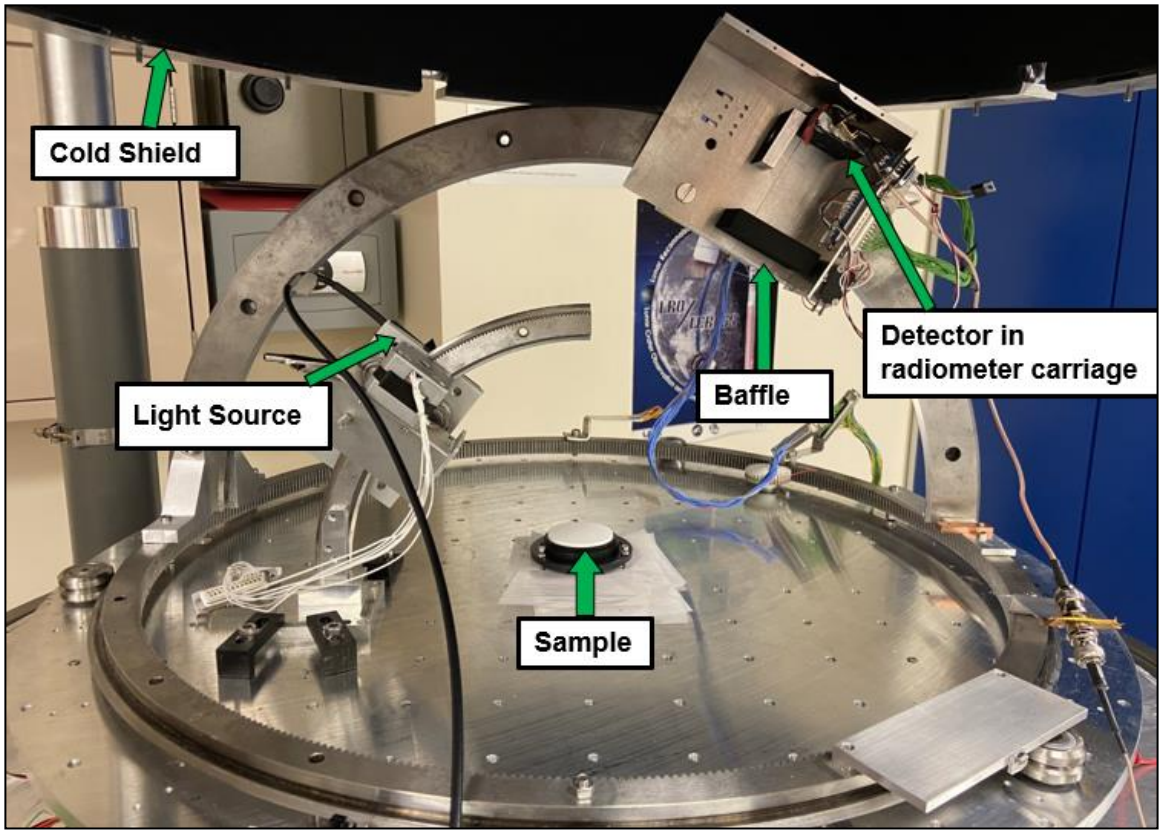

Figure 37: The Visible Oxford Space Environment Goniometer (VOSEG) with major parts labelled, before the black card covering was fixed to the radiometer carriage.

To develop the VOSEG instrument, and to prove its utility as a visible-λ goniometer at the viewing angles required for our BRDF study, various experimental tests were performed. These included 1) mapping the illumination spot and FOV, 2) testing the height and tilt sensitivities of the setup, and 3) observing how the polarization of the green laser affects the measured BRDFs. Each of these tests are described below in Part 4.2. Then, to categorically demonstrate VOSEG's ability to measure a usable BRDF dataset for our study,

measurements of the reflectance standard material White Spectralon® were taken, and how these compare with BUG is described in Part 4.2.5. White Spectralon® is a well-characterised commercial fluoropolymer which is used as a reference calibration standard for BRDF studies—as it has a certified, known, visible phase function (Labsphere, 2017)—and which was measured by BUG in preparation for (Foote *et al.*, 2020).

4.2 Test Datasets

For each of the test datasets detailed in Parts 4.2.1, 4.2.2, 4.2.3 and 4.2.5, the results were equivalent for both the broadband and the green laser light sources; although the uncertainty in the green laser data was generally higher, and this will be explained in Part 4.5. The figures included in these three parts show measurements made using the broadband light source, as it is this setup which forms the basis of the experimental dataset used in Parts 5 and 6. However, Part 4.2.4—which details the green laser polarisation study—shows data taken using the green laser setup.

4.2.1 Illumination Spot and Field of View

VOSEG's FOV was measured by moving a pinhole of light, created by mounting a baffle with a 1 mm outer diameter hole in front of the laser, across the detector FOV in the x- and y-directions using a three-axis stage. A 2D slice (i.e., the x-direction measurements) of the circular FOV of the detector-baffle setup is shown in **Figure 38**, with dotted lines showing one standard deviation from the centre. The effective FOV is ~20 mm. An ideal FOV would be as flat as possible—i.e. a 'top hat'.

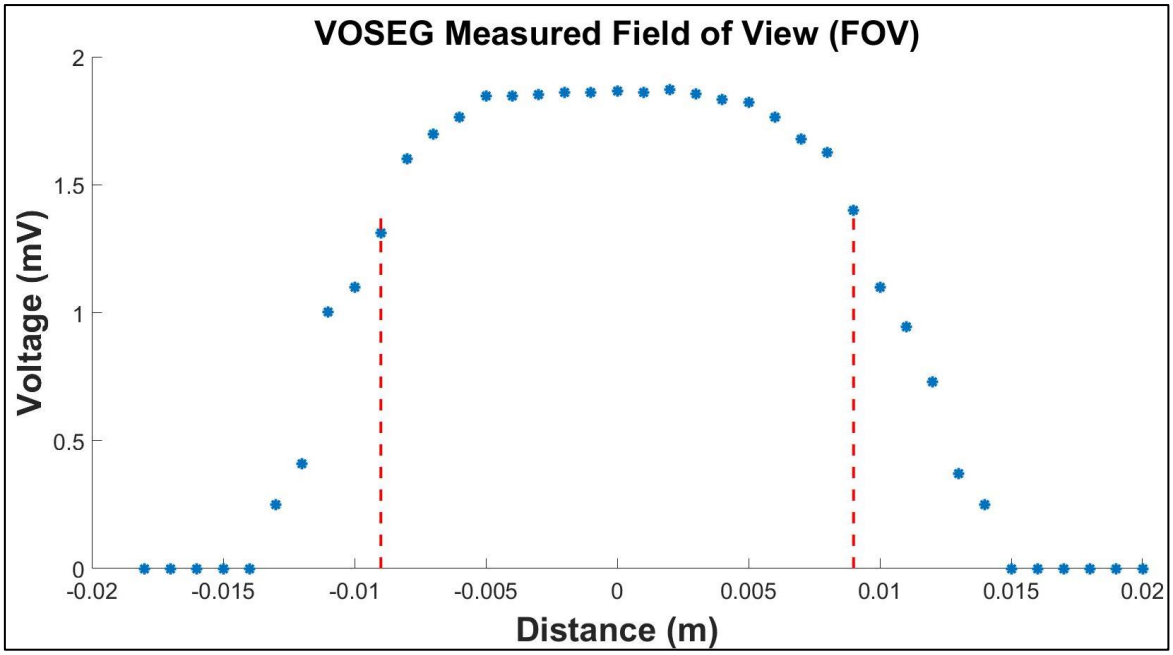

Figure 38: A 2D slice of VOSEG's measured field of view. Blue data points are the measured voltages in millivolts and the red dashed line indicates the effective field of view (e.g., one standard deviation from the centre). Data taken using VOSEG's broadband light source.

The baffle plate attached to VOSEG's radiometer carriage restricts the FOV of the detector to a ~20 mm diameter circle, and this setup—as shown by the agreement between VOSEG and BUG in Part 4.2.5—reduces the contribution from stray light in the lock-in output signal to <1% of the measured BRDF. For our desired lunar regolith BRDF study, the effective spot size must be as large as possible, without exceeding the FOV, to sample as much of the regolith surface as possible. Additionally, the illumination spot must be in the centre of the detector's FOV. If this is not the case, the detector will measure an off-centre region of the illuminated spot, and this will lead to systematic errors in VOSEG's BRDF data. To ensure the full illumination spot is within the FOV at all incidence angles (0-60°), the effective illumination spot must be mapped, and kept to a size of 10% less than the detector's FOV. This is because the illumination spot is aligned to be within the centre of the FOV for each experimental run, and there is an uncertainty in this alignment of ±1 mm, which corresponds to ±5% of the detector's effective FOV. If the effective spot size at 60° incidence angle—which is the maximum spot size, as the lobe increases with $\cos(\theta_i)$—must be kept to 18 mm

(10% less than 20 mm), then at 0° incidence, this spot must have a maximum size of 9 mm (i.e. 18 mm/cos(60)). At 15° incidence, the effective spot size must be a maximum of 9.318 mm (i.e. 9 mm x cos(15)), and so on. **Figure 39** shows the mapped illumination spot for the VOSEG setup at 15° incidence. Using a three-axis stage, the spot was mapped by illuminating the sample whilst the detector FOV was constrained to 1±0.1 mm using a pinhole baffle. The detector was then moved along the x- and y- planes 0.5±0.1 mm at a time. The spot has an effective size of 8.7±0.2 mm and therefore, the spot size at 60° incidence angle will be 17.4±0.4 mm, which is within the desired range. It is not possible to map the spot at 0° incidence, as the light source obstructs the detector.

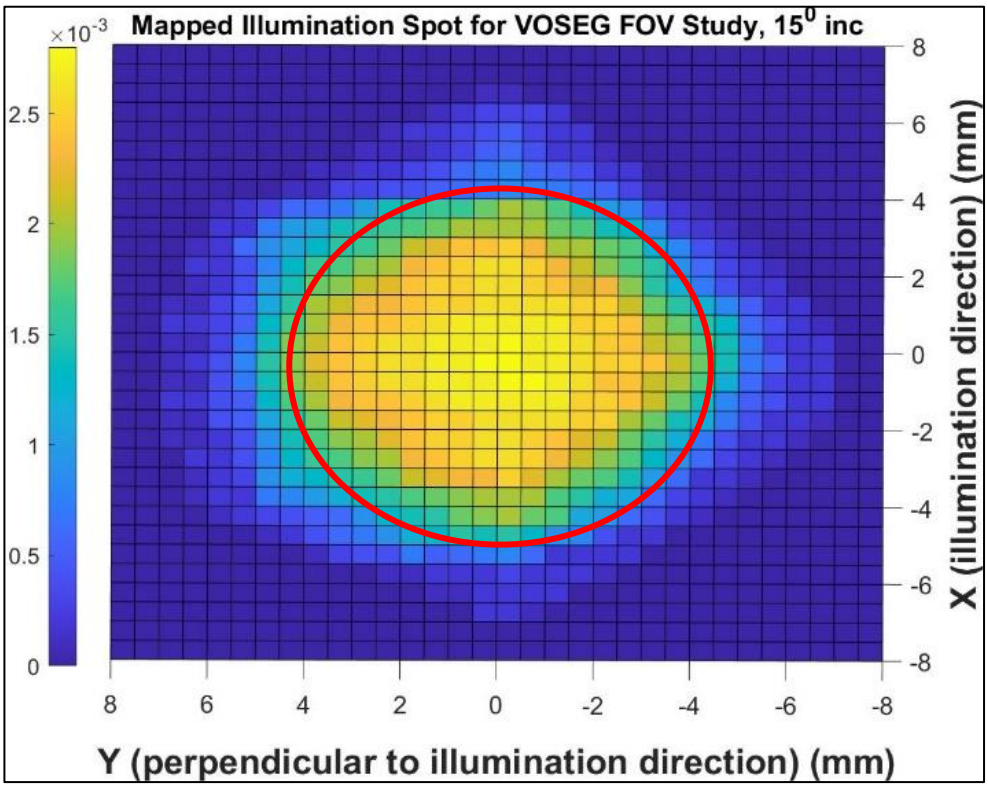

Figure 39: The illumination spot at 15° incidence angle mapped for VOSEG. The red line shows the effective spot size (8.7±0.2 mm) and the z-axis denotes the measured voltage, in V. Data taken using VOSEG's broadband light source.

In summary, the illumination spot becomes ellipsoidal with the semi-major axis, as illustrated in **Figure 40**, and increases to 17.4±0.4 mm at 60° incidence, which is within the upper limit of the ~20 mm FOV of the radiometer carriage setup.

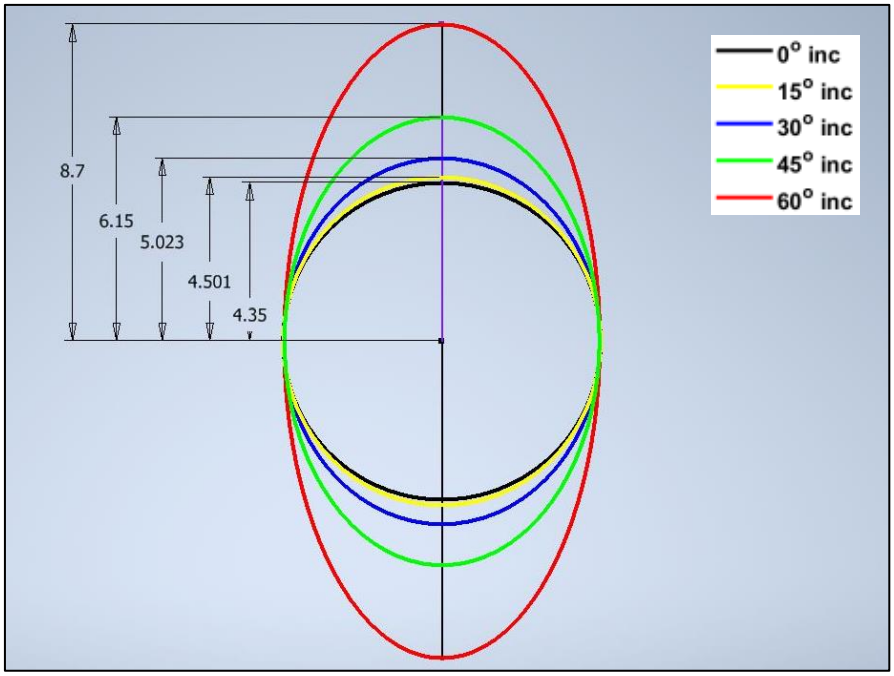

Figure 40: Illustrating how the illumination spot size and shape change with incidence angle variation.

Therefore, the illumination spot and FOV test is complete. However, two factors which may affect the alignment of the illuminated spot with regards to the FOV are the height and tilt of the White Spectralon® calibration target. Hence, tests were carried out to determine VOSEG's sensitivity to height and tilt variations, and these are described in Parts 4.2.2 and 4.2.3 respectively.

4.2.2 Height Study

For the height sensitivity study (where height is defined as the distance between the base plate and the top of the sample cup), the White Spectralon® target was first levelled using a spirit level and set to 24.0±0.3 mm above the base plate of VOSEG. During a measurement run, the tilt does not typically change >0.1°. However, the tilt is checked—and readjusted, if needed—before each measurement run. BRDFs were then measured at 60° incidence angle and over 0° to 70° reflectance angles, for five heights—24.0±0.3 mm, 25.0±0.3 mm, 26.0±0.3 mm (optimum), 27.0±0.3 mm and 28.0±0.3 mm above the base plate—in 1 mm steps. For each experimental run, the height of the White Spectralon® target is measured

using calipers, however, the human error in this method can lead to variations in height of up to ~±0.3 mm.

The optimal height was determined to be 26±0.3 mm before the study, by observing the output of the lock-in amplifier and noting the height at which the signal was at a maximum, when θ_r=0. This was used as the centre height of the study. **Figure 41** shows BRDF measurements of White Spectralon® made by VOSEG for the five heights in this study. It also shows BRDF measurements made by BUG of White Spectralon®, which are measurements VOSEG must match, to within one standard error—calculated as the standard deviation over three measurements—to ensure it agrees with other visible-λ goniometers used in previous planetary photometry studies.

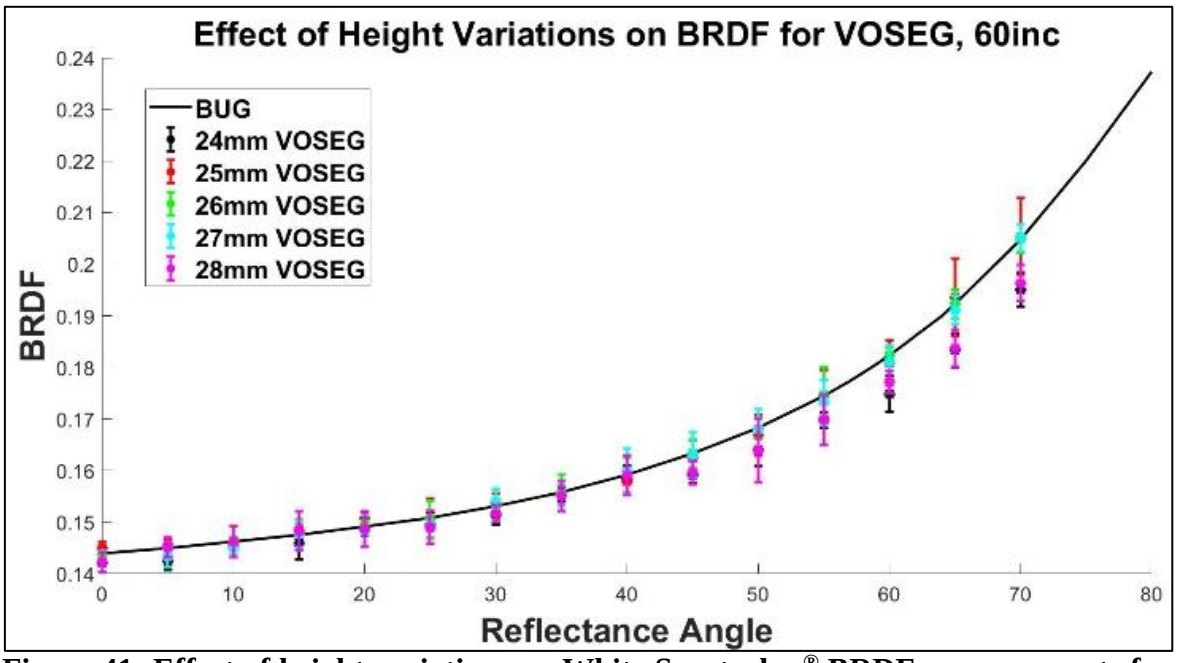

Figure 41: Effect of height variations on White Spectralon® BRDF measurements for VOSEG, at 60° incidence angle, for five heights: corresponding to surfaces at 24.0±0.3, 25.0±0.3, 26.0±0.3, 27.0±0.3 and 28.0±0.3 mm above the base plate; and comparable Bloomsburg University Goniometer (BUG) measurements of White Spectralon®. Data taken using VOSEG's broadband light source.

Figure 41 shows that variations in the height of the White Spectralon® calibration target of <1 mm do not introduce variations in BRDF which are larger than the standard error in the measurements. Therefore, the height variation must not vary by >1 mm over one

experimental run, for the calibration target. Height variations larger than this lead to the illuminated spot drifting from within the centre of the FOV, which, for 60° incidence angle will lead to systematic errors in the measurements of White Spectralon®.

4.2.3 Tilt Study

White Spectralon® BRDFs were measured for a level surface, then for forwards-, backwards-, left- and right-tilted surfaces. To set the tilt, an analogue spirit level was used (to avoid damaging the target) and a backwards tilt was defined as towards 0° azimuthal angle. First, the surface was levelled, and then screws were tightened or loosened on the stage which holds the White Spectralon® target, to adjust the tilt until the spirit level bubble reached a mark which denoted 2°—as determined by comparing the analogue spirit level to the digital spirit level—in whichever direction was required. This resulted in angular variations of 2.00±0.05°, as shown in **Figure 42**.

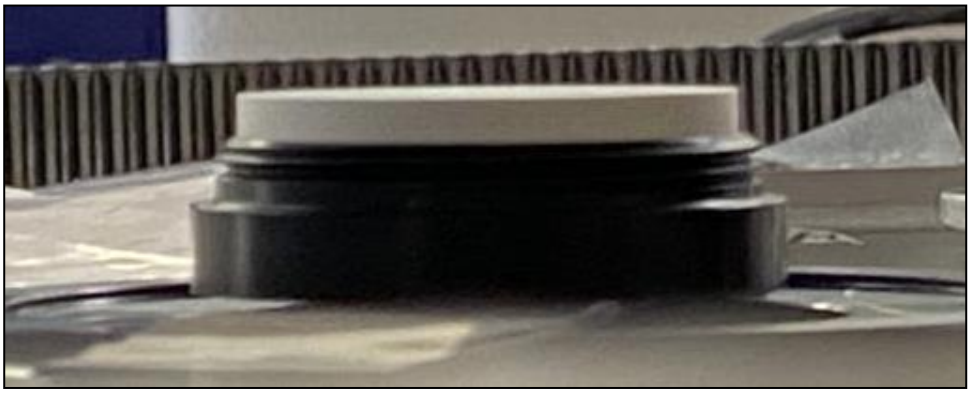

Figure 42: White Spectralon® tilted 'backwards' (i.e. towards 0° azimuthal angle) by 2.00±0.05°.

The initial height was set to 26.0±0.3 mm above the goniometer surface, as determined in Part 4.2.2. The results of the tilt study are shown, alongside the BUG BRDF measurements for White Spectralon®, in **Figure 43**.

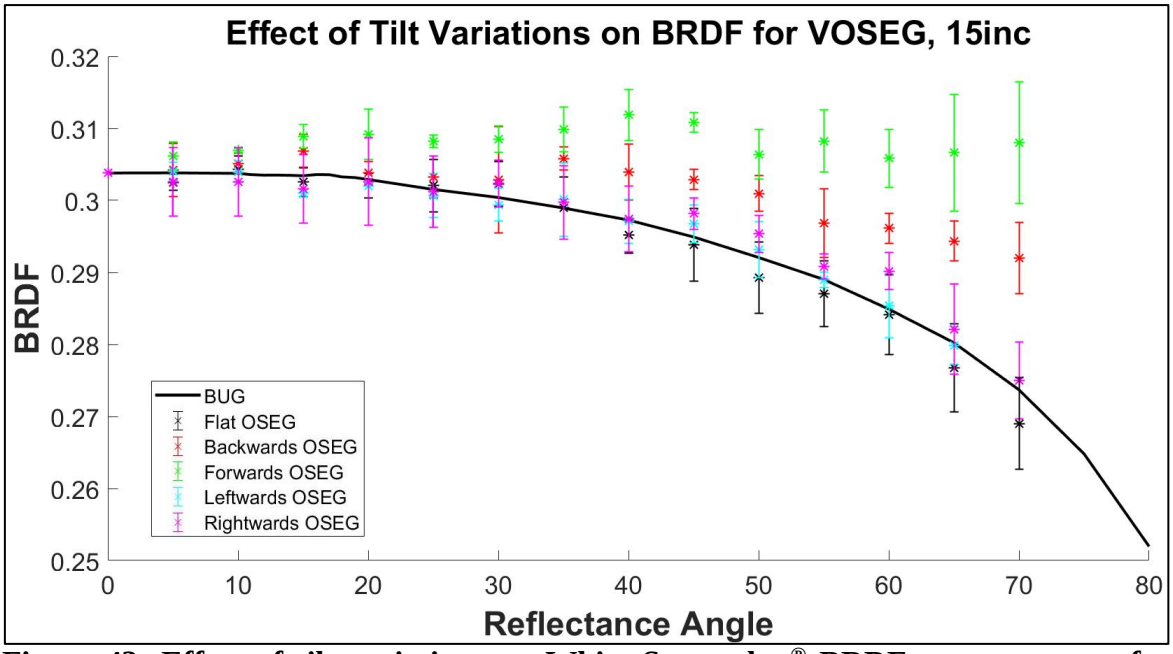

Figure 43: Effect of tilt variations on White Spectralon® BRDF measurements for VOSEG, at 15° incidence angle, for five tilts: corresponding to flat, backwards-tilting, forwards-titling, leftwards-tilting (i.e., 90° azimuthal angle) and rightwards-tilting (i.e., 270° azimuthal angle) surfaces; and comparable Bloomsburg University Goniometer (BUG) measurements of White Spectralon®. This figure shows BRDFs with no angular post-processing, i.e. assuming reflectance angles 0/5/10…70°. (Normalised at 0° reflectance angle to BUG.) Data taken using VOSEG's broadband light source.

To show how post-processing can resolve this issue—as done with measurements taken by the PHIRE-1 and PHIRE-2 goniometer systems (Gunderson, Thomas and Whitby, 2006)—2° reflectance angle changes can be incorporated into the BRDF calculations (i.e. using cos(2/7/12…72°) instead of cos(0/5/10…70°) to calculate the angular drop-off of the curve). This is possible because the VOSEG setup's FOV is larger than the size of the spot illuminating the sample. The corrected BRDFs of the flat, and tilted BRDF measurements are shown in **Figure 44**, and all agree with BUG within one standard error.

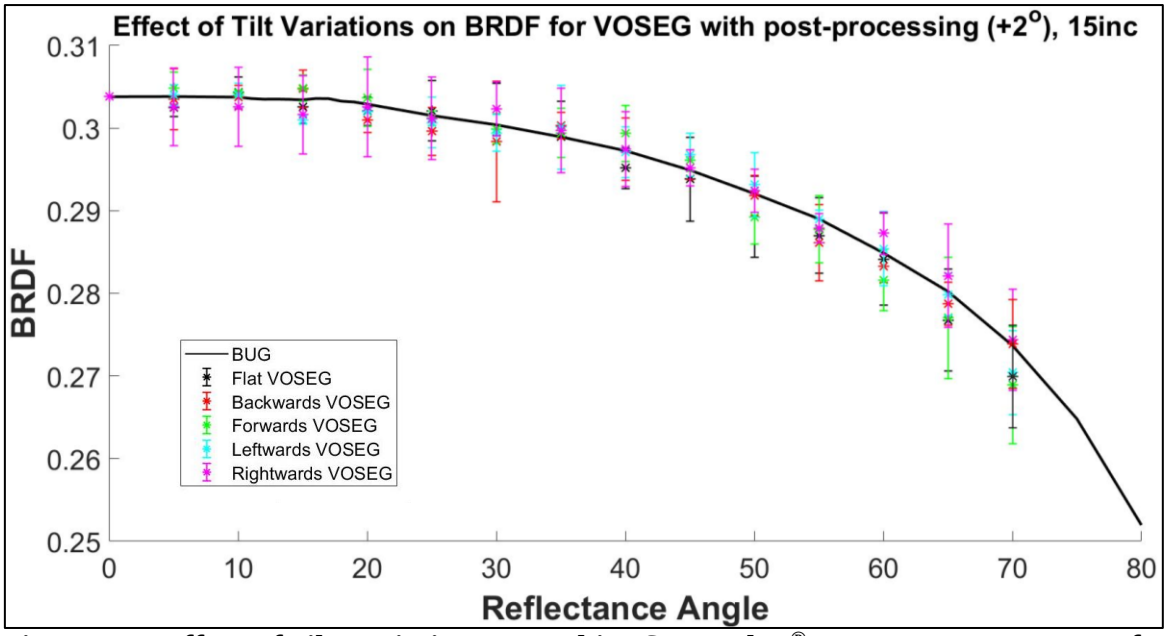

Figure 44: Effect of tilt variations on White Spectralon® BRDF measurements for VOSEG, at 15° incidence angle, for five tilts: corresponding to flat, backwards-tilting, forwards-titling, leftwards-tilting and rightwards-tilting surfaces; and comparable Bloomsburg University Goniometer (BUG) measurements of White Spectralon®. NB: this figure shows BRDFs with angular post-processing: i.e. 2° angular variations are used within the BRDF calculation, using cos(2/7/12…72°) as opposed to cos(0/5/10…70°). (Normalised at 0° reflectance angle to BUG.) Data taken using VOSEG's broadband light source.

It is clear that for well-aligned BRDF measurements to be taken, sample surfaces must be at a height of 26±0.3 mm above the base plate, with variations no larger than 1 mm; and must not have any significant (>1°) tilt to them relative to the measurement plane (i.e. the sample stages must be levelled using a spirit level before each run), or else post-processing must remove the effect on BRDFs due to tilting. Any more than 1 mm height variations, or 1° tilt variations, leads to BRDFs which are not in agreement with BUG measurements, within measured error (~2-5%). VOSEG's requirements can therefore be updated to include: tilt control of <0.5° for each experimental run, or else post-processing must be done; height-control of <1 mm over each experimental run to ensure BRDF variations of <2% (which is within the average uncertainty due to the chopper's frequency drift); and locational variations of the illuminated spot which are <1 mm, to ensure the spot is within the FOV for all incidence angle measurements.

4.2.4 Green Laser Polarization Study

According to its datasheet, the green, 532 nm Thorlabs CPS532 laser which is used in the VOSEG setup produces elliptically polarised light, with a polarisation ratio of 4 dB (ThorLabs, 2013). Before any systematic errors in the VOSEG measurements—which led to disagreements with BUG, within standard error—were attributed to stray light and spot position, the polarisation of the laser was studied. It was suspected that the polarisation of the laser could lead to variations in White Spectralon® BRDFs, in particular for high phase angles, as described in the Hapke BRDF model. To test whether the polarisation of the laser was the contributing factor to the systematic error, the following test was performed across 15-60° incidence angles in the 180° azimuthal angle part of the principal plane (where the effect is maximised): 1) BRDFs were measured using the standard green laser setup; 2) an S-polarising filter was added to the setup, and BRDFs were measured; 3) a P-polarising filter was added to the setup, and BRDFs were measured. Then, finally, 4) the data was analysed to determine whether adding the S- and P-polarised BRDFs together produced the same curve as the BRDFs measured with no polarising filter added. If the added curves produced the same result as the 'no-filter' setup, then polarisation could have contributed to systematic errors in the setup. However, this was not the case, and so polarisation was ruled out as the contributing issue. **Figure 45** shows an example of results from the polarisation study, for 45° incidence.

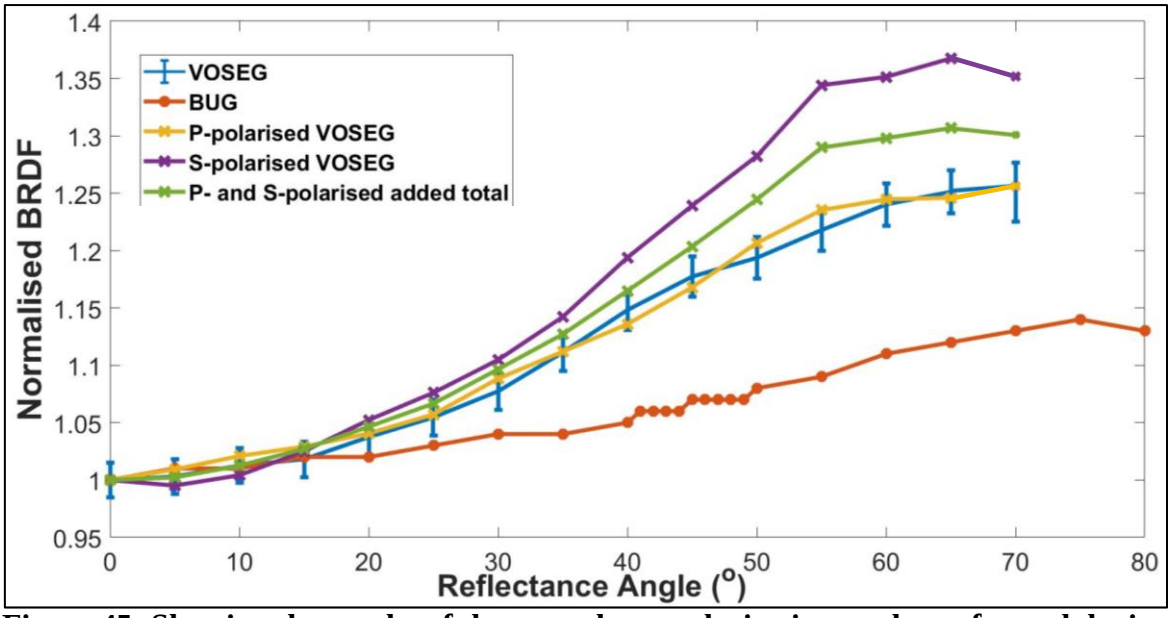

Figure 45: Showing the results of the green laser polarisation study performed during the development of VOSEG's optical setup, for 45° incidence angle and at 180° azimuthal angle. A Thorlabs CPS532 laser was used in the VOSEG setup to measure BRDFs for White Spectralon® with 1) no filter, 2) an S-polarising filter, and 3) a P-polarising filter. These BRDFs were then compared to BUG, to determine whether the polarisation of the laser was a determining factor in the systematic errors observed between VOSEG and BUG.

Figure 45 shows how the polarisation of the laser was not the cause of the systematic errors in VOSEG's BRDF, which led to errors in VOSEG's measured BRDFs—when compared to BUG—which were greater than the standard error. It was only once the steps to improve the optical setup—as detailed in Parts 4.2.1, 4.2.2 and 4.2.3—were taken that VOSEG's BRDF measurements of White Spectralon® began to agree with BUG, within standard error for both the green laser and the broadband light sources. This suggests that stray light was the source of the systematic errors in VOSEG's BRDFs, before the modifications detailed in Part 4.1.2 were made.

In summary, to ensure VOSEG's optical setup was well-aligned—so that its BRDF measurements matched other goniometer systems, such as PHIRE-1, PHIRE-2 and BUG—its illumination spot and FOV were mapped. and tests were performed to determine the tilt and height sensitivity of the setup. Furthermore, for the laser setup, how polarization affected the BRDF measurements of White Spectralon® was also studied. It was only once the

VOSEG setup was optimized using these tests that VOSEG's measured BRDFs of White Spectralon® matched BUG (and other goniometer systems), to within VOSEG's experimental error. These calibration measurements are described in Part 4.2.5.

4.2.5 White Spectralon® Measurements

Since the illumination spot, FOV, height and tilt studies were performed and the setup was modified as in Part 4.1, VOSEG's BRDF measurements for the diffuse, certified Lambertian reflectance standard, White Spectralon® (Labsphere, 2017), are in agreement with those made by BUG, within standard error (Johnson, 2008). BUG measured White Spectralon® for the (Foote *et al.*, 2020) BRDF study as a reference target and hence, VOSEG is also calibrated by taking reflectance measurements of White Spectralon®. With VOSEG, BRDF measurements of samples are calculated from measured lock-in amplifier voltages using the following method:

- Lock-in amplifier voltages for White Spectralon®, V_{Spec}, are measured as a function of reflectance angle, for a set incidence and azimuthal angle. The 180° azimuthal angle plane is the most sensitive to BRDF variations, as it is most sensitive to forward- and backscattering effects.
- Lock-in amplifier voltages for the sample, V_{Sample} are measured as a function of reflectance angle, for the same set incidence and azimuthal angle.
- Using the known reflectance values of the National Institute of Standards and Technology (NIST) certified White Spectralon® target (Labsphere, 2017), r_{spec}, at the appropriate viewing angles, the BRDF of the sample can be calculated—from the reflectance of the sample, r_{Sample}—using Equation 4.1.

$$BRDF_{Sample}(\theta_r) = \frac{r_{Sample}(\theta_r)}{\cos(\theta_i)} \qquad [4.1]$$

Where,

$$r_{Sample}(\theta_r) = \frac{r_{Spec}(\theta_r)}{V_{Spec}(\theta_r)} \times V_{Sample}(\theta_r) \quad [4.2]$$

Dividing by $\cos(\theta_i)$ in Equation 4.1 is necessary due to the design choice of having an illumination spot which is smaller than the FOV. This design choice was made because of the difficulty in creating an illumination spot which is spatially uniform.

Figures 46, **47**, **48** and **49** show BRDF measurements taken by VOSEG and BUG for White Spectralon® at 15, 30, 45 and 60° incidence angles, respectively, in the principal plane (180° azimuthal angle). Note, the BUG study reported no error bars.

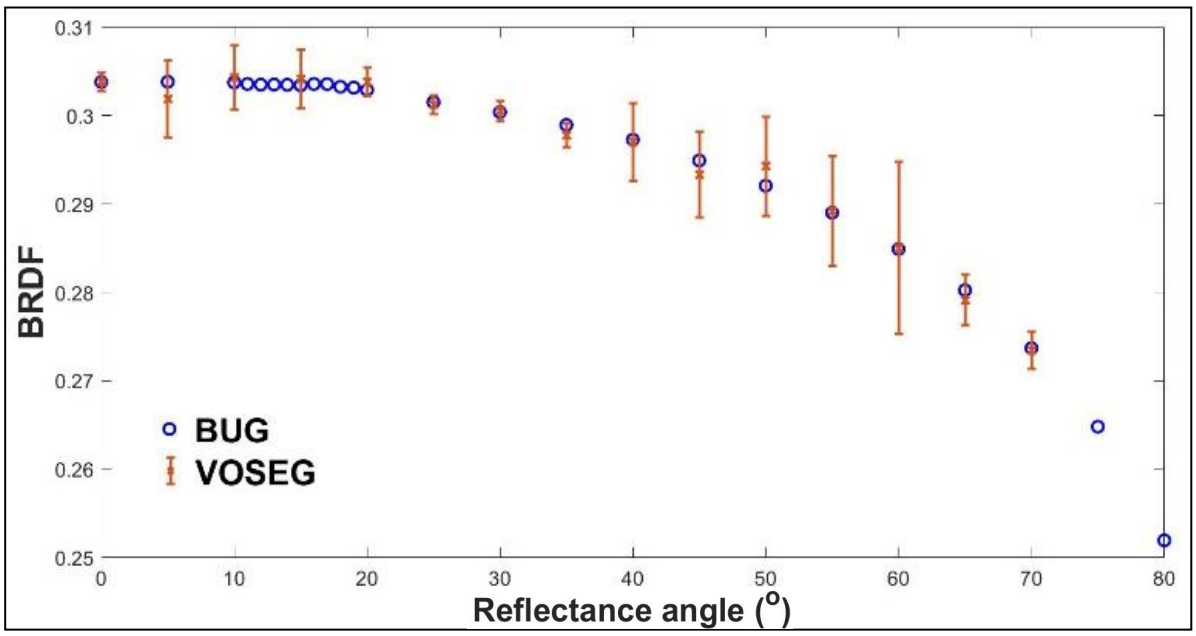

Figure 46: Bidirectional Distribution Function measurements of White Spectralon®, comparing the Bloomsburg University Goniometer to the Visible Oxford Space Environment Goniometer for 15° incidence angle, in the principal plane (180° azimuthal angle). Data taken using VOSEG's broadband light source.

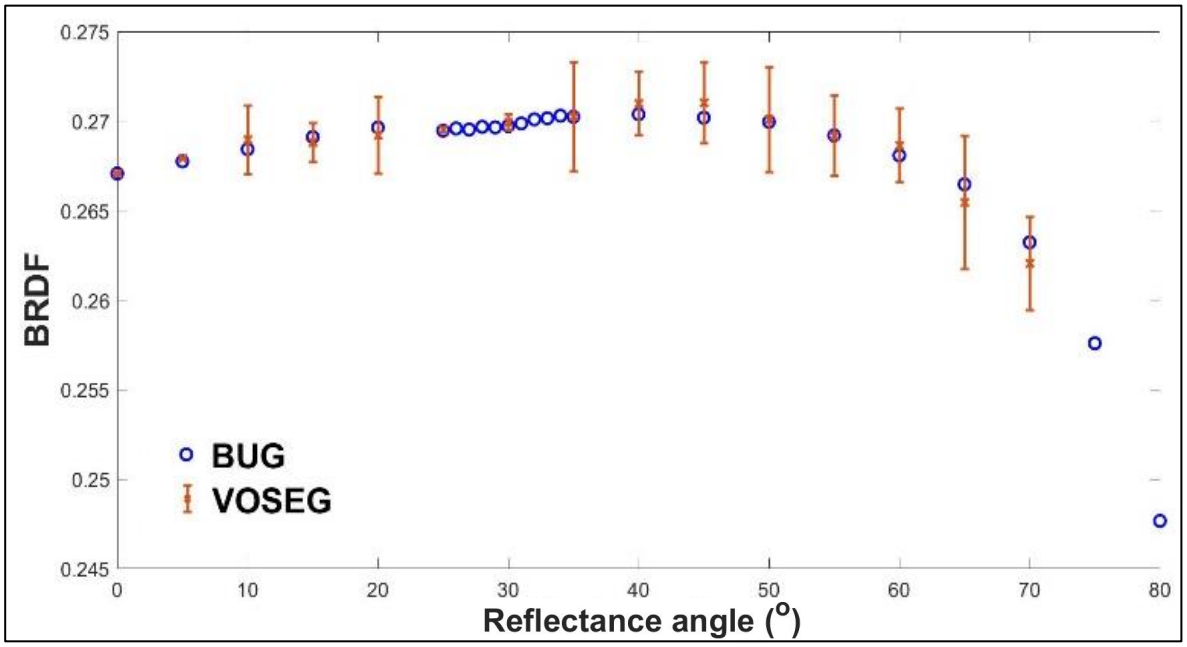

Figure 47: Bidirectional Distribution Function measurements of White Spectralon®, comparing the Bloomsburg University Goniometer to the Visible Oxford Space Environment Goniometer for 30° incidence angle, in the principal plane (180° azimuthal angle). Data taken using VOSEG's broadband light source.

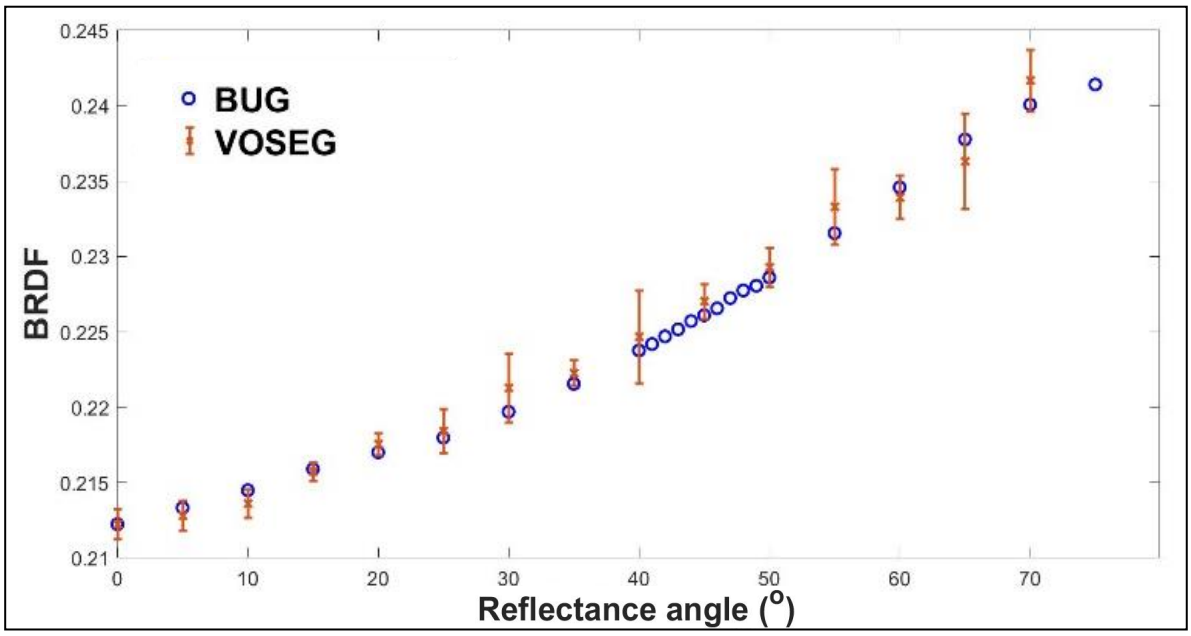

Figure 48: Bidirectional Distribution Function measurements of White Spectralon®, comparing the Bloomsburg University Goniometer to the Visible Oxford Space Environment Goniometer for 45° incidence angle, in the principal plane (180° azimuthal angle). Data taken using VOSEG's broadband light source.

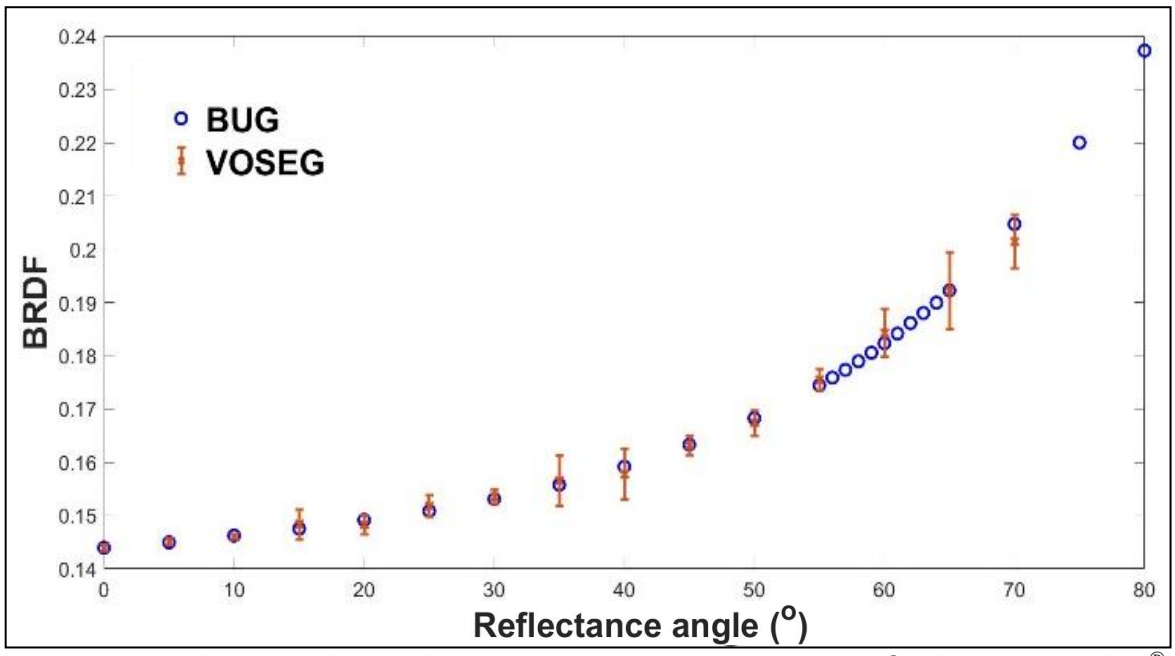

Figure 49: Bidirectional Distribution Function measurements of White Spectralon®, comparing the Bloomsburg University Goniometer to the Visible Oxford Space Environment Goniometer for 60° incidence angle, in the principal plane (180° azimuthal angle). Data taken using VOSEG's broadband light source.

Figures 46, **47**, **48** and **49** show that VOSEG is validated, and that it can be used to measure our required dataset, i.e. a suite of BRDFs for Apollo samples with varying porosity values and surface roughness profiles. Before proceeding with the BRDF measurements, the porosity and surface roughness profiling methodologies must first be detailed, as in Parts 4.3 and 4.4, respectively. Finally, the experimental capabilities and sources of error for our study are summarized in Part 4.5.

4.3 Preliminary Porosity Study Methodology

Due to the suggestion in (Foote *et al.*, 2020) that BRDF variations at high reflectance angles were potentially due to porosity variations, a preliminary study was performed to define how a regolith sample's porosity affects measured BRDFs, and to determine whether surface roughness profiles needed to be incorporated into the study.

For the porosity study, initially a SamCam® non-contact surface profiler was used to determine porosity values across three sample porosity states (which aimed to represent a

range of at least the range of porosity variations present on the lunar surface, as it is impossible to recreate the highly porous regolith structures present on the Moon, due to the Earth's gravity) (Murray, 2020). These porosity states were created using the following sample preparation technique: Firstly, ~4-5 g of the 10084 and 68810 samples were spooned into sample cups. A metal blade was then slid across the top of the sample cups, to produce 'smooth', uncompacted samples. The second preparation was created by manually tapping the sample cups twenty times to reduce the porosity of the samples (to make them partially compacted). Finally, smaller sample cups were used to compress the illuminated parts of the samples, to produce least porous (compacted) samples. **Figure 50** shows these three sample porosity states.

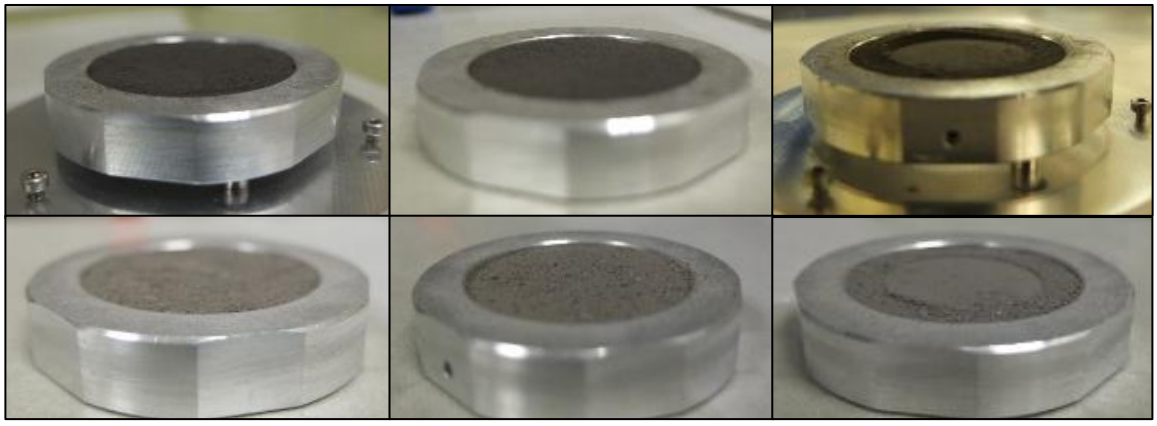

Figure 50: Top row: The Apollo 11 (10084) sample in its initial state (left), tapped state (middle) and compacted state (right). Bottom row: The Apollo 16 (68810) sample in its initial state (left), tapped state (middle) and compressed state (right).

Figure 51 shows three microscope images taken from (Foote *et al.*, 2020) of an Apollo 16 sample (61141—which is similar to 68810 but 68810 could not be used due to the restricted microscope access), for the three compaction states—uncompressed, partially compacted/tapped, and compacted—which have various measured porosities/filling factors, as given in **Table 10**, relating to the mechanism by which the sample was prepared. Converting porosity coefficients into filling factors, φ, or vice versa, is often useful when interpreting data in terms of the Hapke BRDF model.

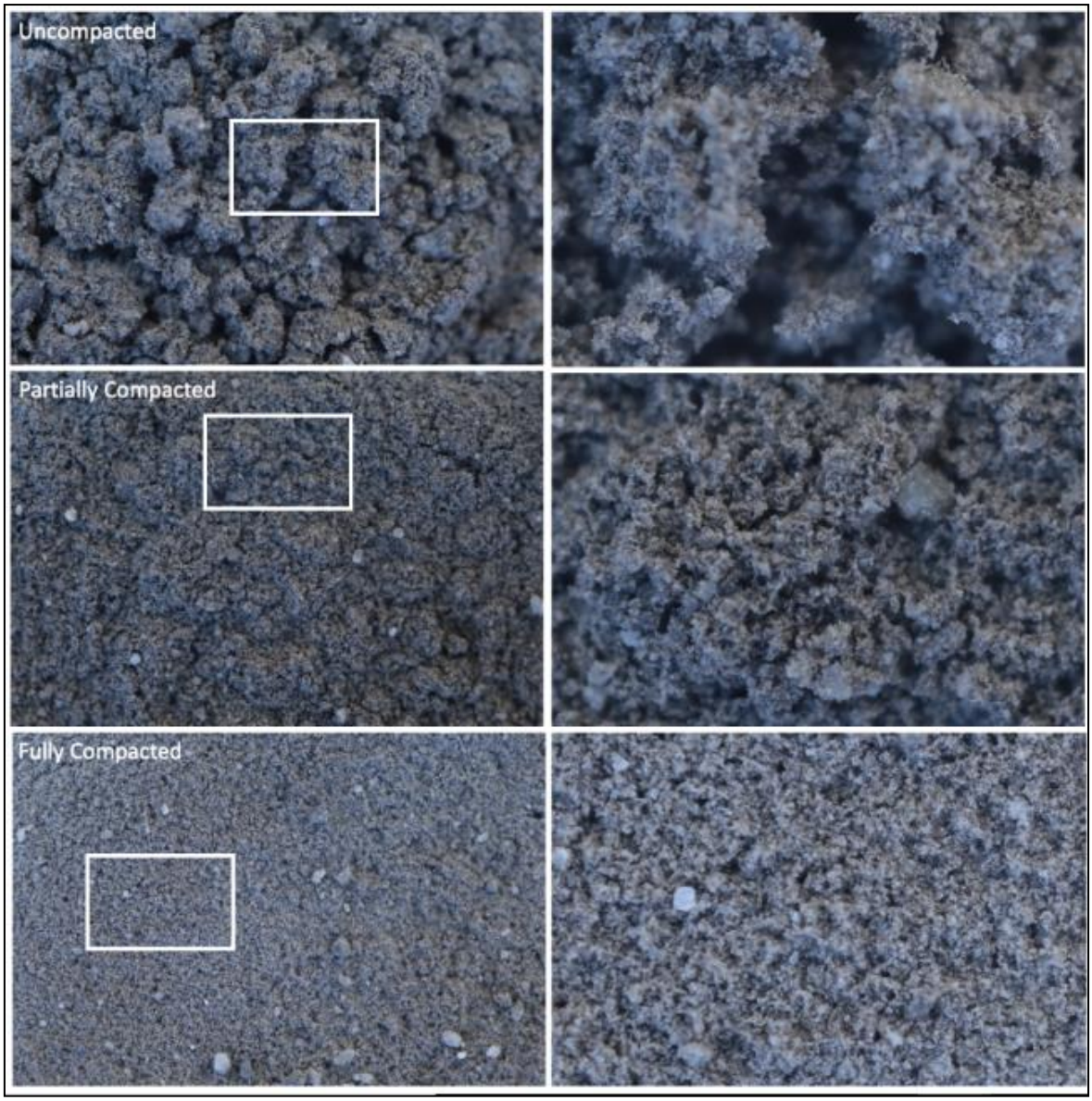

Figure 51: Microscope images of Apollo 16 sample 61141 in the three stages of compaction, related to the VOSEG porosity study. Scale of images in the left column are 10 mm across the frame. The images in the right column are enlargements of the regions of the white boxes of the images in the left column, and these have a scale of 2.7 mm across the image. Image taken from (Foote *et al.*, 2020).

Table 10 gives the calculated densities and filling factors for each compaction state for the preliminary VOSEG study. Filling factors are calculated as in (Hapke and Sato, 2015; E. J. Foote *et al.*, 2020) for consistency, by dividing the bulk density value by the average density of an average Apollo regolith particle, 3100 kg/m^3 (Bird *et al.*, 1970).

Sample	*Azimuthal angle (°)*	ρ_1 *(kg/m³)*	φ_1	ρ_2 *(kg/m³)*	φ_2	ρ_3 *(kg/m³)*	φ_3
Apollo 11 (10084)	180 (PP)	$1.85x10^3$	0.60±0.07	$2.00x10^3$	0.65±0.06	$2.75x10^3$	0.89±0.09
	0 (OPP)	$1.78x10^3$	0.57±0.06	$1.95x10^3$	0.63±0.08	$2.77x10^3$	0.89±0.10
Apollo 16 (68810)	180 (PP)	$1.48x10^3$	0.48±0.04	$1.64x10^3$	0.53±0.04	$2.69x10^3$	0.87±0.05
	0 (OPP)	$1.46x10^3$	0.47±0.05	$1.66x10^3$	0.54±0.04	$3.00x10^3$	0.98±0.02

Table 10: Density and filling factor values for uncompacted (ρ_1 and φ_1), partially compacted (ρ_2 and φ_2) and compacted (ρ_3 and φ_3) Apollo 11 (10084) and 16 (68810) regolith samples. (All φ values recalculated from ρ values given in (Foote *et al.*, 2020).)

Within thermal models, the density range used is set as the range of densities measured by the Apollo Core samples i.e. between ~1,100 kgm^{-3} and ~1,800 kgm^{-3}, thus an increase of ~64% (Hayne *et al.*, 2017). This can be assumed to be a reasonable range for the observed densities (and hence, filling factors) of regolith on the lunar surface. Via the compaction mechanisms detailed in this study, the following density increases are achieved: 10084—54% increase; 68810—105% increase. For 68810, the density range accounts for more than the range observed from the regolith samples collected from the Moon. However, for 10084, the range is 10% less than the full density range desired. This is due to the nature of the Apollo 11, mare regolith (i.e. its particle-size distribution), and the fact that the samples are not compressed with any force that might damage the regolith particles. However, as detailed in Part 4.5, the uncertainty in the density calculations when using SamCam® are ~10%, and so the desired value does fall within the top end of the measured uncertainty.

For each porosity state for both samples, a preliminary suite of BRDFs were measured in the principal plane (at 180° azimuthal angle). BRDFs were shown to increase, in particular at high reflectance angles, for both the samples at all incidence angles, as the porosity of the samples decreased. This is in accordance with what (Foote *et al.*, 2020) suggest in their study, and with what is expected from the Hapke BRDF model (see **Figure 19**). Furthermore, it was shown that decreases in porosity could lead to increases of up to 50±5%

for 10084 and up to 90±10% for 68810 in the BRDF data, at high reflectance angles (>50°). Therefore, the 33% discrepancy for high reflectance angles (>50°) in the (Foote *et al.*, 2020) study between the laboratory goniometer data and the albedos derived from Diviner—see **Figure 30**—may be explained by porosity differences of the sample and of the surface of the Moon. Importantly, however, BRDF increases observed in the data cannot be wholly attributed to variations in the porosity, as variations in surface roughness must also be considered. Whenever a sample's porosity is varied, surface roughness will also be affected, and it is surface roughness variations which, according to Hapke, can lead to variations in BRDF which increase with reflectance angle.

This was further demonstrated in this project through the observation of variations in measured BRDFs when the 10084 and 68810 samples were rotated. Measuring three BRDFs using VOSEG for the same sample—after it was rotated 120º at each step—led to increasing discrepancies, from ~3 to ~10%, as reflectance angles increased from 40° to 70°. This is likely due to the fact that as the surface rotates, the surface profile changes and hence, so does the topography and composition of various parts of the illuminated surface. Changing the topography of the surface (at the ~10 μm scale) alters the ratio of singly/multiply scattered light for a particular viewing angle, in addition to it changing the composition of different areas of the illuminated surface. This could lead to different albedos being measured at specific phase angles. **Figure 52** and **Figure 53** show examples of the rotation study's results at 45° incidence angle, for 10084 and 68810, respectively.

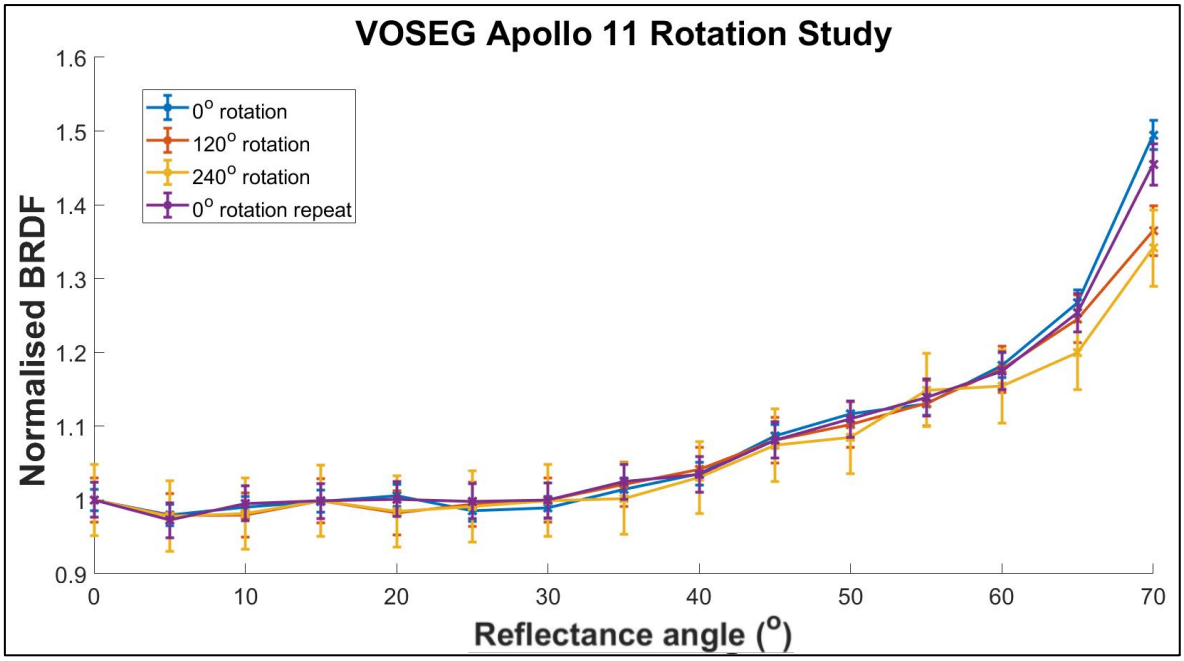

Figure 52: Showing Normalised BRDFs measured by VOSEG for three rotations of a smooth Apollo 11 (10084) sample at 45˚ incidence angle. Sample orientated at 0˚, 120˚, 240˚ (with respect to 0˚ azimuthal angle) and then the 0˚ measurement is repeated, to demonstrate how surface roughness influences BRDF; and hence, this must be captured alongside porosity for a physical property BRDF study.

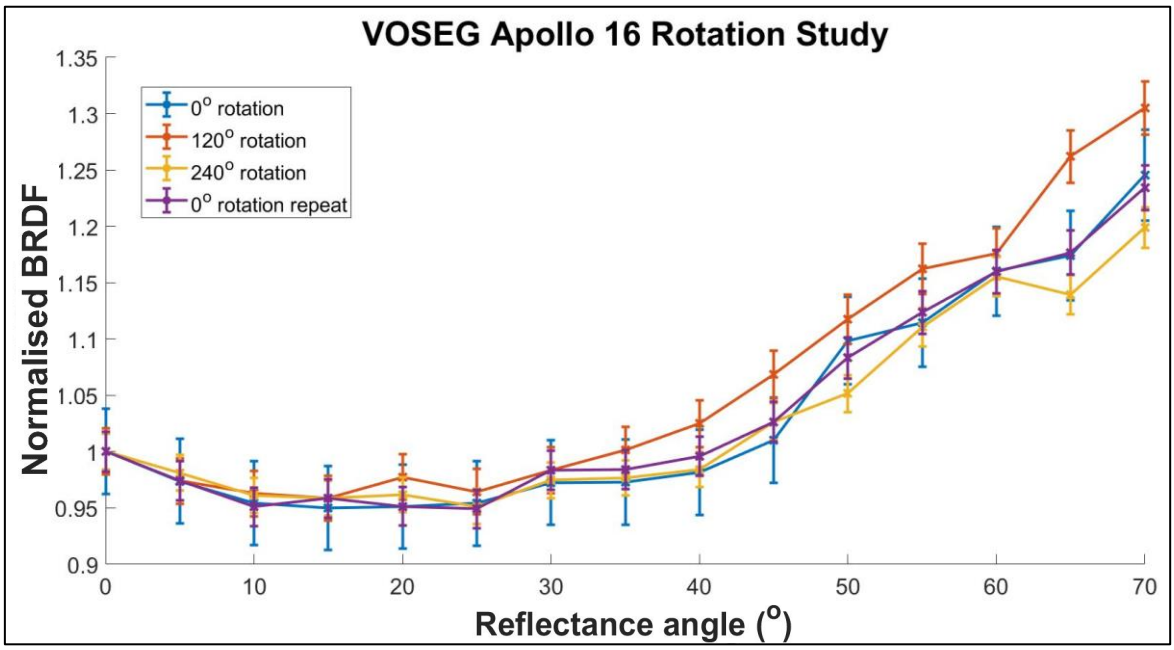

Figure 53: Showing Normalised BRDFs measured by VOSEG for three rotations of a smooth Apollo 16 (68810) sample at 45˚ incidence angle. Sample orientated at 0˚, 120˚, 240˚ (with respect to 0˚ azimuthal angle) and then the 0˚ measurement is repeated, to demonstrate how surface roughness influences BRDF; and hence, this must be captured alongside porosity for a physical property BRDF study.

Such deviations in BRDFs at high reflectance angles suggest that these variations may be attributed to surface roughness, as demonstrated in **Figure 31**. Therefore, 1) to measure

BRDF data for samples with known filling factors, which does not have ~10% measured uncertainty—making it unusable, as the uncertainty in the data must be <3% total—and 2) to measure BRDFs which can be fully interpreted using the Hapke BRDF model in terms of variations due to sample physical property variations, both porosity values and surface roughness profiles for the measured samples must be measured. If filling factors (and hence, K values) and surface roughness profiles (i.e., $\bar{\theta}$ values) are measured for the samples used in our BRDF study, then two of three correlated parameters within the Hapke BRDF model, K, w and $\bar{\theta}$ will be known, making it possible to solve for the third (Hapke, 2012). Hence, the methodology behind profiling the surface roughness of our Apollo samples is detailed in Part 4.4.

4.4 Surface Roughness Study Methodology

The surface roughness of the lunar regolith at the lunar surface at various size-scales (0.085 mm to 85 mm) was studied in (Helfenstein and Shepard, 1999), using stereophotogrammetry images taken during the Apollo missions. This study calculated photometric roughness values—which are directly related to RMS slope angle values—for various regions of the lunar surface, at increasing size-scales. **Figure 22** demonstrates this. The 'size-scale' refers to the resolution used when calculating the RMS slope angle. For instance, a 0.085 mm size-scale implies that RMS slope angles were calculated between points on the image which have a distance between them of 0.085 mm. Using a larger size-scale will naturally lead to lower values in RMS slope angle, as smaller-scale topography variations will not be accounted for.

In addition to measuring RMS slope angle values of lunar regolith on the Moon, it is possible to measure them for regolith samples in the laboratory using a non-contact surface profiler, such as an Alicona® 3D. This device can take surface profiles for a given resolution and enables RMS slope angles to be calculated for regolith samples, at various size-scales, by

loading the point cloud data into MATLAB (Version 2020a) and running an RMS slope angle calculation code (written by the author) over it, in both x- and y-directions. Furthermore, by setting a reference point at the edge of the sample cup, the densities/filling factors of the samples can also be determined using the Alicona 3D®, and this method leads to lower uncertainties (~2%) in the measured densities/filling factor values when compared to using the SamCam® (~10%), as the spatial resolution is an order of magnitude better.

The methodology for measuring the porosity values and surface roughness profiles using the Alicona 3D® for the BRDF study is as follows: Firstly, for each of the Apollo samples, two samples are prepared with different levels of roughness. The first set of samples (which can be treated as the control samples) are prepared in the same way as the smooth samples described in the preliminary porosity study—i.e. regolith is spooned into the sample cups and then the surfaces are smoothed over using the edge of a metal blade. For the second, rough set of samples, the regolith is spooned and sprinkled into the sample cups in such a way as to produce a rough surface. Examples of smooth and rough 68810 samples are shown in **Figure 54**.

Figure 54: Left: a 'rough' Apollo 16 (68810) sample used in the VOSEG physical property variation study. Right: a 'smooth' Apollo 16 (68810) sample used in the VOSEG physical property variation study. Note, the inner diameter of the sample cup is 30 mm.

Once the samples are prepared, they are transported to the Alicona 3D® device. The methodology for measuring the surface profiles of the samples is as follows:

- The regolith sample is placed on the profiler stage and is centred, using two metal spacers. Then, a reference point is set within the software at the edge of the sample cup, so that the height of the sample cup is known for the filling factor calculation.
- The z-direction focuser within the software is set so the minimum and maximum z-axis bounds are two points beyond which all of the profiled region of the surface is in focus, using the 5x0.15 lens.
- The x- and y-axis bounds are set to include the specified sample surface area, e.g., 10x10 mm. An area smaller than the entire surface of the sample was profiled as a homogeneity study confirmed no significant difference (within uncertainty) between 10x10 mm centre regions and entire sample surfaces.

- The vertical resolution is set to be 1 µm and the lateral resolution is set to be 10 µm, as this is the minimum size-scale of the RMS slope angle to be probed within the study.

- A 2D preview scan—an example of which is shown in **Figure 55**—is taken and if the majority of the surface appears in focus, then the profiling process can begin.

Figure 55: Showing a 10x10 mm 2D preview scan of an Apollo 11 (10084) sample which is ready to be profiled using the Alicona 3D® non-contact surface profiler. The width of this square represents a third the width of the sample cup.

- The Alicona 3D® profiling process takes around one hour for a smooth 10x10 mm regolith surface and around two hours for a rough 10x10 mm regolith surface. Profiling rougher surfaces takes longer due to the larger z-axis range needed to capture the variations in surface roughness.

- Once the Alicona 3D® profiling process is complete, RMS slope angle values for the central 10x10 mm region of the surface (i.e. the part for which BRDFs are measured using VOSEG) are calculated using a MATLAB (Version 2020a) code. This is

initially done for the 10 µm size-scale, but the code also decimates the data to output RMS slope angle values at the 50, 100, 500 and 1000 µm size-scales, also.

- Finally, the filling factor of the sample is calculated using the point cloud data and the reference point at the edge of the sample cup. *K* can then be calculated from *φ,* using Equation 2.7.

Figure 56 shows a typical Alicona® 3D surface profile for a rough Apollo 16 (68810) sample, with 10 µm lateral resolution and 1 µm vertical resolution.

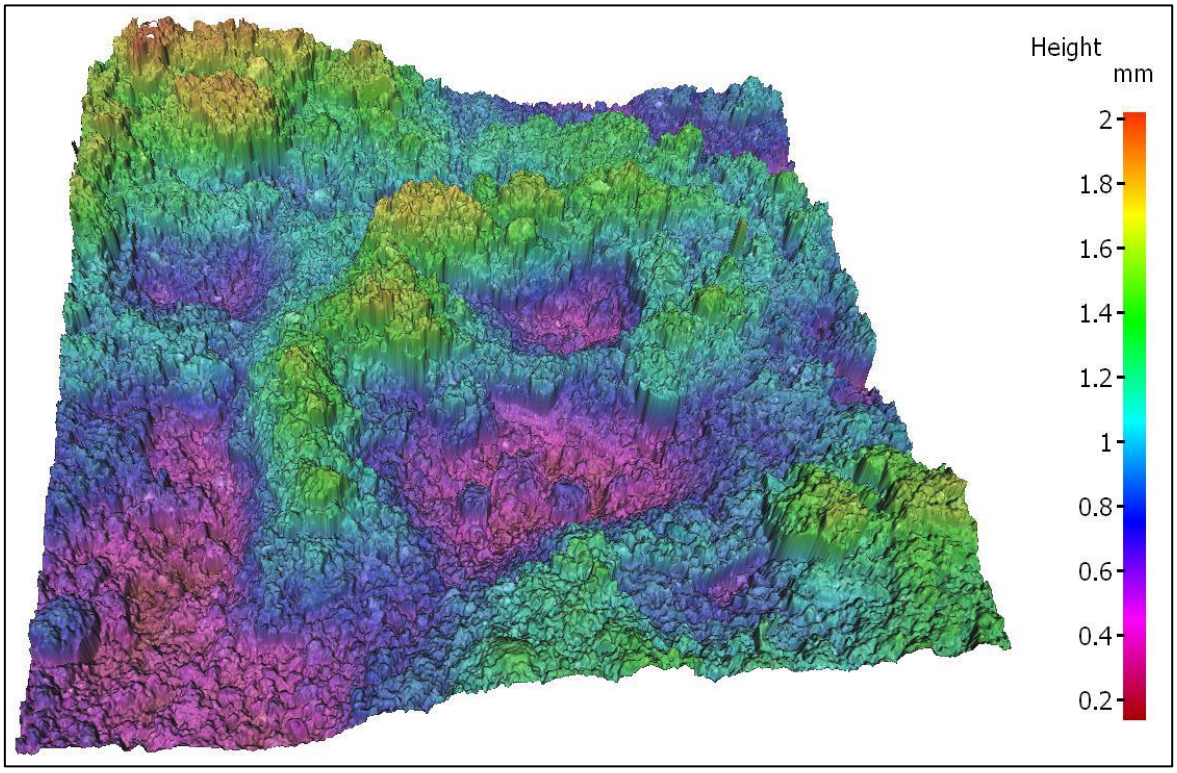

Figure 56: A 3D surface profile taken by the Alicona 3D® for a roughly prepared surface of Apollo 16 (68810) highlands lunar regolith, with 10 µm lateral resolution and 1 µm vertical resolution. The RMS slope angles for this 10x10 mm part of the sample were determined to be: 37.73˚ at 10 µm size-scale, 36.45˚ at 50 µm size-scale, 32.10˚ at 100 µm size-scale, 21.69˚ at 500 µm size-scale, 20.17˚ at 1000 µm size-scale. The width of this square represents a third the width of the sample cup.

The non-contact surface profiling process was performed on smooth and rough 10084 and 68810 samples, providing a range of surface roughness profiles at five different size-scales.

Table 11 details the measured physical properties of the samples used in the VOSEG BRDF

study. To prove the repeatability of the smooth and rough preparation techniques, repeats of the 68810 smooth and rough samples were made.

Sample →	***10084 Rough***	***10084 Smooth***	***68810 Rough***	***68810 Smooth***	***68810 Rough (#2)***	***68810 Smooth (#2)***
Filling factor (φ) →	0.41±0.02	0.60±0.02	0.40±0.02	0.55±0.02	0.39±0.01	0.57±0.02
Size-scale (μm)	***RMS slope angle (°)***					
10	41.036	33.456	37.732	34.539	37.755	33.205
50	40.660	30.571	36.452	32.491	36.607	30.170
100	36.153	24.637	32.097	27.106	32.118	24.034
500	21.283	13.805	21.693	14.271	21.199	12.269
1000	17.338	11.779	20.170	11.799	18.661	10.184

Table 11: Showing the filling factors and RMS slope angle values measured for the Apollo 11 (10084) and Apollo 16 (68810) rough and smooth samples measured in the VOSEG BRDF study. RMS slope angle values are given for the 10, 50, 100, 500 and 1000 μm size-scales.

It is clear from **Table 11** that the sample preparation processes used in this study are highly repeatable, as the filling factor values for the repeated 68810 samples were within ~5% of the initial sample's values, and the RMS slope angle values for the repeated 68810 samples were within ~10% of the initial sample's values.

How the RMS slope angles for the samples used in this study compare to those measured in (Helfenstein and Shepard, 1999) at the lunar surface is shown in **Figure 57**.

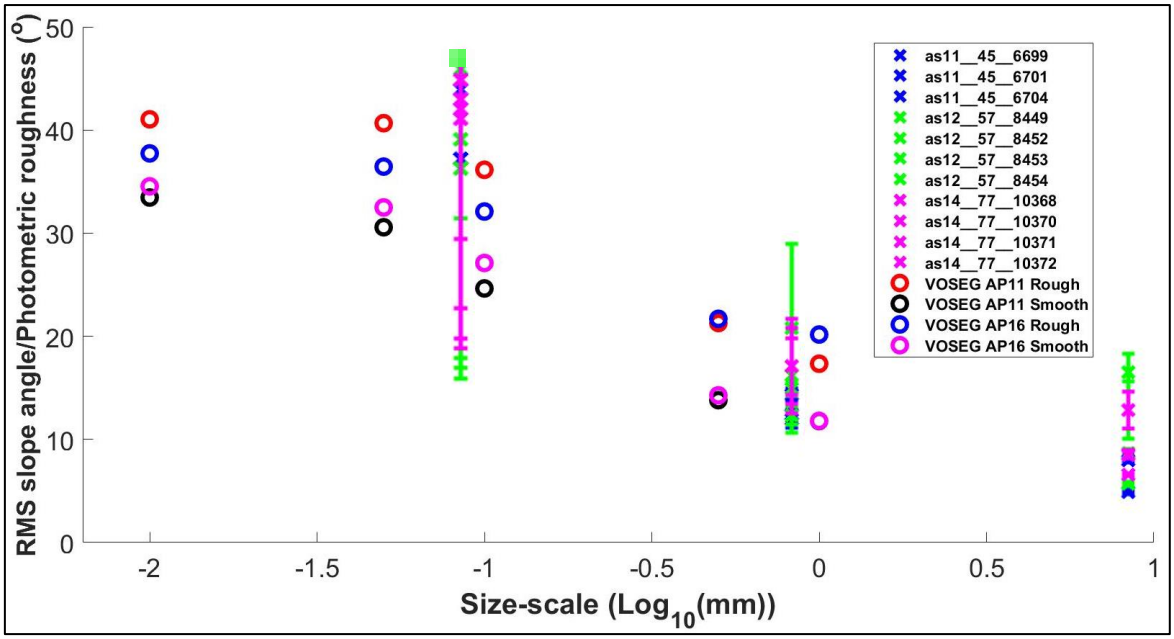

Figure 57: Showing the RMS slope angle values measured for the Apollo 11 (10084) and Apollo 16 (68810) rough and smooth samples used in the VOSEG BRDF study across a range of size-scales (plotted on a $\log_{10}$ scale). Also, for comparison, showing the photometric roughness values determined in the (Helfenstein and Shepard, 1999) stereophotogrammetry study using images of the lunar surface taking during the Apollo 11, 12 and 14 missions. Apollo images named ASXX-YY-ZZZZ, where XX refers to the mission number and YY and ZZZZ refer to the specific image. Upper error bars for the (Helfenstein and Shepard, 1999) data for the lowest measured size-scale (85 mm) are not shown, as they reach up to ~78° RMS slope angle.

Figure 57 demonstrates how the surface roughness profiles of our samples are representative of what was observed at the lunar surface for the Apollo regolith surfaces imaged in (Helfenstein and Shepard, 1999). Although from **Figure 57** it appears the RMS slope angle similarity between our surfaces and those profiled in (Helfenstein and Shepard, 1999) break down for <100 μm size-scales, the error bars given within the stereophotogrammetry study span ~15-78° RMS slope angles and so our surfaces fall well within the uncertainty range.

In summary, measuring a suite of BRDFs for these well-characterized 10084 and 68810 samples for smooth and rough surface profiles will potentially enable the w, K and $\bar{\theta}$ degeneracy to be broken within the Hapke model, allowing Least-Squares fits to be made on the VOSEG data for the three crucial terms: w, b and c. Furthermore, knowledge of the porosity and RMS slope angle values for the samples will enable Diviner's off-nadir data to be interpreted in a novel way, using VOSEG's suite of BRDFs, in accordance with goal G3.

But before continuing to the results section of our study, now that the porosity and surface roughness methodologies have been set out, the complete experimental capabilities and sources of error for our BRDF study can be detailed, as in Part 4.5.

4.5 Experimental Capabilities and Sources of Error

The experimental capabilities and sources of error associated with VOSEG's BRDF study will now be summarised. As detailed above, VOSEG can measure down to ~4° phase angles—which means it can measure part of the opposition effect—and it can take measurements over a range of angles, up to and including 60° incidence and 70° reflectance angles. Height and tilt sensitivity studies have been performed, and these show that to be able to make measurements of White Spectralon® which are in agreement with other goniometer systems, such as BUG, the height must remain 26±1 mm above the base plate of the goniometer, and the tilt of the sample must be ≤0.5°, or else post-processing must be done to correct for this. How VOSEG's experimental capabilities match up to the requirements set out in Part 3.3 is demonstrated in the performance table, **Table 12**.

Property	***Requirement***	***VOSEG performance***
Laser light source stability (over one run)	<1% (<3% total, when combined with 2% chopper frequency drift uncertainty)	~1-2% (over 8 hours)
Broadband light source stability (over one run)	<1% (<3% total, when combined with 2% chopper frequency drift uncertainty)	~0.1% (over 8 hours)
Azimuthal angle range	0-360°	0-360°
Reflectance angle range	0-65°	0-70°
Incidence angle range	0-60°	0-60°
Minimum phase angle	5°	~4°

Uncertainty in reflectance angle	≤0.33°	0.1°
Uncertainty in incidence angle	≤0.33°	0.1°
Uncertainty in azimuth angle	≤0.33°	0.1°
Tilt angle control	≤0.5°	~0.05°
Height control	<1 mm	~0.3 mm
Illumination spot location drift (over one run)	<1 mm	~0.3 mm

Table 12: Performance Table for the current VOSEG setup.

Table 12 shows VOSEG meets all the requirements set out in Part 3.3, with the exception of the stability of the laser light source, which exceeds the upper boundary condition for the light source stability requirement. This is because the uncertainty arising from light source instability over an 8-hour period—i.e. one standard measurement run—must be combined with the uncertainty due to chopper frequency drift (2%), and this combined uncertainty must be <3%, as set out in Part 3.3. Using the broadband light source, the uncertainty in the data remains <3%, but using the laser light source leads to uncertainties between ~3-4%, thus exceeding the requirement. Therefore, only the broadband light source will be used for the experimental study set out in Part 5, as measuring just the broadband dataset still allows all the goals of this study to be met (see **Table 1**).

Before detailing the sources of error in the BRDF measurements for our study, the experimental capabilities associated with the porosity and surface roughness measurements will be explored, using the methodologies detailed in Parts 4.3 and 4.4. For the porosity study, the rotational orientation of the sample led to ~10% error in VOSEG's BRDF measurements, however, this can be overcome by profiling the surface roughness of the sample, and by measuring at a range of azimuthal angles, i.e. 0, 45, 90, 135 and 180°. Within the slope angle parameterization, the orientational variations of the samples are captured, and so this source of error in the BRDF measurements can be ignored.

Additionally, using the SamCam® surface profiler leads to up to ~10% uncertainty in the measured filling factors/porosity coefficients for the samples. Considering **Figures 19** and **20**, this uncertainty is too large for our study—as to be able to discriminate between w, $\bar{\theta}$ and K, the uncertainty in K must be <2%—and so the Alicona 3D® method for determining filling factors is used for our study instead, as this leads to ~1% uncertainty in the measured filling factor values.

For the $\bar{\theta}$ measurements using the Alicona 3D®, there is no significant intrinsic uncertainty arising from the measurement. Furthermore, $\bar{\theta}$ values measured for regolith samples which had been left to sit in the laboratory for up to two days did not vary by more than 0.1° at any size-scale, and neither did $\bar{\theta}$ values measured before and after moving the samples (within the sample cups) around the laboratory. However, to determine the potential variations in measured $\bar{\theta}$ values which might arise due to the drifting of the illumination spot, various parts of the point cloud datasets—shifted 0.5 mm in each direction—were used to calculate various $\bar{\theta}$ values. This process showed that the uncertainties in the $\bar{\theta}$ values for the samples measured in our BRDF study are between ~0.1-0.5%, and demonstrated the robustness of this study's sample preparation and surface profiling processes.

The experimental uncertainty in VOSEG's BRDF measurements must remain below 3% if the data is to be used to meet all four of our goals. In practice, the uncertainty in the measurements is observed to be similar across all reflectance angles—showing the negligibility of stray light contributions—and is primarily due to the factors detailed in **Table 13**, which provides the uncertainty budget for the VOSEG BRDF study.

Source of uncertainty	***Error***		***Contribution to error in BRDF***
Laser light source stability (over one run)	1-2%		1-2%
Broadband light source stability (over one run)	~0.1%		~0.1%
Rotational orientation of sample (for porosity study, without RMS slope angle measurement)	Up to 10%		Becomes negligible when paired with RMS slope angle measurement.
Chopper frequency stability	Up to 2%		Up to 2% (depending on frequency)
Change in height of sample	±0.3 mm		<0.3%, if sample height is checked and adjusted before each run.
Change in tilt of White Spectralon® (over one run)	±0.05˚		<0.2%, if sample tilt is checked and adjusted before each run.
Reflectance/incidence/ azimuthal angle uncertainty	±0.1˚		<0.2%
Uncertainty in filling factor measurement	~10% (Sam-Cam®)	~2% (Alicona 3D®)	NA
Uncertainty in RMS slope angle measurement	0.1-0.5%		NA

Table 13: The uncertainty budget table for the BRDF study of Apollo regolith samples with measured filling factor and RMS slope angle values. The total maximum error is 2.85% (i.e., SQRT(2^2+2^2+0.3^2+0.2^2+0.2^2)).

As each of the experimental requirements are met in **Table 9**, and as **Table 13** shows that—for the broadband light source setup—the combined uncertainty in the data is <3% (i.e. within the acceptable amount), it is now possible to proceed to measure the suite of BRDFs necessary for our study, in accordance with A2. Therefore, Part 5 details the results of our laboratory BRDF study and goes on to analyze and discuss the measured dataset.

5 Results and Discussion

BRDFs were measured using VOSEG for rough and smooth 10084 and 68810 samples across the range of viewing angles set out in Part 4.5 (0-70° θ_r, 15-60° θ_i, and at 0/45/90/135/180° θ_a), and the dataset is given in its entirety in the Appendix. This BRDF dataset can now be used towards achieving the goals of this study, and, in future, it can be used by the wider lunar science community, as it provides a comprehensive description of how mare and highlands Apollo regolith samples scatter light across a wider range of viewing angles than has previously been measured, due to the measurements performed in the diagonal planes (i.e., at 45° and 135° azimuthal angles). Furthermore, the dataset includes BRDFs for samples with well-characterised and varying porosity and surface roughness profiles, as demonstrated in **Table 11** and **Figure 57**. Hence, it is now possible 1) to study the effects of varying regolith surface properties on measured BRDFs; 2) to deduce sets of Hapke parameters for each of the samples; 3) to further constrain the size-scale of the Hapke slope angle, thus enabling a new analysis technique for the interpretation of Diviner's visible off-nadir data; and 4) to set realistic laboratory measured scattering functions within the O3DTM.

5.1 Effect of Regolith Surface Property Variations on Measured BRDFs

5.1.1 Porosity Study

For the VOSEG physical property BRDF study, porosity and surface roughness variations are considered in tandem, because 1) the effect of porosity variations on BRDF cannot be separated from surface roughness variations, as decreasing the porosity of the samples would also lead to a reduction in surface roughness; and 2) this enables two of the key parameters in the Hapke model to be set using laboratory measured data. Therefore, how the BRDFs of

the Apollo regolith samples are affected by porosity and surface roughness variations will be considered in Part 5.1.2, collectively.

Table 11 provided the filling factors measured for the rough and smooth 10084 and 68810 samples, and these values can be converted into porosity coefficients using Equation 2.7, to produce **Table 14**.

Sample	**10084 Rough**	**10084 Smooth**	**68810 Rough**	**68810 Smooth**	**68810 Rough (#2)**	**68810 Smooth (#2)**
Filling factor (φ)	0.41±0.02	0.60±0.02	0.40±0.02	0.55±0.02	0.39±0.01	0.57±0.02
Porosity coefficient (K)	1.20±0.02	1.47±0.04	1.19±0.02	1.38±0.03	1.19±0.01	1.41±0.04

Table 14: Showing filling factor values and porosity coefficients for each of the Apollo regolith samples used in the VOSEG BRDF study.

Table 14 shows that in the process of creating the smooth 10084 sample, the sample's porosity coefficient—which is inversely related to the true porosity of the sample—increases by 22.09%, compared to the rough sample. For the 68810 sample, this increase in porosity coefficient is 15.44%, compared to the rough sample. Higher *K* values are directly related to increased BRDFs across all reflectance angles (see Equation 2.3 and **Figure 19**), and so the advantage of measuring the samples' *K* values is clear, as it enables a more accurate deduction of *w*, when using a fitting approach. Measuring filling factor values using the Alicona 3D® leads to uncertainties within the data which are between 3.33-5.00%, and this range corresponds to uncertainties in porosity coefficients of ~1.50-3.00%. Therefore, this leads to uncertainties in fitted *w* values of <4%, which is below the average uncertainty derived from the BRDF data fitting process (as described in Part 5.2). Thus, the *w* values determined by this study can be treated as 'true' values, in that they are not overestimated,

as may have been the case in previous studies in which *K* was set to be 1 (Sato *et al.*, 2014; Foote *et al.*, 2020).

Additionally, **Table 14** shows that the 10084 sample naturally filled more easily (by ~10%) than the 68810 sample when the smoothing process was performed. This could potentially be due to the larger average particle size of the Apollo 16 highlands regolith sample (~100 µm), compared to the Apollo 11 mare regolith (~80 µm) (Carrier III, Olhoeft and Mendell, 1991). Therefore, the irregularly shaped grains of the 10084 sample could be less obstructive to the resettlement of the grains surrounding them and so they may fall into the gaps more easily. Otherwise, the porosity coefficient values are similar between the corresponding 10084 and 68810 samples—<1% variation between the rough samples, and <7% variation for the smooth samples—showing the repeatability of the rough and smooth sample generation processes.

5.1.2 Surface Roughness Study

Figures 58, **59 and 60** show BRDF data measured by VOSEG in the principal, out-of-principal and diagonal planes for the rough Apollo 11, 10084 sample, respectively. Data at 15**,** 30, 45 and 60˚ incidence angles is included, in addition to Hapke BRDF model best fit curves, calculated by fitting the model to the complete dataset. Filling factors and RMS slope angles (at 500 µm) for each of the samples, measured with the Alicona 3D®, are given in **Table 11**.

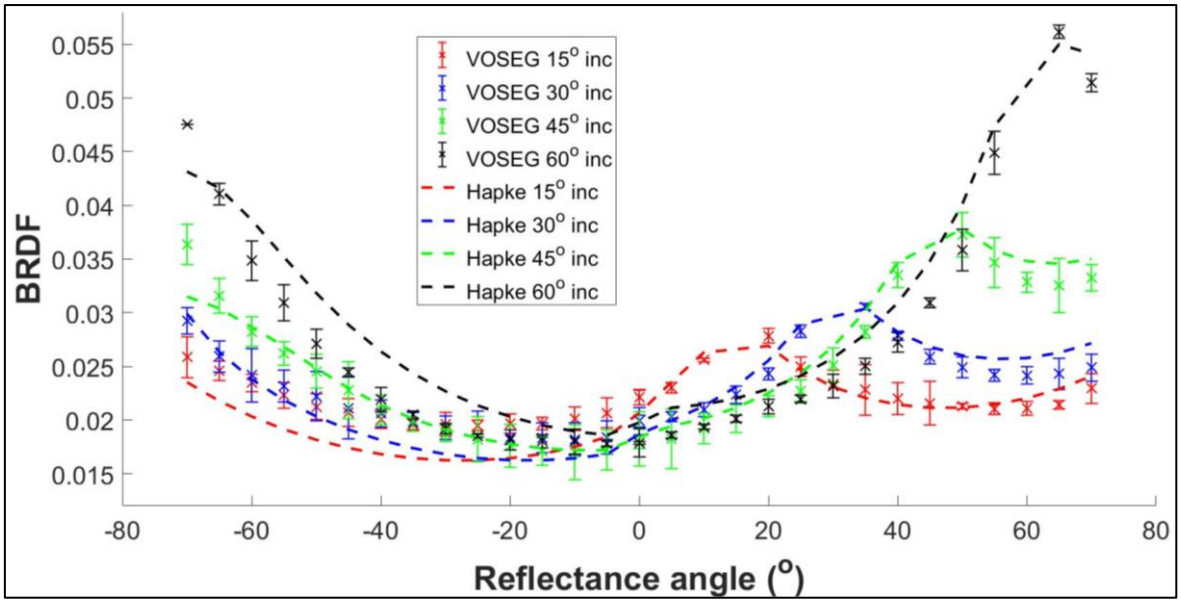

Figure 58: BRDFs measured by VOSEG, and fitted with Hapke over the complete dataset, for the smooth Apollo 11, 10084 sample in the principal plane (i.e., azimuthal angle = 0/180°) at 15° (red), 30° (blue), 45° (green) and 60° (black) incidence angles. Positive θ_r values denote θ_a=0°, and negative θ_r values denote θ_a=180°.

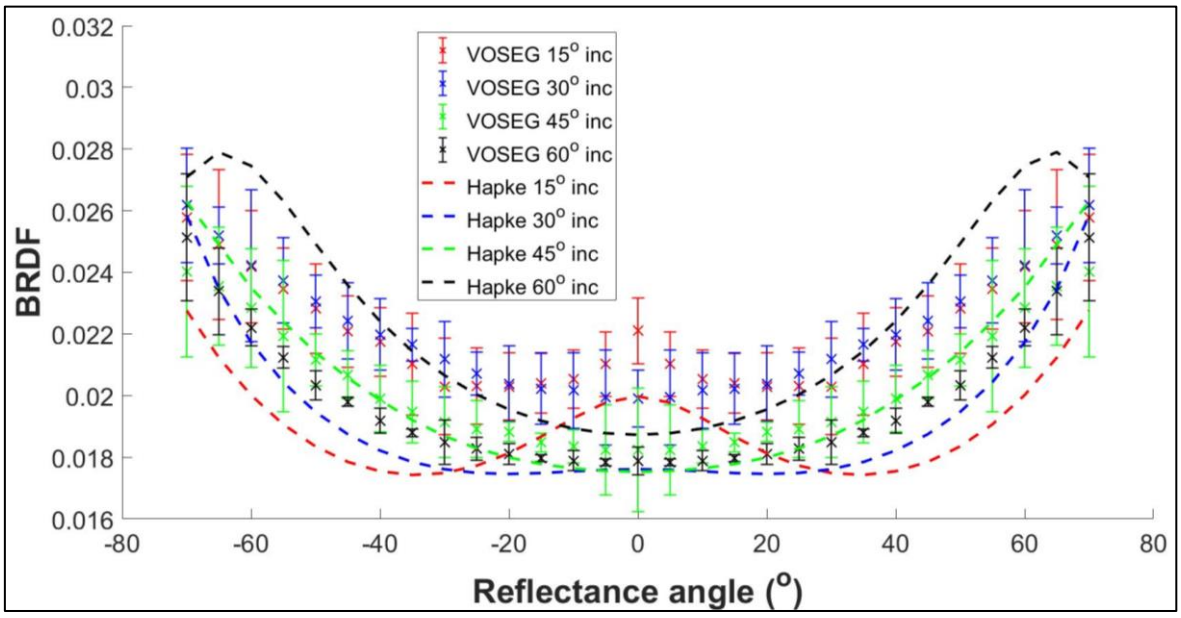

Figure 59: BRDFs measured by VOSEG, and fitted with Hapke over the complete dataset, for the smooth Apollo 11, 10084 sample in the out-of-principal plane (i.e., azimuthal angle = 90/270°) at 15° (red), 30° (blue), 45° (green) and 60° (black) incidence angles. Positive θ_r values denote θ_a=90°, and negative θ_r values denote θ_a=270°. Note that out-of-principal plane data measured at θ_a=90° can be reflected in the θ_a=270° plane, according to Helmholtz reciprocity/Kirchoff's law (Greffet and Nieto-Vesperinas, 1998).

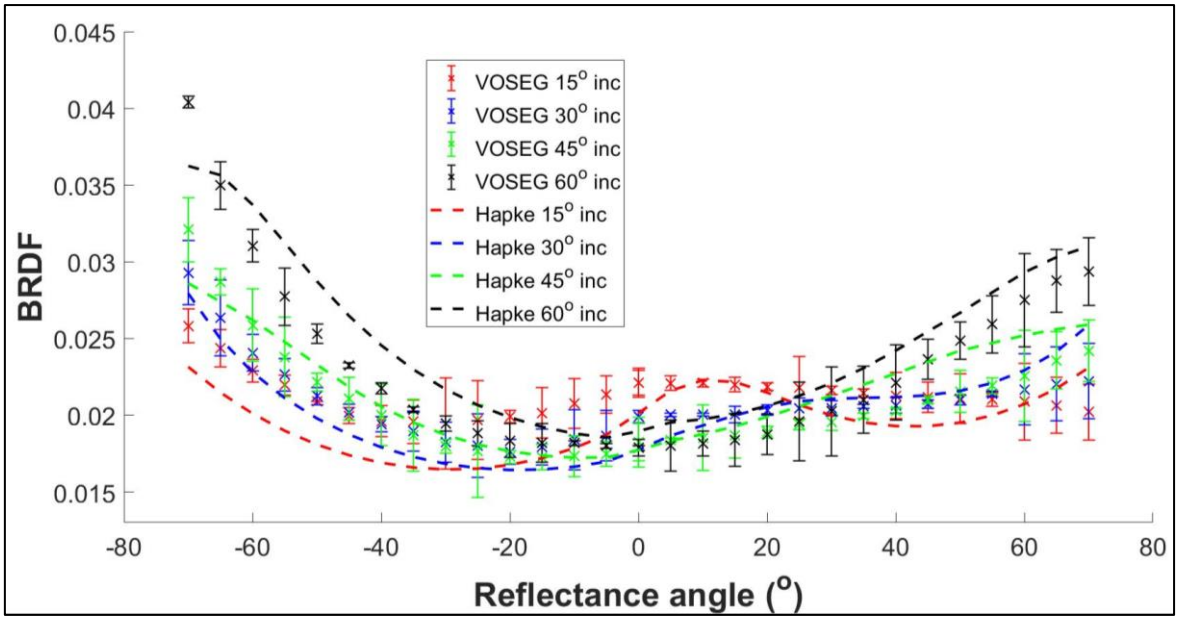

Figure 60: BRDFs measured by VOSEG, and fitted with Hapke over the complete dataset, for the smooth Apollo 11, 10084 sample in the diagonal plane (i.e., azimuthal angle = 45/135°) at 15° (red), 30° (blue), 45° (green) and 60° (black) incidence angles. Positive θ_r values denote θ_a=45°, and negative θ_r values denote θ_a=135°, but this data can be reflected for BRDFs in the opposite diagonal plane.

Figure 61, **62 and 63** now show the equivalent BRDF dataset measured in the principal, out-of-principal and diagonal planes for the rough Apollo 11, 10084 sample. Again, data at 15, 30, 45 and 60° incidence angles is included, in addition to Hapke BRDF model best fit curves, calculated by fitting the model to the complete dataset.

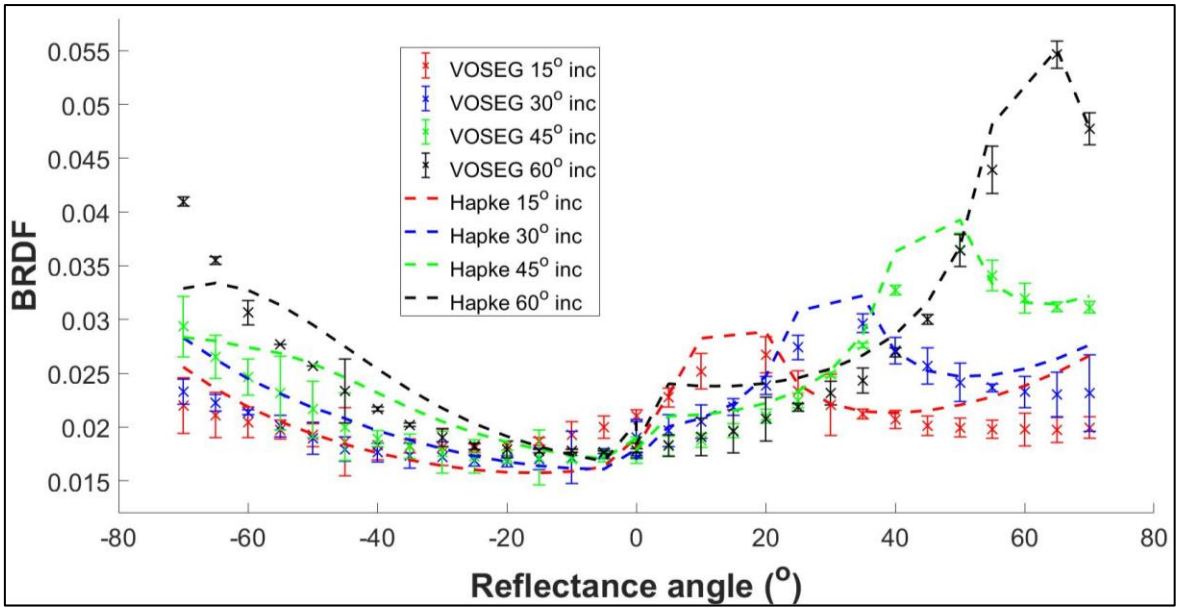

Figure 61: BRDFs measured by VOSEG, and fitted with Hapke over the complete dataset, for the rough Apollo 11, 10084 sample in the principal plane (i.e., azimuthal angle = 0/180˚) at 15˚ (red), 30˚ (blue), 45˚ (green) and 60˚ (black) incidence angles. Positive θ_r values denote θ_a=0˚, and negative θ_r values denote θ_a=180˚.

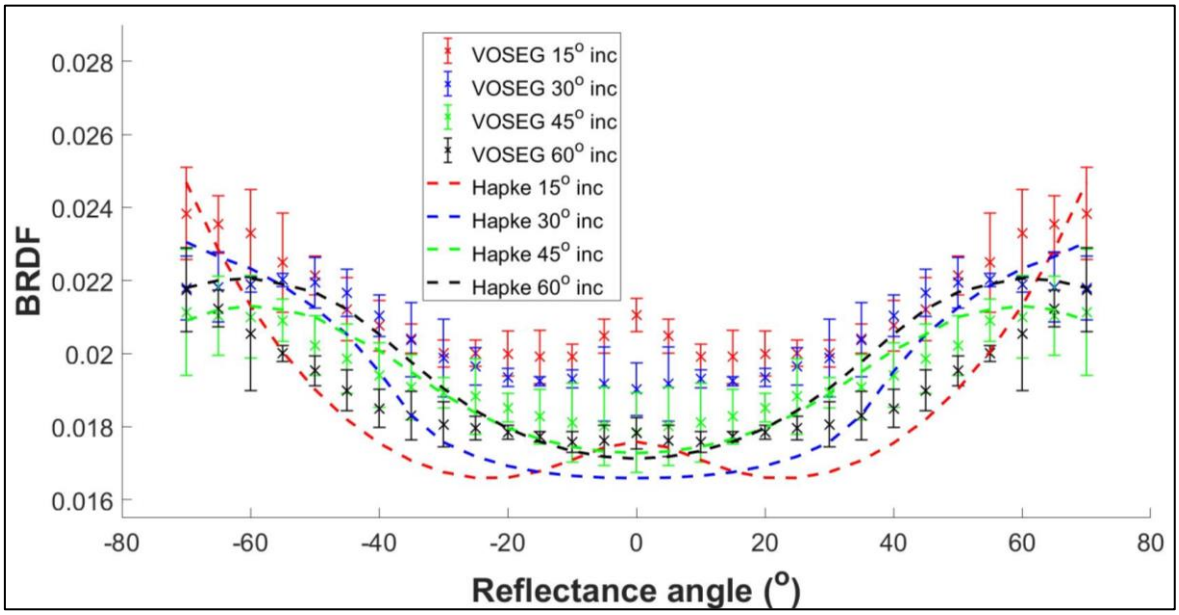

Figure 62: BRDFs measured by VOSEG, and fitted with Hapke over the complete dataset, for the rough Apollo 11, 10084 sample in the out-of-principal plane (i.e., azimuthal angle = 90/270˚) at 15˚ (red), 30˚ (blue), 45˚ (green) and 60˚ (black) incidence angles. Positive θ_r values denote θ_a=90˚, and negative θ_r values denote θ_a=270˚. Note that out-of-principal plane data measured at θ_a=90˚ can be reflected in the θ_a=270˚ plane, according to Helmholtz reciprocity/Kirchoff's law (Greffet and Nieto-Vesperinas, 1998).

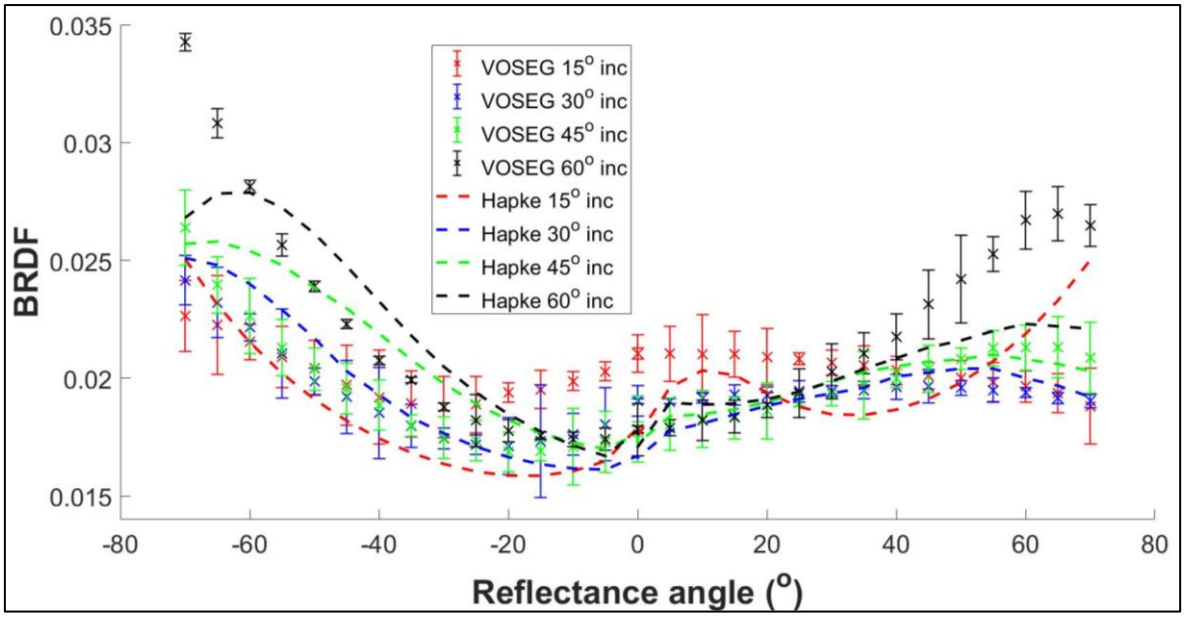

Figure 63: BRDFs measured by VOSEG, and fitted with Hapke over the complete dataset, for the rough Apollo 11, 10084 sample in the diagonal plane (i.e., azimuthal angle = 45/135°) at 15° (red), 30° (blue), 45° (green) and 60° (black) incidence angles. Positive θ_r values denote θ_a=45°, and negative θ_r values denote θ_a=135°, but this data can be reflected for BRDFs in the opposite diagonal plane.

Before discussing the differences between the plots, it is helpful to visualise how the measured BRDFs vary between the rough and smooth 10084 samples across the measured angular range. Therefore, **Figures 64**, **65**, **66 and 67** show the differences between the two samples, by plotting ΔBRDF values for each incidence angle measurement set; calculated as the BRDF profile for the smooth sample minus the BRDF profile for the rough sample.

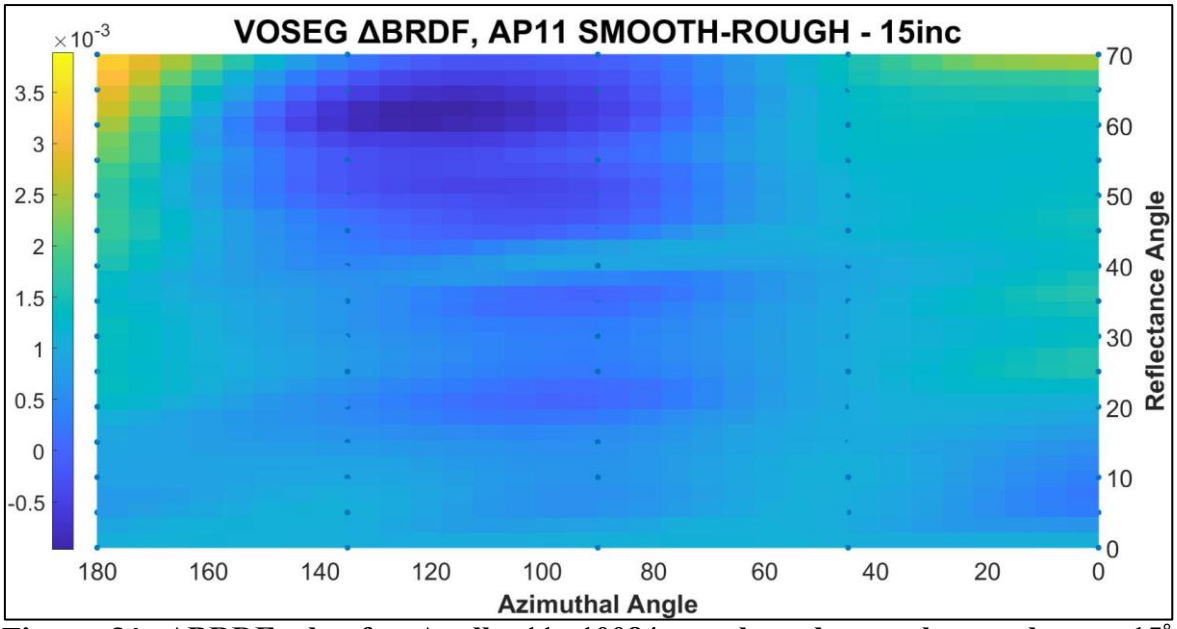

Figure 64: ΔBRDF plot for Apollo 11, 10084 rough and smooth samples, at 15° incidence. ΔBRDF calculated as the smooth BRDF profile minus the rough BRDF profile.

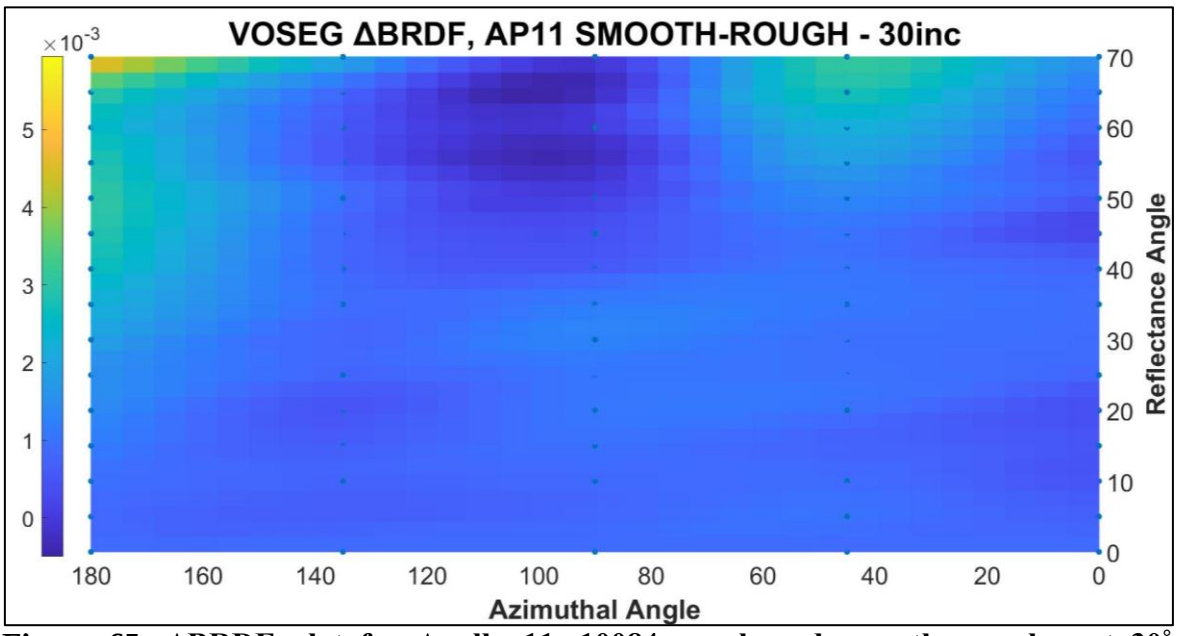

Figure 65: ΔBRDF plot for Apollo 11, 10084 rough and smooth samples, at 30° incidence. ΔBRDF calculated as the smooth BRDF profile minus the rough BRDF profile.

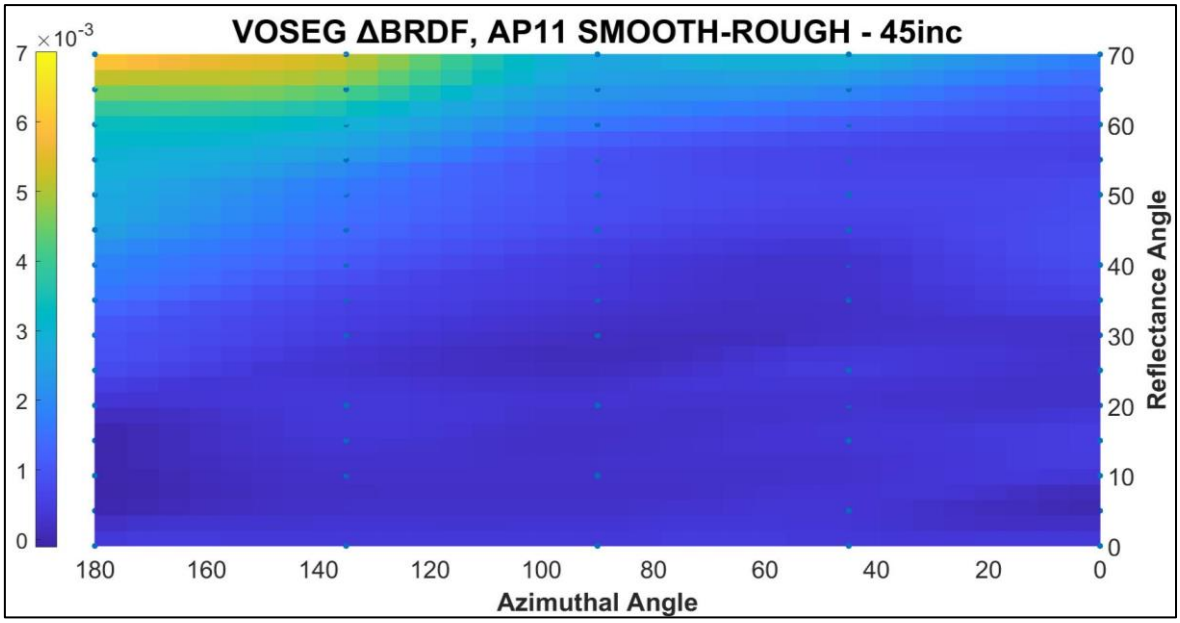

Figure 66: ΔBRDF plot for Apollo 11, 10084 rough and smooth samples, at 45° incidence. ΔBRDF calculated as the smooth BRDF profile minus the rough BRDF profile.

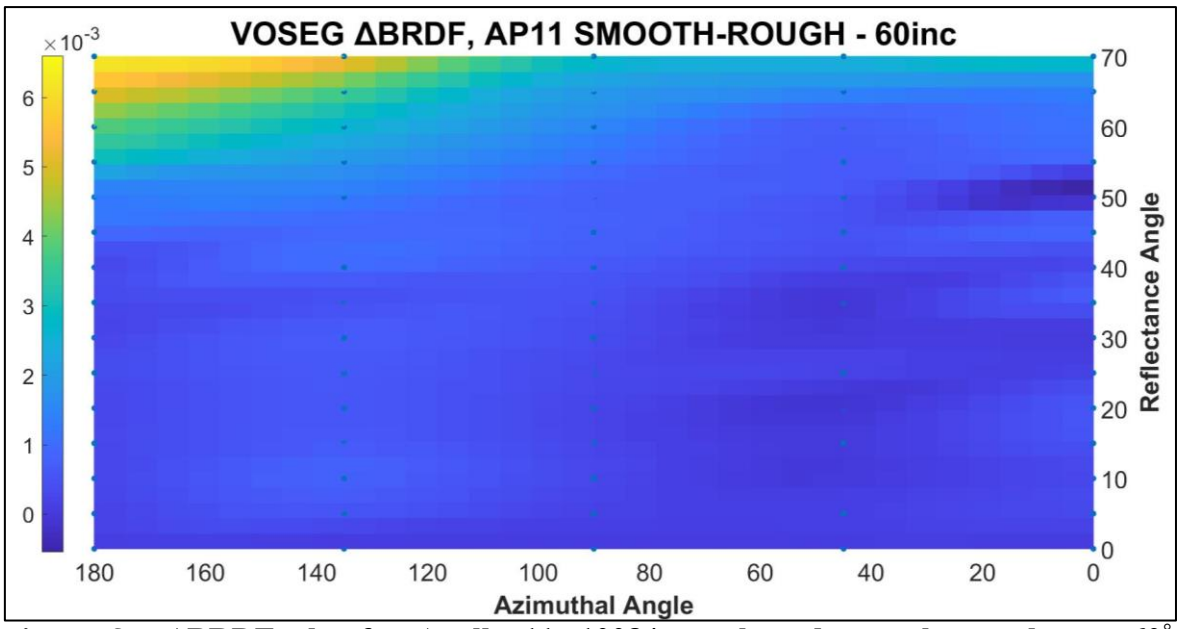

Figure 67: ΔBRDF plot for Apollo 11, 10084 rough and smooth samples, at 60° incidence. ΔBRDF calculated as the smooth BRDF profile minus the rough BRDF profile.

Before also showing the equivalent plots for the Apollo 16, 68810 sample BRDF data, it is helpful to summarize the important observations regarding the measured BRDF data shown in the 10084 plots. Firstly, the ΔBRDF plots at 30, 45 and 60° incidence angles show exclusively positive values, and for the 15° incidence angle plot, there are only a small number of negative values at high reflectance angles, in the 90° and 135° azimuthal angle

planes. This means that in general, the smooth samples have higher BRDF values at all angles than the rough samples, which is to be expected, given the higher filling factors measured for these samples. The negative values observed for the 15° incidence plot are very low in magnitude (-0.5×10^{-3} which is <2.5% of the BRDF values), and so are not significant, given that the uncertainties in the smooth and rough BRDF values are larger than the ΔBRDF values themselves. The fact they are present at high reflectance angles in the 90° and 135° azimuthal planes shows how the effects of shadowing due to surface roughness are most prominent in the principal plane, and for out-of-principal plane BRDFs, shadowing becomes less important.

As predicted by the Hapke BRDF model, BRDFs measured for the rough 10084 samples are suppressed at high reflectance angles (>45°) when compared to the 10084 smooth samples. This is due to the higher levels of shadowing induced by the greater surface roughness profiles (i.e., RMS slope angle values) of the rough samples. The discrepancies between the rough and smooth samples become increasingly prominent as reflectance angles increase, in particular for the principal plane, where shadowing effects dominate.

Generally, below 20° reflectance angle, the BRDFs of the rough and smooth samples agree within experimental uncertainty—with ΔBRDF values of ~0-0.001—and this agreement improves with incidence angle. The 15° incidence angle plot shows the most consistent disagreement between the two samples of ~0.0025, potentially showing that the effect of porosity variations on BRDFs is more dominant at low incidence angles, with such variations becoming less important at higher incidence angles (≥45°). However, the BRDF divergence between the smooth and rough 10084 samples in the principal plane, with increasing reflectance angles, becomes more prominent at high incidence angles—with ΔBRDF=~0.0035 for θ_i=15° and θ_r=70° and ΔBRDF=~0.007 for θ_i=60° and θ_r=70°. This divergence directly demonstrates how increases in shadowing—due to increased RMS slope

angles—affect BRDF profiles as reflectance angles increase, and that this effect is most dominant at higher incidence angles (≥45°), as predicted by the Hapke BRDF model (Hapke, 2012).

The opposition effect can be observed in VOSEG's BRDF measurements of the 10084 samples, and, as expected, it dominates the BRDF signal for measurements taken within ~10° θ_r of the peak. Therefore, the variations in the BRDF curves induced by varying the physical properties of the samples can only be observed for high θ_r values in the θ_a=0° part of the principal plane for the θ_i=15° and θ_i=30° plots. **Figure 64**, for the θ_i=15° measurements, clearly shows how increased shadowing reduces the BRDF at high reflectance angles for θ_a= 0°, once the opposition effect no longer dominates.

Now initial observations have been made regarding the 10084 BRDFs, it is necessary to show the equivalent BRDFs measured for the Apollo 16, 68810 samples, using the same method.

Figures 68, **69 and 70** show BRDF data measured in the principal, out-of-principal and diagonal planes for the smooth Apollo 16, 68810 sample. The images are shown in the same way as for the 10084 BRDF plots, and again, the filling factors and RMS slope angles for each of the samples are given in **Table 11**.

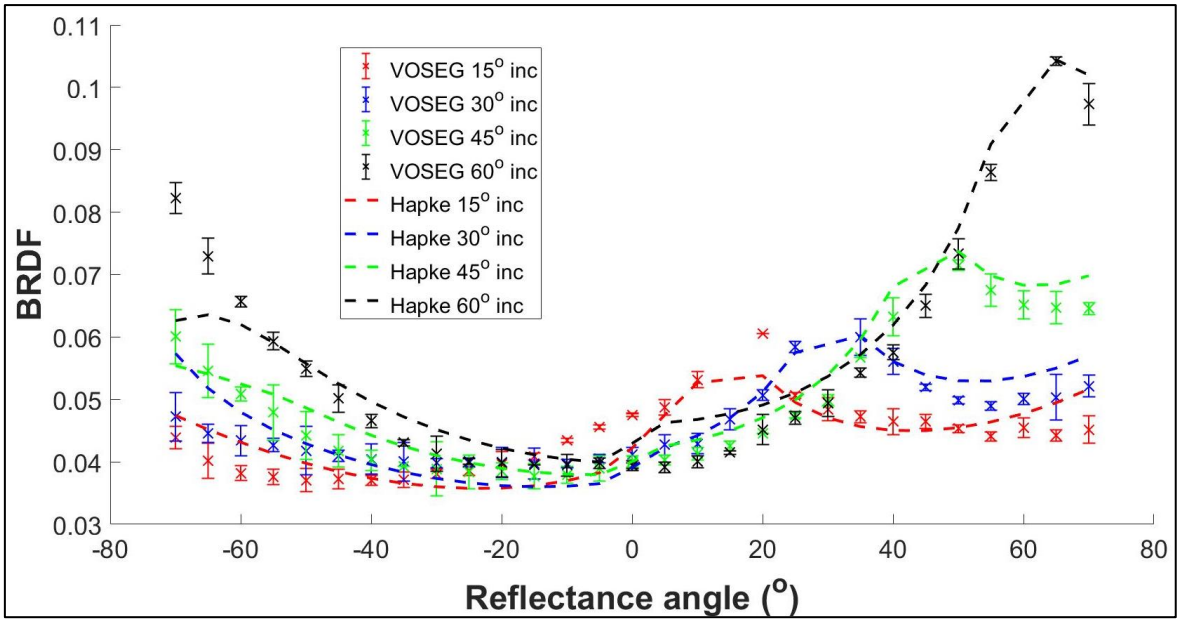

Figure 68: BRDFs measured by VOSEG, and fitted with Hapke over the complete dataset, for the smooth Apollo 16, 68810 sample in the principal plane (i.e., azimuthal angle = 0/180°) at 15° (red), 30° (blue), 45° (green) and 60° (black) incidence angles. Positive θ_r values denote θ_a=0°, and negative θ_r values denote θ_a=180°.

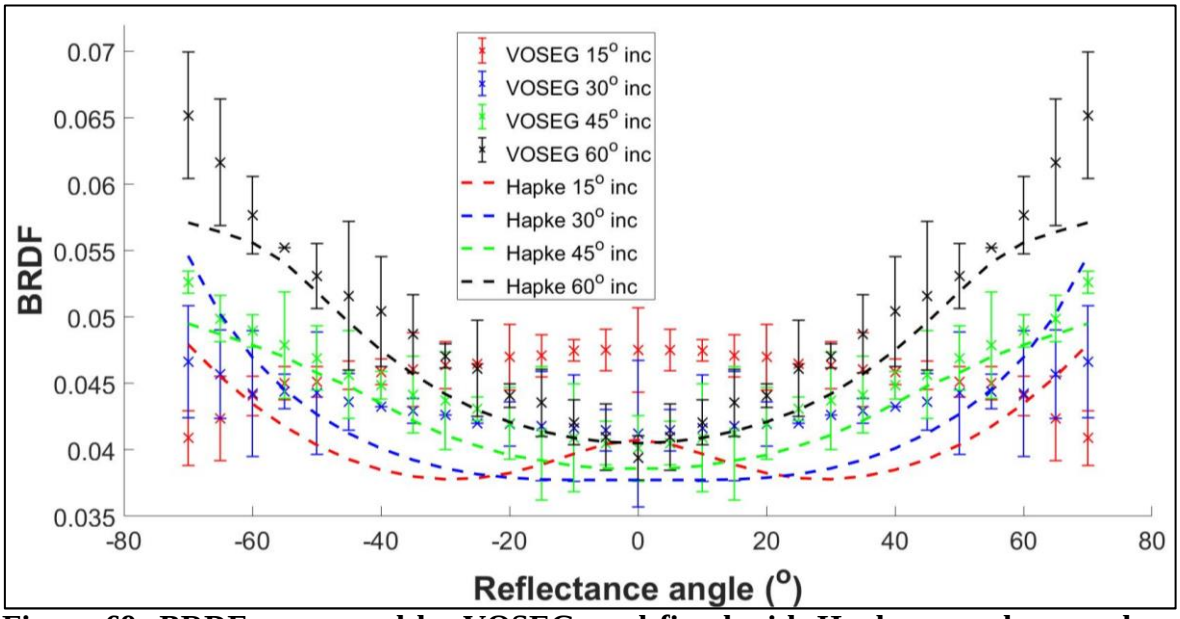

Figure 69: BRDFs measured by VOSEG, and fitted with Hapke over the complete dataset, for the smooth Apollo 16, 68810 sample in the out-of-principal plane (i.e., azimuthal angle = 90/270°) at 15° (red), 30° (blue), 45° (green) and 60° (black) incidence angles. Positive θ_r values denote θ_a=90°, and negative θ_r values denote θ_a=270°. Note that out-of-principal plane data measured at θ_a=90° can be reflected in the θ_a=270° plane, according to Helmholtz reciprocity/Kirchoff's law (Greffet and Nieto-Vesperinas, 1998).

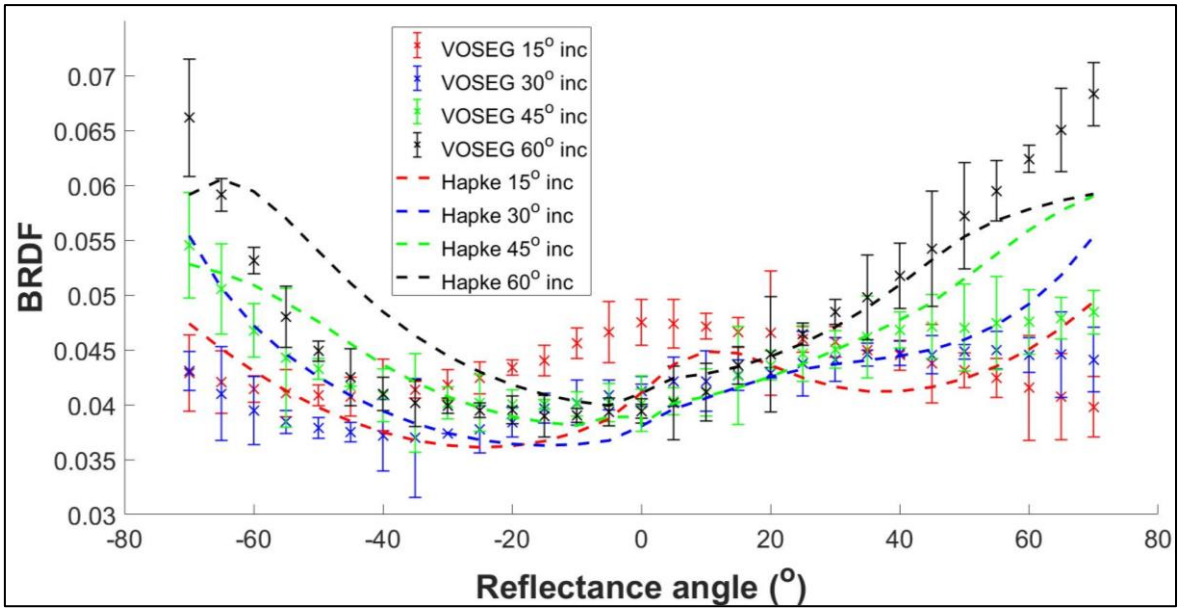

Figure 70: BRDFs measured by VOSEG, and fitted with Hapke over the complete dataset, for the smooth Apollo 16, 68810 sample in the diagonal plane (i.e., azimuthal angle = 45/135°) at 15° (red), 30° (blue), 45° (green) and 60° (black) incidence angles. Positive θ_r values denote θ_a=45°, and negative θ_r values denote θ_a=135°, but this data can be reflected for BRDFs in the opposite diagonal plane.

Figures 71, **72 and 73** now show the equivalent BRDF dataset measured in the principal, out-of-principal and diagonal planes for the rough Apollo 16, 68810 sample. Again, data at 15, 30, 45 and 60° incidence angles is included, in addition to Hapke BRDF model best fit curves, calculated by fitting the model to the complete dataset.

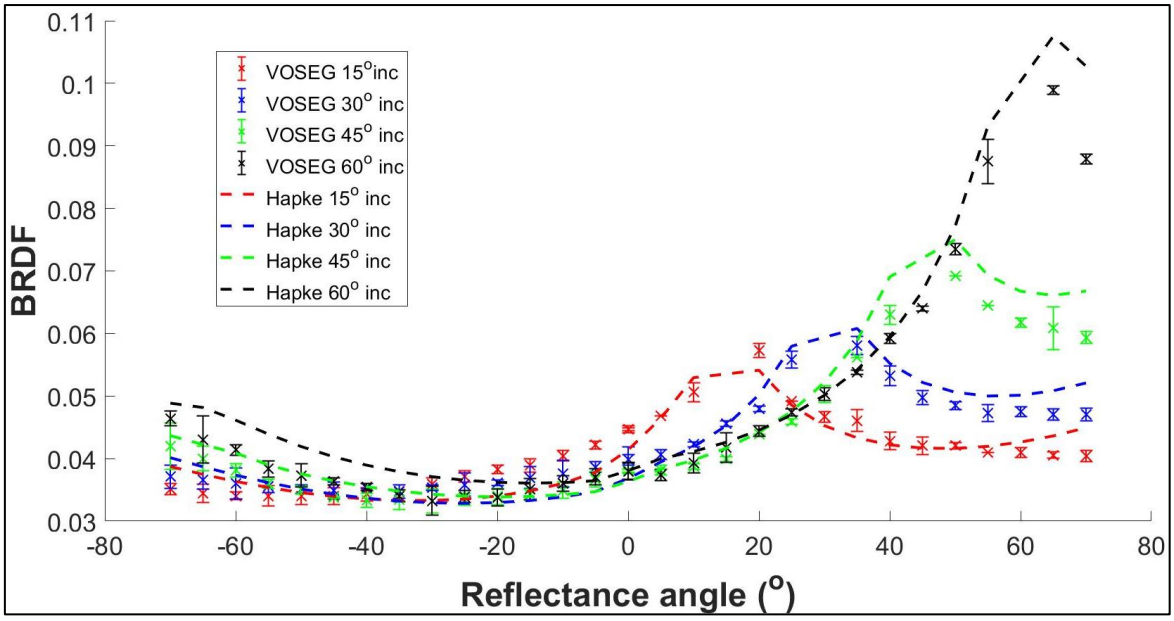

Figure 71: BRDFs measured by VOSEG, and fitted with Hapke over the complete dataset, for the rough Apollo 16, 68810 sample in the principal plane (i.e., azimuthal angle = 0/180°) at 15° (red), 30° (blue), 45° (green) and 60° (black) incidence angles. Positive θ_r values denote θ_a=0°, and negative θ_r values denote θ_a=180°.

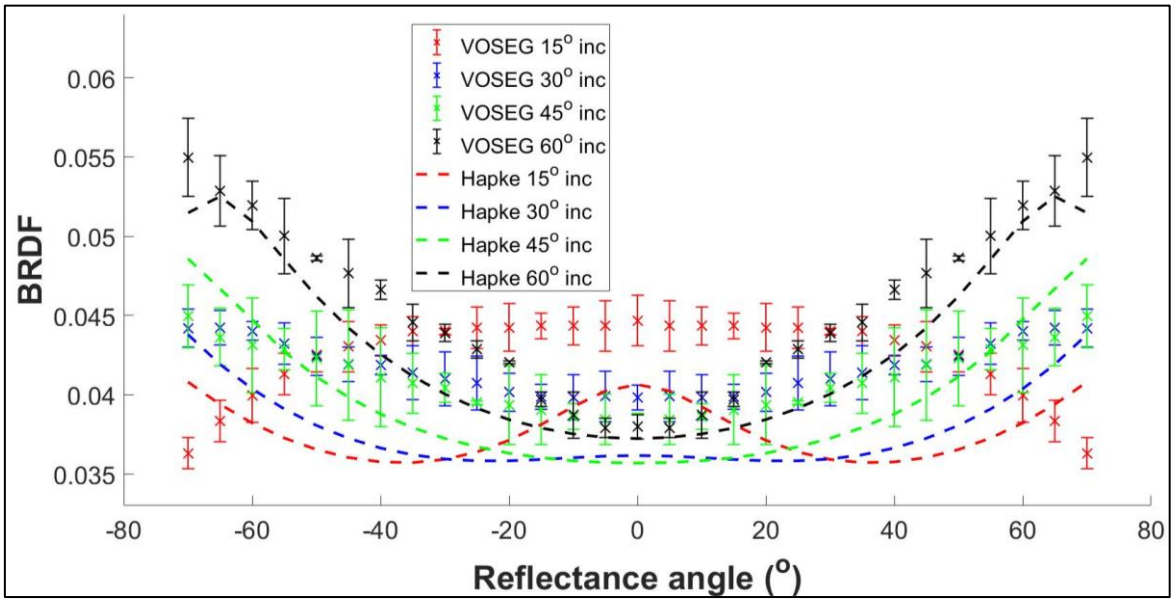

Figure 72: BRDFs measured by VOSEG, and fitted with Hapke over the complete dataset, for the rough Apollo 16, 68810 sample in the out-of-principal plane (i.e., azimuthal angle = 90/270°) at 15° (red), 30° (blue), 45° (green) and 60° (black) incidence angles. Positive θ_r values denote θ_a=90°, and negative θ_r values denote θ_a=270°. Note that out-of-principal plane data measured at θ_a=90° can be reflected in the θ_a=270° plane, according to Helmholtz reciprocity/Kirchoff's law (Greffet and Nieto-Vesperinas, 1998).

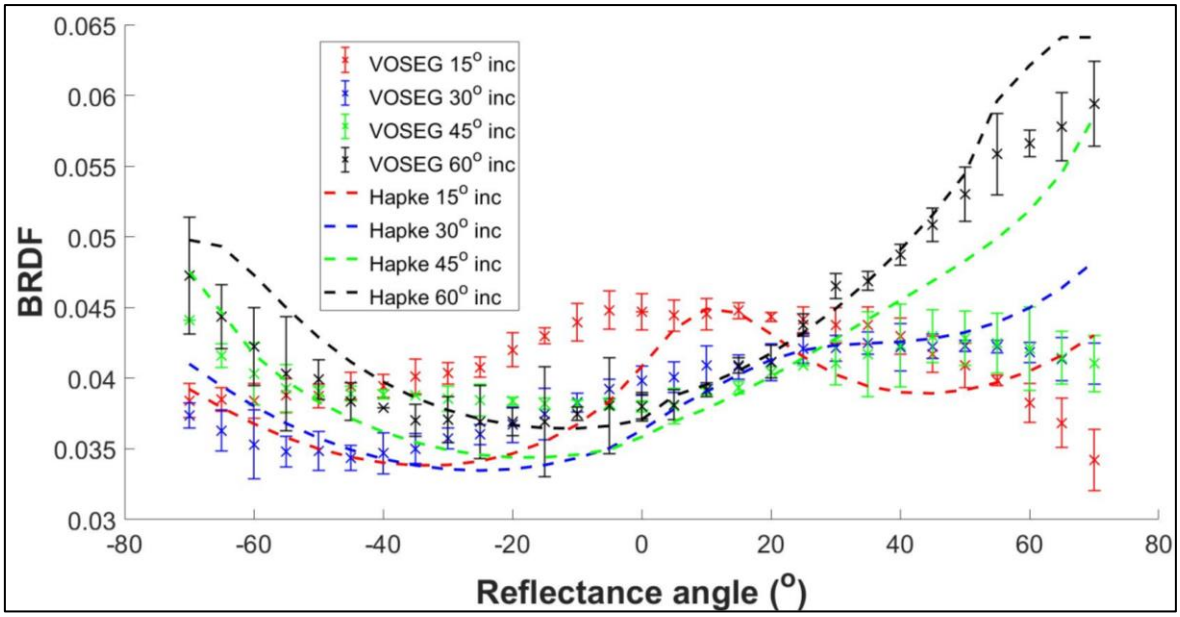

Figure 73: BRDFs measured by VOSEG, and fitted with Hapke over the complete dataset, for the rough Apollo 16, 68810 sample in the diagonal plane (i.e., azimuthal angle = 45/135°) at 15° (red), 30° (blue), 45° (green) and 60° (black) incidence angles. Positive θ_r values denote θ_a=45°, and negative θ_r values denote θ_a=135°, but this data can be reflected for BRDFs in the opposite diagonal plane.

As for the 10084 samples **Figures 74**, **75**, **76** and **77** show the differences between the rough and smooth Apollo 16, 68810 samples, by plotting ΔBRDF values for each incidence angle.

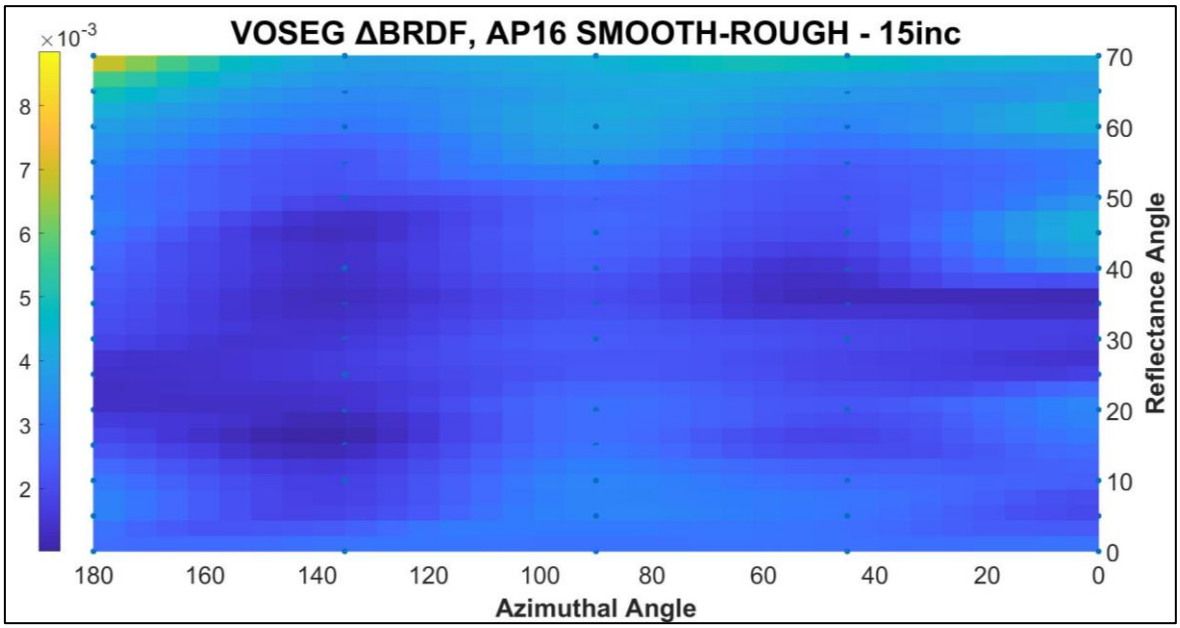

Figure 74: ΔBRDF plot for Apollo 16, 68810, rough and smooth samples, at 15° incidence. ΔBRDF calculated as the smooth BRDF profile minus the rough BRDF profile.

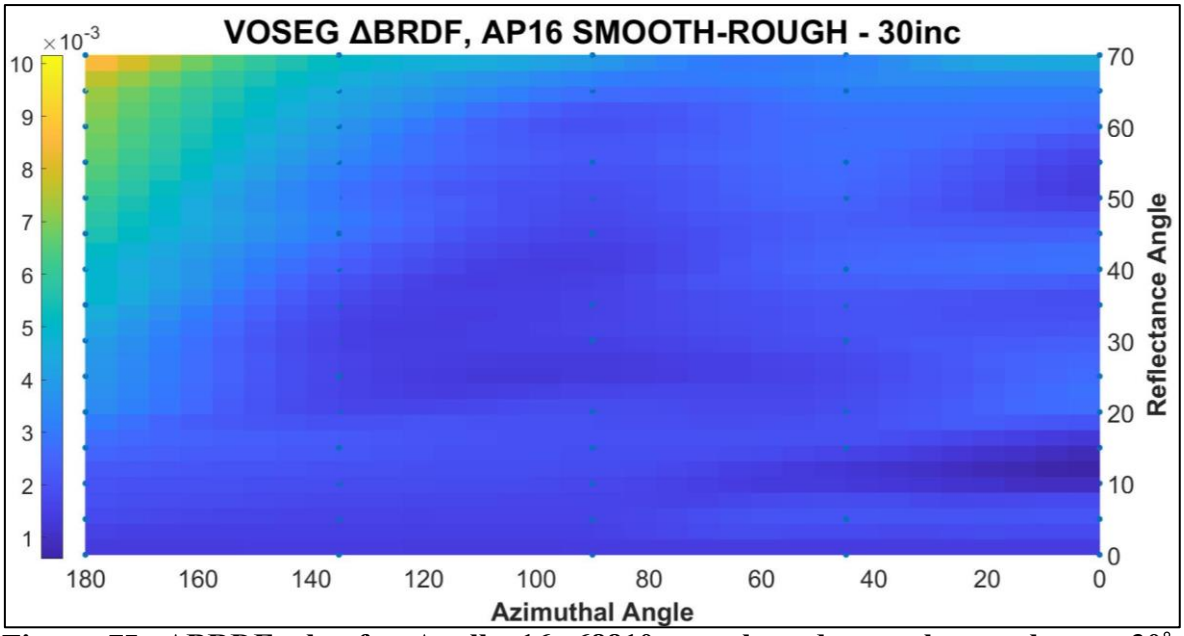

Figure 75: ΔBRDF plot for Apollo 16, 68810, rough and smooth samples, at 30° incidence. ΔBRDF calculated as the smooth BRDF profile minus the rough BRDF profile.

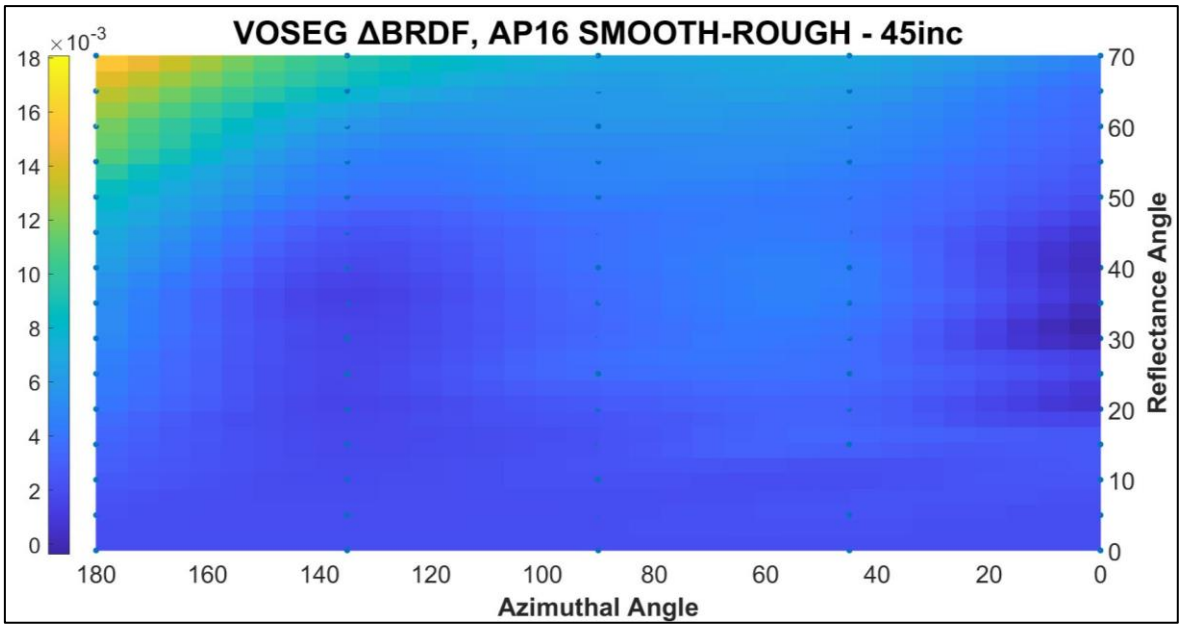

Figure 76: ΔBRDF plot for Apollo 16, 68810, rough and smooth samples, at 45° incidence. ΔBRDF calculated as the smooth BRDF profile minus the rough BRDF profile.

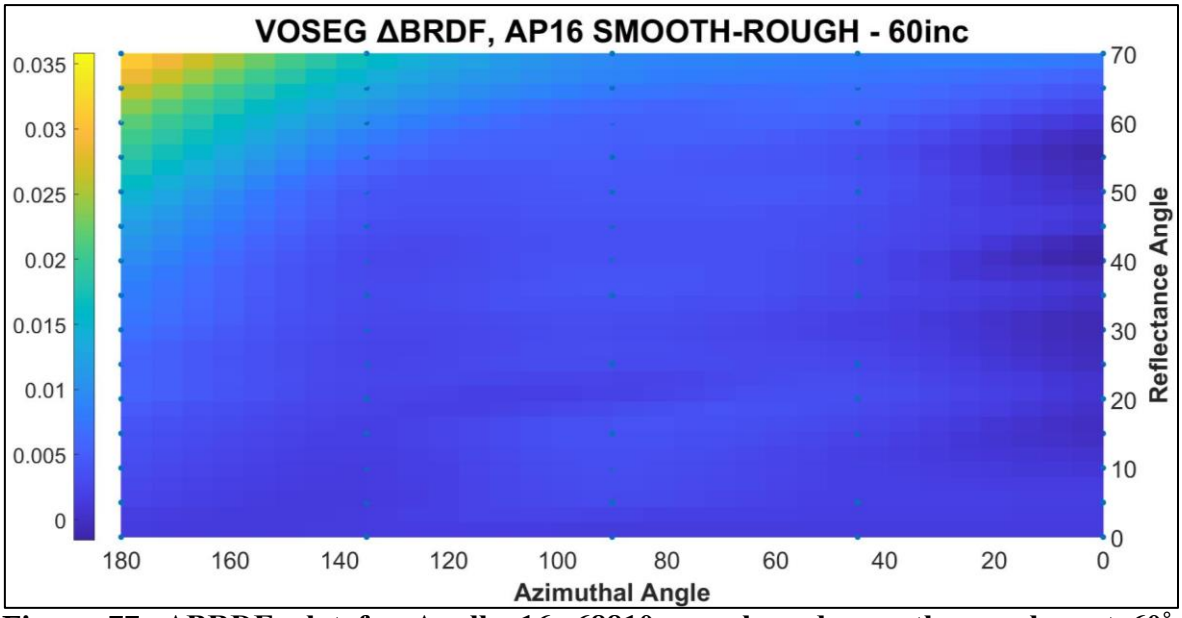

Figure 77: ΔBRDF plot for Apollo 16, 68810, rough and smooth samples, at 60° incidence. ΔBRDF calculated as the smooth BRDF profile minus the rough BRDF profile.

The first observed difference between the 68810 and 10084 samples is that the 68810 samples are generally more reflective than the 10084 samples, and so the BRDF values are consistently higher. This is to be expected, as highlands regolith samples have higher average albedo values than mare regolith samples, as can be observed when viewing the two distinct petrological regions of the Moon with the naked eye. Beyond this difference in albedo, it is necessary to compare the shapes of the 10084 and 68810 BRDF curves to be able to make useful comparisons and deductions about the scattering behaviours of the samples, from these two sets of BRDF profiles.

Importantly, the 68810 ΔBRDF plots show only positive values, meaning that the BRDF of the smooth 68810 sample is consistently higher than the BRDF of the rough 68810 sample, for all incidence angles. As for the 10084 BRDF measurements, this shows how increasing the filling factor leads to higher BRDFs at all reflectance angles, as predicted by the Hapke BRDF model and as demonstrated in **Figure 19** (Hapke, 2012).

As for 10084, BRDFs measured for the rough 68810 sample are suppressed at high reflectance angles when compared to those measured for the 68810 smooth sample, again

due to increases in shadowing for the rough sample, particularly at θ_r>45° and in the principal plane. Generally, as for the 10084 plots, below 20° reflectance angle the BRDFs of the samples agree within experimental uncertainty—with ΔBRDF values of ~0.001-0.005—and for this region the agreement improves with incidence angle. The 15° incidence angle plot shows the most consistent disagreement between the two 68810 samples, with ΔBRDF values of ~0.005, potentially showing that the effect of porosity on BRDFs is more dominant at low incidence angles. However, for the 68810 ΔBRDF plots there seems to be a dependence on azimuthal angle which is different in nature to that of the 10084 BRDF plots.

Figure 74 shows that at θ_i=15°, the 68810 measurements produce a larger discrepancy between the rough and smooth samples at θ_a=90°, than for the θ_a=45° and θ_a=135° measurements. However, **Figure 66** shows that for the 10084 measurements, the largest discrepancies between the samples is observed in the θ_a=45° plane. The difference in BRDF profiles between the 10084 and 68810 samples in the out-of-principal and diagonal planes is evident when comparing the respective figures. The Apollo 11, 10084 samples exhibit increased relative BRDFs, particularly at high reflectance angles, for the θ_a=90° and the θ_a=135° planes than is the case for the 68810 samples. This may be due to differences in the forward- and backscattering natures of the regolith types, but to be able to quantitatively interpret this compositional difference, the BRDFs must be fitted to the Hapke BRDF model, and best fit Hapke parameters must be deduced, as will be done in Part 5.2.

Again, for the rough and smooth 68810 samples, the BRDF divergence in the principal plane, with increasing reflectance angles, becomes more prominent at high incidence angles—with ΔBRDF=~0.008, e.g., the smooth sample is ~21% higher than the rough sample, for θ_i=15° and θ_r=70°; and ΔBRDF=~0.035, e.g., the smooth sample is ~71% higher than the rough sample, for θ_i=60° and θ_r=70°. This is due to increases in surface roughness, as explained previously, and as predicted by the Hapke BRDF model.

The opposition effect is observed for the 68810 samples as for the 10084 samples. Once more, the effect dominates the BRDF signal within ~10° θ_r of the peak, and so variations in the BRDF curves can only be observed for high θ_r values in the θ_a= 0° part of the principal plane for the θ_i=15° and θ_i=30° plots. **Figure 71**, for the θ_i=15° measurements, clearly shows how increased shadowing reduces the BRDF at high reflectance angles for θ_a= 0° once the opposition effect no longer dominates.

Until now, mostly qualitative deductions and comparisons have been made about this study's BRDF measurements. To fully interpret the dataset in a numerical way, the BRDFs can be fitted using the Hapke BRDF model, and best fit Hapke parameters can be determined for each of the samples. Since the filling factors and RMS slope angle values were measured for each of the samples, these parameters can be set within the model, allowing best fit values to be deduced for three key free parameters, w, b and h_S. The methodologies and results of this part of the BRDF study are given in the following section.

5.2 Deduction of Hapke Parameters and Further Constraining the Hapke Slope Angle Parameter Size-scale

As described in Part 2.1, there are nine key parameters in the Hapke BRDF model, and each plays a specific role in governing the shape of the BRDF curve predicted for a particulate surface. Some of the parameters, however, do overlap in their functions and this can be quantified by calculating correlation coefficients for each pair of fitted parameters. *K* and *w* mainly vary the amplitude of the BRDF curve (i.e. the scattering efficiency), and so the measured *K* values for our Apollo samples allow more accurate best fit values to be deduced for *w*. The b and c forward- and backscattering parameters vary the tendency of the BRDF to increase relative to the forward (towards 180° azimuthal angle) or backwards (towards 0° azimuthal angle) planes. These parameters therefore play a similar role to $\bar{\theta}$, which, as

demonstrated in Part 5.1, varies the shape of the BRDF curve at high θ_r values, particularly in the principal plane. The remaining four parameters relate to the opposition effect, the maximum amplitude of which is currently not possible to measure with VOSEG, given that its minimum phase angle is ~4°. However, the width of the opposition effect, described by h_c and h_s, is possible to probe using the VOSEG dataset. Although, since it is not possible without a laboratory polarization study to separate the CBOE and SHOE contributions to the opposition effect, only h_s will be considered. Therefore, given the separate roles of the key parameters within the model (see **Figures 19**, **20** and **23**) and given our knowledge of K and $\bar{\theta}$ for the Apollo samples measured in this study, best fit values for w, b and h_s can be deduced using the VOSEG BRDF dataset. Furthermore, given our knowledge of $\bar{\theta}$ at a range of size-scales for each of the Apollo samples, the 'goodness' of fits derived from using $\bar{\theta}$ at each size-scale can be compared, thus providing information about which size-scale is the most appropriate for setting $\bar{\theta}$ for lunar regolith.

The process of fitting the Hapke BRDF model to measured BRDF data is non-unique, in that 1) the model contains several key terms which can be set in a multitude of ways (dependent on which version of the model is used), and these are often not explained fully in the methodologies detailed within studies; and 2) the model can be fitted to the complete dataset, or to separate parts of the dataset (e.g., data at a specific incidence or azimuthal angle), and the best fit Hapke parameters deduced via these methods will vary. Therefore, this study performs and compares the Hapke fitting process using two alternative methods. The first and most obvious method is to fit the model to the complete dataset for each sample, and to deduce best fit Hapke parameters for the entire dataset, over all incidence, azimuthal and reflectance angles. The second method is to fit the model to the BRDF data at each of the four measured incidence angles, and then to average the four best fit Hapke parameters to give an overall value. The second method may not appear necessary, but given the

discrepancies shown between the Hapke BRDF model and the measured BRDF data in Part 5.1, it is useful to be able to assess whether the model is better at fitting to the laboratory data at a particular range of incidence angles. Furthermore, when fitting to a remote sensing dataset, as is done in Part 5.3, it is useful to know what effect only having limited data at a single incidence angle has on the outputted best fit values, as is the case for the Reiner Gamma target (see **Table 8**).

The methodology used for the complete Hapke fitting process—in which the model is fitted over the entire BRDF dataset measured for a given sample—is described below:

Complete Hapke Fitting Method:

- The measured filling factor value is set within the model—i.e., φ=0.6±0.02, 0.55±0.02, 0.4±0.02 or 0.41±0.02, depending on the sample. The following parameters are also set: the mean particle diameters (by length) are 80 μm and 100 μm, for the Apollo 11 and Apollo 16 samples, respectively; n_r=1.68; n_i=0.003; h_c=0; B_{C0}=0; B_{s0}=0 and c is calculated using the hockey-stick function given in Equation 2.19. All other equations and relations are as described in Part 2.
- Least-squares best fits are found by running MATLAB (Version 2020a)'s inbuilt function *lsqcurvefit*, with three open variables w, b and h_s, over the complete BRDF dataset measured for each sample. This process is performed for each measured slope angle value, corresponding to one of the five measured size-scales, 10, 50, 100, 500 or 1000 μm. The initial guess values were set as w=0.3, b=0.1 and h_s=0.1, as from (Foote *et al.*, 2020), and the boundaries were set to be $0 \leq w \leq 1$, $0.001 \leq b \leq 1$ and $0 \leq h_s \leq 1$. b=0.001 is used as the bottom boundary for b because for values beyond this point, c=2.382, which is the maximum possible value.

- w, b and h_s values are outputted, along with uncertainties and R^2 values, which provide a description of the 'goodness' of the fits. Covariance matrices are outputted for each run, and these are used to calculate correlation coefficients for each pair of fitted parameters using $COR(X,Y) = \frac{COV(X,Y)}{\sigma_X \sigma_Y}$, where $COR(X,Y)$ is the correlation coefficient between X and Y, $COV(X,Y)$ is the covariance between X and Y and σ_X and σ_Y are the standard deviations between X and Y.
- Hapke fitting function runs which produce $R^2 \geq 0.6$ are considered 'good' fits, those which produce $0.6 > R^2 \geq 0.2$ are considered 'poor' fits, and those which produce $0.2 > R^2 \geq 0$ are considered unresolved, or 'very poor' fits. These ranges were selected due to the fact that the R^2 values were broadly split into three distinct groups, each of which denoted how well the Hapke BRDF Model captured the shape of the curve. For the 'good' fits, the model had generally captured both the amplitude of the curve and shape of the 'drop off' in the curve for $\theta_r \geq 45^\circ$ due to shadowing, for the 'poor' fits, the model had only captured the shape of the curve in one way (i.e., either the amplitude or the general shape of the 'drop-off' for $\theta_r \geq 45^\circ$ due to shadowing), and for the 'very poor' fits, the model could not capture either the amplitude or the shape of the curve within the parameter constraints. This is illustrated by **Figure 78**, which shows all R^2 values deduced for the 'complete' and 'split' fitting function runs for the rough and smooth 10084 and 68810 samples (see **Figures 15**, **16**, **17**, **20** and **21**).
- From this dataset a general trend can be deduced across all samples, to determine which size-scale is the most appropriate for the Hapke slope angle parameterization.

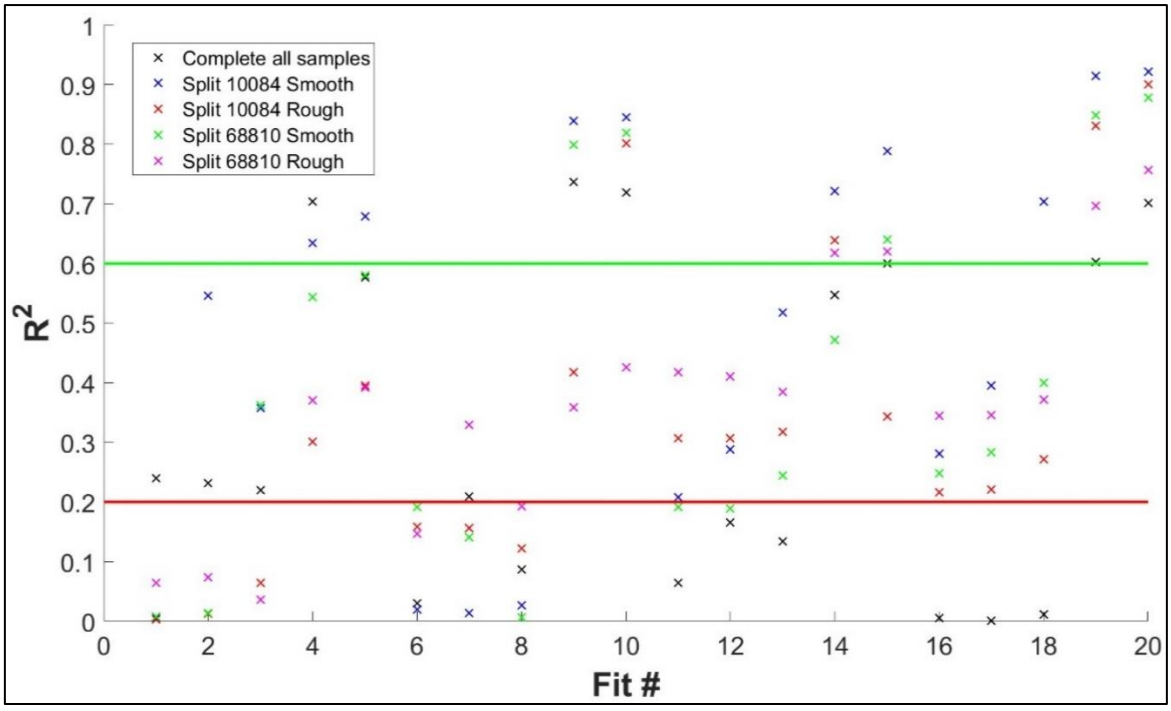

Figure 78: R^2 values determined for all 'complete' and 'split' Hapke fitting function runs for the 'smooth' and 'rough' 10084 and 68810 Apollo samples. The green line at R^2=0.6 indicates the cut-off between 'good' and 'poor' fits, and the red line at R^2=0.2 indicates the cut-off between 'poor' and 'very poor' fits.

Table 15 shows the outputted best fit values for the complete Hapke fitting method used on the VOSEG BRDF data measured for this study's four samples, with 'good' fits highlighted in green, 'poor' fits highlighted in orange and unresolved, or 'very poor' fits highlighted in red. The table shows best fit values calculated when setting $\bar{\theta}$ values to be as measured over the five size-scales (10-1000 μm), and when setting the φ values to be as measured for each of the samples. The table also provides the relative Hapke parameters deduced for the 10084 and 68810 Apollo samples in the (Foote *et al.*, 2020) study (at 550 nm), and the relative Hapke parameters deduced for the mare and highlands regions of the lunar surface in the (Sato *et al.*, 2014) remote sensing study (at 566 nm).

Sample/Study	*Size-scale (μm)*	$\bar{\theta}$ (°)	w	$\pm w$	b	$\pm b$	c	$\pm c$	h_s	$\pm h_s$	R^2
VOSEG—Rough 10084, Apollo 11	10	41.04	0.190	0.031	0.999	0.120	-0.908	2.380	0.236	0.060	0.240
	50	40.66	0.314	0.075	0.417	0.052	-0.748	0.126	0.028	0.022	0.232
	100	36.15	0.268	0.031	0.999	0.151	-0.908	0.000	0.019	0.020	0.220
	500	21.28	0.385	0.014	0.265	0.042	0.061	0.373	0.022	0.006	0.704
	1000	17.34	0.320	0.013	0.001	0.061	2.382	0.206	0.086	0.007	0.676
VOSEG—Smooth 10084, Apollo 11	10	33.46	0.022	0.265	0.999	0.230	-0.908	0.000	0.013	0.012	0.030
	50	30.57	0.500	0.067	0.440	0.184	-0.795	0.524	0.012	0.021	0.209
	100	24.64	0.394	0.143	0.639	0.279	-0.905	0.173	0.057	0.049	0.087
	500	13.80	0.143	0.004	0.334	0.023	-0.436	0.127	0.265	0.023	0.737
	1000	11.78	0.127	0.005	0.311	0.025	-0.297	0.166	0.252	0.025	0.719
VOSEG—Rough 68810, Apollo 16	10	37.73	1.16E-07	0.120	1.00	0.201	-0.907	0.000	0.038	0.081	0.064
	50	36.45	0.015	0.457	0.001	0.196	2.383	1.604	0.168	0.036	0.165
	100	32.10	0.284	0.216	0.014	0.144	2.371	0.987	0.147	0.054	0.134
	500	21.69	0.417	0.035	0.001	0.065	2.382	0.233	0.080	0.011	0.547
	1000	20.17	0.378	0.013	0.001	0.051	2.382	0.146	0.111	0.011	0.600
VOSEG—Smooth 68810, Apollo 16	10	34.54	1.38E-08	0.201	0.999	0.189	-0.908	0.000	8.90E-05	0.131	0.005
	50	32.49	9.96E-11	0.198	1.00	0.112	-0.908	1.810	2.05E-11	0.032	0.001
	100	27.11	0.118	1.645	0.546	0.210	-0.890	0.231	0.016	0.089	0.011
	500	14.27	0.428	0.009	0.117	0.012	1.685	0.126	0.140	0.012	0.602
	1000	11.80	0.383	0.012	0.089	0.016	1.958	0.141	0.169	0.015	0.701
BUG—10084	NA	10.5	0.288	NA	0.292	Na	0.405	NA	0.011	NA	NA
BUG—68810	NA	10.25	0.484	NA	0.277	NA	0.495	NA	0.011	NA	NA
Sato—Mare	NA	23.40	0.201	0.01	0.260	0.01	0.10	0.01	0.050	0.008	0.891
Sato—Highlands	NA	23.40	0.356	0.01	0.230	0.01	0.35	0.01	0.074	0.009	0.891

Table 15: Hapke parameters deduced in the VOSEG study using the complete Hapke fitting process for the four Apollo samples, and comparison to the parameters deduced in the (Sato *et al.*, 2014) (566 nm) and (Foote *et al.*, 2020) (550 nm) studies. $R^2 \geq 0.6$ for green rows, $0.6 > R^2 \geq 0.2$ for orange rows and $0.2 > R^2 \geq 0$ for red rows.

Table 15 shows that using $\bar{\theta}$ values at the three smallest size-scales (10-500 μm) produces unresolved/'very poor', or 'poor' fits to the dataset, for all four samples. In contrast to this, using $\bar{\theta}$ values at the two largest size-scales (500 and 1000 μm) generally produces 'good' fits, except for the marginally 'poor' fit to the rough Apollo 16, 68810 data. For the complete fitting process over the Apollo 11 data, using $\bar{\theta}$ values at the 500 μm size-scale provides the best fits, for both rough and smooth samples. Contrastingly, for the complete fitting process over the Apollo 16 data, using $\bar{\theta}$ values at the 1000 μm size-scale provides the best fits, for both rough and smooth samples. However, fitting with $\bar{\theta}$ values at both these size-scales generally leads to 'good' fits, with $R^2 \geq 0.6$ (with an exception at 500 μm for the rough Apollo 16 sample). Therefore, the appropriate 'practical' size-scale of the Hapke slope angle parameter when fitting the Hapke BRDF model for the lunar regolith can be considered to be between 500-1000 μm. Considering the average particle diameter of the lunar regolith is on the order of ~100 μm, size-scales of a few times this value makes physical sense, because the shadows cast by lunar regolith particles (at the measured range of incidence angles) will be on the order of 10-500 μm (e.g., a 100 μm diameter particle will cast a 173 μm shadow at θ_i=60°). The $\bar{\theta}$ values measured at the 500 μm size-scale (which has the highest average R^2 value) will therefore be used for each of the samples in the Diviner off-nadir study in Part 5.3. Additionally, in Part 5.1, the Hapke BRDF model best fit curves plotted are calculated using $\bar{\theta}$ at 500 μm.

The uncertainties derived using this method for w values are ≤4% for the 'good' fits, and the higher uncertainty values >10% for the 'poor' or unresolved/'very poor' fits are an indication that the function has not been able to find a well-fitted solution. This is also the case for each of the other best fit parameters, with h_S uncertainties generally between 8-10% for the 'good' fits (with the exception of the rough Apollo 11 fit at 500 μm, which is ~27%), and uncertainties in b of 6-17% for the 'good fits', with the exception of the rough Apollo

16 fits (for both 500 and 1000 μm) and the rough Apollo 11 fit (at 1000 μm), at which the function minimises b (i.e., finds a solution at 0.001, the lowest possible value). The higher uncertainty values >30% associated with the 'poor' or unresolved/'very poor' fits are further indication that the function has not been able to find an appropriate fit to the dataset, and these values should be ignored. It is to be expected that if the slope angle value is too high—leading to exaggerated suppression of the curve at high θ_r values—the function will attempt to resolve this by varying b, as this parameter plays a similar role within the model to $\bar{\theta}$. This reiterates the importance of setting an appropriate $\bar{\theta}$ value when fitting the Hapke BRDF model to laboratory or remote sensing data.

To quantitatively assess the correlation between the three fitted parameters correlation coefficients were calculated for each run and these values were averaged to produce the following values for each sample: Apollo 11 (10084)—$COR(w, b)$=0.533±0.061, $COR(w, h_S)$=-0.990±0.001 and $COR(b, h_S)$=-0.926±0.031; Apollo 16 (68810)—$COR(w, b)$=0.518±0.245, $COR(w, h_S)$=0.971±0.006 and $COR(b, h_S)$=-0.641±0.230. These values demonstrate that for both samples, there are strong correlations between w and h_S, with a negative correlation for the 10084 sample and a positive correlation for the 68810 sample. This is to be expected, as increases in w will increase the BRDF across all reflectance angles, and so this will lead to reductions in h_S (and vice versa); although the width of the OE only significantly affects the BRDF for $\theta_p \leq 10^{\circ}$. This is also the case for b and h_S, as variations in the HG function will lead to variations in h_S, again despite the two terms having different functionalities within the model and the fact that h_S only significantly affects the BRDF for $\theta_p \leq 10^{\circ}$. For w and b positive correlations are observed, but these are not as strong as for h_S correlations. This is also to be expected, as the model will attempt to accommodate for changes in w by varying b, despite the different functionalities of the two terms within the model.

The (Sato *et al.*, 2014) study derives the single value of $\bar{\theta}$ it uses for the study (23.4°) by fitting the model to 1x1° tile regions within an equatorial strip of the lunar surface (3°S to 3°N; 0-360°E) and averaging the best fit values. This value of $\bar{\theta}$ is higher than the values measured for the VOSEG Apollo samples at the 500 μm and 1000 μm size-scales. However, it is within 8% of the $\bar{\theta}$ values measured for the rough 10084 and 68810 samples, at 500 μm. This provides an initial indication that the regolith surface roughness profiles present on the lunar surface—as derived using remote sensing data—are similar to those of the rough 10084 and 68810 samples used in this study, and this will be further explored in Part 5.3. The $\bar{\theta}$ values used in the (Foote *et al.*, 2020) study are 10.25° and 10.5° for the 68810 and 10084 samples, respectively. These values are within 15% of the $\bar{\theta}$ values measured for the smooth Apollo samples used in the VOSEG study, at the 1000 μm size-scale; thus, the study suggests the surface roughness profiles present in the lunar regolith are similar to those of the VOSEG study's smooth 10084 and 68810 samples, however, the samples used in the (Foote *et al.*, 2020) study were prepared using a similar method to the smooth samples in this study. In Part 5.3, the visible-λ Diviner off-nadir data will be used to explore this further, for various regions of the lunar surface.

The h_S values deduced by the (Sato *et al.*, 2014) study are 0.050±0.008 and 0.074±0.009, for the mare and highlands regions, respectively. The h_S values deduced by the (Foote *et al.*, 2020) study for the two samples are both 0.011, and for the VOSEG study, the best fit h_S values when fitting with $\bar{\theta}$ values set at 500-1000 μm size-scales, are 0.022±0.006, 0.086±0.007, 0.265±0.023 and 0.252±0.025, with an average of 0.165±0.015 for the 10084 samples; and 0.140±0.012, 0.169±0.016, 0.111±0.011 and 0.080±0.011 with an average of 0.125±0.013 for the 68810 samples. Therefore, the VOSEG study deduces the highest h_S values, with those deduced by the (Sato *et al.*, 2014) study around a half to a third as high, and those deduced by the (Foote *et al.*, 2020) study around an eighth to a tenth as high. For

the (Sato *et al.*, 2014) study, this may be explained by the fact the remote sensing dataset did not contain data at low phase angles (<15°), and so there was insufficient data to accurately constrain the h_S parameter, but for the (Foote *et al.*, 2020) study, the minimum phase angle was 3°—compared to 5° for VOSEG—for the measured principal plane BRDF data, and so this cannot explain the one order of magnitude discrepancy between the deduced values. Therefore, this may also be due to differences in the semi-empirical simplifications performed within the two Hapke BRDF models.

With no information about the physical properties of the lunar surface measured in the (Sato *et al.*, 2014) study, φ is set to 0, and so *K=1*. This should lead to higher *w* values than would be expected if measured values of φ were set, as is done within the model for the VOSEG study (in which φ=0.4-0.6). The (Foote *et al.*, 2020) study does not specify whether it sets φ to be 0, or whether it uses values deduced for the samples, but varying φ between 0-0.6 can vary *K* by up to 46%, and—due to *K* and *w* serving similar functions within the model—setting φ to be 0 can lead to *w* values which are overestimated by up to ~46%. The *w* values deduced for the lunar mare and lunar highlands regions by the (Sato *et al.*, 2014) study are 0.201±0.01 and 0.356±0.01, respectively. The *w* values deduced for the Apollo 11 and Apollo 16 regolith samples in the (Foote *et al.*, 2020) study are 0.288 and 0.484, respectively. For the VOSEG study, when fitting with $\bar{\theta}$ values at the 500-1000 μm size-scales, the deduced *w* values are 0.385, 0.320, 0.143 and 0.127, with an average of 0.244 for the Apollo 11, 10084 samples; and 0.417, 0.378, 0.428 and 0.383, with an average of 0.402 for the Apollo 16, 68810 samples. Therefore, the VOSEG study deduces *w* values for the mare and highlands regolith which are ~21% and ~13% higher than those deduced by the (Sato *et al.*, 2014) study, respectively; but *w* values which are ~18% and ~20% lower than those deduced by the (Foote *et al.*, 2020) study, respectively. If the (Foote *et al.*, 2020) study sets φ to be 0, this discrepancy could be explained by the accurately set φ values within the

VOSEG study. The discrepancy between the (Sato *et al.*, 2014) and VOSEG studies cannot be explained by porosity, however, as the model set φ to be 0, and so K=1. The lunar regolith surface is highly porous, and, considering the low surface gravity on the Moon, the porosities of the lunar regolith surfaces probed by the remote sensing study are likely to be higher still than those of the Apollo samples prepared in the laboratory. If the porosity of these remotely sensed regions was higher than for the VOSEG samples (and so φ was lower), and if the (Sato *et al.*, 2014) ran the model with K=1, instead of a more accurate, higher value (i.e., K=1.115, from φ=0.3), then this would reduce the w value further, thus increasing the discrepancy between the w values deduced by the two studies. Otherwise, the discrepancy may be caused by the various semi-empirical simplifications made within the version of the Hapke BRDF model used in the (Sato *et al.*, 2014) study, or the fact the (Sato *et al.*, 2014) model is run over all mare regions of the lunar surface, and not just for petrologies similar to those of the Apollo 11 regolith samples, which, as is typical for regolith samples, are more plagioclase- and pyroxene-rich than general mare surfaces. This is demonstrated by **Figure 79**, from (Greenhagen *et al.*, 2020).

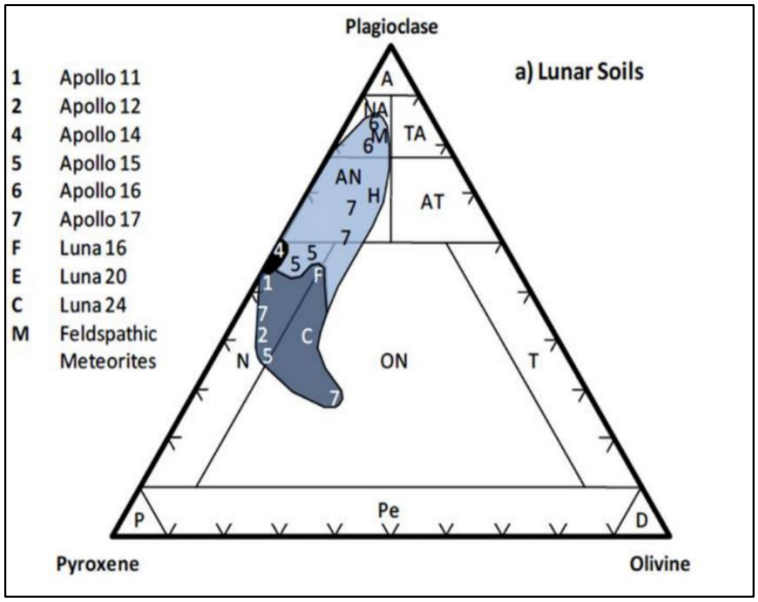

Figure 79: Showing the location of the Apollo regolith (or 'soil') samples on the lunar ternary diagram for plagioclase, pyroxene and olivine, from (Greenhagen *et al.*, 2020).

Setting $\bar{\theta}$ between the range of values used in the three studies, e.g., 10.25-23.40°, will lead to variations in b, as the function attempts to accommodate for the change in curve shape by varying the amplitude of the forward- and backscattering terms. The b values derived for the mare regions of the (Foote *et al.*, 2020) and (Sato *et al.*, 2014) studies are 0.292 and 0.260±0.010, respectively; and for the highlands regions of the two studies, they are 0.277 and 0.230±0.010, respectively. The VOSEG study derives b values between 0.265 and 0.334 for the 10084 samples, when using $\bar{\theta}$ values at 500-1000 μm size-scales. For 68810, the VOSEG study derives b values of 0.117 and 0.089 for the smooth sample, and the function minimises b for the rough sample (as so sets it to be 0.001). This suggests the model struggles to accommodate for the shape of the 68810 laboratory measured data, when fitting over the complete BRDF dataset at once. The (Foote *et al.*, 2020) study did not have the same issue, as it only had to fit to principal plane and out-of-principal plane data. Therefore, the inclusion of BRDFs measured in the diagonal plane appears to disrupt the fitting function, for the 68810 dataset. It is clear from **Figures 71** and **72** that the model produces poorer fits for the 15° incidence dataset in the diagonal planes than for the higher incidence angle datasets, as is also the case for the out-of-principal plane datasets; and at 60° incidence angle for the principal plane datasets. This leads to the question of whether the Hapke BRDF model generally fits to the VOSEG laboratory dataset better at higher, or lower, incidence angles, particularly for the novel diagonal plane dataset. To explore 1) how the 'goodness' of fits might vary if the model was fitted to the dataset at each individual incidence angle, and 2) how the Hapke parameters determined for the samples would be affected if BRDF data were only available at a single, or a limited range of incidence angle(s)—as is often the case in planetary remote sensing studies—the Hapke BRDF model is run over each individual incidence angle dataset. Using this second method, four sets of best fit Hapke parameters can be deduced, and average values can be calculated for each sample.

Split Incidence Angle Hapke Fitting Method:

The method for fitting the Hapke BRDF model to the VOSEG BRDF dataset is the same as the complete dataset fitting method, except that the process is performed over each split incidence angle dataset (15/30/45/60°), individually.

Tables 16 and **17** show the Hapke parameters outputted by this method for the Apollo 11, 10084 smooth and rough samples, respectively.

θ_i	*Size-scale (μm)*	$\bar{\theta}$ (°)	w	$\pm w$	b	$\pm b$	c	$\pm c$	h_s	$\pm h_s$	R^2
15	10	33.46	0.002	0.987	1	0.353	-0.908	0.001	3.65E-05	0.131	0.005
	50	30.57	0.272	0.028	0.001	0.101	2.382	0.535	0.014	0.019	0.546
	100	24.64	0.565	0.025	0.807	0.105	-0.908	0.001	0.005	0.008	0.358
	500	13.81	0.527	0.015	0.797	0.056	-0.908	0.101	0.010	0.005	0.634
	1000	11.78	0.523	0.014	0.805	0.050	-0.908	0.132	0.011	0.006	0.679
30	10	33.46	0.509	0.326	0.359	0.877	-0.559	0.334	3.29E-06	0.029	0.020
	50	30.57	0.499	0.325	0.383	0.883	-0.652	0.235	3.00E-04	0.042	0.013
	100	24.64	0.224	1.076	1.00	2.253	-0.908	9.130	0.040	0.024	0.026
	500	13.81	0.260	0.009	0.061	0.032	2.176	0.206	0.013	0.003	0.839
	1000	11.78	0.258	0.008	0.068	0.031	2.128	0.219	0.014	0.007	0.845
45	10	33.46	0.514	0.231	0.375	0.627	-0.623	0.545	1.15E-04	0.024	0.208
	50	30.57	0.488	0.188	0.375	0.504	-0.623	1.231	3.11E-03	0.058	0.288
	100	24.64	0.428	0.117	0.382	0.320	-0.648	1.538	0.013	0.024	0.518
	500	13.81	0.285	0.027	0.301	0.112	-0.228	0.799	0.034	0.007	0.722
	1000	11.78	0.263	0.046	0.272	0.080	0.006	0.676	0.039	0.005	0.788
60	10	33.46	0.538	0.212	0.432	0.589	-0.780	1.071	5.05E-03	0.139	0.281
	50	30.57	0.518	0.158	0.442	0.433	-0.798	1.643	0.008	0.031	0.395
	100	24.64	0.447	0.078	0.462	0.213	-0.828	0.559	0.024	0.004	0.704
	500	13.81	0.236	0.013	0.257	0.046	0.135	0.425	0.049	0.006	0.915
	1000	11.78	0.216	0.013	0.241	0.046	0.290	0.456	0.053	0.008	0.922

Table 16: Apollo 11, 10084, smooth sample Hapke parameters for each slope angle size-scale, fitted using the split incidence angle VOSEG method, at 15, 30, 45 and 60° incidence angles. Rows highlighted red indicate unresolved or 'very poor' fits (R^2<0.2);

rows highlighted orange indicate 'poor' fits ($0.2 \leq R^2 < 0.6$); rows highlighted green indicate 'good' fits ($R^2 \geq 0.6$). For this sample φ=0.60±0.02.

θ_i	*Size-scale (μm)*	$\bar{\theta}$ (°)	w	$\pm w$	b	$\pm b$	c	$\pm c$	h_s	$\pm h_s$	R^2
15	10	41.04	0.006	0.209	1.000	0.197	-0.908	0.001	0.114	0.012	0.003
	50	40.66	0.001	0.103	1.000	0.398	-0.908	0.003	0.076	0.031	0.012
	100	36.14	0.002	0.933	1.000	0.458	-0.908	0.001	0.004	0.010	0.064
	500	21.28	0.583	0.023	0.869	0.112	-0.908	0.000	0.008	0.010	0.301
	1000	17.34	0.571	0.019	0.878	0.089	-0.908	0.000	0.010	0.009	0.395
30	10	41.04	0.567	0.338	0.354	1.011	-0.536	0.371	5.67 E-07	0.010	0.159
	50	40.66	0.568	0.327	0.361	0.987	-0.567	0.339	1.41 E-05	0.007	0.156
	100	36.14	0.549	0.300	0.353	0.877	-0.532	0.362	3.89 E-05	0.017	0.122
	500	21.28	0.570	0.051	1.000	0.358	-0.908	0.001	0.013	0.008	0.418
	1000	17.34	0.563	0.021	1.000	0.136	-0.908	3.760	0.015	0.004	0.802
45	10	41.04	0.576	0.329	0.360	0.988	-0.563	0.343	4.37 E-08	0.010	0.307
	50	40.66	0.575	0.321	0.358	0.962	-0.554	0.351	9.12 E-07	0.013	0.307
	100	36.14	0.554	0.234	0.351	0.683	-0.522	0.242	7.27 E-05	0.001	0.317
	500	21.28	0.320	0.027	0.205	0.091	0.676	0.954	0.022	0.008	0.639
	1000	17.34	0.312	0.047	0.207	0.196	0.653	1.544	0.033	0.031	0.343
60	10	41.04	0.594	0.411	0.407	1.280	-0.724	0.184	0.002	0.020	0.216
	50	40.66	0.591	0.397	0.405	1.230	-0.718	0.190	0.002	0.012	0.221
	100	36.14	0.582	0.257	0.410	0.783	-0.731	0.146	0.004	0.007	0.271
	500	21.28	0.322	0.022	0.325	0.074	-0.384	0.447	0.041	0.004	0.831
	1000	17.34	0.303	0.015	0.252	0.049	0.182	0.463	0.053	0.006	0.900

Table 17: Apollo 11, 10084, rough sample Hapke parameters for each slope angle size-scale, fitted using the split incidence angle VOSEG method, at 15, 30, 45 and 60° incidence angles. Rows highlighted red indicate unresolved or 'very poor' fits ($R^2 < 0.2$); rows highlighted orange indicate 'poor' fits ($0.2 \leq R^2 < 0.6$); rows highlighted green indicate 'good' fits ($R^2 \geq 0.6$). For this sample φ=0.41±0.02.

Tables 18 and **19** then provide the average values deduced using the split incidence angle fitting method for the smooth and rough 10084 samples, respectively, for $\bar{\theta}$ values at 500-1000 μm size-scales. All fitting function uncertainties are calculated by inputting the uncertainties from the BRDF datapoints into MATLAB (Version 2020a)'s *lsqcurvefit*

function. The uncertainties given in **Tables 18**, **19**, **22** and **23** are then calculated by combining the errors determined for each value.

Hapke parameter	*Average value*	*Uncertainty (±)*
w	0.281	0.028
b	0.238	0.008
h_S	0.032	0.006
φ	0.60	0.02
$\bar{\theta}$ at 500 µm (°)	13.80	NA
$\bar{\theta}$ at 1000 µm (°)	11.78	NA

Table 18: Apollo 11, 10084, smooth sample average Hapke parameters deduced by the split incidence angle VOSEG fitting method.

Hapke parameter	*Average value*	*Uncertainty (±)*
w	0.315	0.021
b	0.261	0.007
h_S	0.039	0.005
φ	0.41	0.02
$\bar{\theta}$ at 500 µm (°)	21.28	NA
$\bar{\theta}$ at 1000 µm (°)	17.34	NA

Table 19: Apollo 11, 10084, rough sample average Hapke parameters deduced by the split incidence angle VOSEG fitting method.

Tables 20 and **21** then show the Hapke parameters outputted by the split incidence angle method for the Apollo 16, 68810 smooth and rough samples, respectively.

θ_i	*Size-scale (μm)*	$\bar{\theta}$ (°)	w	$\pm w$	b	$\pm b$	c	$\pm c$	h_s	$\pm h_s$	R^2
15	10	34.54	0.009	0.023	1.00	0.012	-0.908	3.910	3.84E-08	0.021	0.008
	50	32.49	0.003	0.011	1.00	0.009	-0.908	2.900	8.59E-12	0.012	0.014
	100	27.11	0.289	0.154	0.129	0.090	1.555	0.888	0.428	0.020	0.362
	500	14.27	0.255	0.086	0.289	0.045	-0.139	0.348	0.371	0.012	0.543
	1000	11.80	0.241	0.076	0.225	0.040	0.455	0.422	0.380	0.005	0.580
30	10	34.54	0.717	0.222	0.320	0.826	-0.354	0.535	0.078	0.050	0.191
	50	32.49	0.710	0.222	0.330	0.824	-0.413	0.471	0.015	0.012	0.141
	100	27.11	0.008		1.000	0.246	-0.908	0.000	0.001	0.022	0.007
	500	14.27	0.422	0.015	0.001	0.052	2.382	0.151	0.043	0.005	0.799
	1000	11.80	0.416	0.013	0.001	0.046	2.382	0.119	0.045	0.004	0.819
45	10	34.54	0.730	0.189	0.320	0.718	-0.354	0.449	7.00E-07	0.120	0.191
	50	32.49	0.718	0.165	0.314	0.602	-0.316	0.388	3.33E-09	0.130	0.189
	100	27.11	0.667	0.097	0.286	0.322	-0.115	1.606	0.006	0.012	0.244
	500	14.27	0.467	0.049	0.209	0.155	0.631	1.400	0.074	0.031	0.472
	1000	11.80	0.398	0.112	0.192	0.140	0.824	1.328	0.141	0.010	0.640
60	10	34.54	0.626	0.325	0.651	1.112	-0.906	0.041	1.000	1.110	0.248
	50	32.49	0.607	0.272	0.642	0.834	-0.905	0.866	1.000	0.834	0.283
	100	27.11	0.471	0.222	0.443	0.236	-0.800	0.780	1.000	0.236	0.400
	500	14.27	0.319	0.083	0.190	0.026	0.847	0.300	0.382	0.021	0.849
	1000	11.80	0.306	0.071	0.162	0.024	1.176	0.280	0.334	0.014	0.878

Table 20: Apollo 16, 68810, smooth sample Hapke parameters for each slope angle size-scale, fitted using the split incidence angle VOSEG method, at 15, 30, 45 and 60° incidence angles. Rows highlighted red indicate unresolved or 'very poor' fits (R^2<0.2); rows highlighted orange indicate 'poor' fits (0.2≤R^2<0.6); rows highlighted green indicate 'good' fits (R^2≥0.6). For this sample φ=0.55±0.02.

θ_i	*Size-scale (μm)*	$\bar{\theta}$ (°)	w	$\pm w$	b	$\pm b$	c	$\pm c$	h_s	$\pm h_s$	R^2
15	10	37.73	0.001	0.010	1.000	0.012	-0.908	9.130	0.007	0.102	0.064
	50	36.45	0.008	0.102	1.000	0.051	-0.908	9.130	0.033	0.012	0.074
	100	32.10	0.008	0.020	1.000	0.171	-0.908	9.138	0.035	0.123	0.036
	500	21.69	0.341	0.127	0.001	0.063	2.382	0.220	0.316	0.013	0.371
	1000	20.17	0.334	0.119	0.001	0.058	2.382	0.187	0.315	0.008	0.392
30	10	37.73	0.063	0.932	0.001	0.566	2.382	3.277	0.245	0.566	0.147
	50	36.45	0.566	0.553	0.717	0.201	-0.908	0.016	1.000	0.064	0.329
	100	32.10	0.534	0.599	0.794	0.012	-0.908	0.000	1	0.682	0.192
	500	21.69	0.576	0.554	0.708	0.002	-0.907	0.000	1.000	0.124	0.359
	1000	20.17	0.711	0.078	0.952	0.490	-0.908	0.040	0.039	0.009	0.426
45	10	37.73	0.752	0.193	0.314	0.812	-0.316	0.570	0.002	0.009	0.417
	50	36.45	0.747	0.180	0.315	0.748	-0.322	0.522	0.003	0.010	0.410
	100	32.10	0.717	0.122	0.285	0.455	-0.107	0.994	0.001	0.009	0.384
	500	21.69	0.537	0.025	0.050	0.075	2.242	0.373	0.002	0.006	0.618
	1000	20.17	0.515	0.024	0.024	0.072	2.349	0.276	0.002	0.007	0.620
60	10	37.73	0.653	0.375	0.585	0.231	-0.899	0.186	1.000	0.024	0.345
	50	36.45	0.643	0.340	0.569	0.982	-0.896	0.084	1.000	0.012	0.346
	100	32.10	0.565	0.287	0.422	0.410	-0.760	1.641	1.000	0.410	0.372
	500	21.69	0.301	0.154	0.136	0.007	1.477	0.079	1.000	0.007	0.697
	1000	20.17	0.267	0.132	0.113	0.006	1.727	0.062	1.000	0.006	0.757

Table 21: Apollo 16, 68810, rough sample Hapke parameters for each slope angle size-scale, fitted using the split incidence angle VOSEG method, at 15, 30, 45 and 60° incidence angles. Rows highlighted red indicate unresolved or 'very poor' fits (R^2<0.2); rows highlighted orange indicate 'poor' fits (0.2≤R^2<0.6); rows highlighted green indicate 'good' fits (R^2≥0.6). For this sample φ=0.40±0.02.

Tables 22 and **23** then provide the average values deduced using the split incidence angle fitting method for the smooth and rough 68810 samples, respectively, for $\bar{\theta}$ values at 500-1000 μm size-scales.

Hapke parameter	*Average value*	*Uncertainty (±)*
w	0.388	0.057
b	0.063	0.033
h_S	0.221	0.011
φ	0.40	0.02
$\bar{\theta}$ at 500 μm (°)	14.27	NA
$\bar{\theta}$ at 1000 μm (°)	11.80	NA

Table 22: Apollo 16, 68810, smooth sample average Hapke parameters deduced by the split incidence angle VOSEG fitting method.

Hapke parameter	*Average value*	*Uncertainty (±)*
w	0.485	0.155
b	0.155	0.083
h_S	0.135	0.007
φ	0.55	0.02
$\bar{\theta}$ at 500 μm (°)	21.69	NA
$\bar{\theta}$ at 1000 μm (°)	20.17	NA

Table 23: Apollo 16, 68810, rough sample average Hapke parameters deduced by the split incidence angle VOSEG fitting method.

As for the complete fitting process, using $\bar{\theta}$ values in the split fitting process at the three smallest size-scales (10-500 μm) produces unresolved/'very poor', or 'poor' fits to the dataset, for all four samples and at all incidence angles (except for the 60° incidence angle smooth Apollo 11 dataset). But when assessing the goodness of fits using $\bar{\theta}$ values at the two largest size-scales (500 and 1000 μm) for this method, various patterns emerge. Fitting the model to the BRDF data at 15° and 30° incidence angle generally produces 'poor' or 'very poor'/unresolved fits for both rough Apollo samples, with fits of $R^2<0.45$ (except for the 1000 μm fit at 30° for the 10084 sample, which produces $R^2=0.802$). For 45° and 60° incidence, fitting the model to the 68810 data at the two largest size-scales generally leads to 'good' fits for both samples, with $0.640\leq R^2\leq 0.878$ (except for the smooth sample at 45° incidence and 500 μm, which produces $R^2=0.472$). Fitting to the 10084 data at the two largest size-scales generally leads to 'good' fits for both samples, with $0.639\leq R^2\leq 0.9220$ (except for the rough sample at 45° incidence and 500 μm, which produces $R^2=0.639$).

Another notable result is that the split fitting process generally leads to higher R^2 values than the complete fitting process when the fits are 'good', with R^2 averages of R^2=0.783±0.104 and R^2=0.793±0.111 for the smooth and rough 10084 samples, respectively, and R^2=0.797±0.093 and R^2=0.673±0.067 for the smooth and rough 68810 samples, respectively. For the complete fitting process, the comparative R^2 values are R^2=0.728±0.013 and R^2=0.640±0.091 for the smooth and rough 10084 samples, respectively, and R^2=0.652±0.070 and R^2=0.574±0.037 for the smooth and rough 68810 samples, respectively. Thus, the R^2 values taken from the 'good' fits (using $\bar{\theta}$ values at 500 and 1000 μm size-scales) are consistently higher for the split fitting method than for the complete fitting method. This may be explained by the fact the model does not generally fit as well to the 15° and 30° incidence angle datasets as it does to the 45° and 60° datasets. Therefore, the complete fitting process leads to Hapke parameter values which accommodate for the low incidence angle datasets, thus leading to lower overall 'goodness' of fits than for when the 45° and 60° datasets are fitted separately. This suggests, therefore, that if data at only a limited range of incidence angles is available, the 'goodness' of fits and the resulting output Hapke parameters may vary, depending on whether a study contains high or low incidence angle data. This can be visualised by comparing **Figure 61** with **Figure 80**, which shows the Hapke BRDF model fitted to the VOSEG 10084 BRDF data, over all four incidence angles in the principal plane and using the split fitting method.

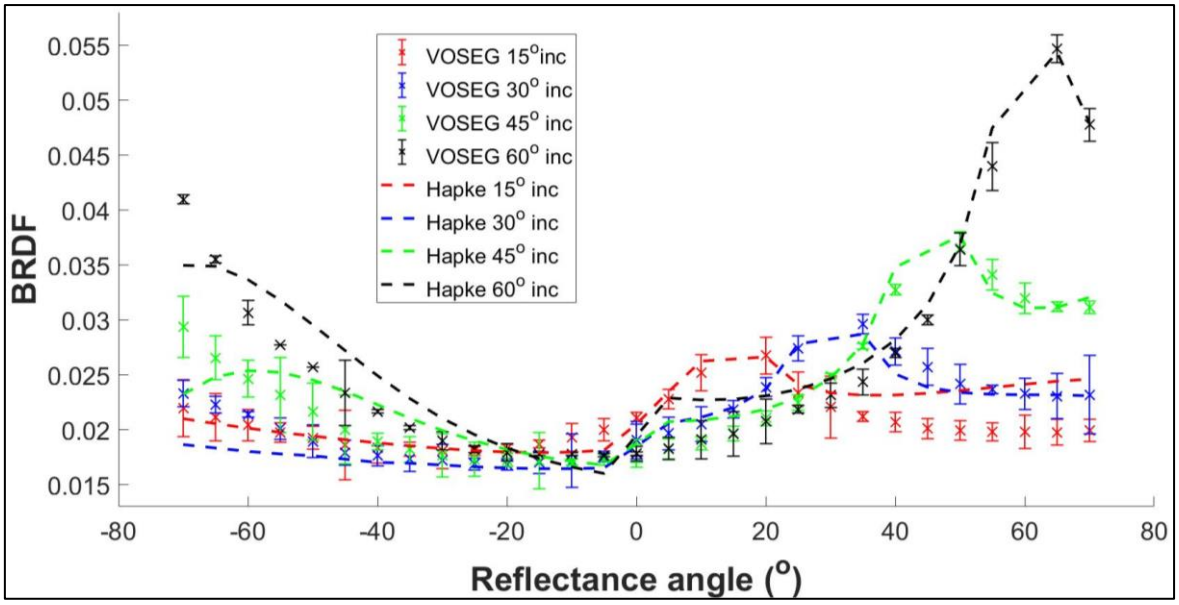

Figure 80: BRDFs measured by VOSEG, and fitted with Hapke over split incidence angle datasets, for the rough Apollo 11, 10084 sample in the principal plane (i.e., azimuthal angle = 0/180°) at 15° (red), 30° (blue), 45° (green) and 60° (black) incidence angles. Positive θ_r values denote θ_a=0°, and negative θ_r values denote θ_a=180°. The slope angle, $\bar{\theta}$, was set to be 21.28°, as measured for the sample at the 500 µm size-scale.

It is clear from **Figure 80** that the fitting process, when split into incidence angles, performs more naturally, and does not compensate for the shapes of the curves at other incidence angles when attempting to fit to the VOSEG BRDF data. Importantly, the split fitting process produces the same result as the complete fitting process when considering which size-scale to use when setting the $\bar{\theta}$ value; in that, for the Apollo 11 dataset, the 500 µm size-scale provides the best fits (by R^2), for both rough and smooth samples, and for Apollo 16, using $\bar{\theta}$ values at the 1000 µm size-scale provides the best fits (by R^2), for both rough and smooth samples.

Using the split fitting method, the average Hapke Parameter values deduced by the study over the 500 µm and 1000 µm size-scales are as follows:

- The average *w* values are determined as 0.281±0.028 and 0.315±0.021 for the 10084 smooth and rough samples, respectively, and 0.388±0.057 and 0.485±0.155 for the 68810 smooth and rough samples, respectively. Therefore, the *w* value determined for the 10084 samples is ~22% higher than for the complete fitting method, and

hence, the value now agrees with the (Foote *et al.*, 2020) study, although it is further from the value determined for the mare in the (Sato *et al.*, 2014) study. The *w* value determined for the 68810 samples using the split fitting method increased by ~9%, as compared to the complete fitting method. Therefore, this value is also now in agreement with the value determined by the (Foote *et al.*, 2020) study, although once again it has diverged further from the value determined for the highlands in the (Sato *et al.*, 2014) study.

- The average b values are determined as 0.238±0.008 and 0.261±0.007 for the 10084 smooth and rough samples, respectively, and 0.063±0.033 and 0.155±0.183 for the 68810 smooth and rough samples, respectively. Hence, the b value determined for the 10084 sample has increased by ~213%, and the b value determined for the 68810 sample has increased by ~22%. This removes the discrepancy between the values determined by the VOSEG and (Sato *et al.*, 2014) studies (e.g., b=0.250±0.008 (VOSEG) and b=0.260±0.010 (Sato)), for the mare/10084 sample, and it brings the value to within ~13% of the value determined in the (Foote *et al.*, 2020) study (b=0.292). For 68810, the average deduced b value has increased by ~22%, as compared to the complete fitting process, although this value is still a factor of 2.5-3 times lower than the values determined in the (Sato *et al.*, 2014) and (Foote *et al.*, 2020) studies. This may be due to inconsistencies in the functions used within the Hapke BRDF Model, thus motivating a standardised modelling approach.
- The average h_S values are determined to be 0.032±0.006 and 0.039±0.005 for the 10084 smooth and rough samples, respectively, and 0.221±0.149 and 0.135±0.148 for the 68810 smooth and rough samples, respectively. Importantly, the split fitting method leads to best fit h_S values which are closer to the values determined in the (Sato *et al.*, 2014) and (Foote *et al.*, 2020) studies, in particular for the rough 10084

sample, which is in agreement with the (Sato *et al.*, 2014) mare value. Although the deduced VOSEG 10084 values are closer to the (Foote *et al.*, 2020) study than for the complete fitting process values, they are still higher than this study's values by approximately a factor of three. Whilst the average deduced h_S value for the 10084 sample has decreased by ~80% for the 10084 sample—meaning the value is closer to the two remote sensing studies—the average deduced h_S value for the 68810 sample has increased by ~42%, meaning the discrepancy has also increased between the VOSEG study and the two remote sensing studies. Again, this may be due to inconsistencies in the functions used within the Hapke BRDF Model.

5.2.1 Effect of Removing the Opposition Effect

Now the two fitting processes, and the Hapke parameter outputs they produce, have been compared, another important consideration is how the opposition effect terms affect the Hapke BRDF model's ability to fit to laboratory data. The opposition effect is vital to the model's ability to fit in the principal plane, and how it dominates the signal at low phase angles is key to understanding what range of phase angles is required for remote sensing studies. Therefore, a key question is: What effect would removing the opposition effect terms from the model—by setting B_{S0}=0 and B_{C0}=0—have on the outputted Hapke parameters? Hence, the complete fitting method is used to fit the Hapke BRDF model over the VOSEG BRDF data, but with the opposition effect terms turned off**. Figures 81**, **82**, **83** and **84** show principal plane VOSEG data and Hapke BRDF model fits without the opposition effect, for the smooth 10084, rough 10084, smooth 68810 and rough 68810 samples, respectively.

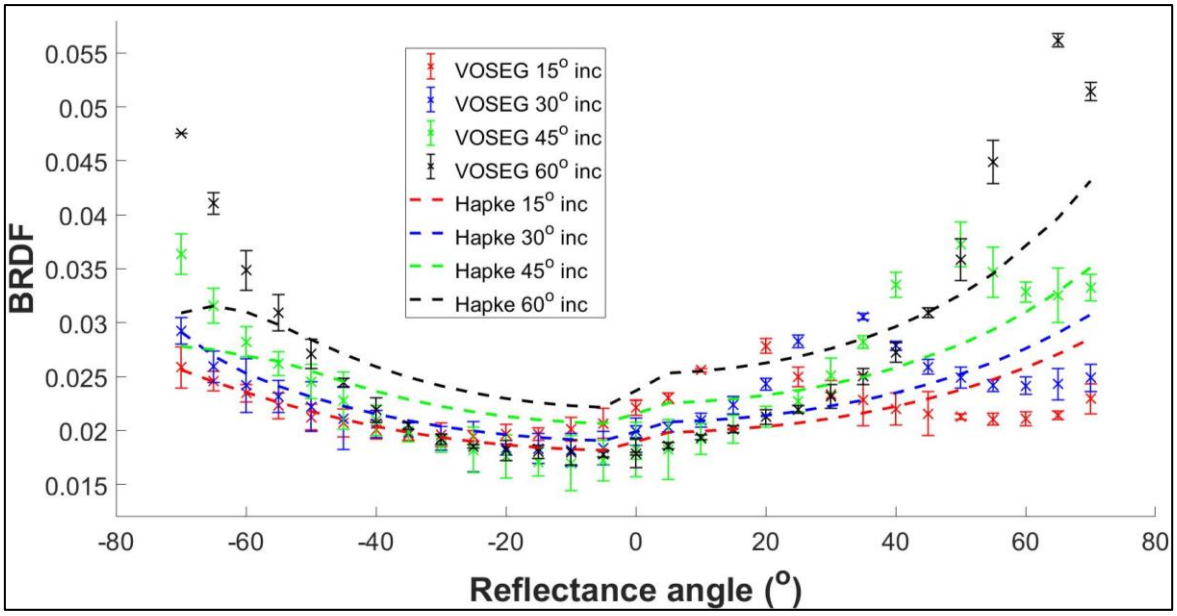

Figure 81: BRDFs measured by VOSEG, and fitted with Hapke over the complete dataset, for the smooth Apollo 11, 10084 sample in the principal plane (i.e., azimuthal angle = 0/180°), at 15, 30, 45 and 60° incidence angles, and with the opposition effect turned off. Positive θ_r values denote θ_a=0°, and negative θ_r values denote θ_a=180°.

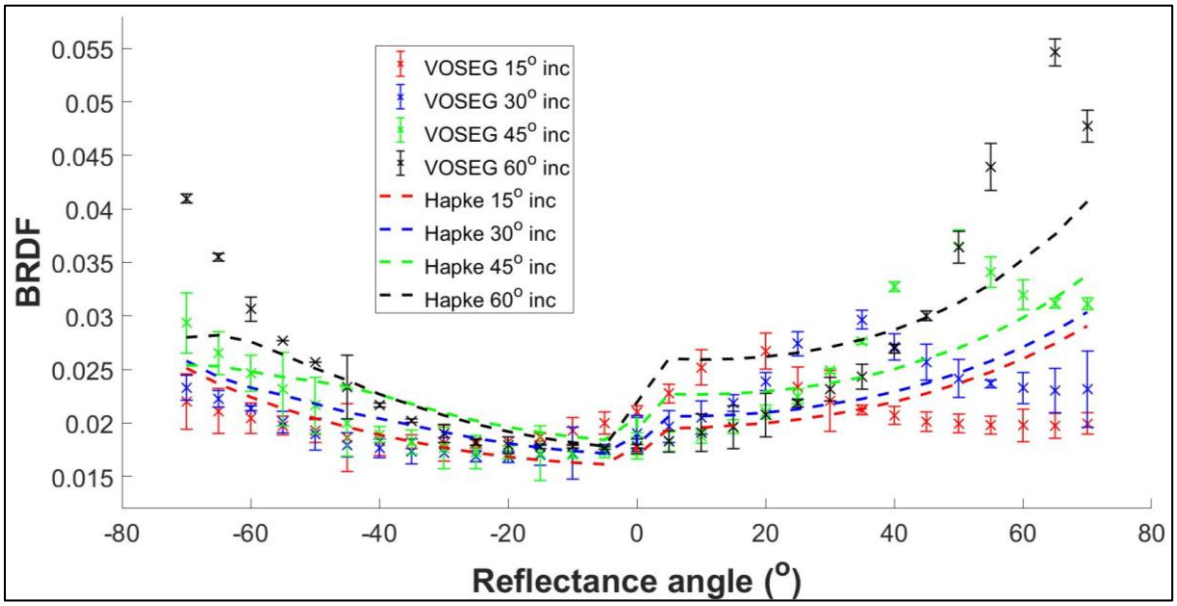

Figure 82: BRDFs measured by VOSEG, and fitted with Hapke over the complete dataset, for the rough Apollo 11, 10084 sample in the principal plane (i.e., azimuthal angle = 0/180°), at 15, 30, 45 and 60° incidence angles, and with the opposition effect turned off. Positive θ_r values denote θ_a=0°, and negative θ_r values denote θ_a=180°.

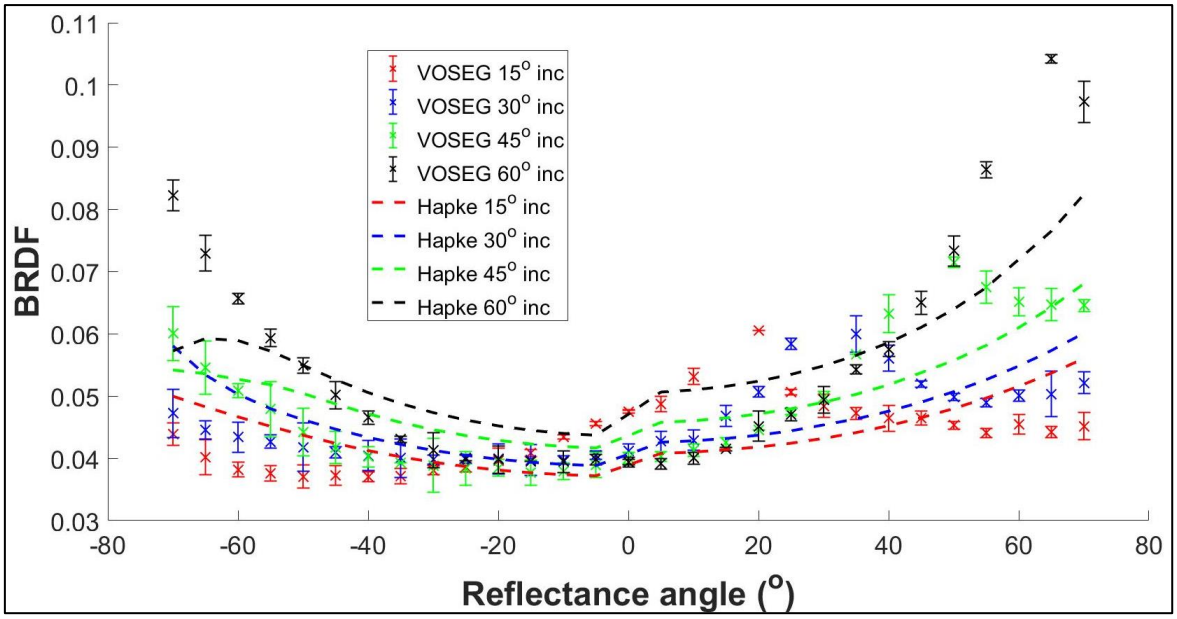

Figure 83: BRDFs measured by VOSEG, and fitted with Hapke over the complete dataset, for the smooth Apollo 16, 68810 sample in the principal plane (i.e., azimuthal angle = 0/180°), at 15, 30, 45 and 60° incidence angles, and with the opposition effect turned off. Positive θ_r values denote θ_a=0°, and negative θ_r values denote θ_a=180°.

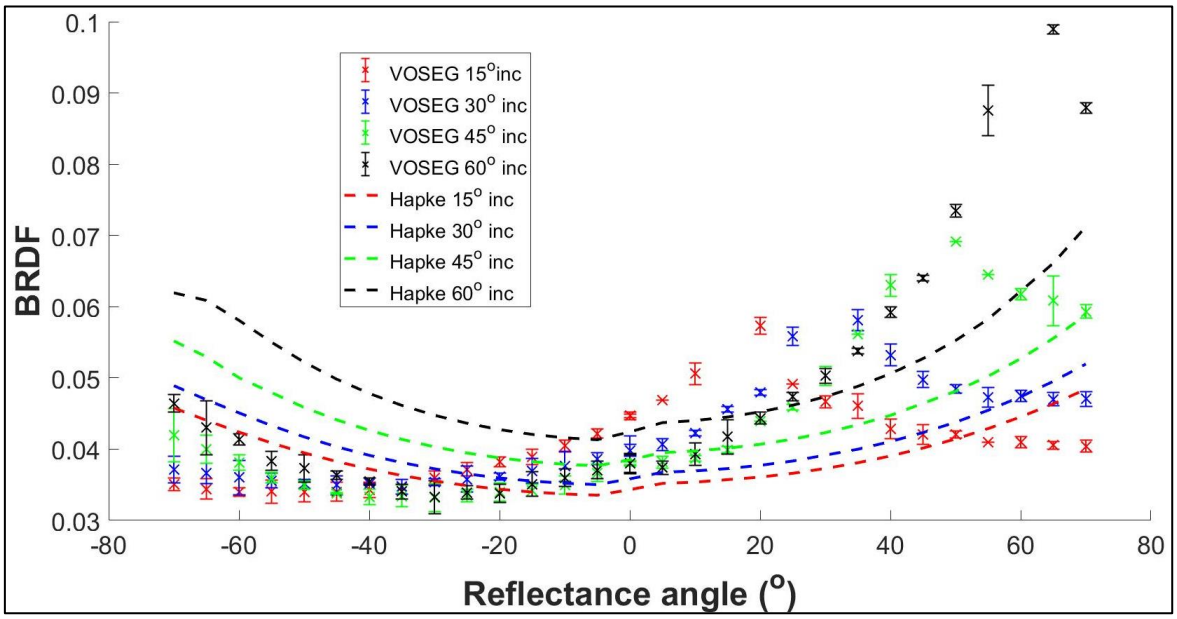

Figure 84: BRDFs measured by VOSEG, and fitted with Hapke over the complete dataset, for the rough Apollo 16, 68810 sample in the principal plane (i.e., azimuthal angle = 0/180°), at 15, 30, 45 and 60° incidence angles, and with the opposition effect turned off. Positive θ_r values denote θ_a=0°, and negative θ_r values denote θ_a=180°.

Figures 81, **82**, **83** and **84** demonstrate the importance of the opposition effect terms, as without their inclusion the model cannot capture the surge in signal in the 0° azimuthal plane. This leads 1) to skewed *w* values, as the model over- or underestimates the scattering efficiency of the sample as it attempts to accommodate for the opposition effect surge, or 2)

to inaccuracies in the *b* parameter outputs, as the model attempts to accommodate for the surge in signal observed in one half of the plane by varying the forward- and backscattering coefficients. **Table 24** shows the best fit Hapke parameters deduced when the opposition effect terms are turned off, and compares them to the original complete fitting method values shown in **Table 15**.

Sample/Study	φ	$\bar{\theta}$ (°)	w	$\pm w$	b	$\pm b$	R^2
Rough 10084 no OE	0.41	21.28	0.362	0.040	0.098	0.034	0.306
Rough 10084 with OE	0.41	21.28	0.385	0.014	0.265	0.042	0.704
Smooth 10084 no OE	0.60	13.80	0.262	0.029	0.007	0.022	0.393
Smooth 10084 with OE	0.60	13.80	0.143	0.004	0.334	0.023	0.737
Rough 68810 no OE	0.40	21.69	0.543	0.056	0.001	0.042	0.255
Rough 68810 with OE	0.40	21.69	0.417	0.035	0.001	0.065	0.547
Smooth 68810 no OE	0.55	11.80	0.480	0.047	0.001	0.023	0.330
Smooth 68810 with OE	0.55	11.80	0.383	0.012	0.089	0.016	0.701
BUG—10084	NA	10.5	0.288	NA	0.292	Na	NA
BUG—68810	NA	10.25	0.484	NA	0.277	NA	NA
Sato—Mare	NA	23.40	0.201	0.01	0.260	0.01	0.891
Sato—Highlands	NA	23.40	0.356	0.01	0.230	0.01	0.891

Table 24: Hapke parameters deduced in the VOSEG study using the complete Hapke fitting process with the opposition effect terms turned off, for the four Apollo samples, and comparison to the parameters deduced in the VOSEG BRDF study, and the (Sato *et al.*, 2014) (566 nm) and (Foote *et al.*, 2020) (550 nm) studies. The values given are for when the model is run with $\bar{\theta}$ values set to those measured at the 500 µm size-scale.

The first result from **Table 24** is that removing the opposition effect within the model leads to consistently poorer fits than when performing the process with the opposition effect terms turned on. Secondly, the best fit parameters shown in the table reiterate that the *w* and *b* values are skewed as described above. Finally, the relative uncertainties derived for each of the best fit *w* and *b* values are consistently larger, as the model struggles to fit to the shape of the laboratory data. This demonstrates the importance of the opposition effect

parameterisation within the Hapke BRDF model, and shows the importance of including data in the principal plane when fitting to laboratory or remote sensing photometry datasets.

Now the Hapke BRDF model and the various practical considerations related to fitting it to laboratory or remote sensing datasets have been thoroughly explored, it is now possible to build upon this process to enable remote sensing data from Diviner to be interpreted in a novel way. The method uses the best fit w Hapke parameters and the physical properties deduced for the Apollo samples measured in the VOSEG study to constrain w and φ when interpreting the visible-λ Diviner off-nadir data. Furthermore, it uses the split incidence angle Hapke fitting process, due to the improved agreement between the VOSEG best fit parameters and those deduced in the (Sato *et al.*, 2014; Foote *et al.*, 2020) studies when using this method.

5.3 Interpreting Diviner Off-nadir Data using the Laboratory BRDF Dataset and Deduction of Hapke Parameters

In the previous section, the practical size-scale of $\bar{\theta}$ was further constrained and best fit w values were deduced, which were not overestimated due to the use of measured φ values (see **Figures 19** and **20**). Therefore, the visible off-nadir data measured by Diviner—as described in Part 1.2.3—can now be interpreted using the Hapke BRDF model, by deducing best fit estimates for b, h_S and $\bar{\theta}$ for the various targets on the lunar surface (see **Table 4**). This process is now possible because w values can be set within the model for mare and highlands regions using the values determined for the rough laboratory samples, which, as is demonstrated in **Figure 85**, appear similar in physical properties to the regolith structures present on the lunar surface. This therefore enables the $\bar{\theta}$ parameter to be set as one of the three open parameters within the model.

The visible-λ off-nadir data measured by channels 1 and 2 (λ=0.35-2.80 μm) of Diviner is yet to be comprehensively analysed, and thus, this is one of the first photometry studies to utilize this dataset (Greenhagen *et al.*, 2017). The methodology used to interpret the Diviner off-nadir data for each target, and hence, to produce best fit Hapke parameters using a fitting process which builds on the work done in Part 5.2, is detailed below:

Step 1—Data preparation

- This study uses raw radiance measurements at different viewing angles as this produces the most comparable data to goniometry measurements. The Diviner off-nadir targets were selected for their flatness and so there is currently no need to take local topography into account.
- For each target, a code scans through the available channels 1 and 2 off-nadir radiance data and all data points at 0/45/90/135/180° azimuthal angles are binned into ±2.5° angle bins. This produces 'first stage' datasets for each azimuthal angle plane.
- These 'first stage' datasets are then split further by binning all data at 0/15/30/45/60° (±2.5°) incidence angles. This produces 'second stage' datasets, which are split by incidence and azimuthal angles, thus producing principal, out-of-principal and diagonal plane datasets.
- The reflectance angles of each data point within the 'second stage' datasets are then rounded to the closest integer value.
- All overlapping data points at each reflectance angle are averaged, and the standard deviation of the values is used as the uncertainty.
- This creates radiance functions which can be translated to BRDFs by shifting the curves so that the values from Diviner and the relevant rough Apollo samples—as measured by VOSEG—at θ_r=0° are equal. Hence, the curves become directly comparable to the

BRDFs measured by VOSEG, and, in step 2, the w and φ parameters can be set as for the relevant rough VOSEG Apollo sample.

Step 2—Hapke BRDF model fitting

- Hapke parameters w and φ are set using the values determined for the appropriate rough Apollo samples in the VOSEG BRDF study—e.g., w=0.405 and φ=0.41 for highlands-like regions, and w=0.315 and φ=0.40 for mare-like regions. This continues with the assumption that the regolith present on the lunar surface is in a similar state to the rough samples used in the VOSEG BRDF study, as is justified by **Figure 85**.
- Optical constants and all other relevant parameters are set as in the methods described in Part 5.2. For highlands regions, 68810 data is used; for mare regions, 10084 data is used; for regions with unconstrained petrologies (e.g., those which have not yet been visited by landers or humans), the method is repeated for both samples and the 'goodness' of fits are compared.
- MATLAB (Version 2020a)'s *lsqcurvefit* function is run with three open variables, b, h_S and $\bar{\theta}$, for each target over all the available data at each incidence angle. Initial guesses are set as $\bar{\theta}$=17°, b=0.1 and h_s=0.01, and the boundaries are set as $5^\circ \leq \bar{\theta} \leq 30^\circ$, $0.001 \leq b \leq 1$ and $0 \leq h_s \leq 1$. Thus, $\bar{\theta}$, b and h_s values are outputted, along with uncertainties, for each incidence angle dataset, and R^2 values are also deduced which provide 'goodness' of fits. Furthermore, covariance matrices are outputted for each run, and these are used to calculate correlation coefficients for each pair of fitted parameters.

The method detailed above provides a novel way of interpreting photometry datasets such as those measured by Diviner's off-nadir campaign. Performing the process on remote sensing data for regions which have similar petrologies to the 'ground truth' samples measured in the laboratory—and whose w and φ values are used when fitting the Hapke

BRDF model—enables deductions to be made regarding 1) the composition of the remotely sensed regolith surface, through derived b and h_s values; and 2) the surface roughness profile of the surface, through derived $\bar{\theta}$ values (Hapke, 2012; Sato *et al.*, 2014).

Furthermore, for regions in which the petrology of the regolith is unknown, the above process can be repeated using w and φ values from both the rough 10084 and 68810 samples, separately. The 'goodness' of fits for the assumed-mare and assumed-highlands fitting processes can then be compared through the derived R^2 values. If one process clearly leads to higher R^2 values than the other, this would suggest the region in question behaves more photometrically akin to the respective lunar mare or highlands. Thus, this may provide a method by which the petrology of unvisited regions of the Moon can be constrained.

The figures produced from plotting the complete Diviner off-nadir dataset for the various targets are too multitudinous to be presented here. However**, Figure 85**, which shows Diviner off-nadir data for the High-latitude Highlands region compared to VOSEG's BRDF measurements of the rough and smooth 68810 samples, demonstrates why parameters relating to VOSEG's rough Apollo samples were used in the methods above, as the curves measured by Diviner are generally in agreement with those measured by VOSEG for the rough Apollo samples. It also provides an example of Diviner off-nadir data, compared with the respective VOSEG smooth and rough BRDF data. For a full set of tables containing the Diviner off-nadir data used in this study, see https://docs.google.com/spreadsheets/d/1BuMxNxlEQ5YlvIlb2S46_xHA85O4KDwOgGUX9ajTvlw/edit?usp=sharing, or contact the author. In future, this dataset will be uploaded onto the Oxford University Research Archive.

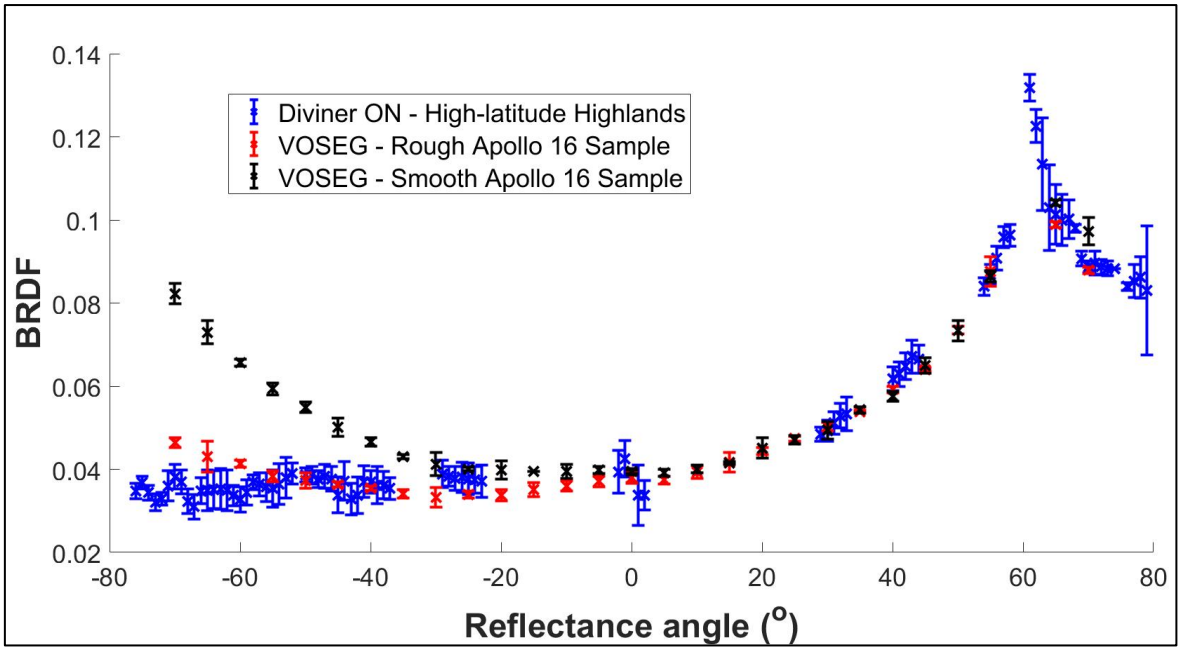

Figure 85: Principal plane, 60° incidence angle Diviner off-nadir data for the High-latitude Highlands region (49.55°N, 109.55°W) compared to the BRDFs measured by VOSEG for the rough and smooth Apollo 16, 68810 samples. The rough sample has a measured RMS slope angle value of $\bar{\theta}$=21.69° at the 500 μm size-scale, and the smooth sample has a measured RMS slope angle value of $\bar{\theta}$=14.27° at the 500 μm size-scale.

Tables 25-37 show the Hapke parameters determined for each of the Diviner targets for which there is sufficient data, at each available incidence angle, to fit the model.

High-latitude Highlands – Apollo 16 Fit												
θ_i (°)	$\bar{\theta}$ (°)	±$\bar{\theta}$ (°)	φ (#)	±φ (#)	*w (rough AP16)*	±*w*	*b*	±*b*	*c*	±*c*	h_S	±h_S	R^2
45	17.00	0.51	0.40	0.02	0.405	0.084	0.101	0.044	1.857	0.411	0.100	0.006	0.866
60	14.11	1.72	0.40	0.02	0.405	0.084	0.001	0.038	2.382	0.082	0.108	0.010	0.832

Table 25: ON High-latitude Highlands Hapke fitting parameters. *w*, $\bar{\theta}$ and φ are taken from the rough Apollo 16 sample results of the VOSEG BRDF study. Rows highlighted green indicate 'good' fits (R^2≥0.6).

High-latitude Mare – Apollo 11 Fit												
θ_i (°)	$\bar{\theta}$ (°)	±$\bar{\theta}$ (°)	φ (#)	±φ (#)	*w (rough AP11)*	±*w*	*b*	±*b*	*c*	±*c*	h_S	±h_S	R^2
60	21.82	0.69	0.41	0.02	0.315	0.021	0.054	0.027	2.219	0.157	0.011	0.003	0.769

Table 26: ON High-latitude Mare Hapke fitting parameters. *w*, $\bar{\theta}$ and φ are taken from the rough Apollo 11 sample results of the VOSEG BRDF study. Rows highlighted green indicate 'good' fits (R^2≥0.6).

Equatorial Mare – Apollo 11 Fit													
θ_i (°)	$\bar{\theta}$ (°)	$\pm\bar{\theta}$ (°)	φ (#)	±φ (#)	*w (rough AP11)*	±*w*	*b*	±*b*	*c*	±*c*	h_S	$\pm h_S$	R^2
60	21.11	1.59	0.41	0.02	0.315	0.021	0.055	0.026	2.213	0.217	0.007	0.003	0.801

Table 27: ON Equatorial Mare Hapke fitting parameters. *w*, $\bar{\theta}$ and φ are taken from the rough Apollo 11 sample results of the VOSEG BRDF study. Rows highlighted green indicate 'good' fits ($R^2 \geq 0.6$).

Reiner Gamma – Apollo 11 Fit													
θ_i (°)	$\bar{\theta}$ (°)	$\pm\bar{\theta}$ (°)	φ (#)	±φ (#)	*w (rough AP11)*	±*w*	*b*	±*b*	*c*	±*c*	h_S	$\pm h_S$	R^2
60	5.00	0.36	0.41	0.02	0.315	0.021	0.052	0.020	2.231	0.366	0.011	0.008	0.912

Table 28: ON Reiner Gamma Hapke fitting parameters. *w*, $\bar{\theta}$ and φ are taken from the rough Apollo 11 sample results of the VOSEG BRDF study. Hence, the method assumes mare-like regolith. Rows highlighted green indicate 'good' fits ($R^2 \geq 0.6$).

Reiner Gamma – Apollo 16 Fit													
θ_i (°)	$\bar{\theta}$ (°)	$\pm\bar{\theta}$ (°)	φ (#)	±φ (#)	*w (rough AP16)*	±*w*	*b*	±*b*	*c*	±*c*	h_S	$\pm h_S$	R^2
60	29.74	0.87	0.40	0.02	0.405	0.084	0.001	0.017	2.382	0.215	0.070	0.009	0.959

Table 29: ON Reiner Gamma Hapke fitting parameters. *w*, $\bar{\theta}$ and φ are taken from the rough Apollo 16 sample results of the VOSEG BRDF study. Hence, the method assumes highlands-like regolith. Squares highlighted orange indicate an issue with the fit; rows highlighted green indicate 'good' fits ($R^2 \geq 0.6$).

Aristarchus Plateau – Apollo 11 Fit													
θ_i (°)	$\bar{\theta}$ (°)	$\pm\bar{\theta}$ (°)	φ (#)	±φ (#)	*w (rough AP11)*	±*w*	*b*	±*b*	*c*	±*c*	h_S	$\pm h_S$	R^2
30	12.01	3.60	0.41	0.02	0.315	0.021	0.300	0.188	-0.221	1.296	0.111	0.018	0.429
60	18.10	0.61	0.41	0.02	0.315	0.021	0.001	0.036	2.382	0.073	0.005	0.004	0.748

Table 30: ON Aristarchus Plateau Hapke fitting parameters. *w*, $\bar{\theta}$ and φ are taken from the rough Apollo 11 sample results of the VOSEG BRDF study. Hence, the method assumes mare-like regolith. Rows highlighted orange indicate 'poor' fits ($0.2 \leq R^2 < 0.6$); rows highlighted green indicate 'good' fits ($R^2 \geq 0.6$).

Aristarchus Plateau – Apollo 16 Fit													
θ_i (°)	$\bar{\theta}$ (°)	$\pm\bar{\theta}$ (°)	φ (#)	±φ (#)	*w (rough AP16)*	±*w*	*b*	±*b*	*c*	±*c*	h_S	$\pm h_S$	R^2
30	16.92	0.08	0.40	0.02	0.405	0.084	0.001	0.070	2.382	0.269	0.093	0.023	0.282
60	12.75	1.87	0.40	0.02	0.405	0.084	0.011	0.008	2.375	0.034	0.138	0.021	0.883

Table 31: ON Aristarchus Plateau Hapke fitting parameters. *w*, $\bar{\theta}$ and φ are taken from the rough Apollo 16 sample results of the VOSEG BRDF study. Hence, the method assumes highlands-like regolith. Rows highlighted orange indicate 'poor' fits ($0.2 \leq R^2 < 0.6$); rows highlighted green indicate 'good' fits ($R^2 \geq 0.6$).

Equatorial Cold Spot – Apollo 11 Fit													
θ_i (°)	$\bar{\theta}$ (°)	$\pm\bar{\theta}$ (°)	φ (#)	±φ (#)	*w (rough AP11)*	±*w*	*b*	±*b*	*c*	±*c*	h_S	$\pm h_S$	R^2
15	10.14	6.48	0.41	0.02	0.315	0.021	1	0.258	-0.908	0.001	0.123	0.031	0.021
45	24.68	0.71	0.41	0.02	0.315	0.021	0.0192	0.029	2.361	0.062	0.003	0.002	0.757
60	21.47	0.99	0.41	0.02	0.315	0.021	0.001	0.028	2.382	0.045	0.003	0.002	0.812

Table 32: ON Equatorial Cold Spot Hapke fitting parameters. *w*, $\bar{\theta}$ and φ are taken from the rough Apollo 11 sample results of the VOSEG BRDF study. Hence, the method assumes mare-like regolith. Rows highlighted red indicate 'very poor' or unresolved fits; rows highlighted orange indicate 'poor' fits ($0.2 \leq R^2 < 0.6$); rows highlighted green indicate 'good' fits ($R^2 \geq 0.6$).

Equatorial Cold Spot – Apollo 16 Fit													
θ_i (°)	$\bar{\theta}$ (°)	$\pm\bar{\theta}$ (°)	φ (#)	±φ (#)	*w (rough AP16)*	±*w*	*b*	±*b*	*c*	±*c*	h_S	$\pm h_S$	R^2
15	12.06	4.83	0.40	0.02	0.405	0.084	0.001	0.098	2.38	0.506	0.086	0.029	0.091
45	18.00	0.31	0.40	0.02	0.405	0.084	0.001	0.046	2.38	0.119	0.081	0.011	0.836
60	13.92	1.46	0.40	0.02	0.405	0.084	0.001	0.057	2.38	0.181	0.058	0.007	0.871

Table 33: ON Equatorial Cold Spot Hapke fitting parameters. *w*, $\bar{\theta}$ and φ are taken from the rough Apollo 16 sample results of the VOSEG BRDF study. Hence, the method assumes highlands-like regolith. Rows highlighted red indicate 'very poor' or unresolved fits; rows highlighted green indicate 'good' fits ($R^2 \geq 0.6$).

Dufay Albedo Anomaly – Apollo 11 Fit													
θ_i (°)	$\bar{\theta}$ (°)	$\pm\bar{\theta}$ (°)	φ (#)	±φ (#)	*w (rough AP11)*	±*w*	*b*	±*b*	*c*	±*c*	h_S	$\pm h_S$	R^2
15	5.00	13.18	0.41	0.02	0.315	0.021	1	0.240	-0.908	0.007	0.132	0.008	0.067
45	23.84	0.63	0.41	0.02	0.315	0.021	0.001	0.026	2.382	0.038	0.010	0.006	0.734
60	21.93	1.41	0.41	0.02	0.315	0.021	0.001	0.044	2.382	0.109	0.030	0.014	0.602

Table 34: ON Dufay Albedo Anomaly Hapke fitting parameters. *w*, $\bar{\theta}$ and φ are taken from the rough Apollo 11 sample results of the VOSEG BRDF study. Hence, the method assumes mare-like regolith. Rows highlighted red indicate 'very poor' or unresolved fits; rows highlighted green indicate 'good' fits ($R^2 \geq 0.6$).

Dufay Albedo Anomaly – Apollo 16 Fit													
θ_i (°)	$\bar{\theta}$ (°)	$\pm\bar{\theta}$ (°)	φ (#)	±φ (#)	*w (rough AP16)*	±*w*	*b*	±*b*	*c*	±*c*	h_S	$\pm h_S$	R^2
15	11.78	5.95	0.40	0.02	0.405	0.084	0.001	0.096	2.382	0.487	0.111	0.025	0.029
45	17.76	0.02	0.40	0.02	0.405	0.084	0.050	0.020	2.242	0.208	0.130	0.039	0.746
60	16.95	1.56	0.40	0.02	0.405	0.084	0.017	0.010	2.365	0.027	0.138	0.018	0.908

Table 35: ON Dufay Albedo Anomaly Hapke fitting parameters. *w*, $\bar{\theta}$ and φ are taken from the rough Apollo 16 sample results of the VOSEG BRDF study. Hence, the method assumes highlands-like regolith. Rows highlighted red indicate 'very poor' or unresolved fits; rows highlighted green indicate 'good' fits ($R^2 \geq 0.6$).

Kepler Crater Ejecta – Apollo 11 Fit													
θ_i (°)	$\bar{\theta}$ (°)	$\pm\bar{\theta}$ (°)	φ (#)	±φ (#)	*w (rough AP11)*	±*w*	*b*	±*b*	*c*	±*c*	h_S	$\pm h_S$	R^2
15	5.00	31.25	0.41	0.02	0.315	0.021	0.999	0.620	-0.908	0.135	0.148	0.080	0.112
60	20.47	0.70	0.41	0.02	0.315	0.021	0.092	0.022	1.931	0.171	0.014	0.004	0.827

Table 36: ON Kepler Crater Ejecta Hapke fitting parameters. *w*, $\bar{\theta}$ and φ are taken from the rough Apollo 11 sample results of the VOSEG BRDF study. Hence, the method assumes mare-like regolith. Rows highlighted red indicate 'very poor' or unresolved fits; rows highlighted green indicate 'good' fits ($R^2 \geq 0.6$).

Kepler Crater Ejecta – Apollo 16 Fit													
θ_i (°)	$\bar{\theta}$ (°)	$\pm\bar{\theta}$ (°)	φ (#)	±φ (#)	*w (rough AP16)*	±*w*	*b*	±*b*	*c*	±*c*	h_S	$\pm h_S$	R^2
15	5.00	28.77	0.40	0.02	0.405	0.084	0.001	0.139	2.382	0.939	0.158	0.015	0.334
60	14.60	2.00	0.40	0.02	0.405	0.084	0.021	0.039	2.357	0.091	0.138	0.009	0.895

Table 37: ON Kepler Crater Ejecta Hapke fitting parameters. w, $\bar{\theta}$ and φ are taken from the rough Apollo 16 sample results of the VOSEG BRDF study. Hence, the method assumes highlands-like regolith. Rows highlighted orange indicate 'poor' fits ($0.2 \leq R^2 < 0.6$); rows highlighted green indicate 'good' fits ($R^2 \geq 0.6$).

From this set of tables, various deductions can be made regarding the physical and compositional properties of the lunar regolith surfaces being measured. The first obvious deduction from the tables is that, as for the Apollo BRDF data, the Hapke BRDF model fits well to the 45° and 60° incidence angle data, with all targets producing $R^2 \geq 0.6$; but 'very poorly', or 'poorly' to the 15° and 30° incidence angle data, with all targets producing $0.021 \leq R^2 \leq 0.429$. This is consistent with the results of Part 5.2, and suggests the model generally fits better to the laboratory and remote sensing data at $\theta_i \geq 45°$. Importantly, for the Diviner off-nadir datasets which produce 'good' fits, there is no significant difference between the average R^2 values for the mare ($R^2 = 0.827 \pm 0.061$) and highlands ($R^2 = 0.862 \pm 0.062$) regions, indicating that the model fits equally well to either type of regolith surface, when using VOSEG data from the two Apollo samples within the fitting method. Furthermore, comparing the R^2 values produced by the two fits (i.e., mare or highlands) provides a method for determining whether the regions with unknown petrologies are more mare- or highlands-like in their scattering behaviours. The resulting R^2 values suggest that the Aristarchus Plateau, the Equatorial Cold Spot, and the Dufay Albedo Anomaly targets are more highlands-like in their scattering behaviours; and conversely, the Kepler Crater Ejecta target is more mare-like. For Reiner Gamma, insufficient data is available to be able to distinguish whether the target is more mare- or highlands-like, as both fits produce R^2 values within ~5% of each other (and >0.9).

As for the 10084 and 68810 laboratory data fitting process, to assess the correlation between the three fitted parameters, correlation coefficients (which quantify the strength of the linear relationship between two variables in a correlation analysis) were calculated for each run and these values were averaged to produce the following values for each sample fitting process. For mare-like fitted regions—$COR(\bar{\theta}, b)$=-0.280±0.445, with a range of -0.571 ≤ $COR(\bar{\theta}, b) \leq 0.754$; $COR(\bar{\theta}, h_S)$=-0.030±0.380, with a range of $-0.196 \leq COR(\bar{\theta}, h_S) \leq 0.852$; and $COR(b, h_S)$=0.862±0.074, with a range of $0.767 \leq COR(b, h_S) \leq 0.973$. For highlands-like fitted regions—$COR(\bar{\theta}, b)$=0.588±0.331, with a range of -0.003 ≤ $COR(\bar{\theta}, b) \leq 0.840$; $COR(\bar{\theta}, h_S)$=0.657±0.386, with a range of -0.027 ≤ $COR(\bar{\theta}, h_S) \leq 0.930$; and $COR(b, h_S)$=0.960±0.044, with a range of $0.809 \leq COR(b, h_S) \leq 0.973$. Minimum and maximum values are given for the off-nadir fitting process due to the quantity of datapoints (i.e., 12-13, as opposed to the 2 data points available for the Apollo laboratory data fitting process in Part 5.2). These values demonstrate that for both mare-like and highlands-like regions, as for the laboratory BRDF study, there is a strong positive correlation between b and h_S; for the same reasons as described in Part 5.2. For both mare-like and highlands-like regions, the strength of the correlation between $\bar{\theta}$ and b was dependent on whether datapoints were available at high reflectance angles (≥50°) and hence the standard deviations of these values are large (as this is the most sensitive region to variations in $\bar{\theta}$ and b). Generally, $\bar{\theta}$ and b have similar functionalities within the model and so the strong observed correlations—of up to $COR(\bar{\theta}, h_S)$=0.840—are to be expected, and these demonstrate the inability to discern between their effects. This reinforces the importance of capturing the surface roughness profiles of the Apollo samples measured in Part 5.2. Finally, for both mare-like and highlands-like regions, the correlations between $\bar{\theta}$ and h_S were dependent on the availability of datapoints at $\theta_p \leq 10^{\circ}$ and on the incidence angle range within the data, with generally stronger correlations observed between $\bar{\theta}$ and h_S for $\theta_i \geq 45^{\circ}$. This is because

the effects on BRDF of the OE and of shadowing due to surface roughness are in competition at high reflectance angles (≥50˚), for high incidence angles in the $\theta_a \leq 0^{\circ}$ plane.

The suggestion that the Aristarchus Plateau target is highlands-like in its scattering behaviour is potentially unexpected, given its location within Oceanus Procellarum, an expanse of lunar mare (Chevrel *et al.*, 2009). However, the region within and around Aristarchus Crater is petrologically and geologically complex. It contains ejecta from the formation of the relatively young, ~450 million years old, Aristarchus Crater, which is brighter than the surrounding plateau, as the rocks are yet to be noticeably darkened by space weathering (i.e., they are optically immature); it contains volcanic ash, a giant rille and is surrounded by flood basalts. In addition, remote sensing observations made by Diviner showed that the region contains thermal inertia anomalies, and observations made by the Clementine mission determined a prominent central peak of anorthosite, which—as mentioned is Part 2.2—is indicative of young (<1 billion years old), bright craters, and which is most common in highlands regions.

If the Aristarchus Plateau target produces more highlands-like scattering behaviour due to the presence of young, bright crater ejecta, then this is potentially also to be expected for the Equatorial Cold Spot target, as cold spots on the lunar surface are associated with regions surrounding young, optically immature craters (Bandfield *et al.*, 2014). **Figure 86**, taken from (Bandfield *et al.*, 2014) shows (left) the colder than average temperatures observed for the Equatorial Cold Spot target viewed in the Diviner off-nadir campaign, and (right) the H-parameter map of this region. This cold spot is located within an equatorial highlands region of the lunar surface.

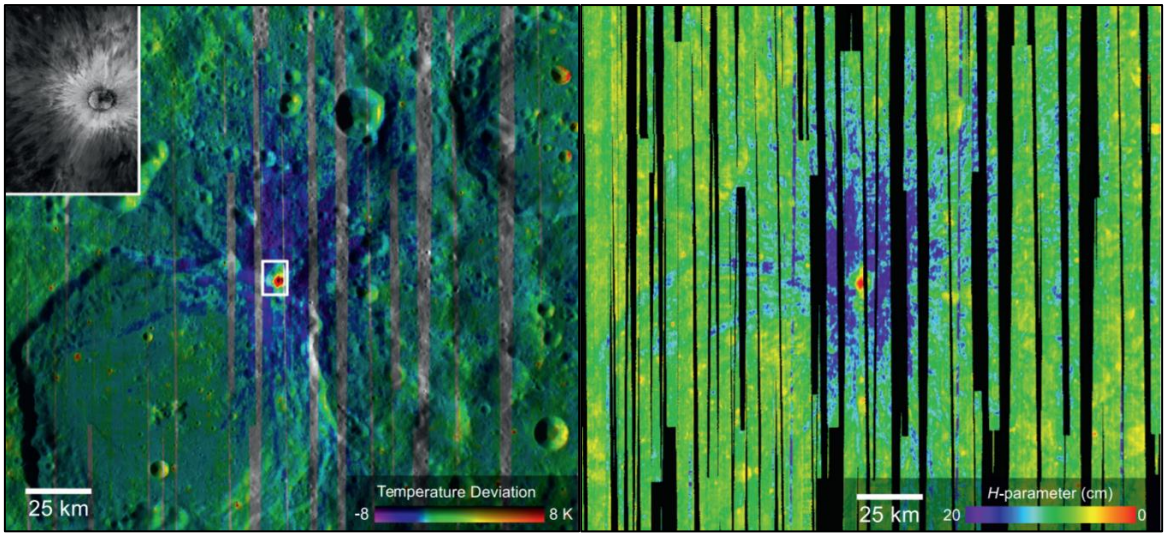

Figure 86: Left—Diviner night-time regolith temperatures relative to the global average, showing the cold spot surrounding a crater near 151.7˚E, 4.1˚S. Rocky surfaces close to the source crater have elevated temperatures (orange and red). The LROC WAC mosaic is used for shading. The white box denotes the area covered by the LROC image mosaic shown in Figure 87 and in the upper left inset. Right—H-parameter values for the large cold spot shown in the top image. Cold spot surfaces have a significantly thicker upper low-density layer relative to typical lunar regolith (Bandfield *et al.*, 2014).

Figure 87, also taken from (Bandfield *et al.*, 2014), shows a zoomed-in image of the Equatorial Cold Spot region, demonstrating how bright, young ejecta is deposited around the source crater.

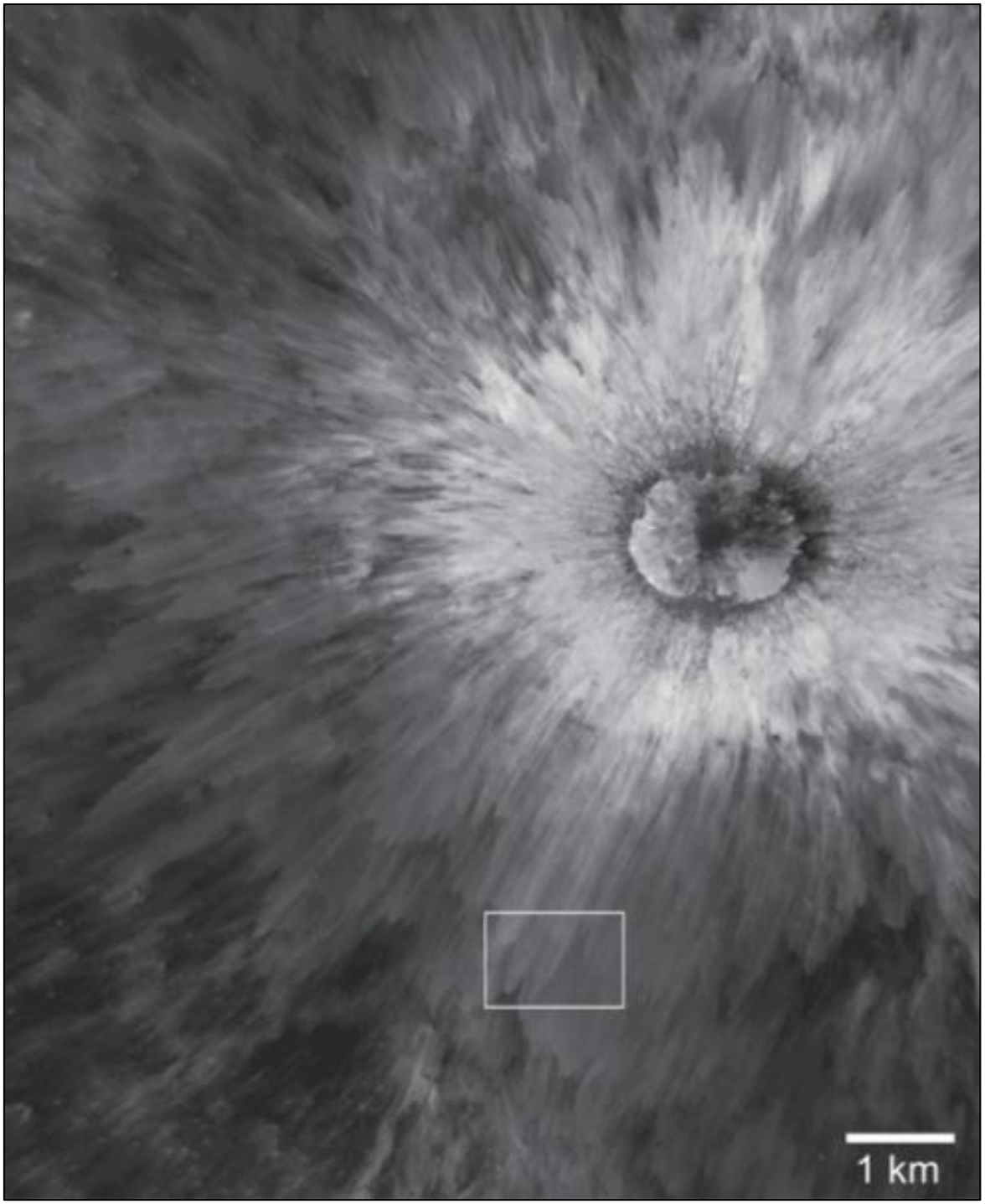

Figure 87: Mosaic of LROC images M110601418L/R and M125936995L/R centred near 151.7˚E, 4.1˚S, showing the young, bright, layered ejecta deposits surrounding the crater with their continuous, striated character. The white box indicates a highly-striated region (Bandfield *et al.*, 2014).

Figure 86 shows that lunar cold spots generally exhibit higher than average H-parameter values (~15-20 cm), indicating the regolith structures within these regions are highly porous, potentially due to the shock effects of the impact which created the source crater (Bandfield *et al.*, 2014). This raises the question: If the Equatorial Cold Spot target measured by Diviner

has a higher H-parameter than average, then is the value of φ used in the VOSEG fitting process inaccurate? And if that is the case, how would this affect the Hapke parameters derived for this target? If the true value is lower than φ=0.40±0.02, this may—in a study which has no way of fixing w—considerably affect the best fit value deduced for w, leading to an underestimated best fit value; but because, in this study, w is set within the model (from the samples used in the VOSEG study), any inaccuracies within the fitting process due to incorrectly set φ values will have limited impact on the three fitted Hapke parameters, which, in this case, are b, h_s and $\bar{\theta}$. Therefore, the more highlands-like scattering behaviour of this target may be indicative of both the highlands region within which it is situated, and of the crater ejecta/cold spot nature of the regolith surface present.

The Dufay Albedo Anomaly target resides in a far-side highlands region of the lunar surface. Specifically, the target is located on the inner wall of the north-western-most crater in the region, which has an anomalously high albedo, potentially due to enhanced levels of Thorium in the surface/subsurface (Lawrence *et al.*, 2003). Its more highlands-like scattering behaviour is to be expected, given the petrology of the region, and once again, the fact that w is fixed within the fitting process, thus reducing the effect of varying φ, is also crucial for this target, because the regolith structures covering steep crater walls generally have lower porosity values than flat regions of the lunar surface, and occasionally, can contain areas of exposed bedrock (King *et al.*, 1977).

The Kepler Crater Ejecta target is located (0.23°N, 1.47°E) of the Kepler Crater—shown in **Figure 88**—which is a Copernican age (<1.1 billion years old) crater in a near-side lunar mare region (Wilhelms, with sections by McCauley and Trask, 1987; Greenhagen *et al.*, 2017).

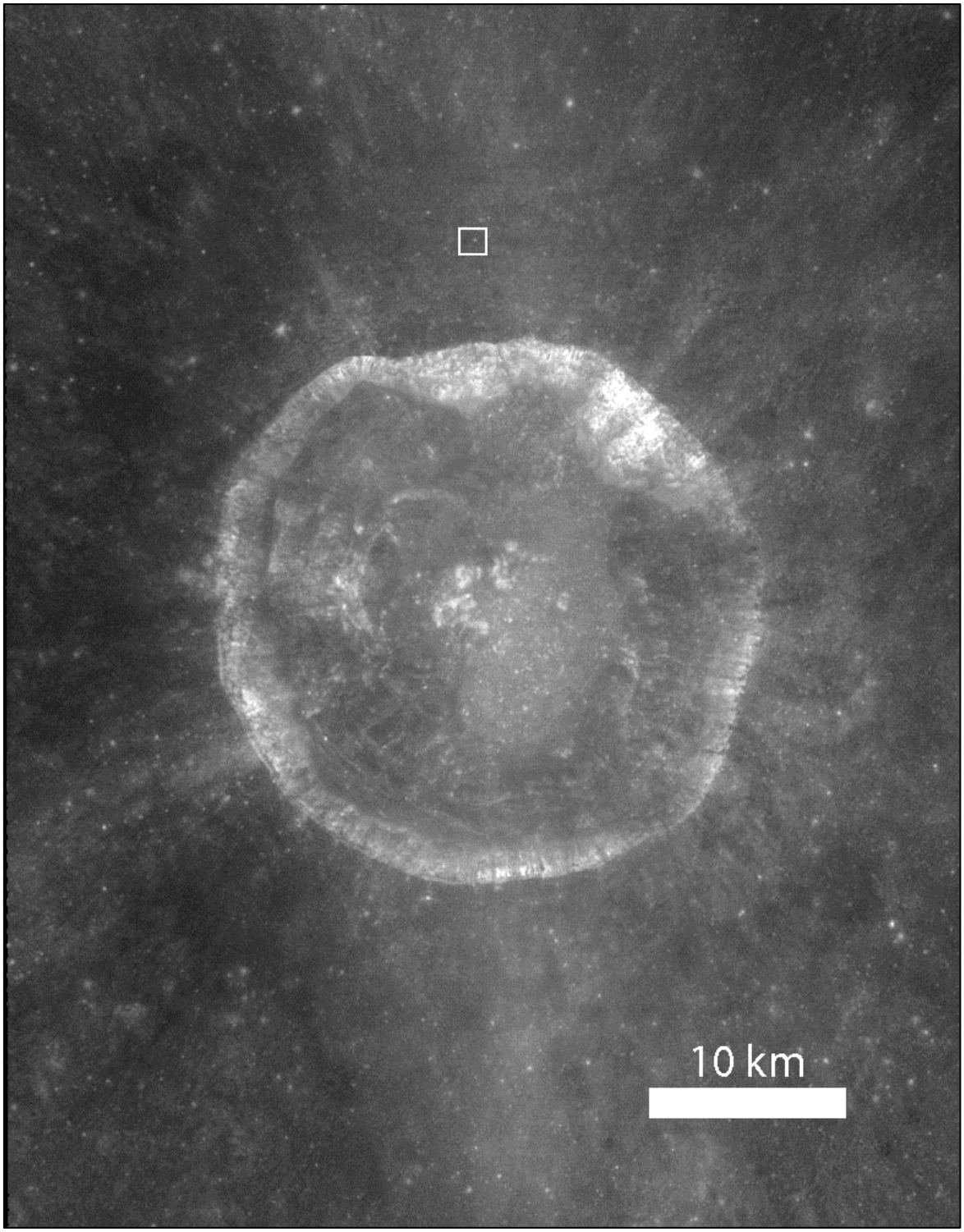

Figure 88: An LROC WAC image of Kepler Crater, which shows the location of a boulder (white box) within the continuous blanket of ejecta surrounding the crater rim. Image credit: NASA/GSFC/Arizona State University.

The area surrounding the crater is covered in a continuous ejecta blanket, with the deepest subsurface material residing closest to the crater—i.e., near the crater rim—and with the top surface material residing farthest away from the crater, due to it being ejected further than

the deeper material (Wilhelms, with sections by McCauley and Trask, 1987). The more mare-like scattering behaviour of the surface is to be expected, given its location within the lunar mare. Due to the crater ejecta nature of the target, it likely consists of regolith which would have been present on the top surface of the pre-impact region which now contains the crater. The Diviner off-nadir measurements for this target therefore provide a BRDF dataset for representative top surface mare ejecta material.

To further explore the scattering behaviour of the Diviner off-nadir targets, the average derived *b* values are plotted for each of the targets in **Figure 89**, alongside those deduced for the lunar mare and highlands by (Sato *et al.*, 2014), and for the 10084 and 68810 Apollo samples by (Foote *et al.*, 2020). Higher *b* values indicate more forward-scattering surfaces.

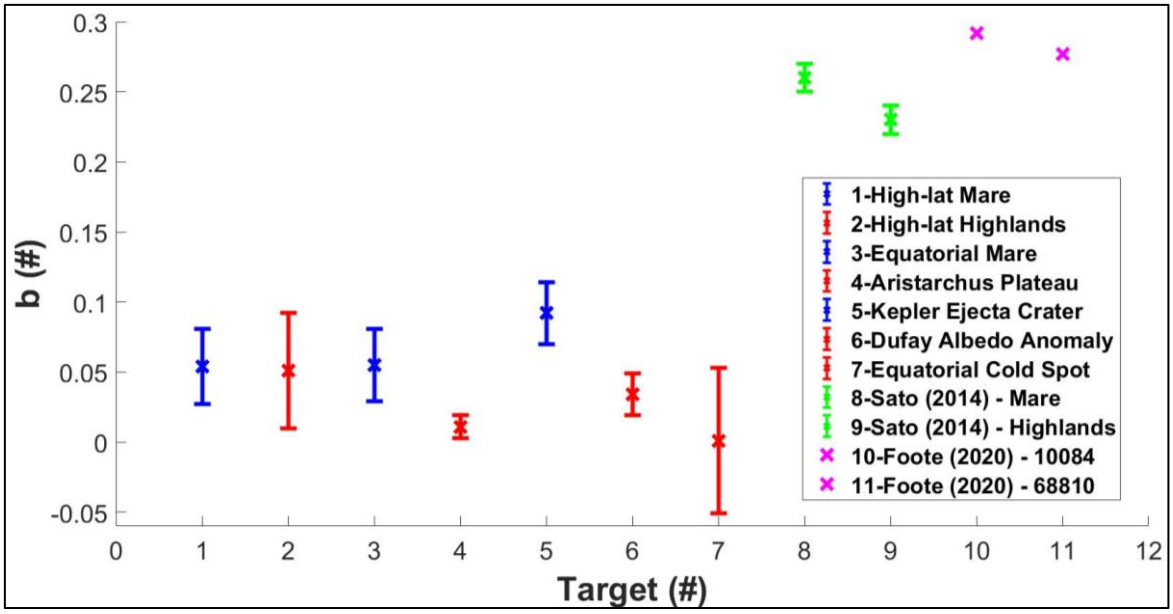

Figure 89: Average *b* values determined in the VOSEG-Diviner off-nadir study for the seven lunar surface targets (blue crosses indicate mare or more mare-like regions and red crosses indicate highlands or more highlands-like regions); and compared to those determined in the (Sato *et al.*, 2014) study for the mare and highlands regions (green crosses), and in the (Foote *et al.*, 2020) study for the 10084 and 68810 Apollo samples (pink crosses).

The first clear observation from **Figure 89** is that the *b* values determined in the VOSEG-Diviner study are systematically lower than those deduced in (Sato *et al.*, 2014) and (Foote *et al.*, 2020), suggesting the lunar regolith surfaces measured by Diviner are generally more

backscattering than those measured in (Sato *et al.*, 2014) and (Foote *et al.*, 2020). For the lunar mare regions, the disagreement with (Sato *et al.*, 2014) cannot be due to variations in the $\bar{\theta}$ values set within the model, as they are ~equivalent; however, the general value of $\bar{\theta}$=23.4˚ used in the (Sato *et al.*, 2014) study is ~50-60% higher than the average $\bar{\theta}$ value determined for the Diviner off-nadir highlands targets. If $\bar{\theta}$ is overestimated within the model, this will lead to suppressed b values, as the model attempts to accommodate for shadowing effects by decreasing the forward-scattering term, b, particularly in the principal plane. The systematic disagreement in b values for the mare may be therefore be due to the semi-empirical simplifications made in the Hapke BRDF model used in (Sato *et al.*, 2014), or to the fact that (Sato *et al.*, 2014) deduces general b values for the entire mare region of the surface, thus skewing the data when compared to specific local regions.

The disagreement between the VOSEG-Diviner study and the values determined in (Foote *et al.*, 2020) may be due to varying assumptions made within the Hapke BRDF model, or to the fact the Apollo samples only represent limited petrologies of lunar regolith; whilst the regions remotely sensed by Diviner are more complex in their petrologies. However, for the mare/10084 sample, the b values determined in (Foote *et al.*, 2020) ~agree with those measured in the VOSEG Apollo BRDF study, and those determined for the mare in (Sato *et al.*, 2014). Thus, the reason for the systematic discrepancy in the VOSEG-Diviner deduction for the mare targets is inconclusive; especially given that for the highlands targets/68810 sample, the b values determined in the VOSEG BRDF study ~agree with those deduced in the VOSEG-Diviner study.

Within the range of values determined by the VOSEG-Diviner study, the mare regions generally exhibit higher b values than the highlands regions, which is consistent with the trends observed in (Sato *et al.*, 2014) and (Foote *et al.*, 2020). This is likely due to higher

contents of SMFe and ilmenite in the interiors of backscattering agglutinates in the mare. The Equatorial Cold spot exhibits the most backscattering behaviour of the seven targets, which is consistent with its highlands-like scattering nature, and may suggest it contains high quantities of anorthosite chips/rocks, which are exposed during crater forming impacts and which have strong backscattering properties (Sato *et al.*, 2014). The Kepler Crater Ejecta target exhibits the most forward-scattering behaviour, which is consistent with the deduction that the region consists of optically mature mare ejecta (Wilhelms, with sections by McCauley and Trask, 1987; Bandfield *et al.*, 2014; Sato *et al.*, 2014). The High-latitude Highlands region has a higher average b value than the other highlands-like targets, potentially suggesting it is more optically mature than highlands regions filled with relatively young (<1 billion years old) craters; however, the uncertainty in this value overlaps with the b values determined for all the other highlands-like regions.

Next, the average h_s values determined for the Diviner off-nadir targets, which relate to the width of the observed opposition effect surges (Hapke, 2012), are plotted in **Figure 90**, alongside those deduced for the lunar mare and highlands in (Sato *et al.*, 2014), and those determined for the 10084 and 68810 Apollo samples in (Foote *et al.*, 2020).

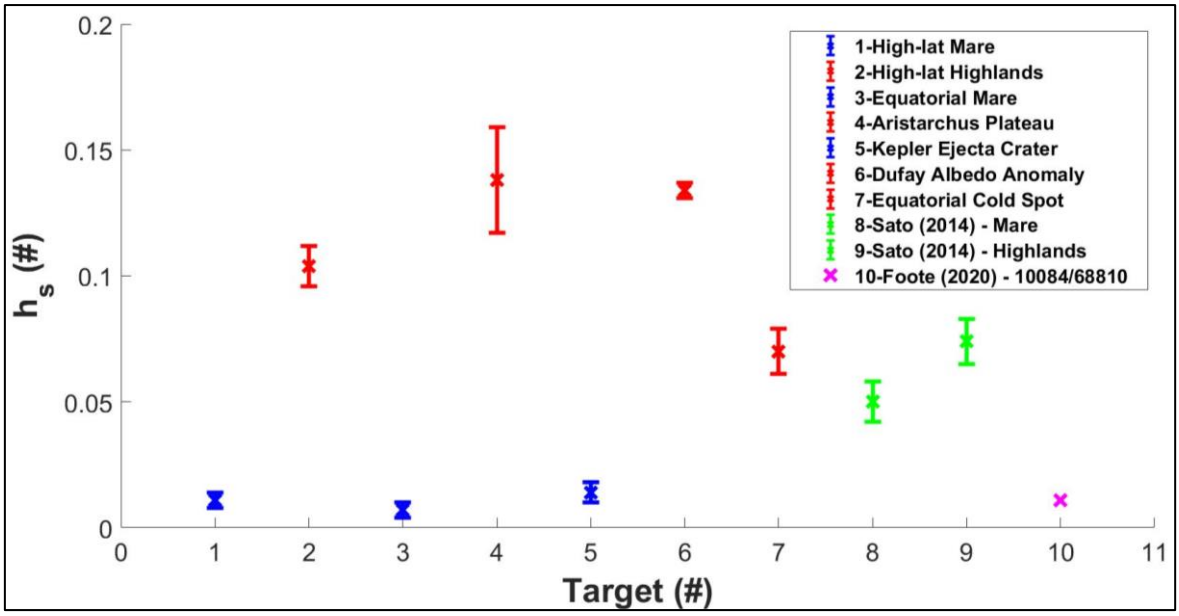

Figure 90: Average h_s values determined in the VOSEG-Diviner off-nadir study for the seven lunar surface targets (blue crosses indicate mare or more mare-like regions and red crosses indicate highlands or more highlands-like regions); and compared to those determined in the (Sato *et al.*, 2014) study for the mare and highlands regions (green crosses), and in the (Foote *et al.*, 2020) study for the 10084 and 68810 Apollo samples (pink crosses).

Figure 90 shows that the h_s values deduced for the seven Diviner off-nadir targets cluster into two distinct ranges. One of these clusters is around h_s=0.010, and is populated by the mare or mare-like targets, and the other is around h_s=0.125, and is populated by the highlands or highlands-like targets. The Equatorial Cold Spot is an exception, with an average value of h_s=0.070±0.009. The two different h_s value ranges are likely due to the two representative petrologies of the mare and highlands regolith (King *et al.*, 1977). **Figure 90** indicates that highlands regolith generally exhibits a larger angular width in the opposition effect peak than the mare regolith, as was observed in the values deduced in (Sato *et al.*, 2014), although the range of values is less pronounced (with $0.050 \leq h_s \leq 0.074$) for both mare and highlands regions. This difference was attributed in (Sato *et al.*, 2014) to the varying grain-size distributions of the two types of regolith. The (Sato *et al.*, 2014) study observed anomalously high h_s values in immature highlands crater ejecta, and this provides a potential explanation as to why the Aristarchus Plateau has the highest observed h_s value of all seven targets. However, the relatively low h_s value observed for the highlands

Equatorial Cold Spot target shows that not all regions containing immature highlands crater ejecta exhibit high (>0.125) h_s values, potentially due to variations in regolith grain-size distributions, or to the expected increase in top-surface (up to ~100 μm) regolith porosities for cold spots (Bandfield *et al.*, 2014). The Equatorial Cold Spot target is the only Diviner off-nadir target with a deduced h_s value which agrees (within uncertainty) with the value determined in (Sato *et al.*, 2014), for the relative highlands/highlands-like region. Conversely, the h_s value determined in the (Foote *et al.*, 2020) study (which is the same for both samples) agrees (within uncertainty) with the values determined for the mare or mare-like Diviner off-nadir targets. The h_s values determined for the highlands or highlands-like Diviner off-nadir targets are greater than those determined in (Sato *et al.*, 2014), by ~30-70%, but to fully relate h_s to the physical nature of the measured regolith surface—independent of h_C—further studies are required, in which polarising filters are used to distinguish the effects of the two factors which contribute towards the opposition surge—e.g., shadow hiding and coherent backscattering (Hapke, 2021).

Finally, observations can be made regarding the $\bar{\theta}$ values determined for the seven Diviner off-nadir targets (see **Table 8**). The $\bar{\theta}$ values deduced for the more mare-like targets cluster at ~15˚, whereas those deduced for the more highlands-like targets cluster at ~21˚, as demonstrated in **Table 38** and **Figure 91**.

Diviner off-nadir target	*Latitude*	*Longitude*	*Best fit $\bar{\theta}$ value (AP11)* (°)	*R^2 for AP11 method*	*Best fit $\bar{\theta}$ value (AP16)* (°)	*R^2 for AP16 method*
High-latitude Mare	52.97°N	71.50°W	**21.82±0.69**	**0.769**	NA	NA
High-latitude Highlands	49.55°N	109.55°W	NA	NA	**15.55±1.12**	**0.849**
Equatorial Mare	1.96°S	0.60°W	**21.11±1.59**	**0.801**	NA	NA
Aristarchus Plateau	27.36°N	51.73°W	15.06±2.11	0.748	**14.84±0.98**	**0.883**
Reiner Gamma	7.41°N	58.98°W	5.00±0.36	0.912	29.74±0.87	0.959
Kepler Crater Ejecta	8.33°N	36.53°W	**20.47±0.70**	**0.827**	14.60±2.00	0.613
Dufay Albedo Anomaly	7.65°N	170.43°E	22.89±1.02	0.668	**15.50±2.51**	**0.827**
Equatorial Cold Spot	3.30°S	151.90°E	18.76±2.73	0.785	**14.66±2.20**	**0.854**

Table 38: The targets viewed in Diviner's off-nadir extended mission campaign, with the associated best fit' $\bar{\theta}$ values and R^2 values derived in the VOSEG-Diviner off-nadir BRDF study. Bold values indicate best fits for a given sample fitting method, using either rough Apollo 11, 10084 or rough Apollo 16, 68810 *w* and φ values. Only limited data at 60° incidence, 0° azimuthal angle, is available for Reiner Gamma, and there is insufficient data to perform the method on the King Crater Melt Pond and Equatorial Highlands regions.

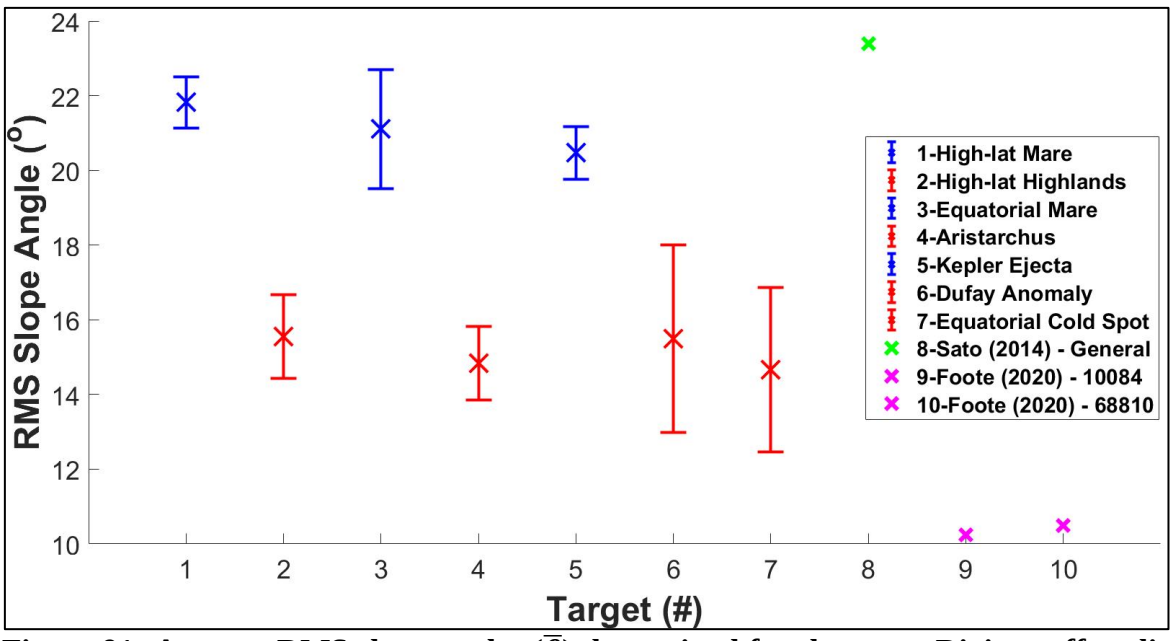

Figure 91: Average RMS slope angles ($\bar{\theta}$) determined for the seven Diviner off-nadir targets for which there is sufficient visible-λ data to derive Hapke parameters using VOSEG's Apollo BRDF measurements and the Hapke BRDF model. Also showing the

$\bar{\theta}$ values from in the (Sato *et al.*, 2014) and (Foote *et al.*, 2020) studies. Red crosses indicate highlands, or highlands-like regions; blue crosses indicate mare, or mare-like regions; the green cross indicates the value used in (Sato *et al.*, 2014); purple crosses indicate the values derived in (Foote *et al.*, 2020) for the 10084 and 68810 Apollo samples.

Figure 91 shows that the $\bar{\theta}$ value derived in (Sato *et al.*, 2014) is most similar to, but ~5-20% higher than, those determined for the Diviner off-nadir mare or mare-like targets, and the $\bar{\theta}$ values deduced in the (Foote *et al.*, 2020) study are ~50% lower than the $\bar{\theta}$ values deduced for the highlands or highlands-like Diviner off-nadir targets. This may therefore explain the disagreement in b values between the VOSEG-Diviner study and the (Foote *et al.*, 2020) study, as the Hapke BRDF model will attempt to accommodate for inaccurately set $\bar{\theta}$ values by varying b. **Figure 91** suggests the $\bar{\theta}$ value used for the entire lunar surface (Sato *et al.*, 2014) is ~correct for the mare regions, but overestimates the value for highlands regions by ~50-60%. This may also partly explain the discrepancy in b values between the VOSEG-Diviner off-nadir study and the (Sato *et al.*, 2014) study.

In addition, the results shown in **Figure 91** potentially indicate a tendency of mare regolith surfaces to form structures on the lunar surface which are generally rougher than those formed by highlands regolith at the size-scales most relevant to visible-λ remote sensing measurements (~500-1000 μm). **Figure 57** demonstrated that the same trend was observed for the Apollo regolith samples prepared in the laboratory across all size-scales (except for the rough samples at 500-1000 μm, for which the $\bar{\theta}$ values are ~equal). This supports the result from the VOSEG-Diviner off-nadir study. However, to relate the $\bar{\theta}$ values determined for the Diviner off-nadir targets to the physical nature of the measured lunar regolith surface—across the complete range of relevant size-scales (10-1000 μm)—it is necessary to determine a relationship between size-scale and $\bar{\theta}$. If a relationship can be found which accurately describes how $\bar{\theta}$ varies with size-scale, then from a single value of $\bar{\theta}$ for a known size-scale, it may be possible to extrapolate; thus, deriving information about the nature of

a regolith surface across 10-1000 μm size-scales. To be able to produce accurate descriptions of regolith surfaces in this way would be particularly useful for digital elevation models, for which the only current constraints are 1) comprehensive remote sensing datasets describing the topography of the lunar surface at ≥25 m scales (i.e. those measured by LOLA), and 2), knowledge of the nature of the lunar regolith at 1-100 μm size-scales derived from particle-size distribution studies of returned samples (such as those from the Apollo missions) (Barker *et al.*, 2016; Huang *et al.*, 2018). It is clear from **Figure 57** that the relationship between size-scale and $\bar{\theta}$ for all four of the samples follows a mirrored Gompertz curve (Gompertz, 1833). Hence, the relationship can be described by Equation 5.1, which is an adaptation of the general form of the Gompertz (power law) equation (in that it is multiplied by -1).

$$Y = \alpha e^{\beta e^{-\gamma X}} \quad [5.1]$$

Where X denotes size-scale in millimetres and α, β and γ are constants. To derive Gompertz approximations for an average rough regolith sample, an average smooth regolith sample, and an overall average regolith sample, MATLAB (Version 2020a)'s *lsqcurvefit* function is run, as with the Hapke BRDF model, over the average $\bar{\theta}$ values of the rough Apollo samples, the smooth Apollo samples, and all four Apollo samples, with α, β and γ as the three open variables. The best fit α, β and γ values deduced for the Gompertz approximations for the four samples, and for the three average cases, are given in **Table 39**.

Case	α	β	γ	R^2
Apollo 11-Rough	44.163	-1.020	-1.587	0.976
Apollo 11-Smooth	39.788	-1.324	-1.079	0.979
Apollo 16-Rough	42.389	-0.807	-1.077	0.967
Apollo 16-Smooth	38.803	-1.315	-1.332	0.979
Rough Average	43.276	-0.914	-0.579	NA
Smooth Average	39.295	-1.319	-0.523	NA
Overall Average	41.286	-1.117	-0.551	NA

Table 39: The best fit Gompertz curve constants, α, β and γ for three 'average' regolith sample cases, derived using RMS slope angle measurements of VOSEG's rough and smooth 10084 and 68810 samples over 10-1000 µm size-scales.

Figure 92 shows the average best fit Gompertz curves overlaid with $\bar{\theta}$ values measured across 10-1000 µm size-scales for the Apollo samples used in the VOSEG study.

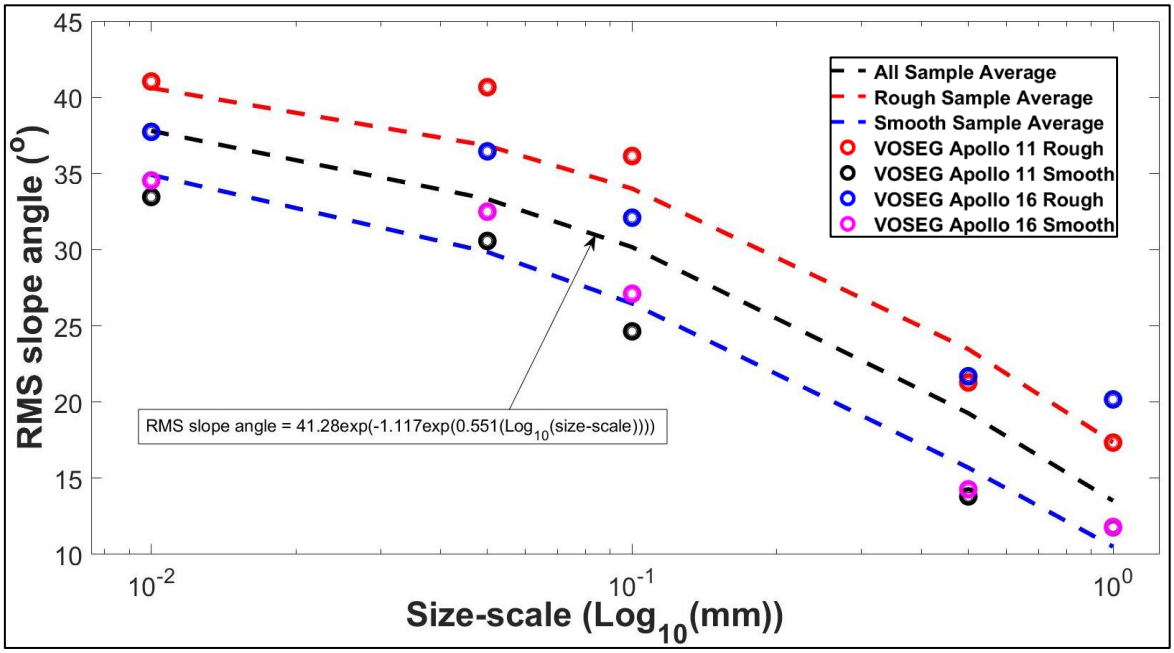

Figure 92: RMS slope angle ($\bar{\theta}$) values measured for the Apollo 11, 10084 and Apollo 16, 68810 samples used in the VOSEG BRDF study (circles), with best fit Gompertz curves (dashed lines). The equation describing the average best fit curve for all four samples is also given (Gompertz, 1833). R^2 values are as follows: AP11 Rough/Rough Average, R^2=0.952; AP11 Smooth/Smooth Average, R^2=0.971; AP16 Rough/Rough Average, R^2=0.915; AP16 Smooth/Smooth Average, R^2=0.974; AP11 Rough/Overall Average, R^2=0.763; AP11 Smooth/Overall Average, R^2=0.764; AP16 Rough/Overall Average, R^2=0.765; AP16 Smooth/Overall Average, R^2=0.889.

These three approximations provide examples of three general cases, but the same process could be performed to derive approximations between $\bar{\theta}$ and size-scale for any of the Apollo samples measured in the VOSEG study.

These results—which build on the stereophotogrammetry results of (Helfenstein and Shepard, 1999)—potentially help to 'bridge' a long-standing knowledge gap in lunar science, by providing information about the nature of the lunar regolith between 100-1000 µm size-scales (Barker *et al.*, 2016). The surface roughness profiles measured in this study may, therefore, be useful to lunar digital elevation models, as they enable constraints to be placed on the topographies formed by the lunar regolith over the full range of size-scales from 10 µm to ~100 m. Furthermore, using the Gompertz relations derived above, it may be possible to extrapolate from the $\bar{\theta}$ values derived for the seven Diviner off-nadir targets, to provide information about the physical nature of the lunar regolith surfaces in these regions, some of which are previously unvisited (Helfenstein and Shepard, 1999; Barker *et al.*, 2016; Chavers *et al.*, 2019). **Figure 93** shows approximations for the surface roughness profiles of the seven Diviner off-nadir targets, derived using the most appropriate Gompertz approximation for each sample, with $\bar{\theta}$ set as the constraint at 500µm size-scale—e.g., for the High-latitude Mare and High-latitude Highlands targets, the rough Apollo 11 and smooth Apollo 16 approximations are used, respectively; for the Equatorial Mare and the Kepler Crater Ejecta, the rough Apollo 11 approximation is used; and for the Aristarchus Plateau, Dufay Albedo Anomaly and Equatorial Cold Spot targets, the smooth Apollo 16 approximation is used. The smooth Apollo 16 approximations are used due to the lower cluster of $\bar{\theta}$ values (~15°) derived for the more highlands-like targets. For more mare-like targets, β and γ are set as the values deduced for the rough Apollo 11 sample, and a best fit value of α is determined using best fit $\bar{\theta}$ values from the VOSEG-Diviner study (for the 500 µm size-scale). For more highlands-like targets, β and γ are set as the values deduced for

the smooth Apollo 16 sample, and a best fit value of α is determined using best fit $\bar{\theta}$ values from the VOSEG-Diviner study (for the 500 μm size-scale).

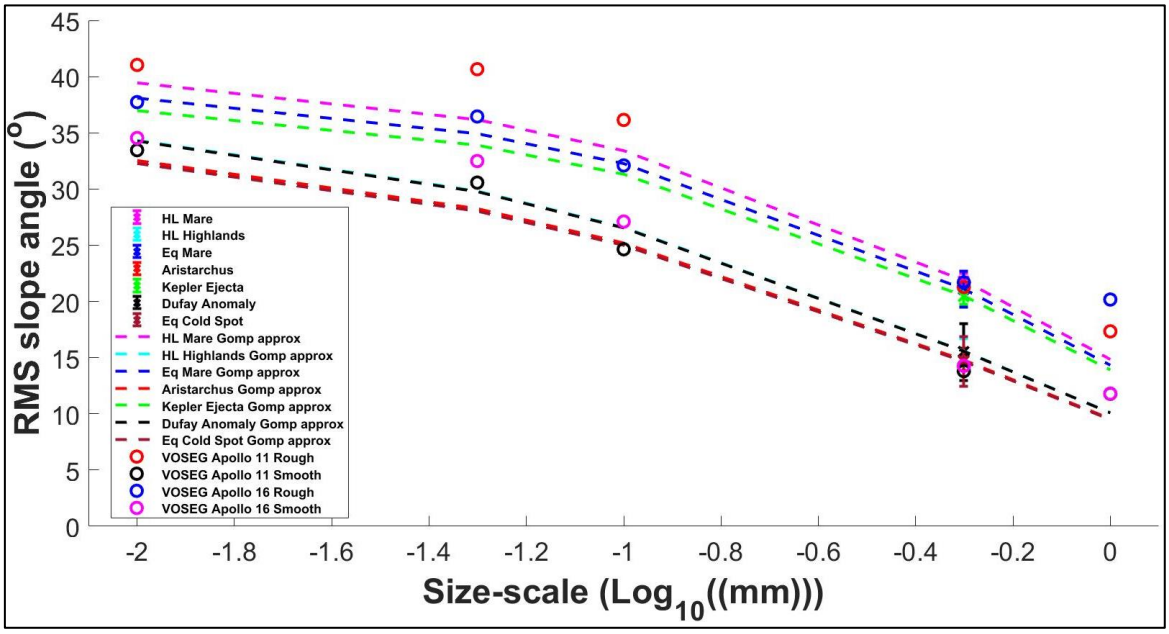

Figure 93: Showing Gompertz approximations derived for each of the Diviner off-nadir targets. For more mare-like targets, β and γ are set as the values deduced for the rough Apollo 11 sample, and a best fit value of α is determined, using best fit $\bar{\theta}$ values from the VOSEG-Diviner study (for 500 μm size-scale). For more highlands-like targets, β and γ are set as the values deduced for the smooth Apollo 16 sample, and a best fit value of α is determined, using best fit $\bar{\theta}$ values from the VOSEG-Diviner study (for 500 μm size-scale). R^2 values are as follows: HL Mare/AP11 Rough Fit, R^2=0.941; HL Highlands/AP16 Smooth Fit, R^2=0.947; Equatorial Mare/AP11 Rough Fit, R^2=0.894; Aristarchus/AP16 Smooth Fit, R^2=0.948; Kepler Ejecta/AP11 Rough Fit, R^2=0.856; Dufay Anomaly/AP16 Smooth Fit, R^2=0.984; Equatorial Cold Spot/AP16 Smooth Fit, R^2=0.946.

The best fit Gompertz equation α values derived for the approximations shown **Figure 93** are given in **Table 40**, in addition to the β and γ constants used for each target.

Diviner off-nadir target	α	β	γ
High-latitude Mare	41.163	-1.020	-1.587
High-latitude Highlands	37.631	-1.315	-1.332
Equatorial Mare	39.748	-1.020	-1.587
Aristarchus Plateau	35.653	-1.315	-1.332
Kepler Crater Ejecta	38.582	-1.020	-1.587
Dufay Albedo Anomaly	37.561	-1.315	-1.332
Equatorial Cold Spot	35.368	-1.315	-1.332

Table 40: Gompertz equation constants deduced for the Diviner off-nadir targets investigated in the VOSEG-Diviner study. Best fit α values determined using $\bar{\theta}$ values from the VOSEG-Diviner study (for 500 µm size-scale) as a constraint. or more mare-like targets, β and γ values are set as determined for the rough Apollo 11 sample measured in the VOSEG BRDF study; for more highlands-like targets, β and γ are set as determined for the smooth Apollo 16 sample measured in the VOSEG BRDF study.

As demonstrated, the VOSEG Apollo BRDF dataset enables a novel method for interpreting remote sensing photometry datasets, such as the visible-λ Diviner off-nadir dataset investigated in this study, in terms of Hapke parameters which represent the compositional and physical properties of various regions of the lunar surface (thus fulfilling goal, G3). In accordance with the aims and goals set out in **Table 1**, the final application of the VOSEG Apollo BRDF dataset to be explored in this thesis is to use it to set scattering function inputs within thermal models; specifically, the O3DTM (King *et al.*, 2019).

6 Use of Laboratory Measured Scattering Functions as Inputs within Thermal Models

The final aim of this thesis, A4, is to explore how incorporating laboratory measured scattering functions within thermal models, such as the O3DTM, affects modelled temperature profiles for the lunar surface.

6.1 1D Thermal Model Results

Firstly, how laboratory measured scattering functions differ from those previously used in thermal models can be demonstrated by **Figure 94**, from (Foote *et al.*, 2020), which shows the solar spectrum averaged directional hemispheric reflectance (a.k.a. hemispheric albedo) functions used in (Keihm, 1984; Vasavada, Paige and Wood, 1999; Hayne *et al.*, 2017), in addition to those derived in (Foote *et al.*, 2020) using Hapke BRDF model best fits for the study's Apollo 11 and Apollo 16 BRDF measurements. Directional hemispheric albedo is calculated by integrating the BRDF over a half-hemisphere of reflectance and azimuthal angles (e.g., from 0 to π, for both), and then multiplying by 2.

As in the (Foote *et al.*, 2020) study, VOSEG's BRDF measurements of the rough and smooth 10084 and 68810 samples were used to derive hemispheric albedo functions, but without first fitting the Hapke BRDF model to the data. The hemispheric albedo values calculated in this study, at each measured incidence angle, are given in **Table 41,** alongside those derived using the (Foote *et al.*, 2020) data.

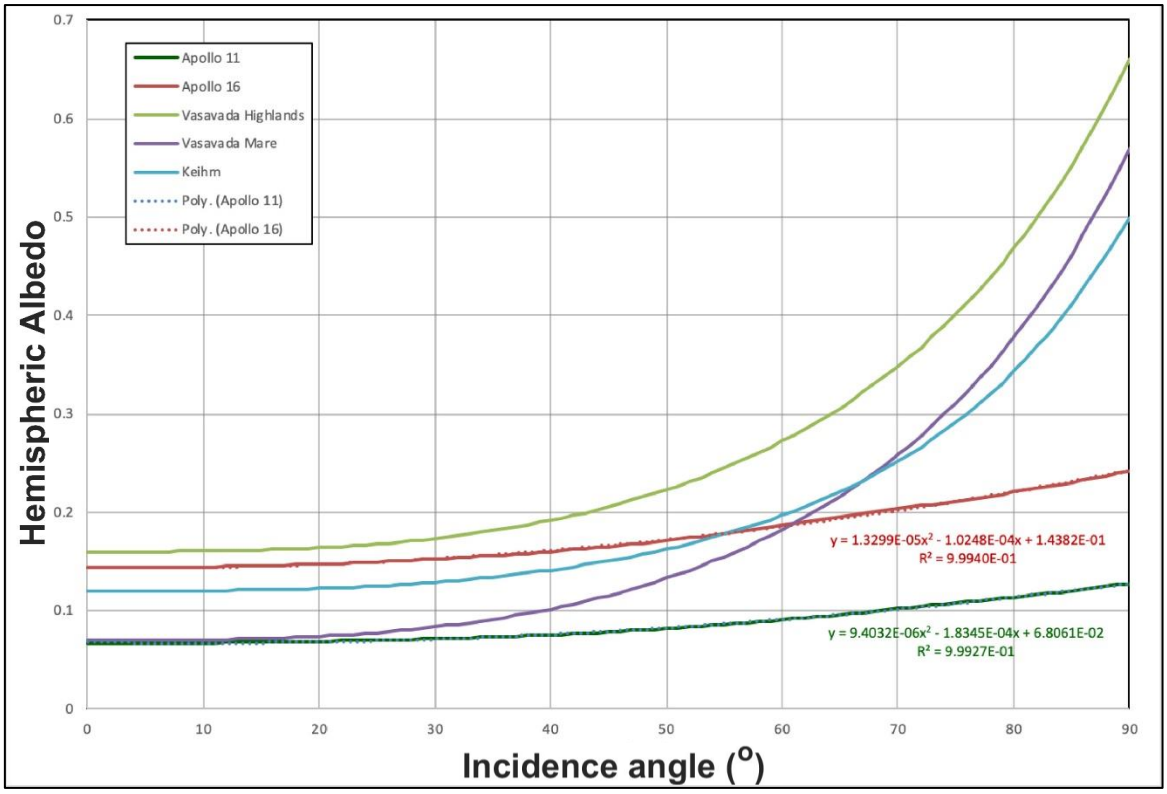

Figure 94: Solar spectrum averaged directional hemispheric albedo functions used in previous thermal models, such as (Keihm, 1984; Vasavada, Paige and Wood, 1999), and those derived using (Foote *et al.*, 2020)'s BRDF measurements of Apollo 11, 10084 and Apollo 16, 68810 regolith samples. To produce this figure, (Foote *et al.*, 2020) fitted the laboratory BRDF data using the Hapke BRDF model, and then interpolated over all incidence angles. Image from (Foote *et al.*, 2020).

Sample/study	Hemispheric albedo			
	θ_i			
	15°	30°	45°	60°
VOSEG—rough 10084	0.1262±0.0059	0.1252±0.0054	0.1272±0.0066	0.1365±0.0042
VOSEG—smooth 10084	0.1330±0.0071	0.1334±0.0070	0.1329±0.0086	0.1413±0.0053
VOSEG—rough 68810	0.2557±0.0066	0.2543±0.0072	0.2565±0.0083	0.2885±0.0089
VOSEG—smooth 68810	0.2729±0.0102	0.2702±0.0129	0.2822±0.0143	0.3184±0.0136

BUG—10084	0.1340	0.1251	0.1152	0.1000
BUG—68810	0.2817	0.2598	0.2351	0.2787

Table 41: Hemispheric albedo values derived from the VOSEG and BUG BRDF measurements of the Apollo 11, 10084 and Apollo 16, 68810 regolith samples. No errors were reported for the BUG data.

From the data given in **Table 41**, hemispheric albedo functions can be approximated for θ_i=0-90˚, as shown in **Figure 95**.

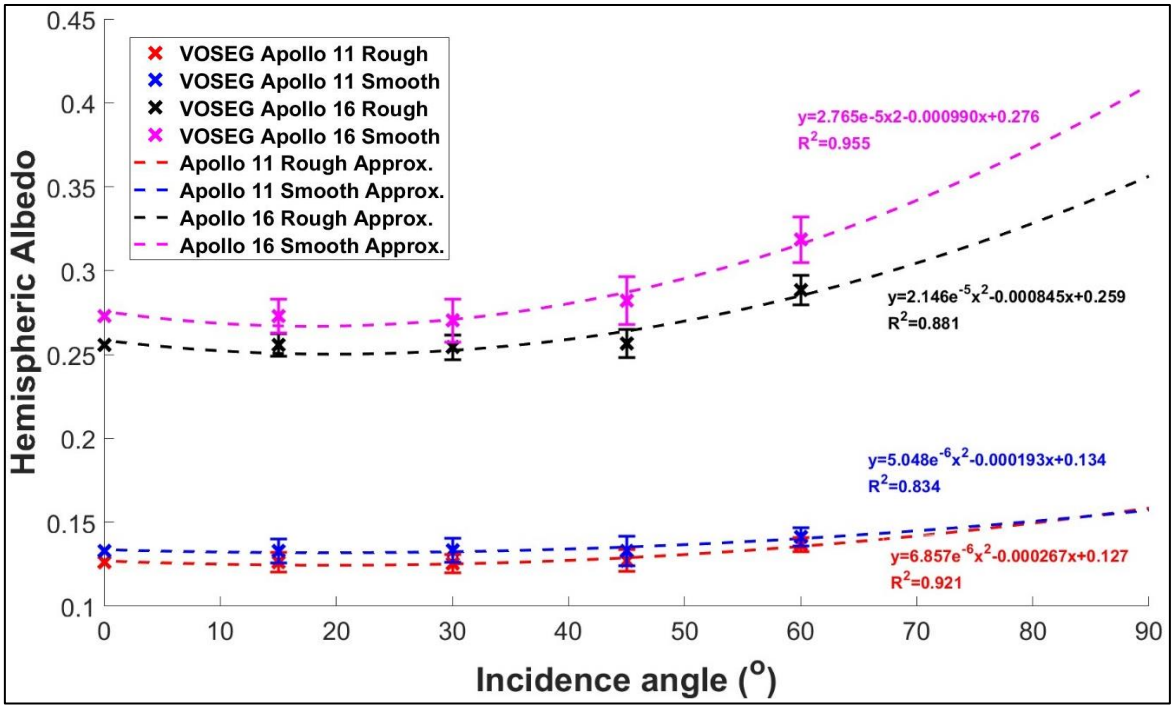

Figure 95: Hemispheric albedo functions derived from VOSEG's BRDF measurements of the Apollo 11, 10084 and Apollo 16, 68810 samples, which were measured at θ_i=15, 30, 45 and 60˚. The values at θ_i=0˚ are assumed to be equal to those at θ_i=15˚, to enable realistic quadratic approximations to be determined. The drop in hemispheric albedo predicted by these quadratic functions for θ_i=0-15˚ does represent the shape of the measured curve, however, this drop is within the measured uncertainty and is not representative of any physical process; the curve is expected to be essentially flat at this range of θ_i values.

Figure 95 demonstrates how hemispheric albedo functions derived from laboratory measurements of the Apollo regolith samples are considerably flatter than those assumed in previous thermal models (Keihm, 1984; Vasavada, Paige and Wood, 1999; Hayne *et al.*, 2017). The shapes of the derived curves are generally concordant with those derived in

(Foote *et al.*, 2020), however, the 68810 sample has a generally higher hemispheric albedo (particularly at $\theta_i \leq 30^\circ$) than was assumed in (Foote *et al.*, 2020) for highlands regolith.

Before considering the 3D case, to investigate how incorporating VOSEG's laboratory measured scattering functions into 1D thermal models affects predicted surface temperature profiles over a complete lunar diurnal cycle, the 1D Hayne model can be run for the 10084 (0.6737°N, 23.4724°E) sample retrieval site and the location assumed in (Foote *et al.*, 2020) to represent the origin of the 68810 sample (-9.0687°N, 15.4755°E). This can be done using 1) the scattering functions derived from VOSEG's rough 10084 and 68810 data, and 2) the highlands and mare scattering functions assumed in previous thermal models, as shown in **Figure 94** (Vasavada, Paige and Wood, 1999). These model predictions can then be compared to the bolometric surface temperature measurements taken by Diviner, as shown in **Figure 96**. To produce this figure, the 1D Hayne model was run with H=0.02 and $\bar{\varepsilon}$=0.99, as is standard for the O3DTM.

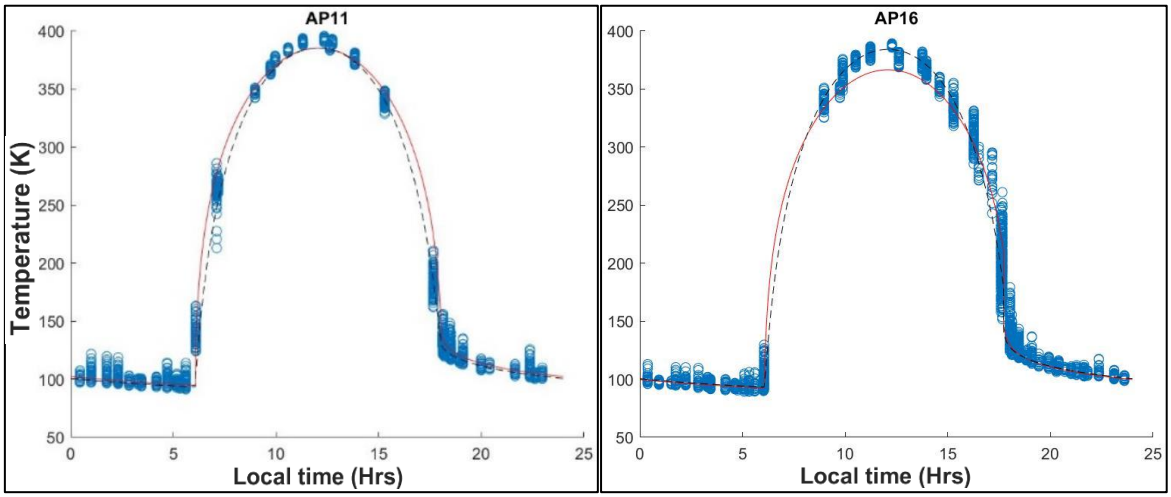

Figure 96: Showing surface temperature vs local time for the Apollo 11 (left) and Apollo 16 (right) targets, as measured by Diviner and as modelled by the 1D Hayne model, using scattering function inputs 1) assumed by Vasavada (black dashed line), and 2) derived from VOSEG's laboratory BRDF measurements (red line). Hayne parameter, H=0.02; emissivity, $\bar{\varepsilon}$=0.99.

For the Apollo 11 target, incorporating the VOSEG-measured scattering function marginally improves the 1D model's fit to the Diviner data by ~1-10 K for when the temperature profile

varies most rapidly, just after sunrise and just before sunset. However, using the laboratory measured Apollo 11 scattering function leads to similarly accurate fits to the Diviner data overall, as compared to using the one assumed for the mare in previous thermal models; particularly around lunar midday when the temperature approaches a maximum.

Conversely, incorporating the laboratory measured Apollo 16 scattering function within the 1D model for the Apollo 16 target leads to a wider and more suppressed (at the maxima) temperature profile (by ~10-20 K) than when using the scattering function assumed for the lunar highlands in previous thermal models. As for the Apollo 11 target, incorporating the VOSEG-measured Apollo 16 scattering function improves the fit to the Diviner data for when the temperature profile is changing most rapidly by up to ~10 K. However, for ~3 hours either side of lunar midday it leads to ~10 K lower temperatures than those measured by Diviner. This could be due to inaccurately set H and $\bar{\varepsilon}$ values within the model, or to the Apollo 16 sample not being representative of the target measured by Diviner (see **Figure 79**). Firstly—before considering the nature of the 68810 sample—the 1D model can be run with $\bar{\varepsilon}$ set as low as possible for the lunar surface ($\bar{\varepsilon}$ is potentially ~0.90 in some cold traps). **Figure 97** shows the 1D Hayne model temperature profiles predicted for the Apollo 11 and 16 targets with the two types of scattering functions, and compares these to Diviner's bolometric surface temperature measurements. To produce this figure, the 1D Hayne model was run with H=0.02 and $\bar{\varepsilon}$=0.90.

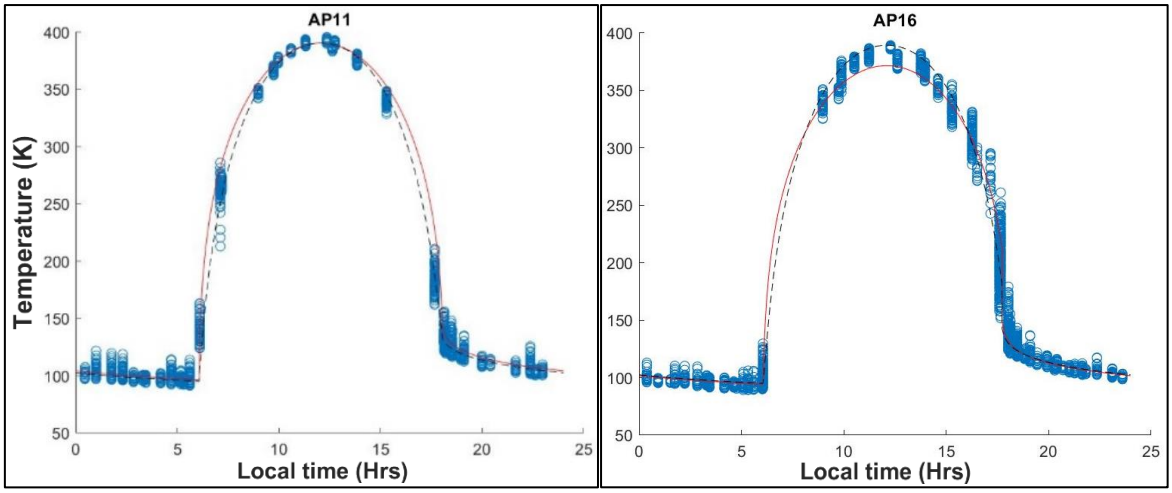

Figure 97: Showing surface temperature vs local time for the Apollo 11 (left) and Apollo 16 (right) targets, as measured by Diviner and as modelled by the 1D Hayne model, using the scattering function inputs as assumed by Vasavada (black dashed line), and as derived from VOSEG's laboratory BRDF measurements (red line). Hayne parameter, H=0.02; emissivity, $\bar{\varepsilon}$=0.90.

For the Apollo 11 target, varying the emissivity does not considerably change the model's fit to the Diviner data. However, for the Apollo 16 target, lowering the emissivity to $\bar{\varepsilon}$=0.90 leads to a ~5 K better fit between the remotely sensed data and the modelled temperature profile, particularly around lunar midday. This reduction in emissivity may be appropriate, given the relatively high albedo of the Apollo 16 sample, in comparison to what is expected for typical highlands regolith (Petro and Pieters, 2006). However, to discern the accuracy of this assumption the Apollo 16 target coordinates, and how they map to the origin of the 68810 sample, must be considered.

The 68810 regolith sample was not scooped up at a known location, but was collected from the spacesuits of the astronauts at the end of the Apollo 16 mission, and so it is a residue sample with no singular location of origin (Butler, 1972). Therefore, the scattering function of the sample could represent 1) the more typical Descartes Highlands plateau regolith located between the North Ray and South Ray craters, or 2) relatively young (<1 billion years), optically immature crater ejecta regolith collected near the North Ray and South Ray craters, or 3) some combination of the various types of regolith encountered during the mission. Hence, the temperature profiles predicted by the 1D Hayne model with the

incorporated 68810 scattering function should not only be compared to Diviner's temperature measurements of the target used in (Foote *et al.*, 2020), but also to measurements of the young, optically immature cratered regions near the Apollo 16 landing site. **Figure 98** shows an albedo map of the Descartes Highlands region with crosses denoting the Apollo 16 landing site and the location assumed in (Foote *et al.*, 2020) to be the origin of the 68810 sample. The two high albedo regions are the North Ray (~50 million years old) and South Ray (<1 billion years old) craters, which were visited during the Apollo 16 mission (although the astronauts only ventured to the edge of South Ray crater, as it was reported to be full of boulders, and so would have been difficult to explore on a rover) (DeJong *et al.*, 1972).

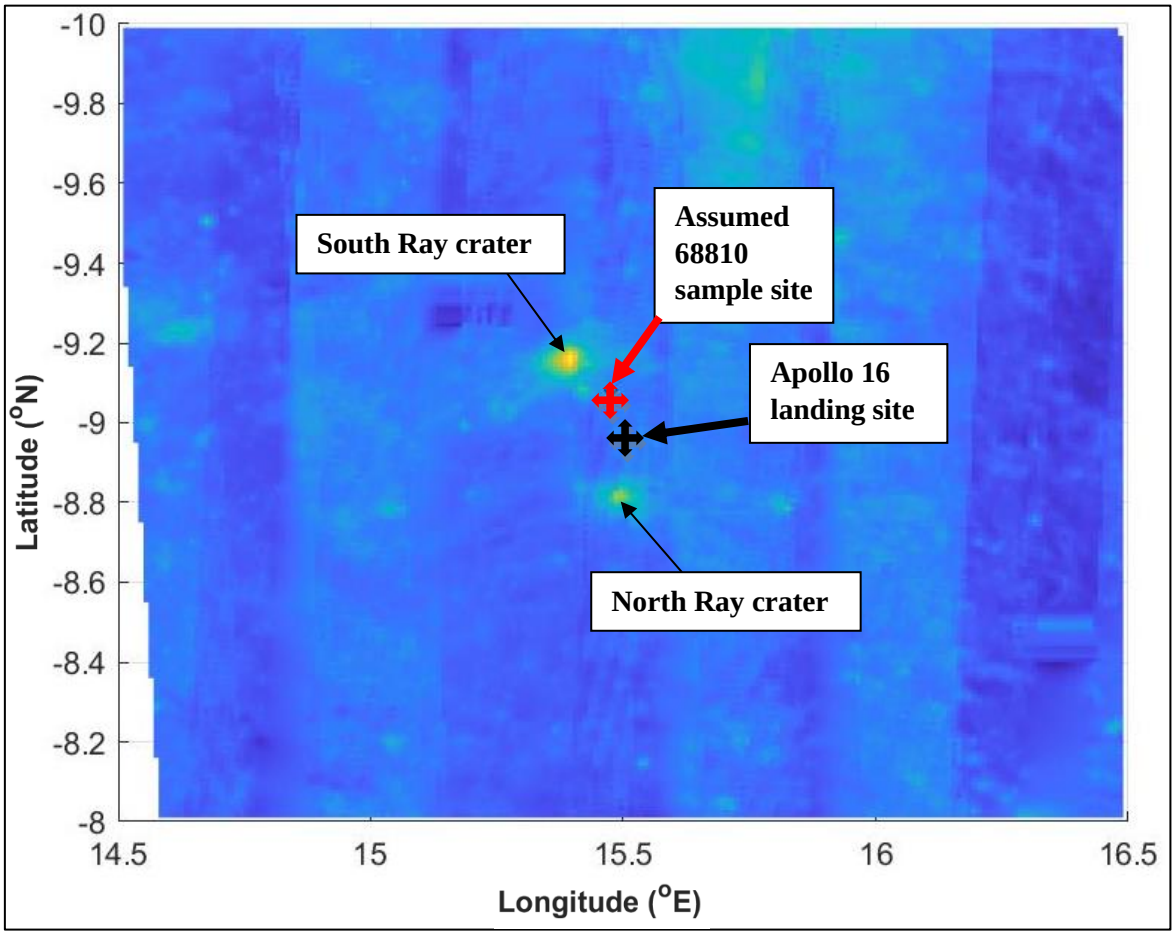

Figure 98: Albedo map of the Descartes Highlands region of the lunar surface. The location of the Apollo 16 landing site is marked by a black cross, and the 68810 sample site assumed in (Foote *et al.*, 2020) is marked by a red cross. The relatively high albedo

North Ray and South Ray craters, which are young (<1 billion years old) optically immature craters, are also labelled.

Figure 99 then shows how 1D thermal model predictions compare to Diviner's temperature measurements for the 68810 sample site assumed in (Foote *et al.*, 2020) (left), and a target centred in the relatively high albedo, optically immature South Ray crater (right).

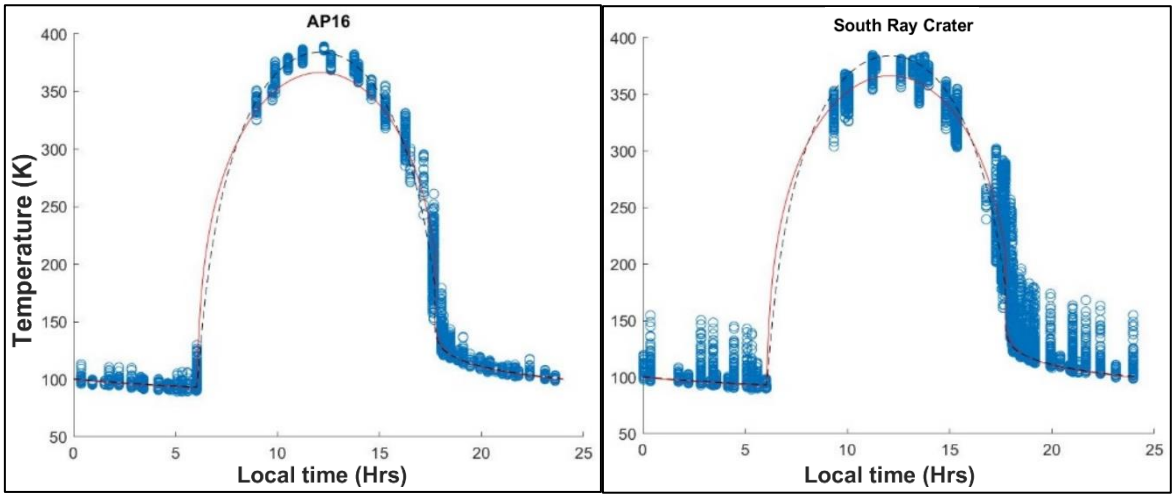

Figure 99: Showing surface temperature vs local time for the 68810 sample site assumed in (Foote *et al.*, 2020) (left) and a target centred in the relatively high albedo, optically immature South Ray crater (right), as measured by Diviner and as modelled by the 1D Hayne model, using the scattering function inputs as assumed by Vasavada (black dashed line), and as derived from VOSEG's laboratory BRDF measurements (red line). Hayne parameter, H=0.02; emissivity, $\bar{\varepsilon}$=0.99.

Figure 99 demonstrates how the surface temperature profile predicted by the 1D Hayne model, with the incorporated VOSEG-measured scattering function, fits Diviner's temperature measurements of the South Ray crater target better (by ~10-15 K) than the assumed 68810 sample site. However, the range in temperature values for the South Ray crater is larger than for the assumed Apollo 16 sample site. This may indicate that the scattering function of the 68810 sample is more representative of higher albedo, crater ejecta regolith than of the more typical highlands plateau regolith found between the North Ray and South Ray craters—and this deduction may be further supported by the results of the Diviner off-nadir study in Part 5.3, in which the Apollo 16 Hapke BRDF model fitting method produced better fits, generally, to the younger, higher albedo targets than it did to the High-latitude Highlands target. (For the Kepler Crater Ejecta (mare), Aristarchus Plateau

(mare), Dufay Albedo Anomaly (highlands) and Equatorial Cold Spot (highlands) targets, the respective R^2 values at θ_i=60° were 0.895, 0.883, 0.908 and 0.871; and for the High-latitude Highlands target, the R^2 value at θ_i=60° was 0.832.) However, the large range of temperature values measured by Diviner for the South Ray crater means that this is inconclusive and so the 68810 BRDF data measured by VOSEG and BUG may represent 1) relatively young, high albedo crater ejecta regolith, 2) typical highlands plateau regolith, or 3) a combination of both.

Now that the inclusion of VOSEG-measured scattering functions within the 1D Hayne model has been considered, the effects of incorporating VOSEG's laboratory data within the O3DTM can be studied. In Part 1.3.3, it was demonstrated that the effects of varying visible-λ scattering within the O3DTM will be most prominent for high-latitude regions, in which PSRs are present. Therefore, in the following section, the results of running the O3DTM with the incorporated VOSEG-measured 68810 scattering function for a high-latitude highlands, South Pole region of the lunar surface (-74 to -80°N; -40 to -80°E) are detailed. Furthermore, the predicted temperature maps produced by the updated model are compared to those produced when using the scattering function previously assumed for highlands regolith in (Keihm, 1984; Vasavada, Paige and Wood, 1999; Hayne *et al.*, 2017).

6.2 3D Thermal Model Results

For the 3D thermal modelling work performed in this study, a high-latitude highlands region of the lunar South Pole (-74 to -80°N; -40 to -80°E) was chosen for its range of topographical features (including PSRs). The O3DTM was run for this region using 1) the previously assumed scattering function for lunar highlands regolith—which from here will be referred to as the 'previous studies' case (Hayne *et al.*, 2017)—and 2) the scattering function derived from VOSEG's BRDF measurements of the rough 68810 sample. These modelled

temperature profiles can be compared to Diviner measurements of the region to deduce how well the two versions of the O3DTM model fit the remote sensing data.

Figure 100 shows the maximum bolometric surface temperature map measured by Diviner for this region.

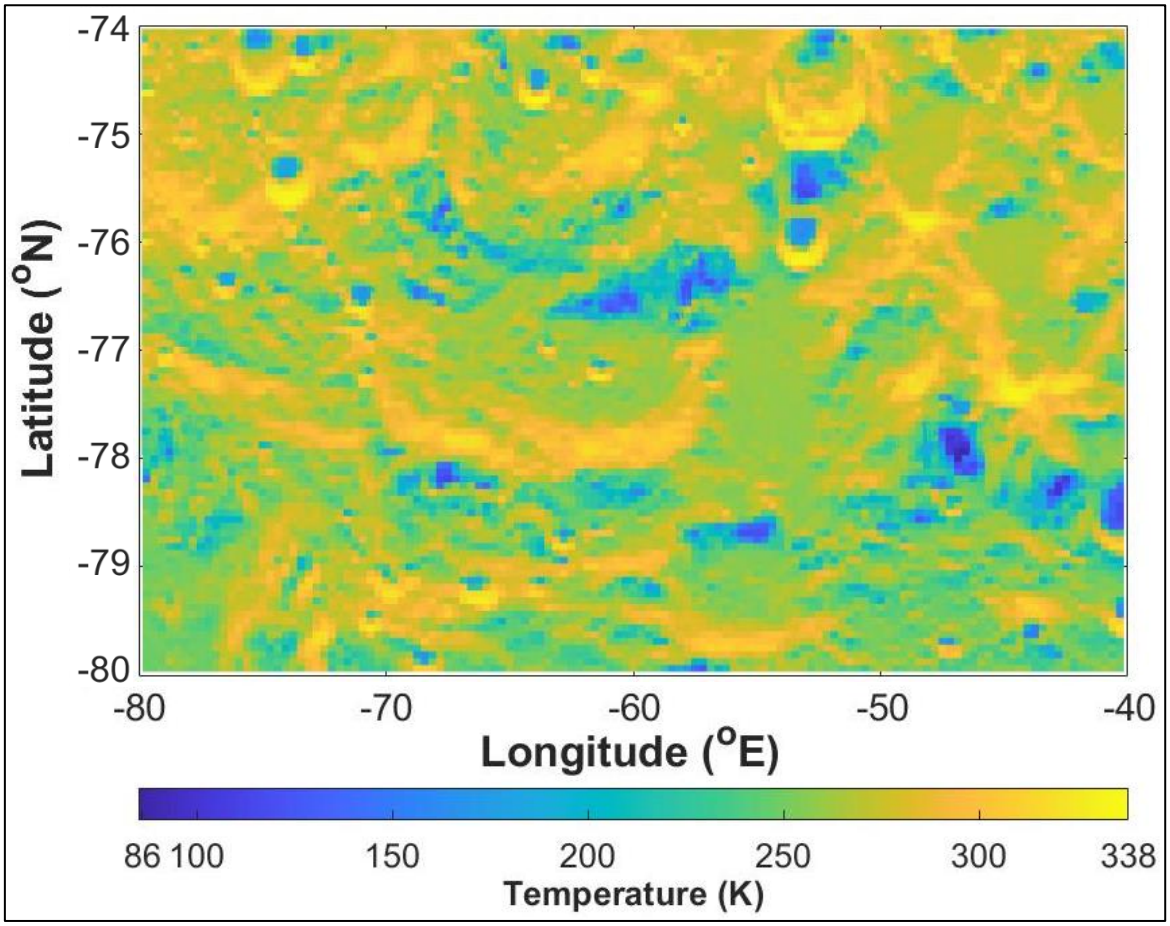

Figure 100: Maximum bolometric surface temperature map measured by Diviner for the high-latitude, highlands region of the lunar South Pole which was selected for the thermal modelling work performed in this study (-74 to -80˚N; -40 to -80˚E). Various cold traps are present within the area's permanently shadowed regions (dark blue regions). Image credit: Dr. Tristram Warren (private communication).

Figure 100 shows the temperature profile of the selected region, and demonstrates how cold traps exist within the area's PSRs. Many of these cold traps are permanently colder than the temperature above which water ice sublimates (~112K).

Before investigating how well the temperature map produced by the O3DTM using the updated 68810 scattering function fits to the Diviner temperature map, the fit using the

previously assumed highlands scattering function should first be considered. Therefore, **Figure 101** shows the discrepancies between Diviner's maximum surface temperature measurements and the maximum temperatures predicted by the O3DTM for the region when using the scattering function assumed for the lunar highlands in previous studies such as (Hayne *et al.*, 2017). This can be considered as the most up to date case, previous to this study, with a goodness of fit of R^2=0.786.

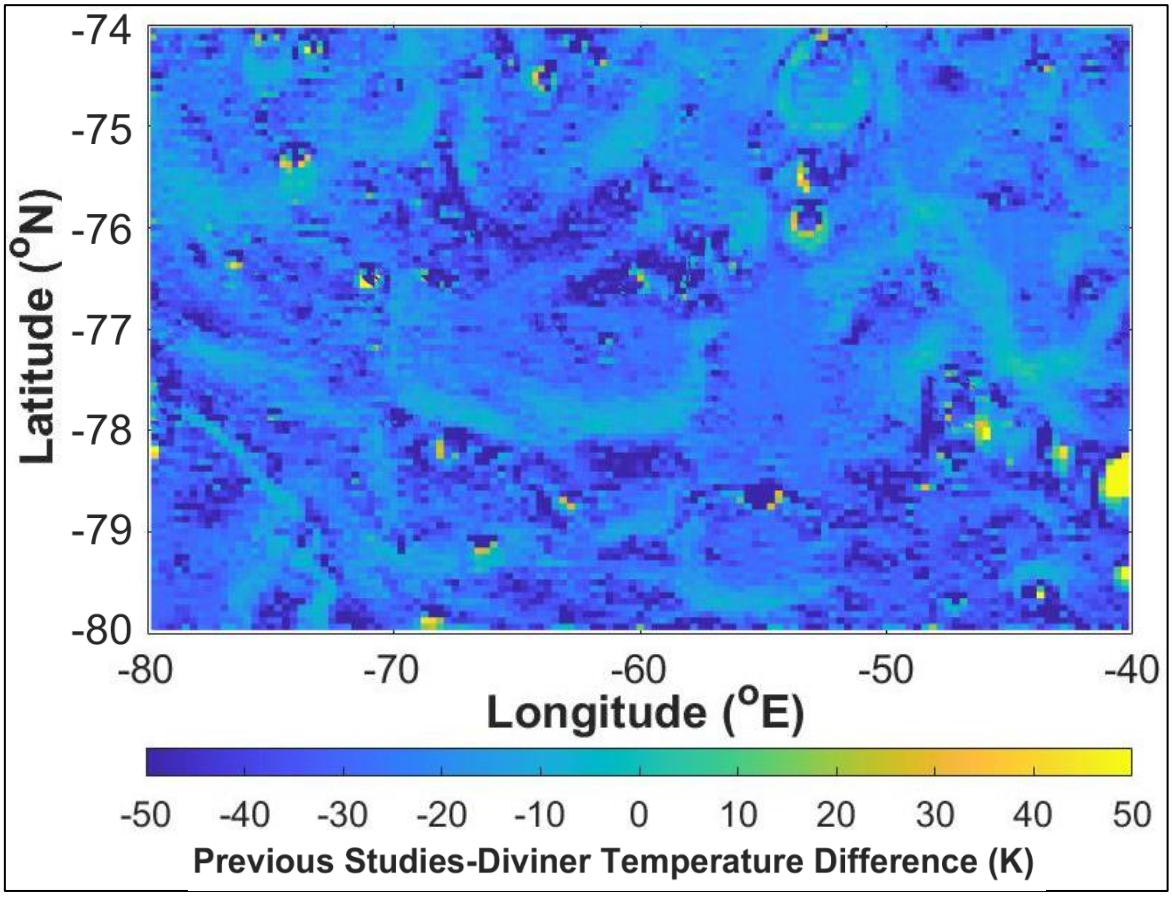

Figure 101: Showing the differences in maximum surface temperatures between Diviner bolometric temperature measurements and the predictions made by the Oxford 3D Thermal Model using the 'previous studies' scattering function case. This is for the high-latitude, highlands region of the lunar South Pole which was selected for the thermal modelling work performed in this study (-74 to -80°N; -40 to -80°E). For this fit, R^2=0.786. Image credit: Dr. Tristram Warren (private communication).

Figure 101 shows discrepancies of up to ±50 K between the O3DTM maximum temperature predictions—when using the 'previous studies' scattering function case—and Diviner's maximum surface temperature measurements. For most of the modelled region, the O3DTM using the 'previous studies' case scattering function underestimates the maximum

temperatures observed by Diviner. However, for many of the areas surrounding cold trap craters, the O3DTM using the 'previous studies' case scattering function overestimates the maximum temperatures observed by Diviner by up to ~50 K. Before showing the equivalent temperature discrepancy plot using the VOSEG-measured 68810 scattering function within the O3DTM—which from here will be referred to as this study's case, **Figure 102** shows the maximum surface temperature maps produced for the two cases.

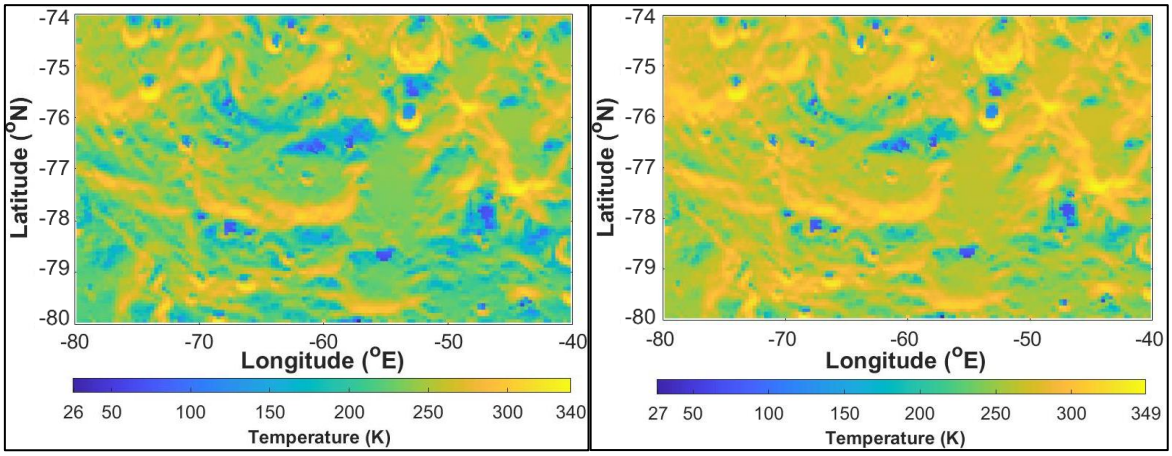

Figure 102: Showing the maximum surface temperature map predicted by the O3DTM using the 'previous studies' scattering function case (left) and this study's scattering function case (right). This is for the high-latitude, highlands region of the lunar South Pole which was selected for the thermal modelling work performed in this study (-74 to -80°N; -40 to -80°E). Image credit: Dr. Tristram Warren (private communication).

The differences between the two cases shown in **Figure 102** are demonstrated quantitively by **Figure 103**, which shows the discrepancies in predicted maximum surface temperatures between using the two scattering function cases within the O3DTM.

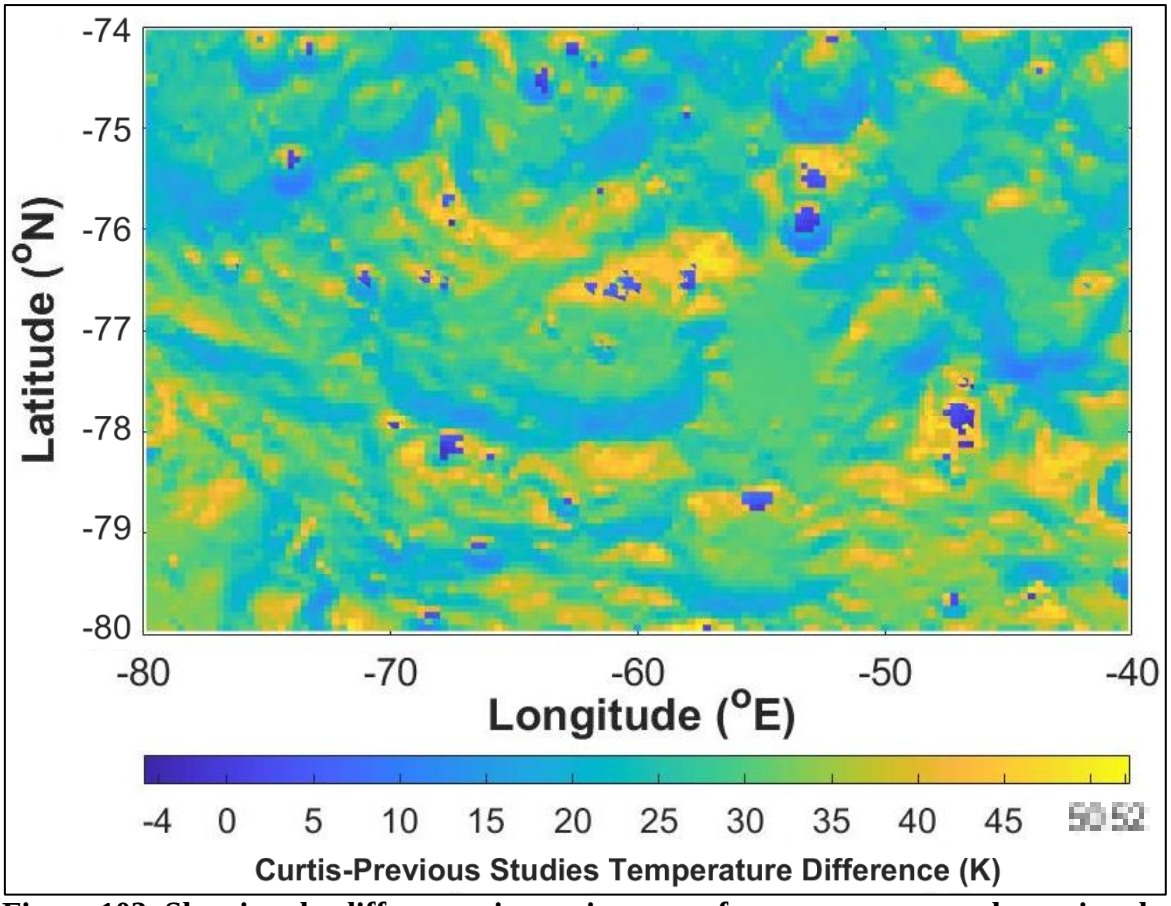

Figure 103: Showing the differences in maximum surface temperatures when using the 'previous studies' or this study's scattering function case within the Oxford 3D Thermal Model. This is for the high-latitude, highlands region of the lunar South Pole which was selected for the thermal modelling work performed in this study (-74 to -80˚N; -40 to -80˚E). Image credit: Dr. Tristram Warren (private communication).

Figure 103 shows how using this study's scattering function case within the O3DTM leads to higher maximum temperature predictions, of up to ~50 K, than using the 'previous studies' scattering function case. When using this study's scattering function case, higher maximum temperatures are predicted for the majority of the region's highlands plateau areas, in addition to the majority of the areas surrounding the region's cold trap craters. The only areas which are modelled to have lower maximum temperature values when using this study's scattering function case are within the region's PSR craters, and these discrepancies are only up to ~4 K. When comparing **Figures 101**, **102** and **103**, it appears the maximum temperature discrepancies observed between Diviner measurements and the O3DTM's predictions when using the 'previous studies' scattering function case are partly resolved by

incorporating this study's scattering function case within the model, and this is demonstrated by **Figure 104**, which shows the discrepancies between Diviner's maximum surface temperature measurements and the maximum surface temperatures predicted by the O3DTM for the region when using this study's scattering function case. This leads to a goodness of fit value, R^2=0.941.

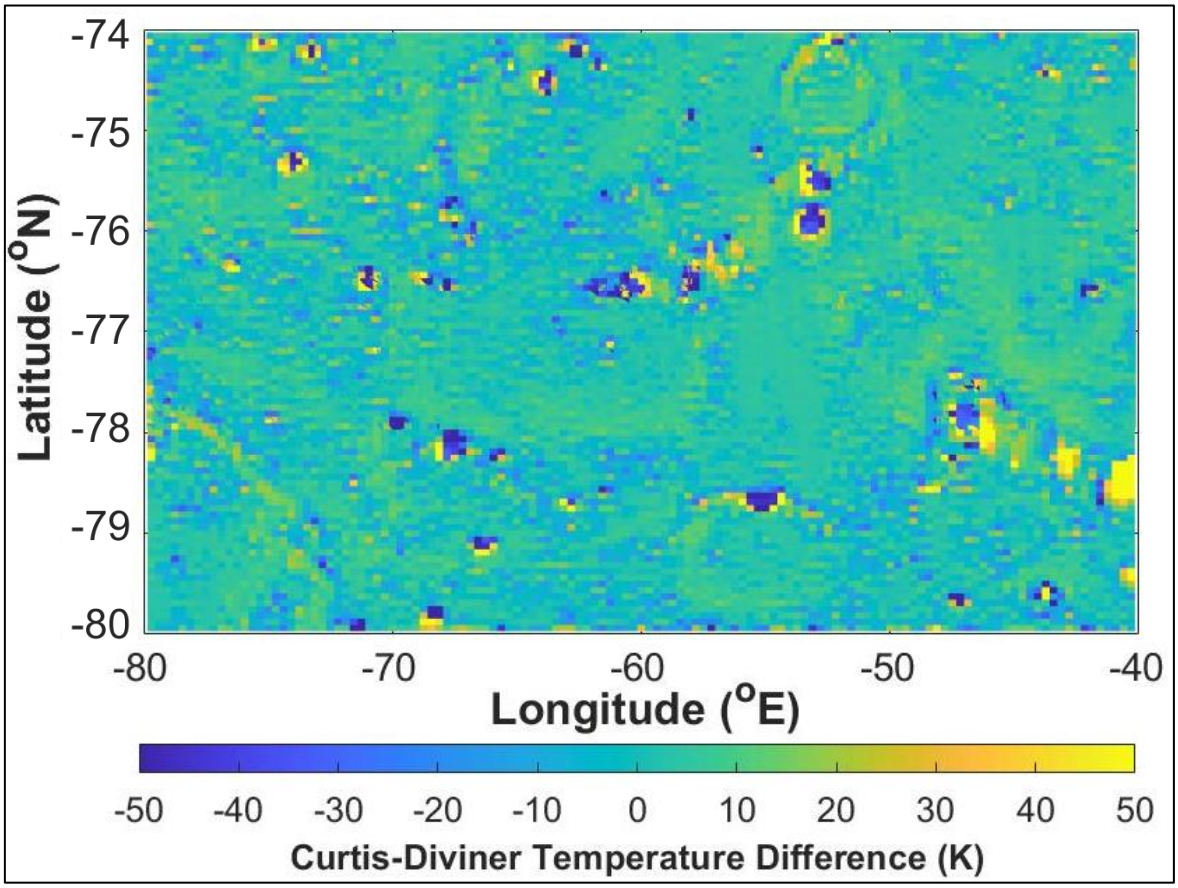

Figure 104: Showing the differences in maximum surface temperatures between Diviner bolometric temperature measurements and the predictions made by the Oxford 3D Thermal Model using this study's 68810 scattering function case. This is for the high-latitude, highlands region of the lunar South Pole which was selected for the thermal modelling work performed in this study (-74 to -80°N; -40 to -80°E). For this fit, R^2=0.941. Image credit: Dr. Tristram Warren (private communication).

Figure 104 shows how the overall fit between the O3DTM maximum surface temperature predictions and the Diviner bolometric surface temperature measurements improves—with discrepancies ~<10 K for the majority of the region, in particular for the highlands plateau areas—as opposed to discrepancies of ~25-50 K observed for the majority of the highlands plateau regions in **Figure 101**. This is demonstrated by the improvement in the goodness of

fit values from R^2=0.786 to R^2=0.941. Nevertheless, discrepancies of up to ~50 K are still observed for the areas surrounding many of the region's cold trap craters (for which Diviner observes higher maximum surface temperatures than are predicted by the O3DTM) and within PSRs (for which Diviner observes lower maximum temperatures than are predicted by the O3DTM). These results suggest that the scattering function derived from VOSEG's measurements of the 68810 sample may generally represent the highlands regolith present in the selected region more accurately than the scattering function previously assumed for the lunar highlands in (Keihm, 1984; Vasavada, Paige and Wood, 1999; Hayne *et al.*, 2017), and this suggests the 68810 sample may be more representative of highlands plateau material than North/South Ray crater material (see Part 6.1). However, the results of this study also suggest that incorporating the VOSEG-measured 68810 scattering function into the O3DTM cannot resolve the maximum temperature discrepancies observed at many of the region's crater rims—or for the areas surrounding many of the region's cold trap craters—as the temperature profiles of these regions are expected to be dominantly influenced by variations in TIR reemission from surrounding local topographies. Nevertheless, so far only maximum surface temperature profiles have been considered (as these are most important for predicting where surficial water ice may be present). Therefore, to demonstrate the improvements and limitations of using this study's scattering function case within the O3DTM for 'cold' and 'hot' targets for all times of day, **Figure 105** shows surface temperature vs time plots for a cold trap area (left), and a high temperature area present within the selected region (right). Temperature predictions made by the O3DTM using the 'previous studies' scattering function case, and bolometric temperature measurements made by Diviner are also included.

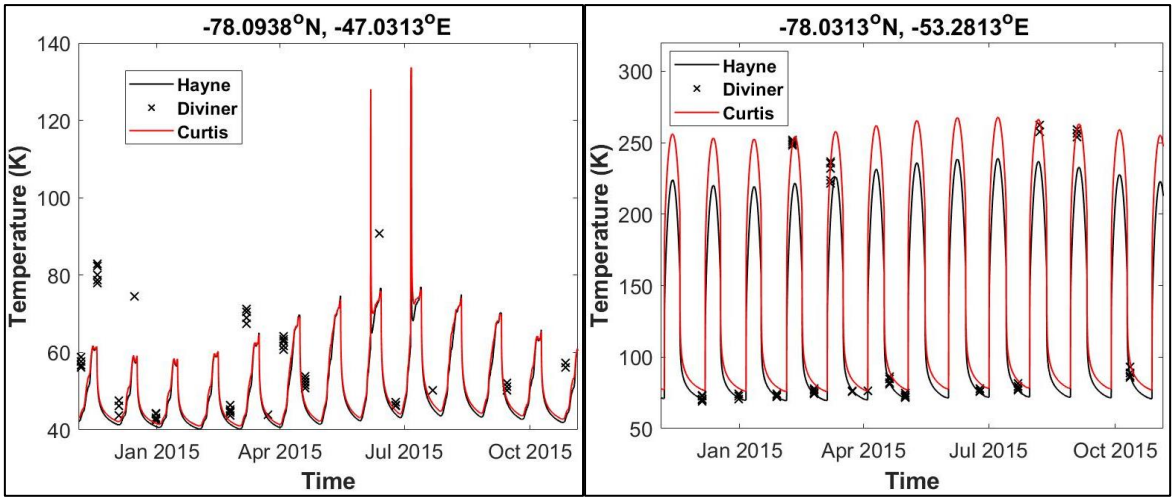

Figure 105: Showing year-long surface temperature vs time plots for a high-latitude lunar highlands cold trap area located at -78.0938°N, -47.0313°E (left), and a high-latitude highlands high temperature area located at -78.0313°N, -53.2813°E (right). Included in the images are Diviner bolometric surface temperature measurements (black crosses), and temperature predictions made by the Oxford 3D Thermal model when using the 'previous studies' scattering function case (black line), and this study's scattering function case.

Figure 105 shows how, for the cold spot region, including this study's scattering function case within the O3DTM leads to a marginally improved (by up to ~2 K) fit to the Diviner measurements, particularly for the time periods when $T \leq 60$ K. However, for both cases, the model is similarly poor at predicting the temperature of the cold trap for the time periods when $T > 65$ K, and this is to be expected, given that visible-λ scattering does not dominate heat transfer for cold trap regions, but reradiation of TIR does. For the high temperature area, including this study's scattering function case within the O3DTM leads to generally better fits (by up to ~25 K) to the Diviner measurements for the time periods when $T > 220$ K. Conversely, including the 'previous studies' scattering function case within the O3DTM does lead to better fits (by ~5 K) to the Diviner measurements for the time periods when $T \leq 75$ K. This may be because the 'previous studies' scattering function case was derived so as to fit the Diviner measurements at these time periods.

Now that the surface temperature discrepancies between Diviner measurements and the O3DTM, when using the scattering function derived from VOSEG's BRDF measurements,

have been shown to improve for the majority of the high-latitude highlands region selected for this study, goal G4 of this project has been fulfilled. However, improvements in 3D thermal modelling for high-latitude regions of the lunar surface are driven by the current interest in discovering, and then studying ice water trapped in the lunar surface/subsurface. Therefore, a key question is: How does incorporating this study's scattering function case into the O3DTM affect the stability of water ice at various depths of the lunar surface? To answer this question, **Figure 106** shows the differences between the depths at which water ice is predicted to be thermodynamically stable by the O3DTM for the high-latitude highlands region selected for this study when using 1) the 'previous studies' scattering function case, and 2) this study's scattering function case.

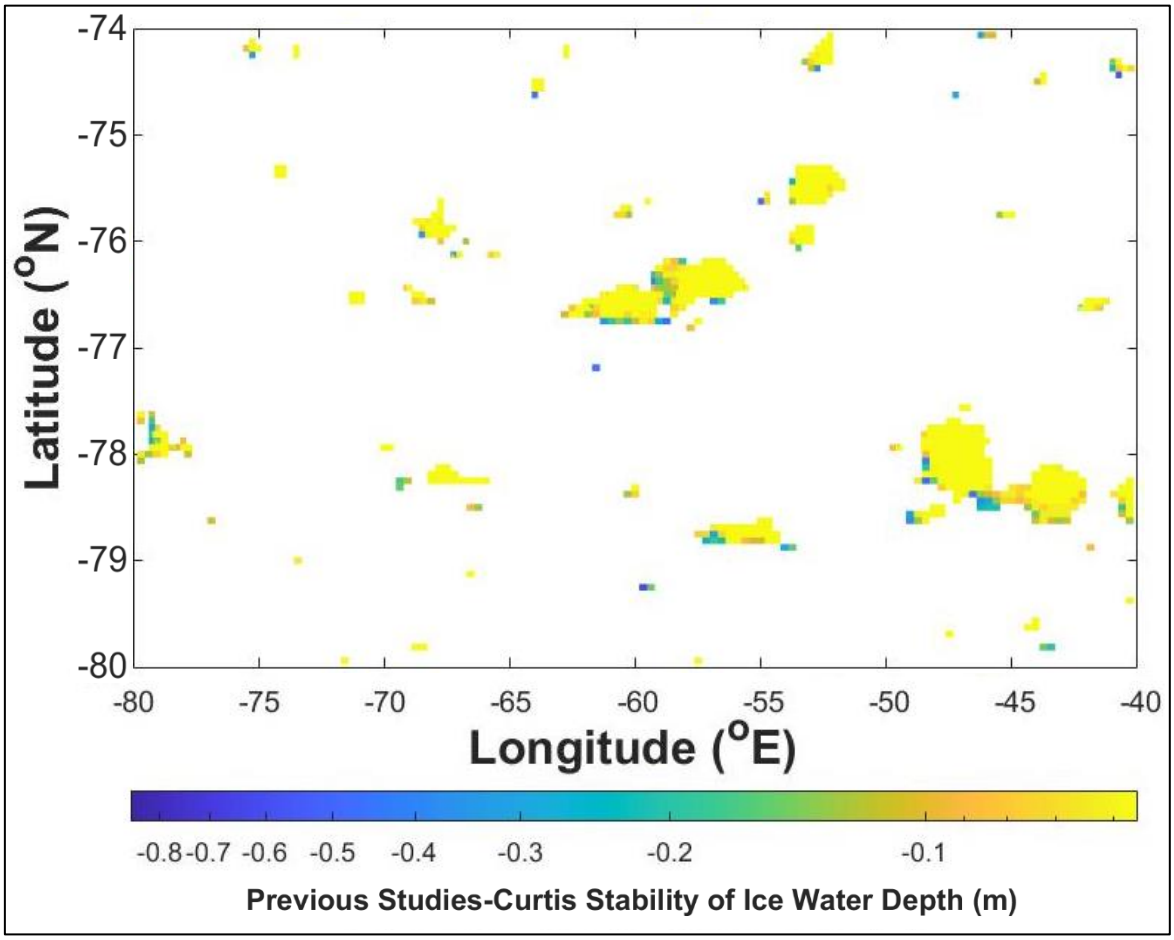

Figure 106: Showing the differences between the depths at which water ice is predicted to be thermodynamically stable by the O3DTM when using 1) the 'previous studies' scattering function case, and 2) this study's scattering function case. This is for the high-latitude, highlands region of the lunar South Pole which was selected for the

thermal modelling work performed in this study (-74 to -80˚N; -40 to -80˚E). Image credit: Dr. Tristram Warren (private communication).

Figure 102 shows how incorporating this study's scattering function case into the O3DTM leads to generally deeper modelled predictions for water ice stability in the lunar regolith subsurface, when compared to using the 'previous studies' scattering function case. The O3DTM using this study's scattering function case predicts that water ice will be driven deeper by ~0.1 m for the majority of the region's possible water ice deposits. However, for some areas, particularly those surrounding cold trap craters, using this study's scattering function case increases the minimum depth at which water ice may be stable in the lunar regolith by up to ~0.8 m. This would be a significant difference in depth if a crewed or robotic mission were to attempt to access water ice deposits located in one of these regions on the Moon. Therefore, the temperature maps produced in this study have demonstrated the necessity of including more realistic, laboratory measured visible-λ scattering functions (and in future, similar TIR emission phase functions) within 3D thermal models, particularly for studies concerning the distribution, nature and analysis of ice water trapped in the lunar surface/subsurface.

The results of this study were produced without incorporating any azimuthal variation into the O3DTM. This modification would considerably increase the computational time needed to run the model, however, may result in further improvements between the temperature profiles modelled by the O3DTM and Diviner's temperature measurements. Furthermore, as discussed in Part 6.1, the 68810 sample used in this study may only represent one type of material present in the highlands region selected for this study. Therefore, to further improve the accuracy of the scattering functions used within thermal models, suites of BRDF measurements for more diverse regolith samples could be measured, as the material present on the lunar surface is complex, and not well-represented by just the 10084 and 68810 Apollo samples.

7 Conclusions and Future Work

This project identified the need for laboratory measured visible scattering functions of the lunar regolith, in light of (Shepard and Helfenstein, 2011; Hapke, 2012; Foote *et al.*, 2020), and hence, it explored the utility of such a laboratory dataset, in terms of 1) testing and constraining key terms within the Hapke BRDF model, 2) interpreting Diviner's visible-λ off-nadir remote sensing measurements, and 3) inputting more realistic scattering functions within 1D and 3D thermal models, such as the 1D Hayne model and the O3DTM. The motivation behind the work derived from the current interest in lunar temperature profiles at high latitudes—due to the potential discovery of ice water, and other ice volatiles, in and around lunar PSRs—coupled with the fact that for some PSRs, Diviner's remote sensing temperature measurements are discrepant with 3DTMs by up to ~15-30 K (dependent on location). Part 1.3 explored various thermal models, and deduced that inaccurately set visible-λ scattering functions within 3DTMs may contribute to the observed temperature discrepancies. This led to the initial goal of this research project, G1—which was to measure a suite of BRDFs for two well-characterised, representative (mare and highlands) Apollo regolith samples. Once this goal was realised, this dataset could be used 1) to test various terms within the Hapke BRDF model (goal G2), 2) to enable Diviner's visible-λ off-nadir data to be interpreted in a novel way (goal G3), and 3) to set realistic scattering functions within thermal models (goal G4).

To design a laboratory setup which could measure the BRDF dataset required to fulfil the aims of the project, various experimental requirements were derived using the Hapke BRDF model, the Diviner visible-λ off-nadir dataset and the O3DTM. These included viewing angle requirements, light source stability requirements, and requirements regarding the preparation and measurement of the lunar regolith samples used in the study. Once the requirements were set out, an automated goniometer setup called VOSEG was developed by

adapting an existing setup called OSEG, which was originally built to measure TIR emission phase functions in lunar-like conditions. The development process involved modifying the optical setup of the goniometer, mapping the illumination spot and FOV and testing how polarisation and height and tilt variations affected measured BRDFs. Once these laboratory studies were complete, the broadband VOSEG setup was shown to meet the experimental requirements set out in Part 3.3, and its BRDF measurements of a White Spectralon® calibration target were shown to agree with the visible-λ goniometer, BUG, within measured uncertainty. This fulfilled aim A1 and goal G0. (In future, filters could be added to the setup which would enable studies of wavelength-dependent factors such as regolith surface roughness at different length scales.)

Thus, the setup was used to measure a suite of BRDFs across a range of viewing angles for two representative Apollo regolith samples, 10084 (Apollo 11) and 68810 (Apollo 16), in line with aim A2. As part of the work done to derive the experimental requirements of the study, the effects of varying sample porosity and surface roughness on BRDF were investigated, and it was found that both porosity and surface roughness needed to be measured for the study to fulfil the aims of the project. Using an Alicona® 3D instrument, the surface profiles of the samples were measured down to 10 μm lateral resolution, enabling filling factor and RMS slope angle values (for size-scales ≥10 μm) to be calculated. This was done for both the rough and smooth 10084 and 68810 samples, and so, four broadband BRDF datasets for regolith samples with well-characterised porosity and surface roughness profiles were measured, fulfilling goal G1.

Each of the four BRDF datasets (given in the Appendix) includes measurements for mare or highlands Apollo regolith samples at 0-70° reflectance angle, in steps of 5°; 0-180° azimuthal angle, in steps of 45°; and at 15, 30, 45 and 60° incidence angles. For each sample, filling factor and RMS slope angle values were determined. This enabled two of the free parameters

within the Hapke BRDF model to be set, allowing deductions to be made for three of the other key parameters, w, b and h_S. The best fit values of w were determined without setting an unrealistic filling factor value for the surface, and so they are not overestimated, as may be the case in previous photometry studies of the lunar surface (Sato *et al.*, 2014). The determination of RMS slope angle values for each sample at 10, 50, 100, 500 and 1000 μm provided a link between the slope angle value described in the Hapke BRDF model, and the physical nature of a regolith sample's surface. To determine the size-scale at which the measured value of $\bar{\theta}$ best described how the Hapke slope angle parameter influenced the shape of a sample's BRDFs, the Hapke BRDF model was fitted to the VOSEG data using measured $\bar{\theta}$ values at each of the five size-scales. 'Goodness' of fit R^2 values were compared for each sample, and a general trend was deduced: that using $\bar{\theta}$ values at 10, 50 and 100 μm generally produced 'very poor', or 'poor' fits to the laboratory measured BRDF data. In contrast, using $\bar{\theta}$ values at 500 and 1000 μm generally produced 'good' fits to the VOSEG BRDF data, and so 500-1000 μm was determined to be the practical size-scale range most well represented by the Hapke slope angle parameter, fulfilling goal G2. Once this size-scale range was determined, the Hapke BRDF model was fitted to the VOSEG Apollo sample BRDF data (using $\bar{\theta}$ values at 500-1000 μm) with w, b and h_S set as the three open parameters. Hence, w, b and h_S values were determined for each sample, by fitting the model to all available data at once (with the complete fitting function method). These values were then compared to the relevant values determined in (Sato *et al.*, 2014; Foote *et al.*, 2020).

Plotting the VOSEG BRDF data alongside the best fit Hapke BRDF model curves showed discrepancies between the model and the laboratory measured data, particularly at low (15° and 30°) incidence angles. These discrepancies at low incidence angles were forcing the model to accommodate at high (45° and 60°) incidence angles, thus leading to w and b values which were not representative of the higher incidence angle data. Therefore, the Hapke

BRDF model was fitted to the four BRDF datasets one incidence angle at a time (with the split incidence angle fitting method), and the best fit curves produced by using the two fitting methods were compared. This part of the study showed that by using a split incidence angle method, higher R^2 values are generally produced, and the deduced best fit w, b and h_S values were more representative of those deduced in (Sato *et al.*, 2014; Foote *et al.*, 2020). Furthermore, this part of the study again showed that the Hapke BRDF model generally fits better to the high (45° and 60°) incidence angle laboratory datasets, than the low (15° and 30°) incidence angle datasets, thus motivating a future study in which datasets at higher incidence angles are measured. This is a key result for remote sensing studies which only use BRDF data at a limit range of incidence angles, and makes the reproducibility of studies which deduce sets of Hapke parameters for a given surface more difficult.

To further explore how varying the initial conditions of the Hapke BRDF model affects its BRDF predictions, the complete fitting method was used to fit the model to the VOSEG BRDF datasets, but with the opposition effect terms turned off (e.g., B_{C0} and B_{S0} were set to 0). This demonstrated the necessity of including the opposition effect within the Hapke BRDF model, even without being able to discern the contributions of the SHOE and CBOE to the total opposition effect. It also demonstrated how the best fit w, b and h_S parameters are affected by removing the opposition effect, as the model attempts to accommodate for the surge in BRDF at low phase angles (<10°) by varying w and b.

In line with aim A3, next, the study built on the previous deductions produced by fitting the Hapke BRDF model to the VOSEG BRDF data, to develop a novel method for interpreting Diviner's visible-λ off-nadir data, for varying targets on the lunar surface. The radiance data for each target was processed through a pipeline which outputted scattering functions at each incidence angle that could be directly compared to those measured for the Apollo samples in the laboratory. After plotting the rough and smooth Apollo BRDFs to the Diviner off-

nadir data, it became immediately clear by eye that the BRDFs of the rough Apollo samples most accurately represented the remote sensing data, as demonstrated in **Figure 85**. Therefore, for each target with a known petrology (i.e., mare or highlands), the best fit w values were set as those determined for the associated rough Apollo sample, as were the φ and $\bar{\theta}$ values—with $\bar{\theta}$ set as the value determined for the laboratory sample at 500 μm size-scale. For the targets which had less well-constrained petrologies, the fitting process was performed using the initial assumptions provided by the BRDF measurements of each rough Apollo sample (10084 and 68810), and the 'goodness' of fits produced by each method were compared. This provided a method by which the scattering behaviour of each target could be compared to both mare-like and highlands-like regolith; thus enabling possible deductions to be made about these regions of the lunar surface, and fulfilling goal G3.

The Diviner off-nadir study showed that, as for the Apollo sample measurements, the Hapke BRDF model produces better fits for high (≥45°) incidence angle data, than for low (≤30°) incidence angle datasets. And although there was insufficient data to make deductions about the Reiner Gamma, King Crater Melt Pond, or High-latitude Mare regions, various patterns emerged from the best fit parameters, b, h_S and $\bar{\theta}$, determined for the other seven targets. As is potentially to be expected, the Aristarchus Plateau, Equatorial Cold Spot, and Dufay Albedo Anomaly targets exhibited more highlands-like scattering behaviours; and the Kepler Crater Ejecta target exhibited more mare-like scattering. As in (Sato *et al.*, 2014), the scattering nature of the targets which contained young crater ejecta—e.g., the Aristarchus Plateau and Equatorial Cold Spot—led to lower deduced b values than for other highlands-like regions, although the range between the values was lower in this study than for the values deduced in (Sato *et al.*, 2014). Furthermore, following the trend demonstrated in (Sato *et al.*, 2014; Foote *et al.*, 2020), the more mare-like regions—e.g. the High-latitude Mare, Equatorial Mare and Kepler Crater Ejecta regions—exhibited higher b values than

those deduced for the more highlands-like regions, indicating more forward-scattering surfaces.

In contrast to the deduced range of w values, the h_S values determined in the VOSEG-Diviner study spanned a larger range than the values determined in (Sato *et al.*, 2014; Foote *et al.*, 2020), which varied between h_S≈0.01 and h_S≈0.06. However, they did follow the same trend as those deduced in (Sato *et al.*, 2014), with highlands-like regions exhibiting larger h_S values than mare-like regions (by a factor of ~10). The cluster formed by the h_S values determined in the VOSEG-Diviner study for the mare-like regions was roughly equal to the value determined (for both mare and highlands regions) in (Foote *et al.*, 2020); and the cluster formed by the h_S values determined for the highlands-like regions was ~30% higher than those determined for both regions in (Sato *et al.*, 2014); with the exception of the Equatorial Cold Spot h_S value, which agreed with the deduced (Sato *et al.*, 2014) highlands value.

However, the fact that this diverse set of Diviner off-nadir targets can only be compared to the two representative Apollo samples measured in this study clearly limits the deductions which can be made for each target. In future, performing the VOSEG-Diviner off-nadir study fitting process using BRDF measurements for a more diverse set of lunar regolith samples may provide a method by which the scattering behaviours of more complex types of lunar regolith may be deduced; other than simply determining whether they are more mare- or highlands-like.

In addition to investigating the scattering nature of the targets, the VOSEG-Diviner off-nadir study also determined $\bar{\theta}$ values, which may be assumed to represent the RMS slope angles of the lunar regolith at ~500 μm. The study showed that the $\bar{\theta}$ values deduced for the off-nadir targets clustered around two distinct values; with mare-like regions exhibiting $\bar{\theta}$ values

around ~21°, and highlands-like regions exhibiting $\bar{\theta}$ values around ~15°. This may be due to artifacts within the fitting process, or it may be an indication that mare regolith tends to create rougher surfaces on the Moon than highlands regolith. Although the $\bar{\theta}$ values for Apollo samples prepared in this study were ~equal at 500-1000 μm size-scales, a similar surface roughness trend was observed for the 10084 (mare) and 68810 (highlands) samples at 10-100 μm size-scales, however, the observed discrepancies were ~4 times less prominent.

Given that $\bar{\theta}$ values were determined for each Diviner off-nadir target at an assumed size-scale of ~500 μm, these values could be extrapolated to a range of size-scales (e.g., 10-1000 μm) using an approximate relationship between RMS slope angle and size-scale. Therefore, the RMS slope angle vs size-scale curves measured for the Apollo regolith samples were used to derive best fit Gompertz functions describing the rough, smooth and average regolith surfaces formed by the laboratory samples. These equations could then be used to determine information about the physical nature of the regolith structures formed on the lunar surface, for each of the seven Diviner off-nadir targets, over 10-1000 μm size-scales. This work may help to bridge a longstanding knowledge gap in lunar science, and in future, may be used to further constrain lunar surface digital elevation models at 10-1000 μm size-scales.

Finally, in accordance with aim A4, VOSEG's laboratory measured BRDFs for the rough 10084 and 68810 samples were used to derive hemispheric albedo functions which could be used to set more realistic scattering function inputs within the O3DTM. The hemispheric albedo functions derived using the BRDF data measured in this study were considerably flatter than those assumed in previous thermal modelling studies of the lunar surface, and the 68810 function was shown to be generally brighter than that which was previously assumed for typical highlands regolith.

To demonstrate how incorporating laboratory measured scattering functions within the 1D Hayne model affected temperature predictions, the model was run with both the 'previous studies' and this study's scattering function inputs for the Apollo 11 landing site, and the site which was previously assumed to be the location of the 68810 sample, with O3DTM standard H-parameter and emissivity values. Using the 10084 scattering function within the 1D model led to only marginal differences in the modelled surface temperature profile of the Apollo 11 landing site, when compared to the previous case. However, for the assumed location of the 68810 sample, using the laboratory measured 68810 scattering function led to considerable variations in modelled temperatures, particularly within ~3 hours of lunar midday, as compared to Diviner measurements and previous thermal model results. Due to these discrepancies, the 1D Hayne model was run using a lower emissivity value (which may be appropriate given the relatively high albedo of the sample, as compared to typical highlands regolith); although lowering the emissivity only partially improved the fit between the Diviner measurements and the 1D Hayne model (with the 68810 scattering function). This led to a further investigation into the nature and origin of the 68810, and it was found that the sample was not scooped up at a particular location, but is a residue sample collected from the spacesuits of the astronauts at the end of the Apollo 16 mission with no singular location of origin. Therefore, the sample could represent a combination of the different regolith types present at the Apollo 16 exploration site, including ejecta from the South Ray and North Ray craters, which are relatively young, bright, optically immature craters. The 1D Hayne model was therefore run for a target centred in the South Ray crater for both scattering function cases and the results were compared to Diviner's surface temperature measurements. This marginally improved the fit between the Diviner measurements and the updated 1D Hayne model (with the 68810 scattering function); potentially suggesting that the 68810 sample is representative of a combination of young, bright, optically immature

crater ejecta and typical highlands plateau regolith. This was further supported by the generally higher R^2 values produced using the 68810 scattering function assumption when fitting the Hapke BRDF model to the Diviner off-nadir data for the relatively high albedo, crater ejecta regions measured in the Diviner off-nadir study in Part 5.3, as compared to the High-latitude Highlands target.

Following on from the 1D thermal model results, to demonstrate the effects of incorporating laboratory measured scattering functions into 3D thermal models, the O3DTM was run for a high-latitude highlands region of the lunar South Pole (-74 to -80°N, -40 to -80°E), for both the 'previous studies' and this study's scattering function cases; and these were compared to the relevant Diviner measurements. This showed that using this study's scattering function case led to generally better modelled temperature predictions (by up to ~30K), when compared to Diviner's surface temperature measurements, than using the previously assumed case, particularly for the highlands plateau and 'hot spot' areas. **Figure 104** shows how the temperature discrepancies between the Diviner measurements and the O3DTM modelled temperature profiles were improved for almost all regions of the surface, fulfilling goal G4, except for the areas within and around PSR craters, for which temperature discrepancies up to ~50K still exist. These results suggest that the scattering function derived from VOSEG's 68810 BRDF measurements generally represents the highlands regolith in the selected region better than what was assumed in previous thermal models; but also that TIR emission phase function measurements, and BRDF measurements of a more diverse set of samples may be needed to improve the accuracy of 3D models for PSR cold traps. In addition, azimuthal angle variations may need to be included for cold trap temperatures to be more accurately modelled, despite the long computational time needed to investigate this.

Finally, due to the current interest in the potential distribution of water ice in the lunar surface/subsurface, the O3DTM was run down to 1m depth, for the high-latitude highlands

region selected in Part 6, to produce 'depth of water ice stability' maps when using both the 'previous studies' and this study's scattering function cases. This showed that incorporating this study's 68810 scattering function case into the O3DTM affected the minimum depth at which water ice could be stable within various regions of the lunar regolith by between ~0.1-0.8 m; generally driving the water ice deeper into the subsurface due to increased modelled temperature profiles predicted across the region. Such updated water ice stability maps may be crucial for future lunar exploration missions which aim to locate, access and study water ice present on the lunar surface/subsurface. However, discrepancies still remain between 3D thermal models and remote sensing measurements which may need to be addressed if the temperature profiles of high-latitude landing sites are to be fully characterised in preparation for crewed or robotic missions.

This study serves as one small step towards the larger goal of fully understanding and utilizing visible-λ scattering functions for the lunar regolith. In future, there may be much gained from BRDF studies of a wider range of returned regolith samples, which could enable 1) more appropriate assumptions to be made when interpreting the Diviner off-nadir dataset, or 2) more diverse scattering functions to be set within thermal models. Due to time constraints, in this project the updated O3DTM was only run for a selected region of the lunar highlands, but ideally, the model would be run for the entire lunar surface/subsurface, with the 10084 and 68810 scattering functions used for the mare and highlands regions, respectively.

Many of the results of this project are dependent upon the physicality of the Hapke BRDF model, which has been updated multiple times since its conception. In terms of further improving the utility of the model, a study in which polarisers are used to distinguish between the effects of the SHOE and CBOE contributions to the total opposition effect may enable deductions to be made in terms of these two sets of parameters, from laboratory and

remote sensing studies of the lunar surface. This may lead to more accurate deductions being made when determining h_S values, such as in Part 5.3. Additionally, in light of this study's investigation into the methods used when fitting the Hapke BRDF model to laboratory or remote sensing BRDF data, it may prove useful to compare the best fit Hapke parameters outputted by this study to those outputted by a Bayesian statistics fitting approach, such as the one detailed in (Belgacem, Schmidt and Jonniaux, 2018), for the Apollo regolith samples and seven off-nadir targets measured by Diviner.

This study demonstrated how laboratory measured BRDFs of Apollo samples could be used to interpret Diviner's off-nadir measurements for various pre-selected targets, which contain a range of lunar surface petrologies and physical properties. However, there are currently only seven targets for which there is sufficient data to fit the Hapke BRDF model and to output best fit Hapke parameters. In future, it would be desirable to be able to compare BRDF measurements of the Apollo samples to Diviner's off-nadir measurements of the stereo imaged Apollo landing sites (Helfenstein and Shepard, 1999), in addition to regions for which the surface is expected to be particularly rough or smooth (Rubanenko *et al.*, 2020). Furthermore, since the 68810 sample was deduced to potentially represent young, bright, optically immature crater ejecta, it may be fruitful to compare VOSEG's 68810 BRDF data to young, bright crater ejecta regions in both mare and highlands areas, in addition to the high albedo, crater ejecta targets previously measured by Diviner. Therefore, in 2021, a range of new Diviner off-nadir targets were suggested by a group of lunar scientists including R. Curtis. These targets are detailed in **Table 42**. For the Apollo 11, 12, 14 and 16 landing sites, full phase function measurements plan to be made; and for the craters/regions determined in (Rubanenko *et al.*, 2020) to represent particularly rough or smooth surfaces, principal plane measurements are planned to be made.

Target	Latitude (°N)	Longitude (°E)	Reason of interest
Apollo 11 (10084)	0.67	23.47	Stereo imaged; VOSEG study.
Apollo 12 (12001)	-3.01	-23.42	Stereo imaged.
Apollo 14 (at ALSEP)	-3.64	-17.48	Stereo imaged.
Apollo 16 (68810)	-8.97	15.48	VOSEG study.
Mare Smythii	-0.23	87.24	Pre-Nectarian (~3.9-4.5 billion years old) mare region with interesting mineralogy and expected to be relatively smooth.
Mendeleev	5.26	142.03	Far-side highlands crater; expected to be relatively rough.
Glushko	8.20	139.90	Young (<1.1 billion years old), high albedo highlands crater; expected to be relatively rough.
Tycho	-43.17	-11.33	Young (~100 million years old), young, high albedo crater; expected to be relatively rough.
Copernicus	9.74	-20.15	Young (<1 billion years old), high albedo mare crater; expected to be relatively rough.
Clavius	-58.40	-14.40	High-latitude highlands crater; potential location of water ice.

Table 42: Detailing the proposed targets which are to be measured by the next stage of the Diviner off-nadir campaign. For the Apollo targets, full phase functions measurements are to be made; for all other targets, principal plane measurements are to be made.

Performing the Hapke BRDF model fitting process on this new set of Diviner off-nadir targets may enable further deductions to be made regarding the compositional and physical properties of the regolith present at each location. Furthermore, it may be possible to compare the BRDFs measured for the Apollo regolith samples in this study to those measured by Diviner for their respective locations of origin. This may enable further deductions to be made for how regolith roughness profiles vary with size-scale, and may help to place further constraints upon lunar digital elevation models for ~10-1000 μm size-scales. In addition, now that visible-λ scattering functions can be set within 3D thermal model using laboratory measurements—as opposed to setting them so that the model best

matches Diviner—it may be possible to study whether the lunar surface exhibits a latitude-dependence on porosity. By interpreting Diviner off-nadir data measured for the new targets detailed in **Table 42**, it may be possible to discern whether regions with similar regolith petrologies, but different latitudes—such as Mendeleev and Clavius—exhibit higher or lower albedo scattering functions, potentially due to variations in porosity.

In conclusion, this project has demonstrated how laboratory measured lunar regolith scattering functions may be used 1) to further constrain key parameters within the Hapke BRDF model, 2) to interpret off-nadir data measured by remote sensing instruments, and 3) to set more accurate scattering functions within thermal models. Yet, the Moon is not the only airless body of interest in the solar system, and studies similar to this one could also be performed for Mercury, asteroids and comets. Although no samples are yet to be returned from Mercury, the production of simulant samples is continuously improving, and much will be learnt about Mercury's surface from the measurements taken by Bepicolombo (Benkhoff *et al.*, 2010). For asteroids and comets, recent successful sample retrieval missions may enable photometric measurements to be made for samples with known locations of origin (Lauretta and Team, 2012); and meteorites collected on Earth soon after impact may also provide samples which can be measured in the laboratory to produce photometric datasets similar to those of the Apollo samples (O'Brien *et al.*, 2022). By further studying these airless bodies, further constraints may be placed upon the distribution, nature and history of water ice in the solar system. This may lead to a further understanding of the history of the Earth and the origins of life upon it.

Bibliography

Arnold, J.R. (1979) “Ice in the Lunar Polar Regions,” *Journal of Geophysical Research*, 84(9).

Bandfield, J.L. *et al.* (2014) “Lunar cold spots: Granular flow features and extensive insulating materials surrounding young craters,” *Icarus*, 231, pp. 221–231. Available at: https://doi.org/10.1016/j.icarus.2013.12.017.

Bandfield, J.L. *et al.* (2015) “Lunar surface roughness derived from LRO Diviner Radiometer observations,” *Icarus*, 248, pp. 357–372. Available at: https://doi.org/10.1016/j.icarus.2014.11.009.

Barker, M.K. *et al.* (2016) “A new lunar digital elevation model from the Lunar Orbiter Laser Altimeter and SELENE Terrain Camera,” *Icarus*, 273, pp. 346–355. Available at: https://doi.org/https://doi.org/10.1016/j.icarus.2015.07.039.

Basilevsky, A.T., Abdrakhimov, A.M. and Dorofeeva, V.A. (2012) “Water and other volatiles on the moon: A review,” *Solar System Research*. Available at: https://doi.org/10.1134/s0038094612010017.

Belgacem, I., Schmidt, F. and Jonniaux, G. (2018) “Estimation of Hapke parameters on selected areas of Europa using a Bayesian approach.”

Benkhoff, J. *et al.* (2010) “BepiColombo-Comprehensive exploration of Mercury: Mission overview and science goals,” *Planetary and Space Science*. Available at: https://doi.org/10.1016/j.pss.2009.09.020.

Bentham (2017) “Bentham IL1 QTH Source,” pp. 1–2.

Biggar, S.F., Thome, K.J. and Wisniewski, W. (2003) “Vicarious radiometric calibration of EO-1 sensors by reference to high-reflectance ground targets,” *IEEE Transactions on Geoscience and Remote Sensing*. Available at: https://doi.org/10.1109/TGRS.2003.813211.

Binder, A.B. (1998) “Lunar prospector: Overview,” *Science*. Available at: https://doi.org/10.1126/science.281.5382.1475.

Bird, M. *et al.* (1970) “Genesis of lunar soil at Tranquillity Base,” *Proc. Apollo 11 Lunar Sci. Conf.*, 1.

Birkebak, R.C. (1974) “Thermal Radiation Properties of Lunar Materials from the Apollo Missions,” *Advances in Heat Transfer*. Available at: https://doi.org/10.1016/S0065-2717(08)70108-4.

Bottke, W.F. and Norman, M.D. (2017) “The Late Heavy Bombardment,” *Annual Review of Earth and Planetary Sciences*. Available at: https://doi.org/10.1146/annurev-earth-063016-020131.

Burke, J.D. (2014) “Planetary Exploration Missions,” in *Encyclopedia of the Solar System*. Available at: https://doi.org/10.1016/b978-0-12-415845-0.00056-6.

Butler, J. (1997) “The migration of volatiles on the surfaces of Mercury and the Moon of the extension probable existence of substantial deposits of ices in permanently shaded polar regions This has renewed the old argument about the of Mercury by Butler were negative local,” *Journal of Geophysical Research*, 102, pp. 283–291.

Butler, P. (1972) *LUNAR SAMPLE INFORMATION CATALOG - APOLLO 16*.

Carrier III, W.D., Olhoeft, G.R. and Mendell, W. (1991) “Physical Properties of the Lunar Surface,” *Lunar Sourcebook*.

Chandrasekhar, S. (1960) “Radiative Transfer.” New York: Dover Publications Inc.

Chavers, G. *et al.* (2019) “NASA’s human lunar landing strategy,” in *Proceedings of the International Astronautical Congress, IAC*.

Chevrel, S.D. *et al.* (2009) “The Aristarchus Plateau on the Moon: Mineralogical and structural study from integrated Clementine UV–Vis–NIR spectral data,” *Icarus*, 199(1), pp. 9–24. Available at: https://doi.org/10.1016/J.ICARUS.2008.08.005.

Chin, G. *et al.* (2007) “Lunar reconnaissance orbiter overview: The instrument suite and mission,” *Space Science Reviews*. Available at: https://doi.org/10.1007/s11214-007-9153-y.

Colaprete, A. *et al.* (2010) “Detection of water in the LCROSS ejecta plume,” *Science*. Available at: https://doi.org/10.1126/science.1186986.

Curtis, R.J., Warren, T.J. and Bowles, N.E. (2021) “LPSC Abstract #1056: Measuring and Interpreting Bidirectional Reflectance Distribution Functions for Apollo Lunar Regolith Samples Using the Visible Oxford Space Environment Goniometer,” in *52nd Lunar and Planetary Science Conference (2021)*, pp. 16–17.

Curtis, R.J., Warren, T.J. and Bowles, N.E. (2021), “Updates to the Oxford Space Environment Goniometer to measure visible wavelength bidirectional reflectance distribution functions in ambient conditions”, *Review of Scientific Instruments*, 92, 034504

DeJong, E. *et al.* (1972) “Apollo 16 Preliminary Science Report,” *Geol. Surv. Misc. Invest. Ser. Map*.

Dunkin, S. and Heather, D. (1999) “New views of the Moon,” *Physics World*.

Fisackerly, R. *et al.* (2015) “Accessing, Drilling and Operating at the Lunar South Pole: Status of European Plans and Activities,” in. Available at: https://doi.org/10.1061/9780784479179.027.

Foote, E. *et al.* (2010) “Apollo 11 and 16 Soil Bi-directional Solar Reflectance Measurements, Models and LRO Diviner Observations,” *AGU Fall Meeting Abstracts*, pp. 1499-.

Foote, E. *et al.* (2020) “The bidirectional and directional hemispheric reflectance of Apollo 11 and 16 soils: Laboratory and Diviner measurements,” *Icarus*, 336, p. 113456. Available at: https://doi.org/https://doi.org/10.1016/j.icarus.2019.113456.

Gold, T. (1955) “The Lunar Surface,” *Royal Astronomical Society*, 115, pp. 585–684.

Gompertz, B. (1833) “On the nature of the function expressive of the law of human mortality, and on a new mode of determining the value of life contingencies. In a letter to Francis Baily, Esq. F. R. S., By Benjamin Gompertz, Esq. F. R. S,” *Abstracts of the Papers Printed in the Philosophical Transactions of the Royal Society of London*, 2, pp. 252–253. Available at: https://doi.org/10.1098/rspl.1815.0271.

Greenhagen, B. T. *et al.* (2017) “Sideways Views of the Moon: Mapping Directional Thermal Emission with Diviner,” in *AGU Fall Meeting Abstracts*, pp. P41D-2850.

Greenhagen, B. T., et al. (2020). “*Abstract #2171 - THE LUNAR MINERALOGY TERNARY TO INTERPRET LRO DIVINER AND FUTURE THERMAL INFRARED DATASETS”, 51st Lunar and Planetary Science Conference Abstracts, #2171*.

Greffet, J.-J. and Nieto-Vesperinas, M. (1998) “Field theory for generalized bidirectional reflectivity: derivation of Helmholtz’s reciprocity principle and Kirchhoff’s law,” *J. Opt. Soc. Am. A*, 15(10), pp. 2735–2744. Available at: https://doi.org/10.1364/JOSAA.15.002735.

Gunderson, K. and Thomas, N. (2008) “Polarimetric NIR reflectance measurements of regolith simulants at zero phase angle,” *Planetary and Space Science*. Available at: https://doi.org/10.1016/j.pss.2008.09.004.

Gunderson, K., Thomas, N. and Whitby, J.A. (2006) “First measurements with the Physikalisches Institut Radiometric Experiment (PHIRE),” *Planetary and Space Science*. Available at: https://doi.org/10.1016/j.pss.2005.12.020.

Hambleton, K. (2020) *Around the Moon with NASA’s First Launch of SLS with Orion | NASA, NASA*.

Hapke, B. (1981) “Bidirectional reflectance spectroscopy: 1. Theory,” *Journal of Geophysical Research: Solid Earth*. Available at: https://doi.org/10.1029/jb086ib04p03039.

Hapke, B. (1984) “Bidirectional reflectance spectroscopy. 3. Correction for macroscopic roughness,” *Icarus*. Available at: https://doi.org/10.1016/0019-1035(84)90054-X.

Hapke, B. (1986) “Bidirectional reflectance spectroscopy. 4. The extinction coefficient and the opposition effect,” *Icarus*. Available at: https://doi.org/10.1016/0019-1035(86)90108-9.

Hapke, B. (1993) “Theory of reflectance and emittance spectroscopy,” *Theory of reflectance and emittance spectroscopy*. Available at: https://doi.org/10.1111/j.1945-5100.2012.01391.x.

Hapke, B. (2011) *Theory of Reflectance and Emittance Spectroscopy*. Cambridge: Cambridge University Press. Available at: https://doi.org/10.1017/CBO9781139025683.

Hapke, B. (2012) “Bidirectional reflectance spectroscopy 7,” *Icarus*. Available at: https://doi.org/10.1016/j.icarus.2012.10.022.

Hapke, B. (2021) “Bidirectional reflectance spectroscopy 8. The angular width of the opposition effect in regolith-like media,” *Icarus*, 354, p. 114105. Available at: https://doi.org/https://doi.org/10.1016/j.icarus.2020.114105.

Hapke, B., Nelson, R. and Smythe, W. (1998) “The Opposition Effect of the Moon: Coherent BackscatterandShadow Hiding,” *Icarus*. Available at: https://doi.org/10.1006/icar.1998.5907.

Hapke, B. and Sato, H. (2015) “The Porosity of the Upper Lunar Regolith,” *Icarus*, 273. Available at: https://doi.org/10.1016/j.icarus.2015.10.031.

Hauri, E.H. *et al.* (2015) “Water in the moon’s interior: Truth and consequences,” *Earth and Planetary Science Letters*. Available at: https://doi.org/10.1016/j.epsl.2014.10.053.

Hayne, P. *et al.* (2013) “Thermophysical Properties of the Lunar Surface from Diviner Observations,” 15(2009), p. 10871.

Hayne, P.O. *et al.* (2010) “Diviner lunar radiometer observations of the LCROSS impact,” *Science*. Available at: https://doi.org/10.1126/science.1197135.

Hayne, P.O. *et al.* (2017) “Global Regolith Thermophysical Properties of the Moon From the Diviner Lunar Radiometer Experiment,” *Journal of Geophysical Research: Planets*. Available at: https://doi.org/10.1002/2017JE005387.

Helfenstein, P. (1988) “The geological interpretation of photometric surface roughness,” *Icarus*. Available at: https://doi.org/10.1016/0019-1035(88)90056-5.

Helfenstein, P. and Shepard, M.K. (1999) “Submillimeter-Scale Topography of the Lunar Regolith,” *Icarus*, 141(1), pp. 107–131. Available at: https://doi.org/10.1006/icar.1999.6160.

Hendrix, J. and Carman, C.H. (2010) *Renaissance Theories of Vision Introduction*, *Renaissance Theories of Vision*. Available at: https://doi.org/10.1163/157338211X607835.

Hiesinger, H. (2006) “New Views of Lunar Geoscience: An Introduction and Overview,” *Reviews in Mineralogy and Geochemistry*. Available at: https://doi.org/10.2138/rmg.2006.60.1.

Honniball, C.I. *et al.* (2021) “Molecular water detected on the sunlit Moon by SOFIA,” *Nature Astronomy*, 5(2), pp. 121–127. Available at: https://doi.org/10.1038/s41550-020-01222-x.

Huang, Y. *et al.* (2018) “A New Lunar DEM Based on the Calibrated Chang’E-1 Laser Altimeter Data,” *Advances in Astronomy*. Edited by J. Yan, 2018, p. 5363797. Available at: https://doi.org/10.1155/2018/5363797.

Mitchell, J.K. Bromwell, L.G. Carrier III, W.D. Costes, N.C. (1971) “Soil mechanics experiment,” *Apollo 14—Preliminary Science Report*, pp. 87–108.

Johnson, J. (2008) “Spectrogoniometric measurements and models of Lunar analog soils,” *Lunar and Planetary*. Available at: https://doi.org/10.1029/2005JE002658.

Keihm, S.J. (1984) “Interpretation of the lunar microwave brightness temperature spectrum: Feasibility of orbital heat flow mapping,” *Icarus*. Available at: https://doi.org/10.1016/0019-1035(84)90165-9.

Kieffer, H.H. (2013) “Thermal model for analysis of Mars infrared mapping,” *Journal of Geophysical Research E: Planets*, 118(3), pp. 451–470. Available at: https://doi.org/10.1029/2012JE004164.

King, E.A. *et al.* (1977) “The lunar regolith: physical characteristics and dynamics,” *Philosophical Transactions of the Royal Society of London. Series A, Mathematical and Physical Sciences*, 285(1327), pp. 273–278. Available at: https://doi.org/10.1098/rsta.1977.0065.

Korotev, R.L. and Gillis, J.J. (2001) “A new look at the Apollo 11 regolith and KREEP,” *Journal of Geophysical Research: Planets*. Available at: https://doi.org/10.1029/2000je001336.

Labsphere (2017) “Spectralon® Diffuse Reflectance Standards,” *Datasheet*. Available at: https://doi.org/10.1007/978-3-642-27851-8_360-1.

Lauretta, D. and Team, O.-Re. (2012) “An Overview of the OSIRIS-REx Asteroid Sample Return Mission,” *Lunar and Planetary Institute Science…*.

Lawrence, D.J. *et al.* (2003) “Small-area thorium features on the lunar surface,” *Journal of Geophysical Research: Planets*, 108(E9). Available at: https://doi.org/https://doi.org/10.1029/2003JE002050.

Lucey, P.G. (2009) “The Poles of the Moon,” *Elements*, 5(1), pp. 41–46. Available at: https://doi.org/10.2113/gselements.5.1.41.

McEwen, A.S. (1996) “A Precise Lunar Photometric Function,” *U.S. Geological Survey*.

McKay C. P., Heiken G. H, V.D.T. and M., and F.B. (1991) “The Lunar Regolith, in The Lunar Sourcebook,” *Cambridge University Press*, pp. 285–356.

Metzger, P., Anderson, S. and Colaprete, A. (2018) “Experiments Indicate Regolith is Looser in the Lunar Polar Regions than at the Lunar Landing Sites,” *Earth and Space 2018: Engineering for Extreme Environments*, pp. 79–85.

Mitchell, D.L. and De Pater, I. (1994) “Microwave Imaging of Mercury’s Thermal Emission at Wavelengths from 0.3 to 20.5 cm,” *Icarus*, 110(1), pp. 2–32. Available at: https://doi.org/10.1006/icar.1994.1105.

Morris, R. V (1983) “Handbook of Lunar Soils: Part I: Apollo 11-15.”

Muehlberger, W. ~R. *et al.* (1980) “Mission objectives for geological exploration of the Apollo 16 landing site,” *Lunar Highlands Crust*, pp. 1–49.

Murray, N. (2020) “Abstract #1265 - 51st Lunar and Planetary Science Conference (2020).,” in *Lunar and Planet. Sci. Conf.*, pp. 2–3.

Nelson, R.M. *et al.* (2000) “The opposition effect in simulated planetary regoliths. Reflectance and circular polarization ratio change at small phase angle,” *Icarus*, 147(2), pp. 545–558. Available at: https://doi.org/10.1006/icar.2000.6454.

Nelson, R.M. *et al.* (2002) “Low phase angle laboratory studies of the opposition effect: Search for wavelength dependence,” *Planetary and Space Science*. Available at: https://doi.org/10.1016/S0032-0633(02)00059-4.

Nicodemus, F.E. (1976) “Comment on ‘Current definitions of reflectance,’” *Journal of the Optical Society of America*. Available at: https://doi.org/10.1364/josa.66.000283.

O. King, T. Warren, N. E. Bowles, E. Sefton-Nash, R. Fisackerly, R.T. (2019) “The Oxford 3D thermophysical model with application to PROSPECT_Luna 27 study landing sites,” *Planetary and Space Science*.

O’Brien, Á.C. *et al.* (2022) “The Winchcombe Meteorite: one year on,” *Astronomy & Geophysics*, 63(1), pp. 1.21-1.23. Available at: https://doi.org/10.1093/astrogeo/atac009.

Paige, D.A. *et al.* (2010) “Diviner lunar radiometer observations of cold traps in the moon’s south polar region,” *Science*. Available at: https://doi.org/10.1126/science.1187726.

Paige, D.A. *et al.* (2010a) “The lunar reconnaissance orbiter diviner lunar radiometer experiment,” *Space Science Reviews*. Available at: https://doi.org/10.1007/s11214-009-9529-2.

Petro, N.E. and Pieters, C.M. (2006) “Modeling the provenance of the Apollo 16 regolith,” *Journal of Geophysical Research*, 111.

Potin, S. *et al.* (2018) “SHADOWS: a spectro-gonio radiometer for bidirectional reflectance studies of dark meteorites and terrestrial analogs: design, calibrations, and performances on challenging surfaces,” *Applied Optics*. Available at: https://doi.org/10.1364/ao.57.008279.

Robinson, M.S. *et al.* (2010) “Lunar reconnaissance orbiter camera (LROC) instrument overview,” *Space Science Reviews*, 150(1–4), pp. 81–124. Available at: https://doi.org/10.1007/s11214-010-9634-2.

Rode, O. (1979) “Atlas of photomicrographs of the surface structures of lunar regolith particles.”

Rozitis, B. and Green, S.F. (2011) “Directional characteristics of thermal-infrared beaming from atmosphereless planetary surfaces - a new thermophysical model,” *Monthly Notices of the Royal Astronomical Society*. Available at: https://doi.org/10.1111/j.1365-2966.2011.18718.x.

Rubanenko, L. *et al.* (2020) “Equilibrium Temperatures and Directional Emissivity of Sunlit Airless Surfaces With Applications to the Moon,” *Journal of Geophysical Research: Planets*, 125(6). Available at: https://doi.org/https://doi.org/10.1029/2020JE006377.

Rubanenko, L., Venkatraman, J. and Paige, D.A. (2019) “Thick ice deposits in shallow simple craters on the Moon and Mercury,” *Nature Geoscience*. Available at: https://doi.org/10.1038/s41561-019-0405-8.

Salisbury, J.W. and Wald, A. (1992) “The role of volume scattering in reducing spectral contrast of reststrahlen bands in spectra of powdered minerals,” *Icarus*, 96(1), pp. 121–128. Available at: https://doi.org/10.1016/0019-1035(92)90009-V.

Sato, H. *et al.* (2014) “Resolved Hapke parameter maps of the Moon,” *Journal of Geophysical Research E: Planets*. Available at: https://doi.org/10.1002/2013JE004580.

Scherer, L.R. (1971) “The Apollo Missions,” *Highlights of Astronomy*. Available at: https://doi.org/10.1017/s1539299600000083.

Shepard, M.K. and Helfenstein, P. (2007) “A test of the Hapke photometric model,” *Journal of Geophysical Research E: Planets*. Available at: https://doi.org/10.1029/2005JE002625.

Shepard, M.K. and Helfenstein, P. (2011) “A laboratory study of the bidirectional reflectance from particulate samples,” *Icarus*. Available at: https://doi.org/10.1016/j.icarus.2011.07.033.

Shoemaker, E.M. *et al.* (1970) “Origin of the lunar regolith at Tranquillity Base.”

Spudis, P.D. *et al.* (2013) “Evidence for water ice on the Moon: Results for anomalous polar craters from the LRO Mini-RF imaging radar,” *Journal of Geophysical Research: Planets*, 118(10), pp. 2016–2029. Available at: https://doi.org/https://doi.org/10.1002/jgre.20156.

Steklov, A. ~F., Vidmachenko, A. ~P. and Minyaylo, D. ~N. (2019) “Ways of human survival on the Moon,” in *New Trends in Astrophysics, Cosmology and HEP after Gamow*, p. 57.

Thomas, G.E. (1974) “Mercury: Does its atmosphere contain water?,” *Science*, 183(4130), pp. 1197–1198. Available at: https://doi.org/10.1126/science.183.4130.1197.

ThorLabs (2013) “CPS532 Specification Sheet,” pp. 5–6.

Tooley, C.R. *et al.* (2010) “Lunar Reconnaissance Orbiter Mission and Spacecraft Design,” *Space Science Reviews*, 150(1), pp. 23–62. Available at: https://doi.org/10.1007/s11214-009-9624-4.

Trautner, R. *et al.* (2018) “Prospect: A novel package for subsurface sample acquisition and analysis of lunar volatiles,” in *Proceedings of the International Astronautical Congress, IAC*.

Vasavada, A.R. *et al.* (2012) “Lunar equatorial surface temperatures and regolith properties from the Diviner Lunar Radiometer Experiment,” *Journal of Geophysical Research E: Planets*, 117(4). Available at: https://doi.org/10.1029/2011JE003987.

Vasavada, A.R., Paige, D.A. and Wood, S.E. (1999) “Near-surface temperatures on Mercury and the Moon and the stability of polar ice deposits,” *Icarus*. Available at: https://doi.org/10.1006/icar.1999.6175.

Ward, W.R. (1975) “Past Orientation of the Lunar Spin Axis,” *Science*, (August), pp. 377–380.

Warren, T. (2015) “Exploring the Moon in the Thermal Infrared : The Space Environment Goniometer.”

Warren, T.J. *et al.* (2017) “The Oxford space environment goniometer: A new experimental setup for making directional emissivity measurements under a simulated space environment,” *Review of Scientific Instruments*. Available at: https://doi.org/10.1063/1.4986657.

Warren, T.J. *et al.* (2019) “Modeling the Angular Dependence of Emissivity of Randomly Rough Surfaces,” *Journal of Geophysical Research: Planets*, 124(2), pp. 585–601. Available at: https://doi.org/10.1029/2018JE005840.

Warren, T.J. *et al.* (2021) “Abstract #2548 - Investigating the Thermal Infrared Emission Phase Function of the Lunar Surface Using the the Diviner Lunar Radiometer,” in *Lunar and Planet. Sci. Conf.*, p. 1890. Available at: https://doi.org/10.2493/jjspe.87.947.

Watson, K., Murray, B. and Brown, H. (1961) “On the possible presence of ice on the Moon,” *Journal of Geophysical Research (1896-1977)*, 66(5), pp. 1598–1600. Available at: https://doi.org/https://doi.org/10.1029/JZ066i005p01598.

Watson, K., Murray, B.C. and Brown, H. (1961) “The behavior of volatiles on the lunar surface,” *Journal of Geophysical Research (1896-1977)*, 66(9), pp. 3033–3045.

Whipple, A.L. (1993) “Dynamics of the Earth-Moon system,” *Advances in Space Research*. Available at: https://doi.org/10.1016/0273-1177(93)90224-Y.

Wilhelms, D.E., with sections by McCauley, J.F. and Trask, N.J. (1987) *The geologic history of the Moon, Professional Paper*. Available at: https://doi.org/10.3133/pp1348.

Williams, J.P. *et al.* (2017a) “The global surface temperatures of the moon as measured by the diviner lunar radiometer experiment,” *Icarus*. Available at: https://doi.org/10.1016/j.icarus.2016.08.012.

Williams, J.P. *et al.* (2017b) “The global surface temperatures of the moon as measured by the diviner lunar radiometer experiment,” *Icarus*. Available at: https://doi.org/10.1016/j.icarus.2016.08.012.

Williams, J.P. *et al.* (2019) “Seasonal Polar Temperatures on the Moon,” *Journal of Geophysical Research: Planets*. Available at: https://doi.org/10.1029/2019JE006028.

Woods-Robinson, R., Siegler, M.A. and Paige, D.A. (2019) “A Model for the Thermophysical Properties of Lunar Regolith at Low Temperatures,” *Journal of Geophysical Research: Planets*. Available at: https://doi.org/10.1029/2019JE005955.

Zelenyi, L.M., Zakharov, A. V. and Zakutnyaya, O. V. (2011) “Will the lunar renaissance come forth?,” *Solar System Research*. Available at: https://doi.org/10.1134/S003809461107029X.

Appendix

Table A.1 shows the BRDF data measured by VOSEG for the smooth and rough Apollo 11, 10084 samples, and the associated best fit Hapke BRDF model predictions for each viewing angle. This data was plotted in **Figures 58**, **59**, **60**, **61**, **62** and **63**.

Viewing angles (°)				*Smooth Apollo 11*				*Rough Apollo 11*		
θ_i	θ_r	θ_a	θ_r *(full plane)*	*BRDF (SR^{-1})*	*BRDF error (±)*	*Hapke BRDF (SR^{-1})*		*BRDF (SR^{-1})*	*BRDF error (±)*	*Hapke BRDF (SR^{-1})*
15	70	180	-70	0.0259	0.0019	0.0235		0.0220	0.0026	0.0256
15	65	180	-65	0.0246	0.0009	0.0218		0.0211	0.0021	0.0236
15	60	180	-60	0.0235	0.0008	0.0203		0.0204	0.0014	0.0219
15	55	180	-55	0.0223	0.0012	0.0191		0.0198	0.0009	0.0205
15	50	180	-50	0.0213	0.0012	0.0182		0.0193	0.0011	0.0194
15	45	180	-45	0.0207	0.0013	0.0174		0.0186	0.0032	0.0184
15	40	180	-40	0.0201	0.0009	0.0168		0.0183	0.0014	0.0176
15	35	180	-35	0.0196	0.0005	0.0164		0.0182	0.0007	0.0169
15	30	180	-30	0.0196	0.0011	0.0162		0.0181	0.0017	0.0164
15	25	180	-25	0.0195	0.0005	0.0162		0.0181	0.0004	0.0160
15	20	180	-20	0.0197	0.0009	0.0164		0.0183	0.0004	0.0158
15	15	180	-15	0.0197	0.0006	0.0168		0.0187	0.0004	0.0157
15	10	180	-10	0.0201	0.0011	0.0175		0.0193	0.0013	0.0159
15	5	180	-5	0.0207	0.0014	0.0184		0.0200	0.0010	0.0163
15	0	0	0	0.0221	0.0007	0.0206		0.0210	0.0006	0.0190
15	0	180	0	0.0221	0.0007	0.0206		0.0210	0.0006	0.0181
15	5	0	5	0.0230	0.0005	0.0235		0.0228	0.0009	0.0230
15	10	0	10	0.0256	0.0002	0.0263		0.0252	0.0017	0.0283
15	20	0	20	0.0278	0.0007	0.0269		0.0267	0.0017	0.0289
15	25	0	25	0.0250	0.0009	0.0246		0.0234	0.0019	0.0240
15	30	0	30	0.0234	0.0013	0.0231		0.0221	0.0028	0.0222
15	35	0	35	0.0228	0.0023	0.0221		0.0212	0.0005	0.0215
15	40	0	40	0.0220	0.0015	0.0214		0.0207	0.0009	0.0213
15	45	0	45	0.0216	0.0020	0.0211		0.0201	0.0009	0.0215
15	50	0	50	0.0213	0.0003	0.0212		0.0199	0.0009	0.0220
15	55	0	55	0.0211	0.0006	0.0214		0.0198	0.0008	0.0228

15	60	0	60	0.0211	0.0006	0.0220		0.0198	0.0015	0.0238
15	65	0	65	0.0214	0.0004	0.0229		0.0197	0.0012	0.0251
15	70	0	70	0.0229	0.0014	0.0241		0.0199	0.0010	0.0266
15	70	135	-70	0.0258	0.0011	0.0231		0.0226	0.0015	0.0251
15	65	135	-65	0.0244	0.0012	0.0215		0.0223	0.0021	0.0231
15	60	135	-60	0.0229	0.0007	0.0201		0.0215	0.0007	0.0215
15	55	135	-55	0.0220	0.0006	0.0190		0.0209	0.0013	0.0202
15	50	135	-50	0.0209	0.0000	0.0181		0.0204	0.0012	0.0191
15	45	135	-45	0.0200	0.0005	0.0174		0.0197	0.0017	0.0182
15	40	135	-40	0.0196	0.0010	0.0169		0.0192	0.0020	0.0174
15	35	135	-35	0.0196	0.0014	0.0166		0.0189	0.0014	0.0168
15	30	135	-30	0.0195	0.0030	0.0165		0.0188	0.0013	0.0164
15	25	135	-25	0.0197	0.0026	0.0165		0.0189	0.0012	0.0160
15	20	135	-20	0.0199	0.0004	0.0168		0.0194	0.0004	0.0159
15	15	135	-15	0.0202	0.0016	0.0172		0.0195	0.0008	0.0159
15	10	135	-10	0.0208	0.0016	0.0179		0.0199	0.0004	0.0160
15	5	135	-5	0.0214	0.0012	0.0187		0.0203	0.0004	0.0165
15	0	45	0	0.0221	0.0008	0.0201		0.0210	0.0002	0.0179
15	0	135	0	0.0221	0.0009	0.0201		0.0210	0.0008	0.0175
15	5	45	5	0.0221	0.0005	0.0216		0.0210	0.0012	0.0196
15	10	45	10	0.0221	0.0002	0.0223		0.0210	0.0017	0.0203
15	15	45	15	0.0220	0.0005	0.0222		0.0210	0.0010	0.0201
15	20	45	20	0.0219	0.0003	0.0215		0.0209	0.0012	0.0194
15	25	45	25	0.0218	0.0020	0.0207		0.0208	0.0003	0.0188
15	30	45	30	0.0216	0.0003	0.0200		0.0207	0.0005	0.0185
15	35	45	35	0.0214	0.0003	0.0195		0.0205	0.0008	0.0184
15	40	45	40	0.0213	0.0015	0.0193		0.0203	0.0006	0.0187
15	45	45	45	0.0212	0.0010	0.0193		0.0201	0.0006	0.0191
15	50	45	50	0.0211	0.0016	0.0195		0.0200	0.0007	0.0198
15	55	45	55	0.0210	0.0005	0.0200		0.0198	0.0008	0.0207
15	60	45	60	0.0209	0.0025	0.0207		0.0197	0.0007	0.0219
15	65	45	65	0.0206	0.0018	0.0217		0.0194	0.0008	0.0233
15	70	45	70	0.0202	0.0018	0.0231		0.0188	0.0016	0.0250
15	70	90	-70	0.0258	0.0020	0.0228		0.0238	0.0013	0.0247
15	65	90	-65	0.0249	0.0024	0.0212		0.0235	0.0008	0.0228
15	60	90	-60	0.0242	0.0018	0.0200		0.0233	0.0012	0.0213

15	55	90	-55	0.0235	0.0013	0.0191		0.0225	0.0014	0.0201
15	50	90	-50	0.0228	0.0015	0.0184		0.0221	0.0005	0.0190
15	45	90	-45	0.0221	0.0012	0.0178		0.0212	0.0009	0.0182
15	40	90	-40	0.0217	0.0011	0.0175		0.0208	0.0007	0.0175
15	35	90	-35	0.0210	0.0017	0.0174		0.0204	0.0004	0.0171
15	30	90	-30	0.0203	0.0016	0.0175		0.0200	0.0004	0.0168
15	25	90	-25	0.0203	0.0012	0.0177		0.0200	0.0004	0.0166
15	20	90	-20	0.0203	0.0011	0.0181		0.0200	0.0006	0.0166
15	15	90	-15	0.0204	0.0010	0.0187		0.0199	0.0007	0.0168
15	10	90	-10	0.0205	0.0009	0.0193		0.0199	0.0003	0.0171
15	5	90	-5	0.0210	0.0010	0.0198		0.0205	0.0005	0.0174
15	0	90	0	0.0221	0.0011	0.0200		0.0210	0.0005	0.0176
15	0	90	0	0.0221	0.0011	0.0200		0.0210	0.0005	0.0176
15	5	90	5	0.0210	0.0010	0.0198		0.0205	0.0005	0.0174
15	10	90	10	0.0205	0.0009	0.0193		0.0199	0.0003	0.0171
15	15	90	15	0.0204	0.0010	0.0187		0.0199	0.0007	0.0168
15	20	90	20	0.0203	0.0011	0.0181		0.0200	0.0006	0.0166
15	25	90	25	0.0203	0.0012	0.0177		0.0200	0.0004	0.0166
15	30	90	30	0.0203	0.0016	0.0175		0.0200	0.0004	0.0168
15	35	90	35	0.0210	0.0017	0.0174		0.0204	0.0004	0.0171
15	40	90	40	0.0217	0.0011	0.0175		0.0208	0.0007	0.0175
15	45	90	45	0.0221	0.0012	0.0178		0.0212	0.0009	0.0182
15	50	90	50	0.0228	0.0015	0.0184		0.0221	0.0005	0.0190
15	55	90	55	0.0235	0.0013	0.0191		0.0225	0.0014	0.0201
15	60	90	60	0.0242	0.0018	0.0200		0.0233	0.0012	0.0213
15	65	90	65	0.0249	0.0024	0.0212		0.0235	0.0008	0.0228
15	70	90	70	0.0258	0.0020	0.0228		0.0238	0.0013	0.0247
30	70	180	-70	0.0292	0.0012	0.0299		0.0233	0.0012	0.0283
30	65	180	-65	0.0259	0.0015	0.0264		0.0223	0.0008	0.0263
30	60	180	-60	0.0242	0.0025	0.0238		0.0214	0.0003	0.0245
30	55	180	-55	0.0232	0.0015	0.0219		0.0201	0.0010	0.0231
30	50	180	-50	0.0222	0.0023	0.0203		0.0189	0.0015	0.0218
30	45	180	-45	0.0211	0.0029	0.0191		0.0179	0.0011	0.0208
30	40	180	-40	0.0206	0.0013	0.0181		0.0176	0.0009	0.0197
30	35	180	-35	0.0198	0.0009	0.0174		0.0174	0.0012	0.0188
30	30	180	-30	0.0193	0.0011	0.0168		0.0172	0.0015	0.0180

30	25	180	-25	0.0185	0.0023	0.0164		0.0169	0.0005	0.0173
30	20	180	-20	0.0184	0.0007	0.0163		0.0168	0.0005	0.0168
30	15	180	-15	0.0183	0.0014	0.0162		0.0170	0.0010	0.0164
30	10	180	-10	0.0182	0.0015	0.0164		0.0172	0.0024	0.0162
30	5	180	-5	0.0184	0.0016	0.0168		0.0175	0.0005	0.0161
30	0	0	0	0.0199	0.0012	0.0187		0.0190	0.0015	0.0179
30	0	180	0	0.0199	0.0006	0.0187		0.0190	0.0017	0.0171
30	5	0	5	0.0203	0.0005	0.0200		0.0196	0.0015	0.0200
30	10	0	10	0.0210	0.0007	0.0213		0.0205	0.0016	0.0208
30	15	0	15	0.0224	0.0008	0.0231		0.0218	0.0008	0.0222
30	20	0	20	0.0243	0.0006	0.0255		0.0239	0.0009	0.0247
30	25	0	25	0.0283	0.0006	0.0289		0.0274	0.0012	0.0308
30	35	0	35	0.0306	0.0003	0.0304		0.0296	0.0009	0.0322
30	40	0	40	0.0279	0.0004	0.0282		0.0271	0.0012	0.0270
30	45	0	45	0.0259	0.0007	0.0268		0.0257	0.0017	0.0252
30	50	0	50	0.0249	0.0010	0.0260		0.0242	0.0018	0.0247
30	55	0	55	0.0242	0.0005	0.0257		0.0237	0.0004	0.0248
30	60	0	60	0.0242	0.0008	0.0258		0.0233	0.0014	0.0254
30	65	0	65	0.0243	0.0014	0.0263		0.0231	0.0021	0.0264
30	70	0	70	0.0249	0.0013	0.0271		0.0232	0.0036	0.0276
30	70	135	-70	0.0293	0.0021	0.0279		0.0242	0.0010	0.0251
30	65	135	-65	0.0263	0.0025	0.0250		0.0232	0.0015	0.0248
30	60	135	-60	0.0241	0.0012	0.0228		0.0222	0.0006	0.0240
30	55	135	-55	0.0226	0.0011	0.0211		0.0210	0.0019	0.0229
30	50	135	-50	0.0213	0.0006	0.0198		0.0199	0.0006	0.0217
30	45	135	-45	0.0202	0.0005	0.0187		0.0192	0.0016	0.0203
30	40	135	-40	0.0194	0.0005	0.0179		0.0185	0.0019	0.0193
30	35	135	-35	0.0190	0.0013	0.0173		0.0180	0.0009	0.0183
30	30	135	-30	0.0182	0.0013	0.0168		0.0174	0.0004	0.0177
30	25	135	-25	0.0180	0.0021	0.0166		0.0172	0.0004	0.0171
30	20	135	-20	0.0176	0.0008	0.0164		0.0171	0.0012	0.0166
30	15	135	-15	0.0179	0.0012	0.0165		0.0173	0.0024	0.0163
30	10	135	-10	0.0184	0.0020	0.0166		0.0176	0.0009	0.0162
30	5	135	-5	0.0187	0.0017	0.0170		0.0180	0.0016	0.0161
30	0	45	0	0.0199	0.0004	0.0177		0.0190	0.0001	0.0167
30	0	135	0	0.0199	0.0004	0.0177		0.0190	0.0007	0.0166

30	5	45	5	0.0200	0.0001	0.0187		0.0190	0.0001	0.0178
30	10	45	10	0.0200	0.0001	0.0193		0.0192	0.0002	0.0181
30	15	45	15	0.0200	0.0005	0.0200		0.0193	0.0004	0.0185
30	20	45	20	0.0203	0.0003	0.0205		0.0193	0.0003	0.0188
30	25	45	25	0.0204	0.0007	0.0209		0.0194	0.0005	0.0191
30	30	45	30	0.0205	0.0005	0.0211		0.0195	0.0002	0.0193
30	35	45	35	0.0206	0.0001	0.0211		0.0195	0.0004	0.0196
30	40	45	40	0.0206	0.0005	0.0212		0.0196	0.0005	0.0201
30	45	45	45	0.0207	0.0003	0.0213		0.0197	0.0007	0.0202
30	50	45	50	0.0210	0.0003	0.0216		0.0196	0.0003	0.0204
30	55	45	55	0.0214	0.0002	0.0221		0.0195	0.0005	0.0204
30	60	45	60	0.0217	0.0023	0.0229		0.0194	0.0002	0.0200
30	65	45	65	0.0220	0.0024	0.0241		0.0192	0.0002	0.0197
30	70	45	70	0.0222	0.0025	0.0259		0.0190	0.0003	0.0192
30	70	90	-70	0.0262	0.0018	0.0258		0.0218	0.0009	0.0230
30	65	90	-65	0.0252	0.0009	0.0235		0.0218	0.0010	0.0227
30	60	90	-60	0.0242	0.0025	0.0217		0.0219	0.0002	0.0223
30	55	90	-55	0.0237	0.0014	0.0204		0.0220	0.0002	0.0219
30	50	90	-50	0.0231	0.0008	0.0195		0.0219	0.0007	0.0213
30	45	90	-45	0.0224	0.0012	0.0187		0.0217	0.0006	0.0205
30	40	90	-40	0.0220	0.0012	0.0182		0.0210	0.0006	0.0195
30	35	90	-35	0.0216	0.0005	0.0178		0.0204	0.0010	0.0183
30	30	90	-30	0.0212	0.0012	0.0176		0.0199	0.0011	0.0176
30	25	90	-25	0.0207	0.0007	0.0175		0.0197	0.0005	0.0172
30	20	90	-20	0.0204	0.0012	0.0175		0.0193	0.0003	0.0169
30	15	90	-15	0.0202	0.0012	0.0175		0.0192	0.0001	0.0168
30	10	90	-10	0.0202	0.0012	0.0175		0.0193	0.0002	0.0167
30	5	90	-5	0.0199	0.0015	0.0176		0.0192	0.0010	0.0166
30	0	90	0	0.0199	0.0009	0.0176		0.0190	0.0007	0.0166
30	0	90	0	0.0199	0.0009	0.0176		0.0190	0.0007	0.0166
30	5	90	5	0.0199	0.0015	0.0176		0.0192	0.0010	0.0166
30	10	90	10	0.0202	0.0012	0.0175		0.0193	0.0002	0.0167
30	15	90	15	0.0202	0.0012	0.0175		0.0192	0.0001	0.0168
30	20	90	20	0.0204	0.0012	0.0175		0.0193	0.0003	0.0169
30	25	90	25	0.0207	0.0007	0.0175		0.0197	0.0005	0.0172
30	30	90	30	0.0212	0.0012	0.0176		0.0199	0.0011	0.0176

30	35	90	35	0.0216	0.0005	0.0178		0.0204	0.0010	0.0183
30	40	90	40	0.0220	0.0012	0.0182		0.0210	0.0006	0.0195
30	45	90	45	0.0224	0.0012	0.0187		0.0217	0.0006	0.0205
30	50	90	50	0.0231	0.0008	0.0195		0.0219	0.0007	0.0213
30	55	90	55	0.0237	0.0014	0.0204		0.0220	0.0002	0.0219
30	60	90	60	0.0242	0.0025	0.0217		0.0219	0.0002	0.0223
30	65	90	65	0.0252	0.0009	0.0235		0.0218	0.0010	0.0227
30	70	90	70	0.0262	0.0018	0.0258		0.0218	0.0009	0.0230
45	70	180	-70	0.0364	0.0019	0.0315		0.0294	0.0028	0.0283
45	65	180	-65	0.0316	0.0016	0.0304		0.0265	0.0020	0.0280
45	60	180	-60	0.0282	0.0014	0.0287		0.0246	0.0017	0.0274
45	55	180	-55	0.0262	0.0011	0.0269		0.0232	0.0034	0.0269
45	50	180	-50	0.0245	0.0016	0.0248		0.0216	0.0026	0.0259
45	45	180	-45	0.0228	0.0027	0.0230		0.0200	0.0031	0.0246
45	40	180	-40	0.0210	0.0014	0.0214		0.0189	0.0007	0.0232
45	35	180	-35	0.0199	0.0009	0.0201		0.0182	0.0011	0.0218
45	30	180	-30	0.0187	0.0007	0.0191		0.0177	0.0019	0.0205
45	25	180	-25	0.0182	0.0021	0.0183		0.0173	0.0015	0.0195
45	20	180	-20	0.0176	0.0020	0.0177		0.0172	0.0006	0.0186
45	15	180	-15	0.0171	0.0013	0.0174		0.0172	0.0026	0.0179
45	10	180	-10	0.0170	0.0025	0.0172		0.0170	0.0003	0.0174
45	5	180	-5	0.0172	0.0019	0.0172		0.0173	0.0006	0.0170
45	0	0	0	0.0182	0.0025	0.0184		0.0178	0.0012	0.0190
45	0	180	0	0.0182	0.0009	0.0184		0.0178	0.0008	0.0179
45	5	0	5	0.0183	0.0028	0.0194		0.0182	0.0009	0.0210
45	10	0	10	0.0192	0.0014	0.0201		0.0188	0.0006	0.0211
45	15	0	15	0.0201	0.0013	0.0211		0.0196	0.0006	0.0215
45	20	0	20	0.0213	0.0010	0.0225		0.0210	0.0007	0.0222
45	25	0	25	0.0227	0.0010	0.0244		0.0225	0.0007	0.0233
45	30	0	30	0.0251	0.0016	0.0268		0.0249	0.0002	0.0252
45	35	0	35	0.0282	0.0006	0.0301		0.0276	0.0002	0.0286
45	40	0	40	0.0335	0.0012	0.0347		0.0327	0.0005	0.0363
45	50	0	50	0.0373	0.0021	0.0378		0.0365	0.0015	0.0393
45	55	0	55	0.0347	0.0023	0.0358		0.0341	0.0014	0.0333
45	60	0	60	0.0328	0.0009	0.0348		0.0320	0.0014	0.0316
45	65	0	65	0.0325	0.0025	0.0346		0.0312	0.0005	0.0314

45	70	0	70	0.0332	0.0012	0.0350		0.0311	0.0005	0.0322
45	70	135	-70	0.0321	0.0021	0.0286		0.0264	0.0016	0.0257
45	65	135	-65	0.0287	0.0009	0.0274		0.0240	0.0012	0.0258
45	60	135	-60	0.0259	0.0024	0.0262		0.0226	0.0016	0.0254
45	55	135	-55	0.0238	0.0026	0.0248		0.0213	0.0012	0.0248
45	50	135	-50	0.0221	0.0006	0.0233		0.0204	0.0009	0.0238
45	45	135	-45	0.0211	0.0014	0.0218		0.0196	0.0011	0.0230
45	40	135	-40	0.0200	0.0020	0.0206		0.0189	0.0011	0.0219
45	35	135	-35	0.0187	0.0023	0.0195		0.0180	0.0005	0.0208
45	30	135	-30	0.0180	0.0004	0.0187		0.0175	0.0009	0.0198
45	25	135	-25	0.0177	0.0030	0.0181		0.0174	0.0009	0.0189
45	20	135	-20	0.0173	0.0004	0.0177		0.0169	0.0008	0.0182
45	15	135	-15	0.0173	0.0008	0.0174		0.0169	0.0004	0.0177
45	10	135	-10	0.0173	0.0013	0.0172		0.0171	0.0016	0.0173
45	5	135	-5	0.0175	0.0008	0.0172		0.0173	0.0013	0.0170
45	0	45	0	0.0182	0.0016	0.0177		0.0178	0.0003	0.0176
45	0	135	0	0.0182	0.0012	0.0177		0.0178	0.0014	0.0172
45	5	45	5	0.0184	0.0002	0.0183		0.0180	0.0011	0.0184
45	10	45	10	0.0185	0.0022	0.0188		0.0183	0.0012	0.0185
45	15	45	15	0.0187	0.0014	0.0193		0.0183	0.0009	0.0187
45	20	45	20	0.0189	0.0004	0.0199		0.0186	0.0012	0.0190
45	25	45	25	0.0194	0.0003	0.0206		0.0190	0.0002	0.0194
45	30	45	30	0.0195	0.0005	0.0213		0.0193	0.0005	0.0199
45	35	45	35	0.0200	0.0002	0.0220		0.0197	0.0014	0.0203
45	40	45	40	0.0203	0.0002	0.0227		0.0200	0.0004	0.0205
45	45	45	45	0.0210	0.0002	0.0235		0.0204	0.0010	0.0207
45	50	45	50	0.0215	0.0014	0.0242		0.0208	0.0005	0.0208
45	55	45	55	0.0219	0.0005	0.0247		0.0213	0.0008	0.0210
45	60	45	60	0.0226	0.0030	0.0252		0.0213	0.0010	0.0208
45	65	45	65	0.0236	0.0019	0.0256		0.0213	0.0013	0.0206
45	70	45	70	0.0242	0.0020	0.0259		0.0209	0.0015	0.0203
45	70	90	-70	0.0240	0.0028	0.0263		0.0211	0.0017	0.0209
45	65	90	-65	0.0236	0.0019	0.0249		0.0210	0.0011	0.0212
45	60	90	-60	0.0228	0.0019	0.0235		0.0210	0.0011	0.0213
45	55	90	-55	0.0219	0.0025	0.0224		0.0209	0.0006	0.0212
45	50	90	-50	0.0212	0.0008	0.0214		0.0202	0.0008	0.0210

45	45	90	-45	0.0207	0.0008	0.0206		0.0199	0.0009	0.0205
45	40	90	-40	0.0199	0.0011	0.0199		0.0194	0.0009	0.0201
45	35	90	-35	0.0195	0.0010	0.0192		0.0191	0.0009	0.0195
45	30	90	-30	0.0191	0.0012	0.0187		0.0189	0.0004	0.0189
45	25	90	-25	0.0189	0.0009	0.0183		0.0188	0.0010	0.0184
45	20	90	-20	0.0188	0.0003	0.0180		0.0185	0.0004	0.0180
45	15	90	-15	0.0185	0.0003	0.0178		0.0183	0.0008	0.0177
45	10	90	-10	0.0184	0.0005	0.0176		0.0181	0.0011	0.0174
45	5	90	-5	0.0182	0.0015	0.0176		0.0180	0.0011	0.0173
45	0	90	0	0.0182	0.0020	0.0175		0.0178	0.0011	0.0173
45	0	90	0	0.0182	0.0020	0.0175		0.0178	0.0011	0.0173
45	5	90	5	0.0182	0.0015	0.0176		0.0180	0.0011	0.0173
45	10	90	10	0.0184	0.0005	0.0176		0.0181	0.0011	0.0174
45	15	90	15	0.0185	0.0003	0.0178		0.0183	0.0008	0.0177
45	20	90	20	0.0188	0.0003	0.0180		0.0185	0.0004	0.0180
45	25	90	25	0.0189	0.0009	0.0183		0.0188	0.0010	0.0184
45	30	90	30	0.0191	0.0012	0.0187		0.0189	0.0004	0.0189
45	35	90	35	0.0195	0.0010	0.0192		0.0191	0.0009	0.0195
45	40	90	40	0.0199	0.0011	0.0199		0.0194	0.0009	0.0201
45	45	90	45	0.0207	0.0008	0.0206		0.0199	0.0009	0.0205
45	50	90	50	0.0212	0.0008	0.0214		0.0202	0.0008	0.0210
45	55	90	55	0.0219	0.0025	0.0224		0.0209	0.0006	0.0212
45	60	90	60	0.0228	0.0019	0.0235		0.0210	0.0011	0.0213
45	65	90	65	0.0236	0.0019	0.0249		0.0210	0.0011	0.0212
45	70	90	70	0.0240	0.0028	0.0263		0.0211	0.0017	0.0209
60	70	180	-70	0.0476	0.0000	0.0432		0.0410	0.0004	0.0329
60	65	180	-65	0.0411	0.0010	0.0416		0.0355	0.0003	0.0334
60	60	180	-60	0.0348	0.0019	0.0386		0.0306	0.0011	0.0327
60	55	180	-55	0.0309	0.0017	0.0352		0.0277	0.0000	0.0313
60	50	180	-50	0.0271	0.0013	0.0318		0.0257	0.0000	0.0295
60	45	180	-45	0.0245	0.0004	0.0289		0.0233	0.0030	0.0275
60	40	180	-40	0.0219	0.0011	0.0264		0.0217	0.0002	0.0254
60	35	180	-35	0.0205	0.0003	0.0243		0.0202	0.0002	0.0235
60	30	180	-30	0.0192	0.0005	0.0227		0.0190	0.0008	0.0218
60	25	180	-25	0.0185	0.0002	0.0214		0.0182	0.0003	0.0203
60	20	180	-20	0.0181	0.0009	0.0203		0.0179	0.0008	0.0191

60	15	180	-15	0.0180	0.0006	0.0195		0.0178	0.0002	0.0182
60	10	180	-10	0.0180	0.0012	0.0189		0.0178	0.0001	0.0174
60	5	180	-5	0.0178	0.0003	0.0186		0.0177	0.0001	0.0168
60	0	0	0	0.0179	0.0013	0.0198		0.0178	0.0007	0.0204
60	0	180	0	0.0179	0.0001	0.0198		0.0178	0.0001	0.0184
60	5	0	5	0.0186	0.0003	0.0211		0.0183	0.0010	0.0240
60	10	0	10	0.0194	0.0002	0.0214		0.0191	0.0017	0.0238
60	15	0	15	0.0201	0.0003	0.0220		0.0196	0.0020	0.0238
60	20	0	20	0.0213	0.0007	0.0229		0.0208	0.0020	0.0241
60	25	0	25	0.0220	0.0004	0.0241		0.0218	0.0004	0.0246
60	30	0	30	0.0232	0.0011	0.0258		0.0231	0.0011	0.0254
60	35	0	35	0.0250	0.0008	0.0280		0.0243	0.0012	0.0267
60	40	0	40	0.0272	0.0009	0.0309		0.0270	0.0004	0.0286
60	45	0	45	0.0309	0.0004	0.0348		0.0300	0.0004	0.0316
60	50	0	50	0.0359	0.0020	0.0401		0.0364	0.0015	0.0368
60	55	0	55	0.0449	0.0020	0.0474		0.0440	0.0022	0.0482
60	65	0	65	0.0562	0.0006	0.0550		0.0547	0.0013	0.0551
60	70	0	70	0.0514	0.0008	0.0541		0.0477	0.0015	0.0478
60	70	135	-70	0.0404	0.0004	0.0362		0.0343	0.0004	0.0268
60	65	135	-65	0.0350	0.0016	0.0356		0.0308	0.0006	0.0278
60	60	135	-60	0.0310	0.0011	0.0337		0.0281	0.0003	0.0279
60	55	135	-55	0.0277	0.0019	0.0312		0.0257	0.0005	0.0272
60	50	135	-50	0.0253	0.0006	0.0287		0.0239	0.0002	0.0261
60	45	135	-45	0.0232	0.0002	0.0265		0.0223	0.0002	0.0248
60	40	135	-40	0.0218	0.0004	0.0246		0.0207	0.0002	0.0233
60	35	135	-35	0.0204	0.0002	0.0230		0.0199	0.0001	0.0218
60	30	135	-30	0.0195	0.0005	0.0217		0.0188	0.0002	0.0205
60	25	135	-25	0.0188	0.0008	0.0207		0.0182	0.0011	0.0194
60	20	135	-20	0.0183	0.0011	0.0199		0.0178	0.0005	0.0185
60	15	135	-15	0.0182	0.0013	0.0192		0.0176	0.0002	0.0177
60	10	135	-10	0.0182	0.0002	0.0188		0.0174	0.0003	0.0171
60	5	135	-5	0.0180	0.0002	0.0185		0.0174	0.0005	0.0167
60	0	45	0	0.0179	0.0002	0.0190		0.0178	0.0011	0.0178
60	0	135	0	0.0179	0.0006	0.0190		0.0178	0.0002	0.0171
60	5	45	5	0.0180	0.0017	0.0195		0.0179	0.0003	0.0190
60	10	45	10	0.0182	0.0008	0.0197		0.0182	0.0009	0.0189

60	15	45	15	0.0184	0.0017	0.0201		0.0184	0.0007	0.0189
60	20	45	20	0.0188	0.0013	0.0206		0.0189	0.0005	0.0191
60	25	45	25	0.0196	0.0026	0.0213		0.0194	0.0010	0.0194
60	30	45	30	0.0203	0.0029	0.0221		0.0203	0.0012	0.0199
60	35	45	35	0.0210	0.0022	0.0231		0.0211	0.0009	0.0204
60	40	45	40	0.0221	0.0024	0.0242		0.0217	0.0010	0.0208
60	45	45	45	0.0237	0.0013	0.0255		0.0231	0.0015	0.0213
60	50	45	50	0.0248	0.0012	0.0267		0.0242	0.0019	0.0216
60	55	45	55	0.0259	0.0019	0.0280		0.0253	0.0007	0.0220
60	60	45	60	0.0275	0.0031	0.0293		0.0267	0.0012	0.0223
60	65	45	65	0.0288	0.0020	0.0303		0.0270	0.0011	0.0222
60	70	45	70	0.0293	0.0022	0.0310		0.0265	0.0009	0.0221
60	70	90	-70	0.0251	0.0021	0.0271		0.0217	0.0011	0.0218
60	65	90	-65	0.0234	0.0014	0.0279		0.0212	0.0005	0.0220
60	60	90	-60	0.0222	0.0006	0.0275		0.0205	0.0016	0.0221
60	55	90	-55	0.0212	0.0003	0.0263		0.0200	0.0002	0.0219
60	50	90	-50	0.0203	0.0005	0.0249		0.0195	0.0004	0.0217
60	45	90	-45	0.0198	0.0001	0.0236		0.0190	0.0006	0.0212
60	40	90	-40	0.0192	0.0004	0.0224		0.0185	0.0005	0.0205
60	35	90	-35	0.0188	0.0001	0.0214		0.0183	0.0007	0.0198
60	30	90	-30	0.0185	0.0007	0.0207		0.0181	0.0006	0.0190
60	25	90	-25	0.0183	0.0004	0.0200		0.0180	0.0003	0.0184
60	20	90	-20	0.0181	0.0003	0.0195		0.0178	0.0002	0.0180
60	15	90	-15	0.0180	0.0001	0.0192		0.0177	0.0001	0.0176
60	10	90	-10	0.0179	0.0003	0.0189		0.0176	0.0003	0.0173
60	5	90	-5	0.0178	0.0001	0.0188		0.0176	0.0004	0.0172
60	0	90	0	0.0179	0.0004	0.0187		0.0178	0.0004	0.0171
60	0	90	0	0.0179	0.0004	0.0187		0.0178	0.0004	0.0171
60	5	90	5	0.0178	0.0001	0.0188		0.0176	0.0004	0.0172
60	10	90	10	0.0179	0.0003	0.0189		0.0176	0.0003	0.0173
60	15	90	15	0.0180	0.0001	0.0192		0.0177	0.0001	0.0176
60	20	90	20	0.0181	0.0003	0.0195		0.0178	0.0002	0.0180
60	25	90	25	0.0183	0.0004	0.0200		0.0180	0.0003	0.0184
60	30	90	30	0.0185	0.0007	0.0207		0.0181	0.0006	0.0190
60	35	90	35	0.0188	0.0001	0.0214		0.0183	0.0007	0.0198
60	40	90	40	0.0192	0.0004	0.0224		0.0185	0.0005	0.0205

60	45	90	45	0.0198	0.0001	0.0236		0.0190	0.0006	0.0212
60	50	90	50	0.0203	0.0005	0.0249		0.0195	0.0004	0.0217
60	55	90	55	0.0212	0.0003	0.0263		0.0200	0.0002	0.0219
60	60	90	60	0.0222	0.0006	0.0275		0.0205	0.0016	0.0221
60	65	90	65	0.0234	0.0014	0.0279		0.0212	0.0005	0.0220
60	70	90	70	0.0251	0.0021	0.0271		0.0217	0.0011	0.0218

Table A.1: Table showing 1) the BRDF data measured by VOSEG for the smooth (light blue) and rough (light orange) Apollo 11, 10084 samples used in this study, and 2) the associated best fit Hapke BRDF model predictions for each viewing angle.

Table A.2 shows the BRDF data measured by VOSEG for the smooth and rough Apollo 16, 68810 samples, and the associated best fit Hapke BRDF model predictions for each viewing angle. This data was plotted in **Figures 68**, **69**, **70**, **71**, **72** and **73**.

Viewing angles (°)				***Smooth Apollo 16***				***Rough Apollo 16***		
θ_i	θ_r	θ_a	θ_r *(full plane)*	***BRDF (SR^{-1})***	***BRDF error (±)***	***Hapke BRDF (SR^{-1})***		***BRDF (SR^{-1})***	***BRDF error (±)***	***Hapke BRDF (SR^{-1})***
15	70	180	-70	0.0439	0.0018	0.0474		0.0351	0.0009	0.0387
15	65	180	-65	0.0402	0.0028	0.0452		0.0344	0.0014	0.0375
15	60	180	-60	0.0382	0.0012	0.0431		0.0340	0.0006	0.0363
15	55	180	-55	0.0376	0.0012	0.0413		0.0340	0.0016	0.0354
15	50	180	-50	0.0370	0.0019	0.0398		0.0340	0.0014	0.0346
15	45	180	-45	0.0373	0.0015	0.0384		0.0340	0.0013	0.0339
15	40	180	-40	0.0370	0.0008	0.0374		0.0343	0.0011	0.0335
15	35	180	-35	0.0371	0.0012	0.0366		0.0347	0.0010	0.0333
15	30	180	-30	0.0381	0.0007	0.0360		0.0360	0.0010	0.0333
15	25	180	-25	0.0386	0.0007	0.0358		0.0371	0.0009	0.0335
15	20	180	-20	0.0396	0.0021	0.0358		0.0382	0.0007	0.0340
15	15	180	-15	0.0409	0.0006	0.0362		0.0389	0.0011	0.0348
15	10	180	-10	0.0434	0.0003	0.0370		0.0405	0.0009	0.0360
15	5	180	-5	0.0456	0.0003	0.0383		0.0422	0.0006	0.0378
15	0	0	0	0.0475	0.0003	0.0422		0.0447	0.0002	0.0414
15	0	180	0	0.0475	0.0002	0.0422		0.0447	0.0006	0.0414
15	5	0	5	0.0488	0.0012	0.0475		0.0469	0.0000	0.0464
15	10	0	10	0.0531	0.0013	0.0527		0.0506	0.0015	0.0529
15	20	0	20	0.0605	0.0000	0.0538		0.0573	0.0012	0.0541

15	25	0	25	0.0507	0.0004	0.0495		0.0491	0.0000	0.0485
15	30	0	30	0.0484	0.0018	0.0471		0.0467	0.0008	0.0453
15	35	0	35	0.0472	0.0010	0.0457		0.0461	0.0018	0.0433
15	40	0	40	0.0464	0.0021	0.0450		0.0428	0.0014	0.0422
15	45	0	45	0.0465	0.0011	0.0450		0.0421	0.0014	0.0417
15	50	0	50	0.0453	0.0006	0.0455		0.0421	0.0005	0.0416
15	55	0	55	0.0441	0.0007	0.0464		0.0410	0.0000	0.0420
15	60	0	60	0.0455	0.0016	0.0477		0.0410	0.0008	0.0426
15	65	0	65	0.0443	0.0009	0.0495		0.0406	0.0005	0.0436
15	70	0	70	0.0452	0.0022	0.0516		0.0404	0.0009	0.0449
15	70	135	-70	0.0429	0.0035	0.0474		0.0384	0.0012	0.0392
15	65	135	-65	0.0420	0.0028	0.0451		0.0385	0.0008	0.0379
15	60	135	-60	0.0414	0.0012	0.0431		0.0384	0.0012	0.0368
15	55	135	-55	0.0411	0.0021	0.0413		0.0388	0.0012	0.0358
15	50	135	-50	0.0409	0.0009	0.0398		0.0387	0.0009	0.0350
15	45	135	-45	0.0407	0.0018	0.0385		0.0394	0.0010	0.0344
15	40	135	-40	0.0409	0.0033	0.0375		0.0394	0.0008	0.0340
15	35	135	-35	0.0414	0.0008	0.0368		0.0401	0.0012	0.0338
15	30	135	-30	0.0418	0.0014	0.0363		0.0403	0.0007	0.0339
15	25	135	-25	0.0424	0.0014	0.0361		0.0408	0.0007	0.0341
15	20	135	-20	0.0434	0.0007	0.0362		0.0420	0.0012	0.0347
15	15	135	-15	0.0440	0.0014	0.0367		0.0430	0.0006	0.0355
15	10	135	-10	0.0456	0.0014	0.0375		0.0440	0.0013	0.0367
15	5	135	-5	0.0466	0.0028	0.0387		0.0448	0.0013	0.0383
15	0	45	0	0.0475	0.0021	0.0411		0.0447	0.0013	0.0408
15	0	135	0	0.0475	0.0021	0.0411		0.0447	0.0000	0.0408
15	5	45	5	0.0474	0.0022	0.0437		0.0444	0.0011	0.0435
15	10	45	10	0.0471	0.0012	0.0448		0.0445	0.0011	0.0449
15	15	45	15	0.0466	0.0013	0.0447		0.0448	0.0006	0.0446
15	20	45	20	0.0465	0.0057	0.0436		0.0443	0.0003	0.0431
15	25	45	25	0.0460	0.0012	0.0425		0.0441	0.0009	0.0415
15	30	45	30	0.0457	0.0014	0.0416		0.0437	0.0013	0.0403
15	35	45	35	0.0450	0.0000	0.0412		0.0437	0.0013	0.0394
15	40	45	40	0.0445	0.0013	0.0412		0.0430	0.0013	0.0390
15	45	45	45	0.0437	0.0036	0.0416		0.0417	0.0013	0.0389
15	50	45	50	0.0431	0.0016	0.0424		0.0409	0.0016	0.0392

15	55	45	55	0.0424	0.0018	0.0435		0.0398	0.0004	0.0397
15	60	45	60	0.0415	0.0048	0.0450		0.0382	0.0014	0.0405
15	65	45	65	0.0407	0.0039	0.0470		0.0368	0.0017	0.0416
15	70	45	70	0.0398	0.0028	0.0494		0.0342	0.0022	0.0430
15	70	90	-70	0.0409	0.0021	0.0479		0.0363	0.0010	0.0408
15	65	90	-65	0.0424	0.0032	0.0455		0.0384	0.0013	0.0394
15	60	90	-60	0.0441	0.0015	0.0435		0.0400	0.0017	0.0382
15	55	90	-55	0.0450	0.0013	0.0418		0.0413	0.0013	0.0373
15	50	90	-50	0.0451	0.0011	0.0404		0.0425	0.0011	0.0365
15	45	90	-45	0.0456	0.0011	0.0393		0.0430	0.0016	0.0360
15	40	90	-40	0.0459	0.0010	0.0385		0.0434	0.0010	0.0358
15	35	90	-35	0.0460	0.0028	0.0380		0.0440	0.0009	0.0357
15	30	90	-30	0.0464	0.0018	0.0378		0.0440	0.0002	0.0359
15	25	90	-25	0.0465	0.0000	0.0379		0.0442	0.0013	0.0364
15	20	90	-20	0.0470	0.0025	0.0382		0.0442	0.0015	0.0371
15	15	90	-15	0.0471	0.0016	0.0389		0.0443	0.0008	0.0381
15	10	90	-10	0.0475	0.0008	0.0397		0.0443	0.0012	0.0392
15	5	90	-5	0.0475	0.0016	0.0404		0.0443	0.0016	0.0402
15	0	90	0	0.0475	0.0032	0.0407		0.0447	0.0016	0.0406
15	0	90	0	0.0475	0.0032	0.0407		0.0447	0.0016	0.0406
15	5	90	5	0.0475	0.0016	0.0404		0.0443	0.0016	0.0402
15	10	90	10	0.0475	0.0008	0.0397		0.0443	0.0012	0.0392
15	15	90	15	0.0471	0.0016	0.0389		0.0443	0.0008	0.0381
15	20	90	20	0.0470	0.0025	0.0382		0.0442	0.0015	0.0371
15	25	90	25	0.0465	0.0000	0.0379		0.0442	0.0013	0.0364
15	30	90	30	0.0464	0.0018	0.0378		0.0440	0.0002	0.0359
15	35	90	35	0.0460	0.0028	0.0380		0.0440	0.0009	0.0357
15	40	90	40	0.0459	0.0010	0.0385		0.0434	0.0010	0.0358
15	45	90	45	0.0456	0.0011	0.0393		0.0430	0.0016	0.0360
15	50	90	50	0.0451	0.0011	0.0404		0.0425	0.0011	0.0365
15	55	90	55	0.0450	0.0013	0.0418		0.0413	0.0013	0.0373
15	60	90	60	0.0441	0.0015	0.0435		0.0400	0.0017	0.0382
15	65	90	65	0.0424	0.0032	0.0455		0.0384	0.0013	0.0394
15	70	90	70	0.0409	0.0021	0.0479		0.0363	0.0010	0.0408
30	70	180	-70	0.0473	0.0039	0.0574		0.0371	0.0019	0.0401
30	65	180	-65	0.0446	0.0015	0.0518		0.0366	0.0015	0.0387

30	60	180	-60	0.0434	0.0024	0.0480		0.0360	0.0024	0.0373
30	55	180	-55	0.0427	0.0011	0.0451		0.0356	0.0011	0.0362
30	50	180	-50	0.0418	0.0038	0.0429		0.0351	0.0007	0.0351
30	45	180	-45	0.0410	0.0009	0.0411		0.0349	0.0014	0.0343
30	40	180	-40	0.0404	0.0024	0.0396		0.0352	0.0000	0.0337
30	35	180	-35	0.0400	0.0031	0.0383		0.0347	0.0010	0.0332
30	30	180	-30	0.0398	0.0007	0.0374		0.0353	0.0005	0.0329
30	25	180	-25	0.0399	0.0007	0.0366		0.0358	0.0019	0.0328
30	20	180	-20	0.0399	0.0024	0.0362		0.0362	0.0004	0.0330
30	15	180	-15	0.0398	0.0025	0.0360		0.0370	0.0017	0.0333
30	10	180	-10	0.0397	0.0007	0.0361		0.0376	0.0021	0.0339
30	5	180	-5	0.0405	0.0007	0.0365		0.0387	0.0008	0.0347
30	0	0	0	0.0412	0.0011	0.0391		0.0398	0.0008	0.0368
30	0	180	0	0.0412	0.0011	0.0391		0.0398	0.0020	0.0368
30	5	0	5	0.0427	0.0016	0.0422		0.0406	0.0008	0.0395
30	10	0	10	0.0429	0.0016	0.0442		0.0423	0.0004	0.0419
30	15	0	15	0.0468	0.0017	0.0470		0.0456	0.0004	0.0453
30	20	0	20	0.0507	0.0009	0.0512		0.0480	0.0004	0.0502
30	25	0	25	0.0584	0.0009	0.0575		0.0558	0.0013	0.0580
30	35	0	35	0.0600	0.0029	0.0602		0.0581	0.0015	0.0608
30	40	0	40	0.0561	0.0021	0.0561		0.0532	0.0015	0.0552
30	45	0	45	0.0519	0.0006	0.0539		0.0498	0.0011	0.0522
30	50	0	50	0.0499	0.0006	0.0530		0.0485	0.0006	0.0506
30	55	0	55	0.0489	0.0007	0.0530		0.0473	0.0013	0.0500
30	60	0	60	0.0501	0.0009	0.0537		0.0475	0.0008	0.0501
30	65	0	65	0.0503	0.0037	0.0550		0.0470	0.0009	0.0508
30	70	0	70	0.0522	0.0018	0.0569		0.0470	0.0011	0.0521
30	70	135	-70	0.0431	0.0018	0.0554		0.0373	0.0009	0.0410
30	65	135	-65	0.0410	0.0043	0.0506		0.0363	0.0015	0.0394
30	60	135	-60	0.0395	0.0031	0.0472		0.0353	0.0024	0.0380
30	55	135	-55	0.0384	0.0011	0.0446		0.0348	0.0011	0.0368
30	50	135	-50	0.0379	0.0010	0.0425		0.0349	0.0014	0.0358
30	45	135	-45	0.0375	0.0009	0.0408		0.0343	0.0009	0.0349
30	40	135	-40	0.0372	0.0033	0.0394		0.0347	0.0014	0.0343
30	35	135	-35	0.0370	0.0054	0.0383		0.0350	0.0011	0.0338
30	30	135	-30	0.0374	0.0000	0.0374		0.0357	0.0007	0.0336

30	25	135	-25	0.0377	0.0022	0.0368		0.0360	0.0007	0.0335
30	20	135	-20	0.0384	0.0014	0.0364		0.0367	0.0013	0.0336
30	15	135	-15	0.0397	0.0014	0.0363		0.0375	0.0018	0.0339
30	10	135	-10	0.0402	0.0021	0.0364		0.0383	0.0007	0.0343
30	5	135	-5	0.0409	0.0014	0.0367		0.0392	0.0007	0.0350
30	0	45	0	0.0412	0.0007	0.0380		0.0398	0.0011	0.0363
30	0	135	0	0.0412	0.0014	0.0380		0.0398	0.0010	0.0363
30	5	45	5	0.0421	0.0022	0.0396		0.0401	0.0011	0.0378
30	10	45	10	0.0421	0.0028	0.0406		0.0409	0.0014	0.0390
30	15	45	15	0.0427	0.0014	0.0416		0.0408	0.0009	0.0403
30	20	45	20	0.0429	0.0005	0.0425		0.0411	0.0013	0.0413
30	25	45	25	0.0437	0.0030	0.0432		0.0421	0.0010	0.0420
30	30	45	30	0.0441	0.0020	0.0437		0.0421	0.0009	0.0423
30	35	45	35	0.0446	0.0010	0.0440		0.0425	0.0008	0.0425
30	40	45	40	0.0447	0.0011	0.0444		0.0422	0.0017	0.0426
30	45	45	45	0.0445	0.0017	0.0450		0.0422	0.0009	0.0428
30	50	45	50	0.0448	0.0006	0.0459		0.0423	0.0004	0.0432
30	55	45	55	0.0450	0.0017	0.0473		0.0422	0.0004	0.0439
30	60	45	60	0.0445	0.0016	0.0492		0.0418	0.0007	0.0450
30	65	45	65	0.0446	0.0039	0.0518		0.0413	0.0015	0.0464
30	70	45	70	0.0441	0.0030	0.0553		0.0410	0.0015	0.0483
30	70	90	-70	0.0466	0.0042	0.0546		0.0442	0.0012	0.0438
30	65	90	-65	0.0457	0.0033	0.0502		0.0442	0.0011	0.0419
30	60	90	-60	0.0442	0.0047	0.0470		0.0440	0.0006	0.0404
30	55	90	-55	0.0444	0.0013	0.0445		0.0432	0.0013	0.0391
30	50	90	-50	0.0443	0.0046	0.0427		0.0424	0.0012	0.0381
30	45	90	-45	0.0436	0.0021	0.0412		0.0419	0.0011	0.0372
30	40	90	-40	0.0433	0.0000	0.0401		0.0419	0.0006	0.0366
30	35	90	-35	0.0429	0.0009	0.0392		0.0414	0.0017	0.0362
30	30	90	-30	0.0426	0.0000	0.0386		0.0410	0.0017	0.0359
30	25	90	-25	0.0420	0.0000	0.0382		0.0407	0.0017	0.0358
30	20	90	-20	0.0420	0.0017	0.0379		0.0402	0.0012	0.0358
30	15	90	-15	0.0418	0.0041	0.0378		0.0399	0.0008	0.0359
30	10	90	-10	0.0416	0.0040	0.0377		0.0398	0.0014	0.0360
30	5	90	-5	0.0415	0.0016	0.0377		0.0399	0.0016	0.0361
30	0	90	0	0.0412	0.0055	0.0377		0.0398	0.0008	0.0362

30	0	90	0	0.0412	0.0055	0.0377		0.0398	0.0008	0.0362
30	5	90	5	0.0415	0.0016	0.0377		0.0399	0.0016	0.0361
30	10	90	10	0.0416	0.0040	0.0377		0.0398	0.0014	0.0360
30	15	90	15	0.0418	0.0041	0.0378		0.0399	0.0008	0.0359
30	20	90	20	0.0420	0.0017	0.0379		0.0402	0.0012	0.0358
30	25	90	25	0.0420	0.0000	0.0382		0.0407	0.0017	0.0358
30	30	90	30	0.0426	0.0000	0.0386		0.0410	0.0017	0.0359
30	35	90	35	0.0429	0.0009	0.0392		0.0414	0.0017	0.0362
30	40	90	40	0.0433	0.0000	0.0401		0.0419	0.0006	0.0366
30	45	90	45	0.0436	0.0021	0.0412		0.0419	0.0011	0.0372
30	50	90	50	0.0443	0.0046	0.0427		0.0424	0.0012	0.0381
30	55	90	55	0.0444	0.0013	0.0445		0.0432	0.0013	0.0391
30	60	90	60	0.0442	0.0047	0.0470		0.0440	0.0006	0.0404
30	65	90	65	0.0457	0.0033	0.0502		0.0442	0.0011	0.0419
30	70	90	70	0.0466	0.0042	0.0546		0.0442	0.0012	0.0438
45	70	180	-70	0.0601	0.0043	0.0554		0.0420	0.0037	0.0437
45	65	180	-65	0.0546	0.0043	0.0541		0.0400	0.0020	0.0422
45	60	180	-60	0.0509	0.0011	0.0525		0.0381	0.0011	0.0409
45	55	180	-55	0.0479	0.0044	0.0508		0.0360	0.0007	0.0390
45	50	180	-50	0.0442	0.0039	0.0487		0.0350	0.0006	0.0375
45	45	180	-45	0.0417	0.0026	0.0464		0.0338	0.0001	0.0364
45	40	180	-40	0.0402	0.0016	0.0443		0.0333	0.0011	0.0355
45	35	180	-35	0.0393	0.0000	0.0425		0.0334	0.0015	0.0348
45	30	180	-30	0.0389	0.0043	0.0410		0.0332	0.0019	0.0343
45	25	180	-25	0.0384	0.0027	0.0399		0.0335	0.0009	0.0340
45	20	180	-20	0.0385	0.0013	0.0390		0.0340	0.0013	0.0339
45	15	180	-15	0.0377	0.0020	0.0384		0.0342	0.0009	0.0339
45	10	180	-10	0.0380	0.0013	0.0380		0.0349	0.0013	0.0342
45	5	180	-5	0.0389	0.0020	0.0379		0.0367	0.0013	0.0347
45	0	0	0	0.0401	0.0009	0.0400		0.0380	0.0004	0.0363
45	0	180	0	0.0401	0.0009	0.0400		0.0380	0.0002	0.0363
45	5	0	5	0.0403	0.0008	0.0425		0.0382	0.0008	0.0383
45	10	0	10	0.0413	0.0010	0.0435		0.0387	0.0004	0.0397
45	15	0	15	0.0425	0.0008	0.0450		0.0399	0.0004	0.0417
45	20	0	20	0.0446	0.0000	0.0471		0.0439	0.0000	0.0442
45	25	0	25	0.0475	0.0004	0.0499		0.0459	0.0004	0.0475

45	30	0	30	0.0499	0.0009	0.0539		0.0503	0.0013	0.0522
45	35	0	35	0.0567	0.0000	0.0596		0.0561	0.0000	0.0588
45	40	0	40	0.0632	0.0030	0.0681		0.0630	0.0015	0.0691
45	50	0	50	0.0715	0.0009	0.0737		0.0692	0.0000	0.0750
45	55	0	55	0.0675	0.0026	0.0698		0.0645	0.0000	0.0693
45	60	0	60	0.0651	0.0022	0.0683		0.0618	0.0007	0.0667
45	65	0	65	0.0647	0.0026	0.0684		0.0608	0.0035	0.0661
45	70	0	70	0.0646	0.0009	0.0698		0.0593	0.0009	0.0668
45	70	135	-70	0.0545	0.0048	0.0528		0.0441	0.0000	0.0476
45	65	135	-65	0.0505	0.0041	0.0520		0.0416	0.0009	0.0447
45	60	135	-60	0.0468	0.0024	0.0509		0.0403	0.0022	0.0417
45	55	135	-55	0.0443	0.0063	0.0493		0.0393	0.0017	0.0398
45	50	135	-50	0.0433	0.0009	0.0476		0.0391	0.0004	0.0383
45	45	135	-45	0.0417	0.0000	0.0455		0.0389	0.0005	0.0372
45	40	135	-40	0.0409	0.0024	0.0437		0.0388	0.0003	0.0362
45	35	135	-35	0.0401	0.0045	0.0421		0.0388	0.0000	0.0355
45	30	135	-30	0.0402	0.0015	0.0407		0.0385	0.0009	0.0349
45	25	135	-25	0.0402	0.0026	0.0397		0.0384	0.0011	0.0346
45	20	135	-20	0.0400	0.0013	0.0389		0.0384	0.0003	0.0344
45	15	135	-15	0.0400	0.0005	0.0384		0.0382	0.0004	0.0344
45	10	135	-10	0.0401	0.0011	0.0381		0.0382	0.0003	0.0346
45	5	135	-5	0.0402	0.0018	0.0389		0.0382	0.0004	0.0349
45	0	45	0	0.0401	0.0013	0.0389		0.0380	0.0003	0.0358
45	0	135	0	0.0401	0.0025	0.0382		0.0380	0.0004	0.0358
45	5	45	5	0.0403	0.0012	0.0401		0.0380	0.0013	0.0369
45	10	45	10	0.0411	0.0022	0.0407		0.0390	0.0002	0.0378
45	15	45	15	0.0427	0.0045	0.0416		0.0393	0.0004	0.0389
45	20	45	20	0.0436	0.0013	0.0426		0.0404	0.0004	0.0401
45	25	45	25	0.0447	0.0025	0.0437		0.0409	0.0000	0.0414
45	30	45	30	0.0450	0.0017	0.0450		0.0411	0.0016	0.0428
45	35	45	35	0.0462	0.0038	0.0463		0.0417	0.0030	0.0442
45	40	45	40	0.0468	0.0016	0.0477		0.0423	0.0029	0.0455
45	45	45	45	0.0471	0.0029	0.0493		0.0430	0.0019	0.0469
45	50	45	50	0.0470	0.0040	0.0515		0.0428	0.0019	0.0483
45	55	45	55	0.0474	0.0042	0.0537		0.0425	0.0021	0.0499
45	60	45	60	0.0475	0.0030	0.0559		0.0421	0.0030	0.0518

45	65	45	65	0.0479	0.0019	0.0577		0.0414	0.0019	0.0545
45	70	45	70	0.0484	0.0020	0.0590		0.0410	0.0020	0.0585
45	70	90	-70	0.0526	0.0008	0.0495		0.0450	0.0020	0.0486
45	65	90	-65	0.0499	0.0018	0.0487		0.0436	0.0018	0.0467
45	60	90	-60	0.0489	0.0012	0.0479		0.0431	0.0030	0.0447
45	55	90	-55	0.0479	0.0040	0.0470		0.0429	0.0013	0.0427
45	50	90	-50	0.0469	0.0024	0.0458		0.0423	0.0030	0.0411
45	45	90	-45	0.0456	0.0033	0.0448		0.0419	0.0035	0.0398
45	40	90	-40	0.0449	0.0010	0.0435		0.0411	0.0031	0.0388
45	35	90	-35	0.0442	0.0029	0.0422		0.0407	0.0019	0.0379
45	30	90	-30	0.0437	0.0037	0.0411		0.0404	0.0009	0.0372
45	25	90	-25	0.0431	0.0009	0.0403		0.0395	0.0001	0.0367
45	20	90	-20	0.0420	0.0027	0.0396		0.0393	0.0025	0.0363
45	15	90	-15	0.0413	0.0050	0.0392		0.0391	0.0022	0.0360
45	10	90	-10	0.0409	0.0041	0.0388		0.0386	0.0008	0.0358
45	5	90	-5	0.0405	0.0016	0.0386		0.0384	0.0016	0.0357
45	0	90	0	0.0401	0.0025	0.0386		0.0380	0.0008	0.0357
45	0	90	0	0.0401	0.0025	0.0386		0.0380	0.0008	0.0357
45	5	90	5	0.0405	0.0016	0.0386		0.0384	0.0016	0.0357
45	10	90	10	0.0409	0.0041	0.0388		0.0386	0.0008	0.0358
45	15	90	15	0.0413	0.0050	0.0392		0.0391	0.0022	0.0360
45	20	90	20	0.0420	0.0027	0.0396		0.0393	0.0025	0.0363
45	25	90	25	0.0431	0.0009	0.0403		0.0395	0.0001	0.0367
45	30	90	30	0.0437	0.0037	0.0411		0.0404	0.0009	0.0372
45	35	90	35	0.0442	0.0029	0.0422		0.0407	0.0019	0.0379
45	40	90	40	0.0449	0.0010	0.0435		0.0411	0.0031	0.0388
45	45	90	45	0.0456	0.0033	0.0448		0.0419	0.0035	0.0398
45	50	90	50	0.0469	0.0024	0.0458		0.0423	0.0030	0.0411
45	55	90	55	0.0479	0.0040	0.0470		0.0429	0.0013	0.0427
45	60	90	60	0.0489	0.0012	0.0479		0.0431	0.0030	0.0447
45	65	90	65	0.0499	0.0018	0.0487		0.0436	0.0018	0.0467
45	70	90	70	0.0526	0.0008	0.0495		0.0450	0.0020	0.0486
60	70	180	-70	0.0823	0.0024	0.0626		0.0464	0.0012	0.0489
60	65	180	-65	0.0730	0.0028	0.0636		0.0430	0.0038	0.0482
60	60	180	-60	0.0657	0.0008	0.0620		0.0414	0.0008	0.0461
60	55	180	-55	0.0593	0.0014	0.0591		0.0384	0.0013	0.0439

60	50	180	-50	0.0549	0.0012	0.0558		0.0373	0.0019	0.0419
60	45	180	-45	0.0501	0.0022	0.0525		0.0363	0.0006	0.0403
60	40	180	-40	0.0466	0.0011	0.0497		0.0355	0.0005	0.0389
60	35	180	-35	0.0431	0.0005	0.0472		0.0340	0.0010	0.0379
60	30	180	-30	0.0413	0.0028	0.0452		0.0333	0.0023	0.0371
60	25	180	-25	0.0400	0.0005	0.0435		0.0339	0.0009	0.0365
60	20	180	-20	0.0398	0.0022	0.0422		0.0338	0.0013	0.0362
60	15	180	-15	0.0395	0.0000	0.0411		0.0351	0.0017	0.0361
60	10	180	-10	0.0395	0.0017	0.0404		0.0360	0.0013	0.0362
60	5	180	-5	0.0398	0.0008	0.0400		0.0371	0.0013	0.0365
60	0	0	0	0.0394	0.0004	0.0430		0.0380	0.0013	0.0381
60	0	180	0	0.0394	0.0008	0.0430		0.0380	0.0014	0.0381
60	5	0	5	0.0391	0.0008	0.0463		0.0374	0.0009	0.0400
60	10	0	10	0.0400	0.0009	0.0468		0.0393	0.0015	0.0411
60	15	0	15	0.0415	0.0003	0.0477		0.0417	0.0024	0.0426
60	20	0	20	0.0451	0.0024	0.0491		0.0444	0.0008	0.0445
60	25	0	25	0.0470	0.0010	0.0510		0.0474	0.0006	0.0470
60	30	0	30	0.0494	0.0022	0.0537		0.0503	0.0010	0.0501
60	35	0	35	0.0543	0.0007	0.0572		0.0538	0.0004	0.0542
60	40	0	40	0.0576	0.0012	0.0619		0.0592	0.0008	0.0595
60	45	0	45	0.0650	0.0019	0.0683		0.0640	0.0004	0.0668
60	50	0	50	0.0734	0.0024	0.0774		0.0734	0.0009	0.0771
60	55	0	55	0.0864	0.0013	0.0909		0.0875	0.0035	0.0932
60	65	0	65	0.1042	0.0007	0.1044		0.0989	0.0007	0.1075
60	70	0	70	0.0973	0.0033	0.1020		0.0879	0.0008	0.1027
60	70	135	-70	0.0662	0.0054	0.0591		0.0472	0.0041	0.0498
60	65	135	-65	0.0591	0.0015	0.0605		0.0443	0.0023	0.0493
60	60	135	-60	0.0531	0.0012	0.0594		0.0422	0.0028	0.0473
60	55	135	-55	0.0480	0.0028	0.0570		0.0403	0.0040	0.0450
60	50	135	-50	0.0449	0.0009	0.0540		0.0399	0.0014	0.0429
60	45	135	-45	0.0425	0.0026	0.0511		0.0383	0.0013	0.0412
60	40	135	-40	0.0410	0.0015	0.0485		0.0379	0.0000	0.0397
60	35	135	-35	0.0401	0.0021	0.0463		0.0370	0.0011	0.0386
60	30	135	-30	0.0399	0.0007	0.0445		0.0371	0.0016	0.0377
60	25	135	-25	0.0395	0.0007	0.0430		0.0369	0.0026	0.0371
60	20	135	-20	0.0395	0.0013	0.0418		0.0369	0.0010	0.0367

60	15	135	-15	0.0390	0.0019	0.0409		0.0369	0.0039	0.0365
60	10	135	-10	0.0390	0.0006	0.0403		0.0375	0.0005	0.0364
60	5	135	-5	0.0393	0.0013	0.0399		0.0380	0.0034	0.0366
60	0	45	0	0.0394	0.0006	0.0410		0.0380	0.0010	0.0371
60	0	135	0	0.0394	0.0011	0.0410		0.0380	0.0009	0.0371
60	5	45	5	0.0401	0.0034	0.0424		0.0381	0.0010	0.0388
60	10	45	10	0.0411	0.0026	0.0428		0.0392	0.0005	0.0395
60	15	45	15	0.0436	0.0017	0.0435		0.0409	0.0005	0.0405
60	20	45	20	0.0446	0.0053	0.0444		0.0412	0.0012	0.0417
60	25	45	25	0.0464	0.0010	0.0456		0.0438	0.0008	0.0432
60	30	45	30	0.0484	0.0012	0.0471		0.0465	0.0009	0.0449
60	35	45	35	0.0498	0.0039	0.0488		0.0469	0.0007	0.0469
60	40	45	40	0.0517	0.0030	0.0509		0.0487	0.0008	0.0491
60	45	45	45	0.0542	0.0053	0.0532		0.0509	0.0012	0.0515
60	50	45	50	0.0572	0.0049	0.0553		0.0530	0.0019	0.0544
60	55	45	55	0.0595	0.0027	0.0568		0.0559	0.0029	0.0596
60	60	45	60	0.0624	0.0012	0.0578		0.0566	0.0009	0.0621
60	65	45	65	0.0650	0.0038	0.0586		0.0578	0.0024	0.0641
60	70	45	70	0.0683	0.0029	0.0592		0.0594	0.0030	0.0641
60	70	90	-70	0.0652	0.0048	0.0571		0.0550	0.0025	0.0515
60	65	90	-65	0.0616	0.0048	0.0564		0.0529	0.0022	0.0525
60	60	90	-60	0.0577	0.0029	0.0556		0.0519	0.0015	0.0509
60	55	90	-55	0.0552	0.0000	0.0541		0.0500	0.0024	0.0485
60	50	90	-50	0.0531	0.0024	0.0519		0.0486	0.0002	0.0462
60	45	90	-45	0.0516	0.0056	0.0496		0.0477	0.0022	0.0442
60	40	90	-40	0.0504	0.0041	0.0475		0.0466	0.0006	0.0425
60	35	90	-35	0.0487	0.0029	0.0457		0.0446	0.0012	0.0412
60	30	90	-30	0.0471	0.0009	0.0442		0.0439	0.0005	0.0400
60	25	90	-25	0.0461	0.0036	0.0430		0.0429	0.0005	0.0391
60	20	90	-20	0.0441	0.0009	0.0421		0.0421	0.0001	0.0384
60	15	90	-15	0.0435	0.0025	0.0414		0.0397	0.0005	0.0379
60	10	90	-10	0.0421	0.0017	0.0409		0.0387	0.0015	0.0375
60	5	90	-5	0.0410	0.0025	0.0406		0.0379	0.0006	0.0373
60	0	90	0	0.0394	0.0017	0.0405		0.0380	0.0008	0.0372
60	0	90	0	0.0394	0.0017	0.0405		0.0380	0.0008	0.0372
60	5	90	5	0.0410	0.0025	0.0406		0.0379	0.0006	0.0373

60	10	90	10	0.0421	0.0017	0.0409		0.0387	0.0015	0.0375
60	15	90	15	0.0435	0.0025	0.0414		0.0397	0.0005	0.0379
60	20	90	20	0.0441	0.0009	0.0421		0.0421	0.0001	0.0384
60	25	90	25	0.0461	0.0036	0.0430		0.0429	0.0005	0.0391
60	30	90	30	0.0471	0.0009	0.0442		0.0439	0.0005	0.0400
60	35	90	35	0.0487	0.0029	0.0457		0.0446	0.0012	0.0412
60	40	90	40	0.0504	0.0041	0.0475		0.0466	0.0006	0.0425
60	45	90	45	0.0516	0.0056	0.0496		0.0477	0.0022	0.0442
60	50	90	50	0.0531	0.0024	0.0519		0.0486	0.0002	0.0462
60	55	90	55	0.0552	0.0000	0.0541		0.0500	0.0024	0.0485
60	60	90	60	0.0577	0.0029	0.0556		0.0519	0.0015	0.0509
60	65	90	65	0.0616	0.0048	0.0564		0.0529	0.0022	0.0525
60	70	90	70	0.0652	0.0048	0.0571		0.0550	0.0025	0.0515

Table A.2: Table showing 1) the BRDF data measured by VOSEG for the smooth (light blue) and rough (light orange) Apollo 16, 68810 samples used in this study, and 2) the associated Hapke BRDF model predictions for each viewing angle.

Table A.3 shows the principal plane BRDF data measured by VOSEG for the smooth and rough Apollo 11, 10084 samples, and the associated best fit Hapke BRDF model predictions for each viewing angle, when the opposition effect is turned off. This data was plotted in **Figures 81** and **82**.

Viewing angles (°)				***Smooth Apollo 11***				***Rough Apollo 11***		
θ_i	θ_r	θ_a	θ_r *(full plane)*	***BRDF (SR^{-1})***	***BRDF error (±)***	***Hapke BRDF (SR^{-1})***		***BRDF (SR^{-1})***	***BRDF error (±)***	***Hapke BRDF (SR^{-1})***
15	70	180	-70	0.0259	0.0019	0.0256		0.0220	0.0026	0.0251
15	65	180	-65	0.0246	0.0009	0.0245		0.0211	0.0021	0.0237
15	60	180	-60	0.0235	0.0008	0.0235		0.0204	0.0014	0.0224
15	55	180	-55	0.0223	0.0012	0.0226		0.0198	0.0009	0.0214
15	50	180	-50	0.0213	0.0012	0.0218		0.0193	0.0011	0.0204
15	45	180	-45	0.0207	0.0013	0.0210		0.0186	0.0032	0.0196
15	40	180	-40	0.0201	0.0009	0.0204		0.0183	0.0014	0.0189
15	35	180	-35	0.0196	0.0005	0.0198		0.0182	0.0007	0.0183
15	30	180	-30	0.0196	0.0011	0.0194		0.0181	0.0017	0.0177
15	25	180	-25	0.0195	0.0005	0.0190		0.0181	0.0004	0.0172
15	20	180	-20	0.0197	0.0009	0.0187		0.0183	0.0004	0.0168

15	15	180	-15	0.0197	0.0006	0.0184		0.0187	0.0004	0.0165
15	10	180	-10	0.0201	0.0011	0.0183		0.0193	0.0013	0.0163
15	5	180	-5	0.0207	0.0014	0.0182		0.0200	0.0010	0.0161
15	0	0	0	0.0221	0.0007	0.0190		0.0210	0.0006	0.0178
15	0	180	0	0.0221	0.0007	0.0190		0.0210	0.0006	0.0169
15	5	0	5	0.0230	0.0005	0.0198		0.0228	0.0009	0.0195
15	10	0	10	0.0256	0.0002	0.0199		0.0252	0.0017	0.0196
15	20	0	20	0.0278	0.0007	0.0204		0.0267	0.0017	0.0200
15	25	0	25	0.0250	0.0009	0.0207		0.0234	0.0019	0.0203
15	30	0	30	0.0234	0.0013	0.0211		0.0221	0.0028	0.0208
15	35	0	35	0.0228	0.0023	0.0216		0.0212	0.0005	0.0213
15	40	0	40	0.0220	0.0015	0.0222		0.0207	0.0009	0.0220
15	45	0	45	0.0216	0.0020	0.0229		0.0201	0.0009	0.0228
15	50	0	50	0.0213	0.0003	0.0238		0.0199	0.0009	0.0237
15	55	0	55	0.0211	0.0006	0.0247		0.0198	0.0008	0.0248
15	60	0	60	0.0211	0.0006	0.0258		0.0198	0.0015	0.0260
15	65	0	65	0.0214	0.0004	0.0271		0.0197	0.0012	0.0274
15	70	0	70	0.0229	0.0014	0.0285		0.0199	0.0010	0.0291
30	70	180	-70	0.0292	0.0012	0.0292		0.0233	0.0012	0.0258
30	65	180	-65	0.0259	0.0015	0.0269		0.0223	0.0008	0.0243
30	60	180	-60	0.0242	0.0025	0.0253		0.0214	0.0003	0.0233
30	55	180	-55	0.0232	0.0015	0.0241		0.0201	0.0010	0.0226
30	50	180	-50	0.0222	0.0023	0.0231		0.0189	0.0015	0.0218
30	45	180	-45	0.0211	0.0029	0.0223		0.0179	0.0011	0.0210
30	40	180	-40	0.0206	0.0013	0.0215		0.0176	0.0009	0.0204
30	35	180	-35	0.0198	0.0009	0.0209		0.0174	0.0012	0.0198
30	30	180	-30	0.0193	0.0011	0.0204		0.0172	0.0015	0.0191
30	25	180	-25	0.0185	0.0023	0.0200		0.0169	0.0005	0.0186
30	20	180	-20	0.0184	0.0007	0.0196		0.0168	0.0005	0.0181
30	15	180	-15	0.0183	0.0014	0.0194		0.0170	0.0010	0.0177
30	10	180	-10	0.0182	0.0015	0.0192		0.0172	0.0024	0.0174
30	5	180	-5	0.0184	0.0016	0.0191		0.0175	0.0005	0.0172
30	0	0	0	0.0199	0.0012	0.0199		0.0190	0.0015	0.0189
30	0	180	0	0.0199	0.0006	0.0199		0.0190	0.0017	0.0179
30	5	0	5	0.0203	0.0005	0.0208		0.0196	0.0015	0.0206
30	10	0	10	0.0210	0.0007	0.0209		0.0205	0.0016	0.0206

30	15	0	15	0.0224	0.0008	0.0211		0.0218	0.0008	0.0208
30	20	0	20	0.0243	0.0006	0.0214		0.0239	0.0009	0.0210
30	25	0	25	0.0283	0.0006	0.0218		0.0274	0.0012	0.0213
30	35	0	35	0.0306	0.0003	0.0228		0.0296	0.0009	0.0222
30	40	0	40	0.0279	0.0004	0.0235		0.0271	0.0012	0.0229
30	45	0	45	0.0259	0.0007	0.0243		0.0257	0.0017	0.0237
30	50	0	50	0.0249	0.0010	0.0252		0.0242	0.0018	0.0247
30	55	0	55	0.0242	0.0005	0.0263		0.0237	0.0004	0.0258
30	60	0	60	0.0242	0.0008	0.0276		0.0233	0.0014	0.0271
30	65	0	65	0.0243	0.0014	0.0291		0.0231	0.0021	0.0286
30	70	0	70	0.0249	0.0013	0.0307		0.0232	0.0036	0.0304
45	70	180	-70	0.0364	0.0019	0.0278		0.0294	0.0028	0.0254
45	65	180	-65	0.0316	0.0016	0.0275		0.0265	0.0020	0.0253
45	60	180	-60	0.0282	0.0014	0.0269		0.0246	0.0017	0.0248
45	55	180	-55	0.0262	0.0011	0.0264		0.0232	0.0034	0.0243
45	50	180	-50	0.0245	0.0016	0.0255		0.0216	0.0026	0.0239
45	45	180	-45	0.0228	0.0027	0.0245		0.0200	0.0031	0.0234
45	40	180	-40	0.0210	0.0014	0.0236		0.0189	0.0007	0.0226
45	35	180	-35	0.0199	0.0009	0.0229		0.0182	0.0011	0.0218
45	30	180	-30	0.0187	0.0007	0.0222		0.0177	0.0019	0.0209
45	25	180	-25	0.0182	0.0021	0.0217		0.0173	0.0015	0.0202
45	20	180	-20	0.0176	0.0020	0.0213		0.0172	0.0006	0.0196
45	15	180	-15	0.0171	0.0013	0.0210		0.0172	0.0026	0.0191
45	10	180	-10	0.0170	0.0025	0.0208		0.0170	0.0003	0.0187
45	5	180	-5	0.0172	0.0019	0.0206		0.0173	0.0006	0.0184
45	0	0	0	0.0182	0.0025	0.0216		0.0178	0.0012	0.0205
45	0	180	0	0.0182	0.0009	0.0216		0.0178	0.0008	0.0194
45	5	0	5	0.0183	0.0028	0.0225		0.0182	0.0009	0.0227
45	10	0	10	0.0192	0.0014	0.0227		0.0188	0.0006	0.0227
45	15	0	15	0.0201	0.0013	0.0229		0.0196	0.0006	0.0227
45	20	0	20	0.0213	0.0010	0.0233		0.0210	0.0007	0.0229
45	25	0	25	0.0227	0.0010	0.0237		0.0225	0.0007	0.0233
45	30	0	30	0.0251	0.0016	0.0243		0.0249	0.0002	0.0237
45	35	0	35	0.0282	0.0006	0.0250		0.0276	0.0002	0.0243
45	40	0	40	0.0335	0.0012	0.0258		0.0327	0.0005	0.0250
45	50	0	50	0.0373	0.0021	0.0280		0.0365	0.0015	0.0270

45	55	0	55	0.0347	0.0023	0.0293		0.0341	0.0014	0.0283
45	60	0	60	0.0328	0.0009	0.0310		0.0320	0.0014	0.0298
45	65	0	65	0.0325	0.0025	0.0329		0.0312	0.0005	0.0317
45	70	0	70	0.0332	0.0012	0.0351		0.0311	0.0005	0.0338
60	70	180	-70	0.0476	0.0000	0.0309		0.0410	0.0004	0.0280
60	65	180	-65	0.0411	0.0010	0.0315		0.0355	0.0003	0.0282
60	60	180	-60	0.0348	0.0019	0.0310		0.0306	0.0011	0.0276
60	55	180	-55	0.0309	0.0017	0.0298		0.0277	0.0000	0.0264
60	50	180	-50	0.0271	0.0013	0.0284		0.0257	0.0000	0.0251
60	45	180	-45	0.0245	0.0004	0.0271		0.0233	0.0030	0.0240
60	40	180	-40	0.0219	0.0011	0.0259		0.0217	0.0002	0.0227
60	35	180	-35	0.0205	0.0003	0.0249		0.0202	0.0002	0.0217
60	30	180	-30	0.0192	0.0005	0.0241		0.0190	0.0008	0.0207
60	25	180	-25	0.0185	0.0002	0.0235		0.0182	0.0003	0.0199
60	20	180	-20	0.0181	0.0009	0.0230		0.0179	0.0008	0.0192
60	15	180	-15	0.0180	0.0006	0.0226		0.0178	0.0002	0.0186
60	10	180	-10	0.0180	0.0012	0.0223		0.0178	0.0001	0.0182
60	5	180	-5	0.0178	0.0003	0.0221		0.0177	0.0001	0.0178
60	0	0	0	0.0179	0.0013	0.0237		0.0178	0.0007	0.0219
60	0	180	0	0.0179	0.0001	0.0237		0.0178	0.0001	0.0219
60	5	0	5	0.0186	0.0003	0.0253		0.0183	0.0010	0.0260
60	10	0	10	0.0194	0.0002	0.0255		0.0191	0.0017	0.0259
60	15	0	15	0.0201	0.0003	0.0258		0.0196	0.0020	0.0260
60	20	0	20	0.0213	0.0007	0.0263		0.0208	0.0020	0.0262
60	25	0	25	0.0220	0.0004	0.0268		0.0218	0.0004	0.0266
60	30	0	30	0.0232	0.0011	0.0276		0.0231	0.0011	0.0271
60	35	0	35	0.0250	0.0008	0.0285		0.0243	0.0012	0.0278
60	40	0	40	0.0272	0.0009	0.0296		0.0270	0.0004	0.0287
60	45	0	45	0.0309	0.0004	0.0310		0.0300	0.0004	0.0298
60	50	0	50	0.0359	0.0020	0.0326		0.0364	0.0015	0.0312
60	55	0	55	0.0449	0.0020	0.0345		0.0440	0.0022	0.0330
60	65	0	65	0.0562	0.0006	0.0397		0.0547	0.0013	0.0376
60	70	0	70	0.0514	0.0008	0.0431		0.0477	0.0015	0.0407

Table A.3: Table showing 1) the principal plane BRDF data measured by VOSEG for the smooth (light blue) and rough (light orange) Apollo 11, 10084 samples used in this study, and 2) the associated best fit Hapke BRDF model predictions for each viewing angle, when the opposition effect is turned off.

Table A.4 shows the principal plane BRDF data measured by VOSEG for the smooth and rough Apollo 16, 68810 samples, and the associated best fit Hapke BRDF model predictions for each viewing angle, when the opposition effect is turned off. This data was plotted in **Figures 83** and **84**.

Viewing angles (°)				*Smooth Apollo 16*				*Rough Apollo 16*		
θ_i	θ_r	θ_a	θ_r *(full plane)*	*BRDF (Sr^{-1})*	*BRDF error (±)*	*Hapke BRDF (Sr^{-1})*		*BRDF (Sr^{-1})*	*BRDF error (±)*	*Hapke BRDF (Sr^{-1})*
15	70	180	-70	0.0439	0.0018	0.0500		0.0351	0.0009	0.0458
15	65	180	-65	0.0402	0.0028	0.0483		0.0344	0.0014	0.0441
15	60	180	-60	0.0382	0.0012	0.0467		0.0340	0.0006	0.0424
15	55	180	-55	0.0376	0.0012	0.0451		0.0340	0.0016	0.0409
15	50	180	-50	0.0370	0.0019	0.0437		0.0340	0.0014	0.0395
15	45	180	-45	0.0373	0.0015	0.0424		0.0340	0.0013	0.0383
15	40	180	-40	0.0370	0.0008	0.0412		0.0343	0.0011	0.0372
15	35	180	-35	0.0371	0.0012	0.0402		0.0347	0.0010	0.0363
15	30	180	-30	0.0381	0.0007	0.0394		0.0360	0.0010	0.0355
15	25	180	-25	0.0386	0.0007	0.0387		0.0371	0.0009	0.0349
15	20	180	-20	0.0396	0.0021	0.0381		0.0382	0.0007	0.0344
15	15	180	-15	0.0409	0.0006	0.0377		0.0389	0.0011	0.0340
15	10	180	-10	0.0434	0.0003	0.0374		0.0405	0.0009	0.0337
15	5	180	-5	0.0456	0.0003	0.0372		0.0422	0.0006	0.0335
15	0	0	0	0.0475	0.0003	0.0389		0.0447	0.0002	0.0343
15	0	180	0	0.0475	0.0002	0.0389		0.0447	0.0006	0.0343
15	5	0	5	0.0488	0.0012	0.0408		0.0469	0.0000	0.0352
15	10	0	10	0.0531	0.0013	0.0410		0.0506	0.0015	0.0354
15	20	0	20	0.0605	0.0000	0.0418		0.0573	0.0012	0.0361
15	25	0	25	0.0507	0.0004	0.0424		0.0491	0.0000	0.0366
15	30	0	30	0.0484	0.0018	0.0432		0.0467	0.0008	0.0373
15	35	0	35	0.0472	0.0010	0.0441		0.0461	0.0018	0.0381
15	40	0	40	0.0464	0.0021	0.0452		0.0428	0.0014	0.0390
15	45	0	45	0.0465	0.0011	0.0465		0.0421	0.0014	0.0402
15	50	0	50	0.0453	0.0006	0.0480		0.0421	0.0005	0.0414
15	55	0	55	0.0441	0.0007	0.0497		0.0410	0.0000	0.0429

15	60	0	60	0.0455	0.0016	0.0516		0.0410	0.0008	0.0445
15	65	0	65	0.0443	0.0009	0.0537		0.0406	0.0005	0.0464
15	70	0	70	0.0452	0.0022	0.0560		0.0404	0.0009	0.0484
30	70	180	-70	0.0473	0.0039	0.0581		0.0371	0.0019	0.0489
30	65	180	-65	0.0446	0.0015	0.0534		0.0366	0.0015	0.0469
30	60	180	-60	0.0434	0.0024	0.0503		0.0360	0.0024	0.0451
30	55	180	-55	0.0427	0.0011	0.0480		0.0356	0.0011	0.0433
30	50	180	-50	0.0418	0.0038	0.0462		0.0351	0.0007	0.0417
30	45	180	-45	0.0410	0.0009	0.0447		0.0349	0.0014	0.0403
30	40	180	-40	0.0404	0.0024	0.0434		0.0352	0.0000	0.0391
30	35	180	-35	0.0400	0.0031	0.0422		0.0347	0.0010	0.0381
30	30	180	-30	0.0398	0.0007	0.0413		0.0353	0.0005	0.0372
30	25	180	-25	0.0399	0.0007	0.0405		0.0358	0.0019	0.0365
30	20	180	-20	0.0399	0.0024	0.0399		0.0362	0.0004	0.0360
30	15	180	-15	0.0398	0.0025	0.0394		0.0370	0.0017	0.0355
30	10	180	-10	0.0397	0.0007	0.0390		0.0376	0.0021	0.0352
30	5	180	-5	0.0405	0.0007	0.0388		0.0387	0.0008	0.0350
30	0	0	0	0.0412	0.0011	0.0406		0.0398	0.0008	0.0358
30	0	180	0	0.0412	0.0011	0.0406		0.0398	0.0020	0.0358
30	5	0	5	0.0427	0.0016	0.0426		0.0406	0.0008	0.0368
30	10	0	10	0.0429	0.0016	0.0428		0.0423	0.0004	0.0369
30	15	0	15	0.0468	0.0017	0.0432		0.0456	0.0004	0.0373
30	20	0	20	0.0507	0.0009	0.0437		0.0480	0.0004	0.0377
30	25	0	25	0.0584	0.0009	0.0444		0.0558	0.0013	0.0383
30	35	0	35	0.0600	0.0029	0.0463		0.0581	0.0015	0.0400
30	40	0	40	0.0561	0.0021	0.0476		0.0532	0.0015	0.0411
30	45	0	45	0.0519	0.0006	0.0490		0.0498	0.0011	0.0423
30	50	0	50	0.0499	0.0006	0.0507		0.0485	0.0006	0.0438
30	55	0	55	0.0489	0.0007	0.0526		0.0473	0.0013	0.0455
30	60	0	60	0.0501	0.0009	0.0548		0.0475	0.0008	0.0474
30	65	0	65	0.0503	0.0037	0.0573		0.0470	0.0009	0.0495
30	70	0	70	0.0522	0.0018	0.0601		0.0470	0.0011	0.0519
45	70	180	-70	0.0601	0.0043	0.0542		0.0420	0.0037	0.0552
45	65	180	-65	0.0546	0.0043	0.0536		0.0400	0.0020	0.0530
45	60	180	-60	0.0509	0.0011	0.0527		0.0381	0.0011	0.0500
45	55	180	-55	0.0479	0.0044	0.0518		0.0360	0.0007	0.0479

45	50	180	-50	0.0442	0.0039	0.0504		0.0350	0.0006	0.0459
45	45	180	-45	0.0417	0.0026	0.0488		0.0338	0.0001	0.0441
45	40	180	-40	0.0402	0.0016	0.0472		0.0333	0.0011	0.0426
45	35	180	-35	0.0393	0.0000	0.0458		0.0334	0.0015	0.0414
45	30	180	-30	0.0389	0.0043	0.0446		0.0332	0.0019	0.0403
45	25	180	-25	0.0384	0.0027	0.0437		0.0335	0.0009	0.0395
45	20	180	-20	0.0385	0.0013	0.0429		0.0340	0.0013	0.0388
45	15	180	-15	0.0377	0.0020	0.0423		0.0342	0.0009	0.0382
45	10	180	-10	0.0380	0.0013	0.0419		0.0349	0.0013	0.0379
45	5	180	-5	0.0389	0.0020	0.0417		0.0367	0.0013	0.0377
45	0	0	0	0.0401	0.0009	0.0436		0.0380	0.0004	0.0385
45	0	180	0	0.0401	0.0009	0.0436		0.0380	0.0002	0.0385
45	5	0	5	0.0403	0.0008	0.0458		0.0382	0.0008	0.0395
45	10	0	10	0.0413	0.0010	0.0460		0.0387	0.0004	0.0397
45	15	0	15	0.0425	0.0008	0.0465		0.0399	0.0004	0.0401
45	20	0	20	0.0446	0.0000	0.0471		0.0439	0.0000	0.0407
45	25	0	25	0.0475	0.0004	0.0480		0.0459	0.0004	0.0414
45	30	0	30	0.0499	0.0009	0.0490		0.0503	0.0013	0.0423
45	35	0	35	0.0567	0.0000	0.0503		0.0561	0.0000	0.0434
45	40	0	40	0.0632	0.0030	0.0518		0.0630	0.0015	0.0447
45	50	0	50	0.0715	0.0009	0.0557		0.0692	0.0000	0.0481
45	55	0	55	0.0675	0.0026	0.0582		0.0645	0.0000	0.0502
45	60	0	60	0.0651	0.0022	0.0610		0.0618	0.0007	0.0527
45	65	0	65	0.0647	0.0026	0.0643		0.0608	0.0035	0.0555
45	70	0	70	0.0646	0.0009	0.0681		0.0593	0.0009	0.0588
60	70	180	-70	0.0823	0.0024	0.0573		0.0464	0.0012	0.0619
60	65	180	-65	0.0730	0.0028	0.0593		0.0430	0.0038	0.0609
60	60	180	-60	0.0657	0.0008	0.0589		0.0414	0.0008	0.0581
60	55	180	-55	0.0593	0.0014	0.0572		0.0384	0.0013	0.0550
60	50	180	-50	0.0549	0.0012	0.0550		0.0373	0.0019	0.0522
60	45	180	-45	0.0501	0.0022	0.0527		0.0363	0.0006	0.0498
60	40	180	-40	0.0466	0.0011	0.0506		0.0355	0.0005	0.0478
60	35	180	-35	0.0431	0.0005	0.0488		0.0340	0.0010	0.0461
60	30	180	-30	0.0413	0.0028	0.0474		0.0333	0.0023	0.0448
60	25	180	-25	0.0400	0.0005	0.0462		0.0339	0.0009	0.0436
60	20	180	-20	0.0398	0.0022	0.0452		0.0338	0.0013	0.0427

60	15	180	-15	0.0395	0.0000	0.0445		0.0351	0.0017	0.0421
60	10	180	-10	0.0395	0.0017	0.0440		0.0360	0.0013	0.0416
60	5	180	-5	0.0398	0.0008	0.0437		0.0371	0.0013	0.0413
60	0	0	0	0.0394	0.0004	0.0471		0.0380	0.0013	0.0424
60	0	180	0	0.0394	0.0008	0.0471		0.0380	0.0014	0.0424
60	5	0	5	0.0391	0.0008	0.0507		0.0374	0.0009	0.0437
60	10	0	10	0.0400	0.0009	0.0510		0.0393	0.0015	0.0440
60	15	0	15	0.0415	0.0003	0.0516		0.0417	0.0024	0.0445
60	20	0	20	0.0451	0.0024	0.0524		0.0444	0.0008	0.0452
60	25	0	25	0.0470	0.0010	0.0535		0.0474	0.0006	0.0462
60	30	0	30	0.0494	0.0022	0.0549		0.0503	0.0010	0.0474
60	35	0	35	0.0543	0.0007	0.0566		0.0538	0.0004	0.0488
60	40	0	40	0.0576	0.0012	0.0586		0.0592	0.0008	0.0506
60	45	0	45	0.0650	0.0019	0.0611		0.0640	0.0004	0.0527
60	50	0	50	0.0734	0.0024	0.0640		0.0734	0.0009	0.0552
60	55	0	55	0.0864	0.0013	0.0674		0.0875	0.0035	0.0583
60	65	0	65	0.1042	0.0007	0.0765		0.0989	0.0007	0.0661
60	70	0	70	0.0973	0.0033	0.0824		0.0879	0.0008	0.0712

Table A.4: Table showing 1) the principal plane BRDF data measured by VOSEG for the smooth (light blue) and rough (light orange) Apollo 16, 68810 samples used in this study, and 2) the associated best fit Hapke BRDF model predictions for each viewing angle, when the opposition effect is turned off.